A STUDY OF FLAME DEVELOPMENT WITH ISOOCTANE-ALCOHOL BLENDED FUELS IN AN OPTICAL SPARK IGNITION ENGINE

Submitted in accordance with the requirements for the degree of

Doctor of Philosophy

By

Benjamin G Moxey

BEng (Hons.)

Department of Mechanical, Aerospace and Civil Engineering

College of Engineering, Design and Physical Sciences

Brunel University London

September, 2014

The candidate confirms that the work submitted is his own and that appropriate credit has been given where reference has been made to the work of others.

Abstract

The work was concerned with experimental study of the turbulent flame development process of alcohol fuels, namely ethanol and butanol, in an optically accessed spark ignition research engine. The fuels were evaluated in a single cylinder engine equipped with full-bore overhead optical access operated at typical stoichiometric part-load conditions with images captured using high-speed natural light imaging techniques (or chemiluminescence).

The differences in flame development between the fuels was analysed to understand better the impact of high and low alcohol content fuels on combustion. Advanced image analysis, in conjunction with Ricardo WAVE simulation, allowed for the conclusion that the faster burning exhibited by ethanol was the result of the marginally higher laminar burning velocity providing a faster laminar burn phase and accelerating the flame into the turbulent spectrum thus reducing bulk flame distortion and better in-cylinder pressure development. Such physical reactions are often over-looked in the face of chemical differences between fuels.

A further study into the variation of maximum in-cylinder pressure values was conducted focussing on iso-octane and ethanol. This study identified two phenomena, namely “saw-toothing” and “creep” in which cluster of cycles feed into one another. From this it became clear that the presence of high pressure during the exhaust process had a large influence on the following cycles. This is another often overlooked phenomenon of direct cycle-to-cycle variation whereby in-cylinder pressures during blowdown can dictate the duration, load or stability output of the following cycle.

Finally the work investigated the impact on flame development of alcohol fuels when the overlap duration was altered. While the engine produced counter-intuitive figures of residual gas, ethanol was confirmed as having greater synergy with EGR by displaying less impacted combustion durations c.f. iso-octane. Care should be taken however when analysing these results due to the unique valve configuration of the engine.

Acknowledgements

I wish to sincerely thank my supervisor, Professor Alasdair Cairns, for his invaluable guidance and help during this work. He is the only reason I've been able to get as far as I have academically due to various tutoring meetings and 'catch-up' sessions at the start and the patience to proof-read chapter after chapter sent over to him. I would also like to thank Professor Hua Zhao for his wise words when sought.

I am also eternally grateful of my colleague, Simon Dingle, for his advice and help during the project but especially at the beginning. None of this work would be at all possible without the excellent help of the barrage of technicians in the laboratory: Andy Selway, Ken Anstiss, Clive Barrett, Keith Withers, Peter Wilson, Guy Fitch and Les & Paul from Stores – the Waldorf and Astoria of Brunel.

Financial support for this work was very gratefully received from the Thomas Gerald Gray Charitable Trust Scholarship Scheme and from the School of Engineering and Design. My upmost thanks go to Mrs Lyn Gray for being able to make the dream of studying a passion into a reality and to Professor Nicos Ladommatos for his probing questions and challenging thinking at every encounter.

Thank you also to my parents, David and Julie. While you were not able to support me as a unit during this work, I know you both were there for me during this in your own way. That is all I need and it fills my heart to have it.

Final thanks go to Ashley; often times you are/were the only one who keeps/kept me sane and upright. Your support and willingness to change plans at the last minute and to lose your boyfriend to the office/lab for hours on end has been invaluable. You are my rock and I dedicate this thesis to you. And on the plus side, you did get a sparkly new ring and frequently-misspelt new last name out of it. Thank you with all my heart.

This thesis took one thousand and forty-eight days to write between November 13th 2011 and September 26th 2014. During writing I consumed 125 gallons of coffee, 98 gallons of tea, ran roughly 555 miles and flew 34,961 miles. The average daytime temperature 11.402° C. I wrote 58,784 words over 266 pages and in this time I lost four pairs of socks but gained a wife.

Contents

Abstract ii

Acknowledgements iii

Contents iv

Figures ix

Tables xxi

Nomenclature xxiii

1. Introduction 1

1.1 General Background 1

1.2 Thesis Outline 1

2. Combustion in Spark Ignition Engines 4

2.1 Introduction 4

2.2 History of the Internal Combustion Engine 4

2.2.1 Huygens and Otto 4

2.2.2 Ricardo and Octane Numbers 5

2.3 Turbulent Combustion 10

2.3.1 Basics of Turbulent Combustion 10

2.3.2 Turbulent Flow 11

2.3.3 Charge Motion Effects 14

2.3.3.1 Swirl 14

2.3.3.2 Squish and Tumble 15

2.3.4 Ignition 16

2.3.5 Processes of Laminar and Turbulent Combustion 18

2.3.5.1 Laminar Pre-mixed Combustion 18

2.3.5.2 Turbulent Combustion 21
2.4 Exhaust Gas Recirculation 24
2.4.1 Internal and External EGR 24
2.4.2 EGR Fuel Economy Effects 26
2.4.2 EGR Emission Effects 26
2.4.3 Synergy with Alcohol Fuels 27
2.5 Alcohol Fuels 28
2.5.1 Background and Alcohol Types 28
2.5.2 Interaction with EGR and other Vehicle Modifications 32
2.5.3 Performance Characteristics 34
2.5.4 Emissions Effects 37
2.5.4.1 Nitrogen Oxides (NOx) 37
2.5.4.2 Carbon Monoxide 38
2.5.4.3 Unburnt Hydrocarbons 38
2.5.4.4 Unregulated Emissions 38
2.5.4.5 Emissions After-Treatment 39
3. Experimental Facilities and Diagnostics 56
3.1 Introduction 56
3.2 Lister TS-1 Assembly 56
3.2.1 Research Engine Background 56
3.2.2 Basic Engine Geometry 56
3.2.3 Ignition 58
3.2.4 Ports and Valvetrain 59
3.3 Optical Head Assembly 60
3.3.1 Window Material and Installation 60
3.3.2 Other optical opportunities 62

3.3.3 Testing and Shakedown 62
3.4 Mixture 62
3.4.1 Airflow 63
3.4.2 EGR System 64
3.4.3 Fuel Supply 64
3.5 Control and Diagnostics 65
3.5.1 Engine and Dynamometer 66
3.5.2 Ignition and Injection Control Board 66
3.5.3 High-Speed Camera Timing 67
3.5.4 Pressure Logging 67
3.5.5 Temperature Logging 69
3.5.6 Speed and Crank Angle Measurement 69
3.5.7 Crank Angle Encoder 70
3.5.8 Testing Procedure 71
4. Flame Imaging Techniques and Analysis 82
4.1 Introduction 82
4.2 Natural Light Flame Imaging 84
4.3 Schlieren and Shadowgraph Flame Imaging 88
4.3.1 Profile 88
4.3.2 Distinctions between Methods 89
4.4 Laser Sheet Flame Imaging 90
4.4.1 Mie Scatter 91
4.4.2 Planer Laser Induced Fluorescence (PLIF) 92
4.5 Comparison of Imaging Methods 93
4.6 Flame Image Processing 97
4.7 Experimental Procedure 97

4.7.1 Intensifier Sweep 98

5. Optical & Thermodynamic Processing **115**

5.1 Introduction 115

5.2 Engine Characterisation 115

5.2.1 Glass vs. Metal 116

5.2.1.1 Motored 116

5.2.1.2 Combustion 116

5.2.2 Central versus Side Spark 117

5.2.3 Ethanol versus Iso-Octane with Variable Spark 120

5.2.4 Valve Overlap and Timing 121

5.2.5 Pressure and Volume Curves 121

5.3 Cyclic Variation, Sample Size and Cycle Selection 122

5.4 Image Capture Methods 125

5.4.1 Flame Image Processing 125

5.4.2 Flame Image Read 126

5.4.3 Noise Suppression and Masking 126

5.4.4 Image Binarisation 127

5.4.5 Calculations 128

5.4.6 Flame Radius 129

5.4.7 Flame Speed and Shape Factor 130

5.5 Heat Release Analysis 131

5.5.1 Rate of Heat Release/Rassweiler and Withrow 131

5.5.1.1 Signal Filtering 133

5.5.2 Wiebe Function 134

5.5.3 Wiebe Function vs. Rate of Heat Release 135

5.6 Thermodynamic Analysis 135

5.6.1 Basic Model 136
5.6.2 Inlet and Exhaust 136
5.6.3 In-Cylinder Modelling 137
5.6.4 Model Validation 139
6. Results and Analysis **163**
6.1 Introduction 163
6.2 Optical Fuels Comparison 166
6.2.1 Fixed versus MBT Spark Timing (λ=1) 166
6.2.2 Cyclic Variation Effects (Fixed Spark, λ=1) 167
6.2.3 Air-to-Fuel Ratio Effects (MBT) 169
6.2.4 Effects of Carbon Levels in Alcohol (MBT, λ=1) 172
6.3 Cyclic Variation Phenomena and its Impact on Fuel Types 174
6.3.1 Sawtoothing Effects 174
6.3.2 Creep Effects 177
6.4 Valve Overlap Duration Sweep 179
7. Conclusions and Recommendations **217**
7.1 Summary of Findings 217
7.2 Recommendations for Future Work 223
8. References **226**

Figures

Figure 2.1	Diagram of the Hugyens engine [Taken from Cummins Jr., 1976]	Page 41
Figure 2.2	Diagram of the atmospheric engine developed by Nikolaus Otto in 1876 [Taken from Cummins Jr., 1989]	Page 41
Figure 2.3	Cross-section of the turbulent head developed by Harry Ricardo in 1920 [Ricardo, 1968]	Page 42
Figure 2.4	The steady development of both the octane number of fuel and the compression ratio over time. [Adapted from McCarthy, 2011]	Page 42
Figure 2.5	Thermal Efficiency as a function of the compression ratio for differing gamma values where $\gamma = c_p/c_v$	Page 43
Figure 2.6	Thermodynamic split of losses compared to the ideal constant-volume cycle at 2000 RPM and 3 bar Net MEP [Adapted from Kulzer et al., 2006]	Page 43
Figure 2.7	The laminar burning velocity for several fuels as a function of the equivalence ratio [Metghalchi & Keck, 1980 & 1982]	Page 44
Figure 2.8	Comparison between laminar and turbulent burning flame fronts for a pre-mixed composition [Adapted from Stone, 1992]	Page 44
Figure 2.9	(a) Cylinder Pressure vs crank angle for three distinct spark timings (overadvanced, MBT and retarded); (b) Effect of spark advance on the brake torque highlighting MBT for a given engine [adapted from Amann, 1985]	Page 45
Figure 2.10	The effects spark plug gap width on the AFR at the lean limit point. [adapted from Heywood, 1988]	Page 45
Figure 2.11	General correlation of turbulent burning velocities in terms of dimensionless groups [adapted from Abdel-Gayed, Al-Khishali and Bradley, 1984]	Page 46
Figure 2.12	Borghi diagram showing the different regimes of turbulent premixed flames [Peters, 1986; Borghi, 1988]	Page 46
Figure 2.13	Various turbulent flame regimes in an engine on a graph of the Damköhler number versus the turbulent Reynolds number [Abraham, Williams and Bracco, 1985]	Page 47

Figure 2.14	A BMEP trace of an advanced downsized engine showing three keys areas where EGR would be employed [Moxey et al., 2012]	Page 47
Figure 2.15	Example of the external EGR routing employed by Cairns, Blaxill and Irlam [2006]	Page 48
Figure 2.16	NOx emissions in ppm against an increasing amount of EGR [Heywood, 1988]	Page 48
Figure 2.17	Conversion efficiency for NO, CO and HC for a three-way catalyst as a function of the AFR [Heywood, 1988]	Page 49
Figure 2.18	The volumetric energy content of ethanol gasoline blends displaying the fact that as the ethanol content rises, the energy content falls in a linear fashion [Turner et al., 2007]	Page 49
Figure 2.19	Experimental values of the enthalpy of vaporisation of a fuel mixture for increasing ethanol content [Kar et al., 2008]	Page 50
Figure 2.20	Comparing the vapour pressure of both gasoline and ethanol and effect temperature has on the theoretical AFR [Nakajima, Saiki and Goryozono, 2007]	Page 50
Figure 2.21	a) Torque curve for both single and dual intake valves over time and b) the pressure curve showing the load increase to cause the misfire [Nakajima , Saiki and Goryozono, 2007]	Page 51
Figure 2.22	Engine torque at varying speeds with increasing methanol content (by percentage) [Suga and Hamazaki, 1992]	Page 51
Figure 2.23	BSFC reductions as the engine load rises from 2 bar to 4 bar at 2000RPM indicating performance of the fuels while downsizing [Cairns et al., 2009]	Page 52
Figure 2.24	The rise in BSFC as the engine speed rises from 2000RPM to 4000RPM at 2 bar BMEP, also showing the cost of downsizing [Cairns et al., 2009]	Page 52
Figure 2.25	NOx emissions for ethanol blends at differing speeds and loads showing that NOx emissions in alcohol combustions are not dependent on speed or load [adapted from Wallner and Frazee, 2010]	Page 53
Figure 2.26	CO emissions for ethanol blends at differing speeds and loads [adapted from Wallner and Frazee, 2010]	Page 53

Figure 2.27 HC emissions for ethanol blends at differing speeds and loads showing that HC emissions in alcohol combustions are not dependent on speed or load [adapted from Wallner and Frazee, 2010] Page 54

Figure 2.28 The acetaldehyde levels for gasoline and ethanol at differing speeds showing the much higher levels of emission from ethanol than from gasoline [adapted from Varde and Manoharan, 2009] Page 54

Figure 2.29 Aldehyde emissions over the LA-4 cycle for an M85 fuelled Honda FFV [Suga and Hamazaki, 1992] Page 55

Figure 3.1 A Lister TS-1 engine with cut-away to display the single cylinder Page 74

Figure 3.2 **a.** Overhead view of the re-designed Lister head with the inlet valves shown in blue, the exhaust valves shown in red, the side windows in green and spark location identified in purple
b. A cross-sectional view of the engine showing the inlet and exhaust runner geometry Page 75

Figure 3.3 Schematic of the experimental engine control, image capture and data acquisition systems Page 76

Figure 3.4 An image of the engine showing the belt and pulley arrangement with the intake cam on the right of the image and exhaust on the left. The belt is driven off a pulley connected to the crankshaft via a toothed gear Page 77

Figure 3.5 An image of the engine showing the locations of the thermocouples for temperature logging with the belt and pulley arrangement in the foreground Page 78

Figure 3.6 Cross-sectional view of the cylinder head, looking from the bottom of Figure 3.2a with the inlet on the right. Circled in red are two of the eight clamping bolts Page 79

Figure 3.7 A breakout from the above cross-section showing the window and its clamping shoe Page 79

Figure 3.8 A schematic diagram of the engine's intake system indicating the passage of air through the throttle, plenum and heater before being mixed with the fuel Page 80

Figure 3.9 A schematic diagram of the engine's fuelling system. The 5L fuel tank leading to fuel pump and filter before being Page 80

injected into the intake manifold

Figure 3.10 Screenshot of the data acquisition software. Figure 3.9 a is 'YanTech' GUI, a Brunel University, in-house software allowing for interaction with the DAQ card. Figure 3.9 b is the MBE Easimap 6 GUI for controlling the ECU and dictating spark timing and fuel duration as well as displaying the TPS information Page 81

Figure 4.1 The design for the Bowditch piston as taken from the US Patent filed for invention [Bowditch 1960] Page 102

Figure 4.2 Smith's captured density profile in a) an oscillogram output of the intensity of the light scattered from the laser beam as a function of the distance through the flame and b) a schematic of the oscillogram's display clearly showing a pocket of unburnt gas 'trapped' behind the flame front. [Smith, 1982] Page 103

Figure 4.3 Shadowgraph images of flames propagating towards the camera at differing engine speeds, the speed in RPM is noted in the top left hand corner of the slates with the piston speed noted in the bottom right [Smith, 1982] Page 104

Figure 4.4 Molecules becoming excited by exothermic reactions which raise them to an excited state. Their decay then produces a photon. Page 105

Figure 4.5 Typical schlieren setup with concave mirrors and a knife edge to clean up the resulting image and remove shadowing [Adapted from Zhao and Ladommatos, 2001] Page 105

Figure 4.6 Image of a laser profile displaying laser speckle issues Page 106

Figure 4.7 Gaussian intensity distribution of a typical HeNe laser Page 106

Figure 4.8 A graph displaying the diffuser transmission for the two grades of ground glass trialled in this work displaying differing angles. From this it is clear that the 220 grit gives greater diffusion and the 1500 has a better transmittance [Thorlabs website, Accessed 15th July 2012] Page 107

Figure 4.9 Recollimated shadowgraph setup [Adapted from Zhao and Ladommatos, 2001] Page 107

Figure 4.10 The multiple laser sheet setup used by Hicks et al. [1994] to provide a three dimensional imaging data supply Page 108

Figure 4.11 The calculated angular distribution of the light intensity scattered by a sphere [adapted from Cairns, 2001] Page 108

Figure 4.12 Graphic detailing a standard image captured during combustion. The bore is evident from the 'halo' of light around it with the propagating flame clear in the centre. The burst of light on the right-hand side is to indicate TDC Page 109

Figure 4.13 Photograph of the natural light imaging setup for this experiment showing the NAC MEMRECAM fx6000 joined to a DRS Hadland Intensifier position directly in front of the engine and aligned with the 45° mirror Page 109

Figure 4.14 The cumulative percentage error in COV of IMEP over the 300 cycles captured Page 110

Figure 4.15 Flame radii for the three light intensity settings for the image intensifier. The spark is located at 29° bTDC for stoichiometric, MBT combustion at 1500 RPM Page 110

Figure 4.16 Apparent flame speeds for the three light intensity settings for the image intensifier Page 111

Figure 4.17 Side by side comparison of images for the three intensity settings running stoichiometric fuelling at 5° intervals, beginning 9° after the spark event. The cycles chosen were so because they are closest in PMax and APMax to the mean cycle Page 112

Figure 4.18 Flame radii for the three light intensity settings for the image intensifier. The spark is identified at 35° bTDC for lean (λ=1.22), MBT combustion at 1500 RPM Page 113

Figure 4.19 Flame speeds for the three light intensity settings for the image intensifier Page 113

Figure 4.20 Side by side comparison of images for the three intensity settings running lean limit fuelling (λ=1.22) at 5° intervals, beginning 9° after the spark event. The cycles chosen were so because they are closest in PMax and APMax to the mean cycle Page 114

Figure 5.1 The motored in-cylinder pressure for both glass and metal windows Page 141

Figure 5.2 The temperatures in the head and the exhaust bridge for both the glass and metal windows (motoring only) Page 141

Figure 5.3 Comparison of the combustion pressure traces for the differing window material and spark timing combinations Page 142

Figure 5.4 A side-by-side comparison of the temperatures in the head and exhaust bridge for the differing window material and spark timing combinations Page 142

Figure 5.5 The spark timings and burn durations of the three differing window material and spark timing combinations Page 143

Figure 5.6 The net IMEP and stability for the differing window material and spark timing combinations Page 143

Figure 5.7 In-cylinder pressure traces for the spark locations and timings Page 144

Figure 5.8 Head and exhaust bridge temperatures for the spark locations and timings Page 144

Figure 5.9 Net IMEP and stability for each of the spark locations and timings Page 145

Figure 5.10 IMEP vs CA50 for identical spark timings at both central and side locations Page 145

Figure 5.11 Spark and combustion timings for each of the spark locations and timings Page 146

Figure 5.12 Mass fraction burned curves for each of the spark locations and timings Page 146

Figure 5.13 In-cylinder pressure traces for the two fuels and spark plug locations Page 147

Figure 5.14 Head and exhaust bridge temperatures for the two fuels and spark plug locations Page 147

Figure 5.15 Net IMEP and stability for the two fuels and spark plug locations Page 148

Figure 5.16 Spark and combustion timings for the two fuels and spark plug locations Page 148

Figure 5.17 Log Pressure/Log Volume for the mean iso-octane cycle with combustion Page 149

Figure 5.18	Comparison of the two motored cycles – one with iso-octane injected, the other without	Page 149
Figure 5.19	The cumulative percentage error indicating the reducing of COV of IMEP over 300 cycles	Page 150
Figure 5.20	All 300 cycles displayed together with the arithmetic mean cycle, fast cycle and slow cycle superimposed on top	Page 150
Figure 5.21	A cropped version of Figure 5.20 allowing for better understanding of the variation between different cycles after the spark	Page 151
Figure 5.22	The arithmetic mean cycle with its three closest cycles indicating that achieving the 'optimum mean' cycle is impossible	Page 151
Figure 5.23	The arithmetic mean cycle with the theoretical fastest and slowest cycles	Page 152
Figure 5.24	The three cycles closest to the arithmetic mean	Page 153
Figure 5.25	Varying steps of image analysis shown together for the same initial image: Initial image taken with ICCD, mask-filtered binary image and the final inverted white-on-black arrangement (left to right)	Page 154
Figure 5.26	Application of the masking tool in MATLAB to designate the area of the bore	Page 154
Figure 5.27	Example of the issue involved with using the Otsu method of binarisation	Page 154
Figure 5.28	Identification of the triangle region to be used in the triangle value method of binarisation [Zack et al., 1977]	Page 155
Figure 5.29	The best-fit circle (red) superimposed on to the flame contour	Page 155
Figure 5.30	Diagram of a basic low energy pressure trace (black) and the heat release function (red) with the burn duration identified [Adapted from Kirkpatrick, 2006]	Page 156
Figure 5.31	A graph showing the effect of varying the differential interval size when calculating using the ROHR method	Page 156
Figure 5.32	Cropped version of Figure 5.31 showing greater detail of the combustion event	Page 157

Figure 5.33 A graph showing the effect of varying box filter width for calculating using the ROHR method Page 157

Figure 5.34 A cropped version of Figure 5.33 showing greater detail of the combustion event Page 158

Figure 5.35 Comparing the raw data, the maximum interval filter used, the maximum box width used and the 2-stage combination filter for calculating using the ROHR method Page 158

Figure 5.36 Definition of the flame-development angle ($\Delta\theta_d$) and the rapid-burning angle ($\Delta\theta_b$) set over a mass fraction burnt curve [Adapted from Heywood, 1988] Page 159

Figure 5.37 Ricardo WAVE's GUI with the 'Elements' library files on the left side and the model in the centre of the graphical display on the right Page 159

Figure 5.38 The thermodynamic model used for this work. Detailed in Box 1 are the inlet manifold, runners and the fuel injector, in Box 2 is the combustion chamber and engine block and in Box 3 is the exhaust runner Page 160

Figure 5.39 The Engine General Panel in Ricardo WAVE where key engine geometry is entered Page 160

Figure 5.40 The inlet valve lift profile dialog box in Ricardo WAVE Page 161

Figure 5.41 Ricardo WAVE Combustion panel where several models can be chosen from and customised to fit real-world data Page 161

Figure 5.42 WAVE's in-cylinder pressure trace superimposed with the experimental data. This model was run without any blowby modelling. The pink trace is real world data, the blue trace is computer simulated data Page 162

Figure 5.43 WAVE's in-cylinder pressure trace superimposed with the experimental data. This model was run with an assumed 15% blowby. The pink trace is real world data, the blue trace is computer simulated data Page 162

Figure 6.1 In-Cylinder Pressure Traces for the cycle closest to the optical mean for each fuel series under fixed spark conditions and MBT conditions (top and bottom respectively) Page 183

Figure 6.2	Net IMEP and combustion stability figures for the cycle closest to the optical mean for each fuel series under fixed and MBT spark conditions (top and bottom respectively)	Page 184
Figure 6.3	Key mass fraction burned timings for all fuels under fixed spark conditions	Page 185
Figure 6.4	Mean flame radius development for the natural light flame imaged cycles at both fixed and MBT spark conditions (top and bottom respectively)	Page 176
Figure 6.5	Developing flame contours for each of the mean optical cycles of each fuel run under fixed spark conditions. The first contour shown is at 18°bTDC/0.6ms after ignition; subsequent frames are a further 6°CA/0.6ms	Page 187
Figure 6.6	Experimental in-cylinder pressure data for the mean optical cycles and relevant fastest and slowest cycles	Page 188
Figure 6.7	Computed values of unburnt gas temperatures for the three base fuels obtained from the Ricardo WAVE simulation model	Page 188
Figure 6.8	Computed values of laminar burning velocity for the three base fuels obtained from the Ricardo WAVE simulation model	Page 189
Figure 6.9	Calculated values of flame speed for the three base fuels taken from the natural light flame imaged cycles at fixed spark conditions	Page 189
Figure 6.10	Calculated values of shape factor for the three base fuels against the flame radius taken from the natural light flame imaged cycles at fixed spark conditions	Page 190
Figure 6.11	Net IMEP and combustion stability figures of the mean optical cycles and relevant lean and rich cycles for each fuel. From top to bottom: Iso-Octane and Ethanol	Page 191
Figure 6.12	Various mass burned intervals for the mean optical cycles and relevant lean and rich cycles for each fuel. From top to bottom: Iso-Octane and Ethanol	Page 192
Figure 6.13	Computed values for in-cylinder mass during combustion obtained from the Ricardo WAVE simulation model for each fuel. From top to bottom: Stoichiometric, Lean & Rich	Page 193
Figure 6.14	Computed values for the ratio of specific heats during combustion obtained from the Ricardo WAVE simulation model for each fuel. From top to bottom: Stoichiometric, Lean and Rich	Page 194
Figure 6.15	Computed values for unburned gas temperature during combustion obtained from the Ricardo WAVE simulation model for each fuel. From top to bottom: Lean and Rich	Page 195

Figure 6.16 Computed values for in-cylinder pressure obtained from the Ricardo WAVE simulation model compared to experimental data for each fuel. On the left: Iso-Octane and on the right: Ethanol; from top to bottom: Stoichiometric, Lean and Rich Page 196

Figure 6.17 Laminar burning velocity correlations of gasoline/air, ethanol/air, butanol/air and iso-octane/air mixtures [adapted from Beeckmann, Kruse and Peters, 2010] Page 197

Figure 6.18 Laminar burning velocity correlations of iso-octane/air and ethanol/air mixtures [adapted from Gülder, 1982] Page 197

Figure 6.19 Laminar burning correlations from various authors [Bradley, Lawes and Sheppard, 2000] Page 198

Figure 6.20 Calculated values of flame speed against flame radius for the two fuel sets taken from the natural light flame imaged cycles for the lean and rich combustion cycles (top and bottom respectively) Page 199

Figure 6.21 Calculated values of shape factor against flame radius for the two fuel sets taken from the natural light flame imaged cycles for the lean and rich combustion cycles (top and bottom respectively) Page 200

Figure 6.22 In-cylinder pressure traces for the cycle closest to the mean for the two fuel series under stoichiometric MBT conditions Page 201

Figure 6.23 Net IMEP and combustion stability figures for the cycle closest to the mean for the two fuel series under stoichiometric MBT conditions Page 201

Figure 6.24 Key mass fraction burned timings for the cycle closest to the mean for the two fuel series Page 202

Figure 6.25 Mean flame radius development for the natural light flame imaged cycles of the two fuel series Page 202

Figure 6.26 Calculated values of shape factor taken from the natural light flame imaged cycles of the two fuel series Page 203

Figure 6.27 Maximum in-cylinder pressure values relating to each imaged combustion cycle for iso-octane MBT combustion. Creep cases are identified in red, saw-toothing cases in green Page 203

Figure 6.28 Net IMEP figures for the iso-octane saw-tooth cycles identified in green in Figure 6.27 Page 204

Figure 6.29 Key mass fraction burned timings for the iso-octane saw-tooth cycles identified in green in Figure 6.27 Page 204

Figure 6.30 Mean flame radius development for the natural light imaged cycles for the iso-octane saw-tooth cycles identified in green in Figure 6.27 Page 205

Figure 6.31 Calculated values for shape factor for the natural light imaged cycles for the iso-octane saw-tooth cycles identified in green in Figure 6.27 Page 205

Figure 6.32 Ratio of exhaust-to-inlet pressures for the iso-octane saw-tooth cycles identified in green in Figure 6.27, set against PMax values for said cycles Page 206

Figure 6.33 Computed values for in-cylinder mass at IVC for the iso-octane saw-tooth cycles identified in green in Figure 6.27 Page 206

Figure 6.34 Computed values for in-cylinder mass at EVO for the iso-octane saw-tooth cycles identified in green in Figure 6.27 Page 207

Figure 6.35 Computed values for in-cylinder mass at IVC for the iso-octane saw-tooth cycles identified in green in Figure 6.27 Page 207

Figure 6.36 Maximum in-cylinder pressure values relating to each imaged combustion cycle for ethanol MBT combustion. Creep cases are identified in red, saw-toothing cases in green Page 208

Figure 6.37 Key mass fraction burned timings for the ethanol saw-tooth cycles identified in green in Figure 6.36 Page 208

Figure 6.38 Computed values for in-cylinder mass at EVO for the ethanol saw-tooth cycles identified in green in Figure 6.36 Page 209

Figure 6.39 Computed values for in-cylinder mass at IVC for the ethanol saw-tooth cycles identified in green in Figure 6.36 Page 209

Figure 6.40 Key mass fraction burned timings for the iso-octane creep cycles identified in red in Figure 6.27 Page 210

Figure 6.41 Net IMEP figures for the iso-octane creep cycles identified in red in Figure 6.27 Page 210

Figure 6.42 Calculated values for shape factor for the natural light imaged cycles for the iso-octane creep cycles identified in red in Figure 6.29 Page 211

Figure 6.43 Computed values for in-cylinder mass at IVC for the iso-octane creep cycles identified in red in Figure 6.27 Page 211

Figure 6.44 Computed values for in-cylinder mass at IVO for the iso-octane creep cycles identified in red in Figure 6.27 Page 212

Figure 6.45 Valve lift profiles of the inlet cam and the exhaust cam positions for the three overlap cases Page 212

Figure 6.46 Early combustion duration (0-10% mass fraction burned) for each fuel series for the three overlap cases Page 213

Figure 6.47 Combustion duration (10-90% mass fraction burned) values for each fuel series running the three overlap cases Page 213

Figure 6.48 Values for net IMEP for each fuel series running the three overlap cases Page 214

Figure 6.49 COV of IMEP trendlines for the arithmetic mean for each fuel series for the three valve overlap cases Page 214

Figure 6.50 Computed pressure difference between the intake and exhaust valves for the three overlap cases running iso-octane during the overlap period Page 215

Figure 6.51 Pressure difference across the values between EVO and IVC for the three overlap cases running iso-octane Page 215

Figure 6.52 In-Cylinder Pressure for the three fuel sets and overlap cases during the overlap durations Page 216

Tables

Table 2.1	Properties of iso-octane and gasoline compared with two LCA (ethanol and methanol) and hydrogen [adapted from Heywood, 1988; Turner et al., 2007; Li, Zhao and Brouzos, 2008 and ORNL, 2011]	Page 31
Table 2.2	E-85 Fuel Contamination Tests [Galante-Fox et al., 2007]	Page 33
Table 3.1	Basic redesigned Lister-Petter TS-1 Geometry	Page 58
Table 3.2	Fuel properties entered into the ETAS Lambda meter for all fuel blends used [Heywood, 1988; ORNL, 2011 and Coryton, 2013]	Page 65
Table 4.1	Emission peaks of key combustion species in IC engine [Yang, Zhao and Megaritis, 2009]	Page 86
Table 4.2	Comparison of the major methods of visualising flame propagation in the cylinder [Zhao and Ladommatos, 2001; Nori and Seitzmann, 2008]	Page 94
Table 5.1	The test locations and their spark timings	Page 118
Table 5.2	Calculated values for compression ratio and polytropic index	Page 121
Table 5.3	Power and Pressure for the mean experimental data and two WAVE models for validation	Page 140
Table 6.1	Fuel properties of the four baseline fuels [Heywood, 1988; Cairns et al., 2009; Broustail et al., 2011; ORNL, 2011; Coryton, 2013]	Page 164

Table 6.2	Engine Operating Parameters	Page 166
Table 6.3	MBT Spark Timings	Page 166
Table 6.4	Spark Timings of the two fuel sets at each mixture	Page 170
Table 6.5	In-cylinder pressure 10° CA before EVO	Page 174
Table 6.6	Mass fraction and mass of residuals in the cylinder at IVO	Page 176
Table 6.7	Mass of inducted charge constituents and pressures of the inlet, exhaust and in-cylinder at IVC	Page 177
Table 6.8	MBT spark timings for each fuel and overlap setting	Page 180
Table 6.9	Levels of residual gas relative to valve overlap duration	Page 181

Nomenclature

Symbols

a	-	Wiebe function constant
A	mm^2	Area
A_c	mm^2	Cross sectional area of the cylinder
B	mm	Bore
C	mm	Conrod Length
c_p	kJ/kg.K	Specific heat capacity at constant pressure
c_v	kJ/kg.K	Specific heat capacity at constant volume
Da	-	Damköhler number
L	-	Litre (capacity)
Le	-	Lewis number
l_I η	mm	Integral length scale
l_k	mm	Kolmogorov length scale
K	-	Karlovitz stretch factor
Ma	-	Markstein number
m	-	Wiebe function constant
$\dot{m}$	kg/s	Measured flow rate
m_e	kg/s	Entrained mass
m_f	kg/s	Fuel mass
m_r	kg/s	Burned mass
N	RPM	Engine speed
N_c	-	Total number of measurements
N_d	-	Number of data points taken
N_i	-	Total number of measurements inside a given crank angle window
P	bar	Pressure
Q	kJ/s	Heat Transfer
r	mm	Radius
R	-	Gas constant
$\bar{r}$	mm	Mean flame radius
R_c	-	Compression Ratio
R_s	-	Ratio of swirl
R_T	-	Ratio of tumble
Re_T	-	Turbulent Reynolds Number
S	mm	Stroke
S_L	ms^{-1}	Unstretched laminar burning velocity
S_n	ms^{-1}	Stretched laminar burning velocity
S_P	ms^{-1}	Instantaneous piston speed
$\overline{S_P}$	ms^{-1}	Mean piston speed
t	sec	Time
T	K	Temperature
	Nm	Torque
T_f	K	Adiabatic flame temperature
U	ms^{-1}	Fluid velocity
$\overline{U}$	ms^{-1}	Mean flow velocity
u'	ms^{-1}	r.m.s. Turbulence velocity

u'_k	ms^{-1}	Local effective r.m.s. turbulence velocity
u_{te}	ms^{-1}	Turbulent entrainment velocity
V_B	mm^3	Volume of the piston bowl
V_c	m^3	Piston-Head clearance volume
V_d	m^3	Engine displacement volume
v_{sq}	ms^{-1}	Squish velocity
V	ms^{-1}	Velocity
x_b	-	Mass fraction burnt

Greek Symbols

α_1	-	Inlet valve opening
α_2	-	Inlet valve closing
γ	-	Ratio of specific heats
δ	mm	Flame thickness
η	-	Efficiency
θ	-	Crank angle in degrees
λ	-	Relative air/fuel ratio
ρ	kg/m^3	Density
ϕ	-	Equivalence ratio
τ_I	sec	Integral time scale
τ_K	sec	Kolmogorov time scale
ω_s	ms^{-1}	Average angular velocity of the flow
ω_T	ms^{-1}	Average angular velocity of the tumble
x_b	-	Burned gas fraction

Abbreviations

AFR	Air-fuel ratio
AKI	Anti-knock index
APMax	Angle of Maximum Pressure
aTDC	Crank angle after Top Dead Centre
BMEP	Brake mean effective pressure
Buxx	Butanol percentage (xx%) in an Butanol/Iso-Octane fuel blend
bTDC	Crank angle before Top Dead Centre
BSFC	Brake specific fuel consumption
CAxx	Crank angle of xx% mass burnt
CAI	Controlled auto-ignition
CFD	Computational fluid dynamics
CFR	Co-operative fuel research (engine)
CO	Carbon monoxide
CO_2	Carbon dioxide
COV	Coefficient of variation
DAQ	Data acquisition
DBL	Detonation borderline
DI	Direct injection
Exx	Ethanol percentage (xx%) in an Ethanol/Iso-Octane fuel blend
ECU	Engine control unit
EGR	Exhaust gas recirculation
EMS	Engine management system
EU	European Union
EVC	Exhaust valve closing
EVO	Exhaust valve opening

FFV		Flex-fuel vehicle
GHG		Greenhouse gases
HC/uHC		Hydrocarbons/unburnt hydrocarbons
IEGR		Internal exhaust gas recirculation
IMEP		Indicated Mean Effective Pressure
IVC		Inlet Valve Closing
IVO		Inlet Valve Opening
LCA		Low Carbon Alcohol
LHV	kJ/kg	Lower Heating value of fuel
LDV		Laser Doppler Velocimetry
Mxx		Methanol percentage (xx%) in an Methanol/Iso-Octane fuel blend
MBT		Maximum Brake Torque
MFB		Mass Fraction Burnt
MON		Motor Octane Number
NA		Naturally Aspirated
NEDC		New European Drive Cycle
NOx		Nitrogen Oxides
OEM		Original Equipment Manufacturer
OPEC		Organisation of Petroleum Exporting Countries
PFI		Port Fuel Injection
PIV		Particle Image Velocimetry
PLIF		Planar Laser Induced Fluorescence
Pmax		Maximum Pressure
ppm		Parts per Million
ptb		Pounds per Thousand Barrels
RPM		Revolutions per Minute
RON		Research Octane Number
RVP		Reid Vapour Pressure
SI		Spark Ignition
TDC		Top Dead Centre
US/USA		United States/United States of America
VVA/VVT		Variable Valve Actuation/Variable Valve Timing
WOT		Wide Open Throttle

Subscripts and Superscripts

Δ	Difference
°	Degree
ave	Average
c	Combustion
cyl	Cylinder
f	Fuel
g	Gas
i	Indicated
l	Laminar
max	Maximum
me	Mean effective
t	Time Turbulent
v	Volume

Introduction

1.1 General Background

Two main drivers lie behind the push for adopting alcohol fuels in Internal Combustion (IC) engines. The first is to negate environmental damage caused by the combustion of carbon-based fossil fuels [Karman, 2003; Varde and Manoharan, 2009; Wallner and Frazee, 2010] while the second is to seek energy security. With the former, in 2004 transport made up ~23% of the world's greenhouse gas emissions, with road vehicles accounting for roughly three-quarters of that figure [OECD, 2010]. To tackle this, carbon emissions from passenger vehicles in the EU are currently limited to 130 gCO_2/km for 80% of all new vehicle registrations, with planned reduction to 95 gCO_2/km by 2020 [Council Regulation EU, 2009]. In the past few decades the EU has widely adopted the turbo-diesel unit as the favourable solution. However, efficient distillation of crude oil produces large amounts of both gasoline and diesel fuel [Louis, 2001] and as a result of significant turbo-diesel market penetration Europe can become "diesel lean" at times. It is therefore widely acknowledged that in the shorter term gasoline engines must improve and in the longer term suitable alternatives to crude oil must be sought.

If attained from biomass, alcohol fuels present a highly attractive solution provided they can be widely implemented in a near carbon-neutral manner. The use of alcohol fuels in internal combustion engines has been considered since the onset of IC engine propelled automotive transportation [White, 1902; Schelp, 1936]. However, widespread interest has only emerged since the 1990s, with several workers investigating the role of so-called first-generation fuels. Most of the alcohols available in the current Spark Ignition (SI) engine marketplace are gasoline-ethanol blends, with 5-10% volume alcohol typically allowed. In the United States (US), the EPA-implemented Clean Air Act mandated that 10% of all forecourt gasoline must be ethanol (corn-produced); while most of Europe adds up to 5%. The major exception to such low volume blending is Brazil, which produces 'gasohol' from sugar cane containing between 22% and 100% ethanol [Kremer and

Fachetti, 2000]. Beyond this mainstream adoption there are also many markets for Flex-Fuel Vehicles (FFVs). In the US there are currently over 30 types of FFVs running up to 85% ethanol concentration blends (E85) and in 2007 there were an estimated 5 million FFVs on the roads [Gingrich, Alger and Sullivan, 2009] albeit only accounting for ~2% of the total US automotive market. Concerns remain about the ability of first-generation fuels to take a bigger share of the automotive market due to production via feedstock. Therefore next-generation production processes are currently being investigated to produce fuels via sources such as cellulose, algae or even recovered waste [Griffin, Lave and McLean, 2001; Dohmel, 2008].

Overall, such alternative fuels can reduce carbon impact especially when coupled with technologies such as engine downsizing for further increased efficiency [Bisordi et al., 2012; Stansfield et al., 2012]. Given that competing technologies such as fuel cells or electric vehicles remain so insufficiently advanced the internal combustion engine looks set to remain the dominant source of vehicle propulsion for decades to come (as recently acknowledged in the roadmaps produced by the UK Automotive Council [2013]).

The work presented in this thesis attempts to examine the suitability of alcohol fuels – both neat and blended – when combusted in a Spark Ignition (SI) engine. This will involve high-speed imaging of the moments directly before and after the ignition to gain a greater understanding of the way in which ethanol and butanol fuels burn differently to iso-octane and gasoline fuels and to each other. This data will then be correlated against a one-dimensional, reverse mode analysis thermodynamic model from which further data can be extracted to allow the author to make conclusions about what fundamental charge and mixture differences exist between the fuel types and how these impact upon combustion. In tandem to that study a closer inspection of the nature of cycle-to-cycle variation will be made to gain better understanding of what causes cyclic variation and how each different fuel type responds to those causes.

In addition, a fixed overlap sweep will investigate the effect of differing residual gas fractions upon the fuels as will a sweep of air-fuel mixtures. From these main

streams of work an attempt will be made to draw conclusions from the research and provide direction for future work. With this the author hopes that this work will form part of a big picture of the processes and events that occur during combustion of alcohol fuels in an SI engine.

1.2 Thesis Outline

As stated above the currently reported work is concerned with improving fundamental understanding of the effects of potential future ethanol blends on turbulent flame propagation and hence ultimately in-cylinder pressure development in next-generation SI engines. In Chapter 2, a literature review is presented which includes details of the basic theory and techniques for defining turbulent in-cylinder flow and combustion with conventional and alcohol fuels. In Chapter 3, full details are given of the experimental research engine and the ancillary equipment employed. Provided in Chapter 4 is a review of the optical flame imaging techniques currently available, with justification of the adopted methods also provided. Set out in Chapter 5 are details of the methods used for both the optical and thermodynamic analysis of each imaged cycle as well as a basic characterisation of the engine's performance. In Chapter 6 the results and analysis are provided, which includes novel observations on the behaviour of the fuels in terms of steady state performance and more extreme cases due to cyclic variations. Finally the conclusions and recommendations for future work are provided in Chapter 7.

Chapter 2

Combustion in Spark Ignition Engines

2.1 Introduction

Since its inception the SI engine has been extensively researched in terms of fluid flow, combustion phenomena and fuel effects. With charge mixing dependent on the turbulence of an inducted flow, the effect of various charge motion profiles have been investigated. This includes both swirling and tumbling flows, with the impact of these bulk flows on the formation and evolution of the large and small scale eddies previously well quantified. In addition, further studies have attempted to quantify the interaction of the flow with the combustion and vice versa under varied conditions. From early intrusive techniques to modern non-intrusive laser diagnostics, researchers can now fully describe fluid motion and combustion and, using advanced and correlated computer simulation models, ultimately predict engine performance.

Set out below is an overview of key prior research into such fluid dynamics, ignition characteristics, reuse of exhaust gases to lower combustion temperatures and finally the increasing use of alcohol fuels in internal combustion engines.

2.2 History of the Internal Combustion Engine

2.2.1 Huygens and Otto

The internal combustion engine dates back to work conducted by Christiaan Huygens, who developed gunpowder engines in the late 17th century. In this rudimentary engine (Figure 2.1) a free piston, suspended in a cylinder, was propelled upwards by a combusting charge (usually gunpowder) at the base of the cylinder. While the concept was designed, Huygens apparently never made a working prototype [Cummins Jr., 1976].

In 1867 Nikolaus A. Otto incorporated this design into that of his ‘Atmospheric Engine’ which possessed an armature at the top of the piston that

would rise via expansion due to combustion. This could conceivably run a water pump or similar device, but due to its 13ft headroom, a weight in excess of 50kg and with a three Brake Horsepower (BHP) output, the concept was inappropriate for personal transport. Otto then developed this further with the 1876 'Otto engine' (Figure 2.2). In this he replaced the single-event free piston with a four-stroke engine, designed with a toothed con-rod rotating a large flywheel from which mechanical drive could be attained [Heywood, 1988].

When building the 1876 engine, Otto used coal-gas which had been in use for a decade or so in atmospheric engines but he later moved away from such 'basic' fuels in favour of fuels with a higher calorific content for better combustion. Otto began to look for a way to stratify a liquid fuel mixture in the cylinder for a more progressive burn (akin to what is now referred to as 'stratified charge' combustion). As for the fuelling itself, the trend at the time involved measuring a fuel's volatility only. A 'good' fuel was measured by its relative density and would usually have a paraffin base (giving a modern-day octane number of around 45). These fuels were successful because the maximum compression ratio (R_c) of the time was only 4:1 although the volatile nature of the vapours could cause sudden and sporadic combustion. Eventually, Otto moved engine operation to ligroin (petroleum ether) and finally gasoline [Arcoumanis, 1988].

2.2.2 Ricardo and Octane Numbers

In the late 1910s Sir Harry Ricardo postulated (and subsequently proved via experiment) that if the compression ratio could be raised, then power output and fuel economy could also be improved. During such fundamental work Ricardo was also able to demonstrate that pre-ignition and detonation were different processes (though they are fundamentally related and can occur at the same time or in quick succession) [Ricardo, 1968; Arcoumanis, 1988]. Using a simple window, Ricardo showed that detonation (and its audible output 'knock') was preceded by normal spark ignition combustion and the noise is due to pressure pulses emitted from rapid combustion of the end-gas of a burning mixture which occurs ahead of the flame front. Pre-ignition, on the other hand, was defined as a rapid combustion reaction of a mixture prior to the arrival of the normal flame front, often instigated

by a hot surface or “hot spot” such as a valve face or deposit on the cylinder wall. Both of these phenomena have the ability lead to serious overheating and structural damage to the engine, in particular if the events become self-supporting and lead to “runaway” knock. To delay the knock limit and so attain higher output Ricardo suggested moving to ‘heavier’ fuels, such as benzene, which offered high knock resistance due to an aromatic ring structure [Ricardo, 1968]. He also investigated the knocking characteristics of numerous hydrocarbon fuels, including alcohols and paraffins. It was found that fuels like iso-octane and iso-pentane had good knock and pre-ignition resistance, while the aromatic fuels could be split into two sections: those who have a high knock and pre-ignition resistance (e.g. xylene and toluene) and those which are knock resistant but succumbed easily to pre-ignition (e.g. benzene and cumene).

From such early work Ricardo was able to develop the ‘turbulence head’ in 1920 as shown in Figure 2.3. For some years beforehand it had been known that increased in-cylinder turbulence could lead to faster combustion and improved performance in high-speed engines, again due to prior research by Ricardo [Ricardo, 1968]. This design adopted the side-mounted valves many engines were fitted with at the time but added a restricted inlet runner after the valve which increased turbulence during compression as the inducted gases were pushed back up into the runner. The four-stroke, side-valve engine was then a more efficient and higher output unit with performance closer to that of modern overhead engines but at a much cheaper production cost.

Engine geometry changes are not the only method of increasing engine performance, with prior research of fuel characteristics during turbulent combustion providing significant gains as indicated in Figure 2.4. In the 1930s the Waukesha Company, in collaboration with the Co-operative Fuel Research (CFR) Committee set out to provide a benchmark with which to compare differing fuels [Heywood, 1988; Owen and Coley, 1995]. Most fuels in use today are a blend of the four main hydrocarbon classes: paraffins, cyclanes, olefins and aromatics. One key method used to classify automotive engine fuel is to measure the resistance to knock, defined by the octane number – the higher the octane number, the more

resistant to knock. It is based on a sliding scale with two hydrocarbon fuels at either end. At 'zero' on the scale is n-heptane (nC_7H_{16}) and at '100' is iso-octane (C_8H_{18}). At the time of the test's inception, iso-octane was the highest number available without adding tetraethyl lead. For the evaluation work Waukesha devised the CFR engine – a single cylinder large bore and stroke engine with a variable R_c.

Nowadays two common octane rating methods exist to define either a Research Octane Number (RON) or Motoring Octane Number (MON). For each test, the engine is run with the fuel for analysis in either research or motoring conditions. The Air-to-Fuel Ratio (AFR) is then altered to induce the maximum knock, at which the compression ratio is altered until the knocking occurs at a consistent intensity. Once this is established the engine is stopped, flushed and run again with the two reference fuels splash-blended into the inlet simultaneously until the knocking intensity equals that of the analysed fuel. In the case of MON the test conditions are more severe - with a higher speed, compression ratio and inlet temperature. Ultimately the ratio of iso-octane to n-heptane is used to define the associated octane number (RON or MON).

The octane numbers are not without fault; especially given both are produced by a single-cylinder engine running at a constant speed, temperature and spark timing at wide-open throttle. Consequently both metrics cannot fully account for fluctuations in driving style or ambient conditions. In addition, while RON is correlated at lower speeds, MON is argued to be more relative to higher speeds [Heywood, 1988]. Ultimately real-world driving conditions may fall somewhere between the two values leading some countries including the US to develop the Anti-Knock Index (AKI), defined by:

$$AKI = \frac{RON + MON}{2} \tag{2.1}$$

The RON test is undertaken with the inlet air charge temperature set to 52°C. Ultimately this fails to fully account for "charge cooling" effects and cannot guarantee that the influence of varying fuel boiling points (and/or curves) has been

taken into account. The MON test is arguably less affected by this as it requires the mixture entry temperature to be 149°C [Foong et al., 2013], however an additional key issue is this is unrealistic for a typical intake charge temperature in a modern vehicle.

As well as fuel characteristics, the octane number can vary depending on many factors including ambient temperatures, the engine's running conditions, the engine's fuel or oil history and the engine geometry, most notably the highest point of the piston. The top dead centre (TDC) position is crucial as it dictates the lowest volume of the cylinder (V_c) and is linked to the compression ratio (R_c) by Equation 2.2 [Heywood, 1988]:

$$R_c = \frac{maximum\ cylinder\ volume}{minimum\ cylinder\ volume} = \frac{V_d + V_c}{V_c} \tag{2.2}$$

where V_d is the swept volume. Moving on from RON/MON, an engine's efficiency can also be a contributing factor in extracting the maximum work possible, and therefore the maximum power output, from a fuel. The ideal Otto cycle efficiency is a direct function of the compression ratio as shown in Equation 2.3. It should be noted however that a rising R_c means a falling V_c. As V_c reduces, heat density of the compressed mixture will rise and this can encourage pre-ignition. Regardless, based upon the ideal gas law, Figure 2.5 illustrates the impact of compression ratio on thermal efficiency. Power output and efficiency will rise and eventually plateau at a maximum. One of the physical limits to the R_c is the DBL (Detonation Borderline), the point at which combustion is certain to knock. To raise the DBL ceiling, the combustion duration must be shortened or the auto-ignition time must be increased, the latter of which can be achieved by varying the fuel type to raise the AKI.

$$\eta = 1 - \frac{1}{{R_c}^{(\gamma-1)}} \tag{2.3}$$

The efficiency can also be altered due to changes in the ratio of specific heat values (γ). In Figure 2.5 three different values for γ are used to indicate the impact on efficiency. To raise γ one can increase the excess air in the mixture, making the value closer to that of the diatomic gas value ($\gamma = 1.4$). However, a lower amount of fuel (if at wide open throttle) will cause a drop in power. Furthermore, lean conditions will slow the rate of combustion allowing for stretching and distorting of the propagating flame, resulting in a less stable combustion and, ultimately, misfire. In addition the three-way catalytic converter is no longer capable of efficiently converting engine-out NOx.

In reality such an idealistic approach to efficiency is inappropriate with a tendency to over-estimate thermal efficiency, predominantly due to the assumption of constant volume combustion and the omission of major irreversibilities such as heat transfer and in-cylinder mass blowby. Kulzer et al. [2006] devised a tool for analysing the pressure trace to determine potential sources of thermodynamic loss by comparing the 'perfect engine' to the experimental data. The authors applied the following losses to the ideal engine model (shown in Figure 2.6):

- Combustion phasing from the ideal 50% mass fraction burnt (MFB) location, which will effectively reduce the R_c.
- Incomplete combustion emissions, no combustion is ever 100% so some energy is wasted in Hydrocarbon (HC)/Carbon Monoxide (CO) emissions
- Flame shape and duration effects due to charge motion dynamics
- Gas behaviour due to calorific properties which are a function of pressure and temperature
- Heat losses to the walls and valves
- Gas exchange losses accounting for the negative work done over the cycle or for mass losses past the piston rings (blow-by)
- Mechanical losses due to friction on the piston rings, bearings, valves, cams and numerous other locations.

The end result being that Kulzer et al. were able to demonstrate that Equation 2.3 may indicate an efficiency of 60% for the experimental engine but in actuality this will only be an effective efficiency of ~30% depending on the engine and fuel's unique characteristics and operating conditions. At best modern homogeneous SI engines may achieve a thermal efficiency of ~35% [Zhao, 2009] falling to <10% in some cases at the worst case engine idle condition where pumping and heat transfer losses can be at the relative highest [Heywood, 1988].

2.3 Turbulent Combustion

By characterising the features of turbulent in-cylinder flow and understanding its effect on combustion, it is possible to achieve optimum turbulence conditions thus improving combustion and raising efficiency and power. Alternatively, knowledge and understanding of turbulent flow may allow for efficient lean-burn or high residual rate combustion which, if implemented successfully (usually along with high energy ignition) can improve fuel economy and lower emissions.

There are many 'types' of fluid motion that may be imposed within an engine's cylinder. Axial swirl (often referred to as just 'Swirl') is a bulk air motion during which the fluid rotates about a central axis parallel or coincident to the cylinder's own. Such bulk motion has been previously shown to persist throughout the cycle, with high turbulence generated locally at the walls [Heywood, 1988]. Barrel swirl, better known as 'Tumble', is similar but with the axis perpendicular to the cylinder, where the piston motion results in an acceleration of the bulk flow and (ideally) break-up with rapid generation of smaller-scale turbulence immediately prior to ignition [Pulkrabek, 2004]. In modern engines these bulk flow patterns are often used together to manipulate the turbulence.

2.3.1 Basics of Turbulent Combustion

All internal combustion engines, whether they are spark ignition or compression ignition require two main constituents for pre-mixed combustion: atomised fuel and air. The quantity of fuel is controlled so that the ratio of the mass of air to the mass of fuel is (typically for most "common" SI fuels) in the

combustible range of between 12:1 and 18:1 (for a homogeneous spark-ignition engine). The AFR is, however, misleading under some circumstances as it does not account for when the charge is liquefied. For example, when an engine is cold-started or using alcohol fuels, the fuel could well not be at the desired temperature or pressure to vaporise. Heating the charge prior to ignition can avoid the issues related to cold starts and flame speed but is difficult to effectively implement in a practical and affordable manner. Just as the colder temperatures affect the likelihood of combustion, so too do they affect the speed of the flame. As the unburned gas temperature rises, the turbulent flame speed experienced after the spark also increases, which can have a direct knock-on effect on the subsequent flame development.

Metghalchi & Keck [1980 & 1982] showed the variable nature of the burning velocity and its dependency on the AFR for differing fuels (Figure 2.7). The maximum velocity is actually shown to be slightly rich of stoichiometric as, due to dissociation at high temperatures following combustion, molecular oxygen can be found in the burned gases when at stoichiometric fuelling, thus some additional fuel can be added and burned, increasing the temperature and pressure providing a higher Indicated Mean Effective Pressure (IMEP) [Heywood, 1988]. However, either side of this optimum there is a very steep drop-off in the speeds recorded. Under yet richer conditions, the lack of available oxygen and a low ratio of specific heats initially leads to charge cooling and knock reduction but such a lack of oxygen results in a vast reduction in combustion (and three-way catalyst) efficiency and, ultimately, misfire. However some caution is required when reviewing such data obtained under laminar like conditions due to considerable spread amongst the data, primarily associated with differences in measurement and/or calculation techniques and/or whether or not the influence of flame cellularity and/or stretch have been considered [Heywood, 1988; Gillespie et al., 2000].

2.3.2 Turbulent Flow

There are many advantages to the generation and management of turbulence in the engine's cylinder. It can accelerate burn rates to make combustion more complete and can aid better mixing of the charge as seen in

Figure 2.8 (and as an extension allow for greater dilution tolerance than in a quiescent flow). Without turbulence there would not be enough time for efficient combustion within a typical automotive internal combustion engine. In addition, deliberately increased rates can assist with charge mixture preparation and ensure thorough mixing with any residual gases so as to help ensure high dilution tolerance. Ultimately improved thermal efficiency and increased output may be attained. However, there are limits. Excessive turbulence can cause flame quenching and increased combustion duration, reducing combustion efficiency leading to increased pollutant emissions. By its very nature turbulence varies from cycle-to-cycle as it is unsteady, with both large and small scale motions co-existing in a chaotic manner. Ultimately statistical analysis is required, where under steady conditions the instantaneous local fluid velocity U is defined as [Heywood, 1988]:

$$U(t) = \overline{U} + u(t) \tag{2.4}$$

where $\overline{U}$ is the mean flow velocity and is defined as the time average of $U(t)$. The universal fluctuating velocity component u can be defined by its root mean square value u' to give the turbulence intensity:

$$u' = \lim_{\tau - \infty} \left[\frac{1}{\tau} \int_{t_0}^{t_0+\tau} (U^2 - \overline{U}^2) dt \right]^{\frac{1}{2}} \tag{2.5}$$

Inside any turbulent flow event there are a number of different length scales which help give the flame front its ‘wrinkled’ shape as seen in Figure 2.8. The eddy patterns and size are influenced by the engine’s geometry; the largest is governed by the cylinder height and/or bore and the smallest by molecular diffusion. On an intermediate basis, the turbulence is often characterised by the integral length scale (l_I), which can be imagined to represent an average intensity of the average sized eddies. Experimentally l_I is defined as the integral of the coefficient of the fluctuating velocity (R_x) at two points in the flow with respect to the distance between them [Heywood, 1988; Gillespie et al., 2000]:

$$l_I = \int_0^\infty R_x dx \tag{2.6}$$

where $R_x = \frac{1}{N_d - 1} \sum_{i=1}^{N_d} \frac{u(x_0)u(x_0+x)}{u\prime(x_0)u\prime(x_0+x)}$ and N_d is the number of data points taken.

The application of this technique however is fraught with issues and a vast amount of information must be produced in order to statistically "bottom-out" cyclic variation effects. To calculate the integral length scale, many early researchers attempted to find a correlation between it and the much easier to measure integral time scale (τ_I), which also correlates between two velocities but at a fixed point in space with differing times as opposed to trying to follow the flow around the bore [Heywood, 1988]:

$$\tau_I = \int_0^\infty R_t dt \tag{2.7}$$

where $R_t = \frac{1}{N_d - 1} \sum_{i=1}^{N_d} \frac{u(t_0)u(t_0+t)}{u\prime(t_0)u\prime(t_0+t)}$

From this Tabaczynski [1976] was able to find a link between the scales when the turbulence is relatively weak:

$$l_I = \overline{U}\tau_I \tag{2.8}$$

With Equation 2.8 now providing a method of calculating the largest length scales, a method must be found for calculating the smallest and therefore first scales a flame encounters. This is known as the Kolmogorov length scale (l_k) and at this scale the molecular viscosity will dampen any kinetic energy, dissipating it to thermal energy. So if ε represents the dissipation per unit mass and ν is the kinematic viscosity, then the Kolmogorov length and time scales can be defined as [Tabaczynski, 1976; Heywood, 1988]:

$$l_k = \left(\frac{\nu^3}{\varepsilon}\right)^{\frac{1}{4}} \tag{2.9}$$

$$\tau_k = \left(\frac{\nu}{\varepsilon}\right)^{1/2} \tag{2.10}$$

The Kolmogorov length scale (Equation 2.9) shows the size of the smallest eddies in the flow while the Kolmogorov time scale (Equation 2.10) characterises the momentum-diffusion of the structures.

2.3.3 Charge Motion Effects

2.3.3.1 Swirl

As already mentioned previously, swirl is the rotation of the charge in the cylinder around a central axis. It is invoked by inducting a charge with an initial angular momentum which (largely) persists during combustion. The ratio of the swirl (R_s) defines the magnitude of the swirl and is found by dividing the average angular velocity of the flow (ω_s) by the angular speed of the crankshaft (N) [Heywood, 1988; Pulkrabek 2004]:

$$R_s = \frac{\omega_s}{N} \tag{2.11}$$

There are many ways in which to induce swirl in a charge including adding a tangential component to the flow via shaped or contoured intake manifolds, piston crowns or, similar to those used by Ricardo in his 1920s turbulence head, valve port sculpting. The swirl enhances the mixing of air and fuel in the charge to encourage a homogenous mixture. Early experiments to measure swirl involved using a tracking paddle wheel that pivoted about the cylinder axis [Nagayama, Araki and Iioka, 1977]. This method has now been entirely replaced by Laser Doppler Velocimetry (LDV) and Particle Image Velocimetry (PIV) tracking [Fujimoto & Tabat, 1993; Li et al. 2001]. Indeed Nordgren et al. [2003] performed a comparison between PIV, CFD simulations and a traditional paddle wheel in which they proved that the old-

fashioned wheel could not correct for, or predict, the swirl centre migrating away from the cylinder axis, whereas CFD and PIV could.

In Equation 2.11, the average angular momentum must be used as it can be non-uniform throughout the flow field, being much lower nearer the walls than in the centre due to viscous drag and friction. In the modern engine R_s is constantly changing and can be as high as 5 or 10 [Pulkrabek, 2004]. Much of the angular momentum induced is then lost as the mixture is compressed but swirl is not completely dissipated; indeed, when it is compressed another form of motion can be created: Squish.

2.3.3.2 Squish and Tumble

As the piston arrives at TDC at the end of the compression stroke the mixture on the outer edges of the cylinder undergoes 'squish' – a phenomenon in which the reduction in volume at the outer edges forces the mixture towards the cylinder axis in a radial inward motion. If the engine has a pent-roofed, flat-bottomed combustion chamber, the amount that the mixture will squish is different to one with a flat-top or a bowl piston crown.

The amount of squish is defined by the percentage squish area – the percentage of the cross sectional area of the piston crown ($A_c = \pi B^2/4$) that is nearest to the cylinder head as the piston approaches TDC [Heywood, 1988]. The instantaneous displacement of the charge over the 'inner area' of the squish region (usually the outer section of the piston crown, especially in bowl crowns) required to satisfy the mass conservation is seen as the theoretical value for squish.

For a simple pent-roof design the velocity is:

$$\frac{v_{sq}}{S_P} = \frac{A_s}{b(Z+c)}\left[1 - \frac{Z+c}{C+Z}\right] \tag{2.12}$$

where A_s is the squish area, b is the width of the squish region (usually the bore), Z is the distance between the piston crown top and the cylinder head and C is the

conrod length. While these models do omit blow-by and friction losses they do provide a very good estimate for the squish velocity [Heywood, 1988].

Tumble, however, is more closely linked to swirl in its motion and movements; hence it is sometimes referred to as 'barrel swirl'. Modern engines have designed inlet ports and pent-roofed cylinder heads to impose motions such as this (as investigated by Ricardo, 1920). Similar to Equation 2.11 the tumble ratio is defined as:

$$R_T = \frac{\omega_T}{N} \tag{2.13}$$

where ω_T is the angular speed of the tumble. However this is seen as tough to accurately define in an engine flow field as, like swirl, the axis of rotation is constantly shifting under compression. As a result the reference axis through the centre of mass is an estimate. Tumble ratios have been shown to have a value between 1 and 2 as the piston approaches TDC [Pulkrabek, 2004].

2.3.4 Ignition

Stone [1992] stated that combustion can be divided into three time components for use when analysing the burn duration:

- Initial laminar burn – before the kernel is large enough to be influenced by turbulence, usually 1-10% MFB
- Turbulent burning – wide flame front and pockets of unburnt mixture entrained behind the front. This is usually referred to as 10-90% MFB
- Final burn – last few segments of charge to burn. The thermal boundary slows dramatically here.

For the propagation of a spherical laminar flame, with a radius of r, the geometrical stretch rate is [Bradley & Lung, 1987]:

$$\frac{1}{A}\left(\frac{dA}{dt}\right) = \frac{2}{r}\left(\frac{dr}{dt}\right) \tag{2.14}$$

This stretch rate is very high during the early phase as the flame can buckle and extinguish with only the high temperature plasma between the two spark electrodes able to counteract the stretch rate's desire to quench the flame.

In this situation, spark timing is very important as it will ultimately heavily influence the work extracted from the charge. If the spark is too early in the compression stroke (too advanced from TDC), then the work from the initial flame will be lost as negative work against the rising piston; if the spark is too late (too far retarded towards or beyond TDC), then the expanding volume results in reducing temperatures, slower burning rates and ultimately reducing combustion and thermal efficiencies. The optimum timing lies between the two. Figure 2.9a, from Amann [1985], shows three ignition timings – advanced, close to Maximum Brake Torque (MBT) and retarded. While the advanced spark has the highest release of pressure, the torque output will be low as shown in Figure 2.9b which demonstrates that MBT timing is shortly after the 30° spark timing employed here. For the majority of SI engines MBT relates to 50% of the mass burned occurring (CA50) between 8° and 10° aTDC with an APMax at about 16°aTDC.

As Heywood [1988] points out there are numerous ways of inciting spark ignition and combustion in a cylinder that is primed with combustible material. As shown in Figure 2.10 spark gap geometry can have an effect on the engine's lean limit – if the electrode cannot expel enough energy and/or create a high enough temperature to induce continuous flame propagation, then the flame will quench and misfire will occur. Davis, Bouboulis and Heil [1999] investigated the use of a multi-spark discharge to combat the issue of poor cold starting in FFVs. After running a range of experiments with varied configurations of spark geometry and ethanol blended fuels, it was shown that a multiple spark discharge improved the startability response time of ethanol. The authors postulated that E85 has such poor startability as it is reluctant to vaporise at low temperatures due to the higher heat of vaporisation possessed by ethanol (tests were run at -6°C) which causes liquid fuel to deposit on the spark plug and short out the plug or generally inhibited 'light-off'. At the end of the paper, the authors stated that the multi-spark method provided quicker response times when cold starting and improved idle quality (the

OEM/multi-spark combination allowed for a 100 RPM lower idle point than the other setups).

2.3.5 Processes of Laminar and Turbulent Combustion

At the spark event, the released energy raises the electrical potential across the divide until the mixture between the electrodes ignites. Ionising streams propagate from one electrode to another and the spark arc is formed. This arc is constructed of plasma which expands due to exothermic reactions between the species in the mixture. At this point the bulk motion of mixture around the spark can have a huge impact and is a key source of cyclic variation.

From this point the spark kernel will propagate outwards in a near spherical manner (under laminar conditions) provided the quenching effects of any heat sinks (spark plug, walls, etc.) may be overcome. In reality the IC engine is subject to turbulent conditions however in order to understand such burning an understanding of laminar effects is also required.

2.3.5.1 Laminar Pre-mixed Combustion

Laminar combustion defines not only the combustion of a quiescent mixture ahead of the flame but also the combustion of entrained, unburnt mixture behind the flame front. The unstretched laminar burning velocity (S_L) is the threshold velocity at which the flame initiates combustion and has a huge influence on the remainder of combustion as the interaction between the early combustion and the charge motion will persist during combustion, dictating flow and burn patterns. The laminar burning velocity is dependent on a combination of the mixture composition, the induction temperature and pressure in the cylinder and is defined as the global rate of chemical reaction in the mixture. While accurate data of laminar burning velocities at typical internal combustion engine operating conditions is scarce, studies by Metaghalchi and Keck [1982] and Gülder [1984] arguably provide a good basis of study given the degree of experimental correlation. However, it should be noted that these experiments were conducted in a bomb without optical windows and may not account for the effects of flame cellularity, high turbulence or wall friction.

The laminar burning velocity can be sub-divided into two regimes: Stretched (S_n) and Unstretched (S_L) which are linked by:

$$S_L - S_n = \ell \frac{1}{A}\left(\frac{dA}{dt}\right) \tag{2.15}$$

where ℓ is the proportionality constant. This constant defines the effect of the stretch and is often referred to as the 'Markstein length'. This length defines the amount of stretch the flame will experience. When expressed in dimensionless form it reads as thus:

$$\frac{S_L - S_n}{S_L} = \frac{1}{A}\left(\frac{dA}{dt}\right)\left(\frac{\delta_L}{S_L}\right)\left(\frac{\ell}{\delta_L}\right) = KMa \tag{2.16}$$

where δ_L is the laminar flame thickness and Ma represents the earlier defined Markstein length as a dimenionless group, while the Karlovitz stretch factor (K) is a grouping of the first three terms of Equation 2.16. Laminar flames propagating through any fuel, air and residual gas mixed charge are identified by the laminar flame speed S_L and thickness δ_L. Defining the laminar thickness can be done with a molecular diffusivity D_L [Heywood, 1988]:

$$\delta_L = \frac{D_L}{S_L} \tag{2.17}$$

It is complicated to achieve a reliable value for Ma and though much work has been undertaken to rectify this [Bradley, Lawes and Sheppard, 2000; Gu et al., 2000], it is traditional to instead use another more achievable factor: the Lewis number, which is known to increase in linear proportion to Ma thus giving a known yardstick [Harper, 1989].

$$Le = \frac{k}{\rho c_p D_L} \tag{2.18}$$

where k is the thermal conductivity, ρ is the density of the mixture and c_p is the specific heat capacity of a constant pressure system. A flame, at its core, is a self-sustaining chemical reaction that occurs in the flame front when an unburnt mixture is heated and converted to products. The flame front is actually made of two regions:

- Preheat Zone: Unburnt mixture is heated via conduction. No energy release occurs here
- Reaction Zone: Once the mixture is heated in the preheat zone, it transitions to the reaction zone where an exothermic reaction begins at T_{CRIT}. This temperature is dependent on the fuel composition and mixture ratios

The rate of this transition is governed by the temperature, pressure and species concentration of the burning mixture thus the laminar burning velocity is defined as (where $\dot{m}_r$ is the rate of production of burned gas):

$$S_L = \frac{\dot{m}_r}{A\rho_u} \tag{2.19}$$

It should be noted that the rate of mass entrainment into the flame ($\dot{m}_e$) does not always equate to $\dot{m}_r$ due to the finite flame front. In addition, S_L varies with not only temperature and pressure but the equivalence ratio and fuel type:

$$S_L = S_{L,0}\left(\frac{T_u}{T_O}\right)^{\alpha}\left(\frac{P}{P_O}\right)^{\beta} \tag{2.20}$$

where α, β and $S_{L,0}$ all vary with the fuel type and depend on the equivalence ratio. Ultimately the laminar burning velocity can be considered to provide an indication of the global rate of chemical reaction for a given mixture at a given temperature and pressure. Such a metric hence provides a useful method for describing

potential differences in chemistry at differing pressures and temperatures with different fuels.

2.3.5.2 Turbulent Combustion

During turbulent flame propagation the turbulence can distort and stretch the flamelet so far that fluid dynamic strain becomes applicable, expressed via the Karlovitz stretch factor, which is the ratio of the chemical life of the combustion to the turnover time of the eddies dictating the amount of chemical reactions that can occur before the eddy extinguishes.

$$K = \frac{u'}{l_I}\frac{\delta_L}{S_L} \qquad (2.21)$$

$$K = \frac{\tau_L}{\tau_T}$$

The inverse of the Karlovitz stretch factor is the Damköhler number which was used by Abraham, Williams and Bracco [1985] in their construction of a "map" showing the differing flame regime areas in pre-mixed SI engines – weak turbulence, reaction sheets and distributed regions. From investigations by Abdel-Gayed, Al-Khishali and Bradley [1984] a correlation was found between the Karlovitz factor and the turbulent Reynolds number, Re_T:

$$K = 0.157\left(\frac{u'}{S_L}\right)Re_T^{-0.5} \qquad (2.22)$$

The laminar burning velocity is important to the turbulent entrainment velocity and the former can help define the latter. As the initial laminar flame front propagates from the kernel, it becomes stretched. Here the velocity can be calculated from the rate of entrained mixture into the flame front's reaction zone. Using the stretched laminar burning velocity, the turbulent entrainment velocity can be found:

$$u_{te} = \frac{\dot{m}_e}{\rho_u A_i} \tag{2.23}$$

where A_i is equal to the area of a circle whose radius is equal to that of the flame. From this velocity, Abdel-Gayed published correlations of flame regions (Figure 2.11). The dotted lines across the graph are calculated using the constant stretch factor (Equation 2.16) which is a product of KLe. The magnitude of this stretch factor determines the structure of the flame relating to the level of turbulence in the bore which Abdel-Gayed defines as one of four burning regimes:

- Continuous laminar flame sheet; $KLe < 0.15$
- Flame sheet begins to break-up; $0.15 < KLe < 0.3$
- Localised quenching occurs making a fragmented reaction zone; $0.3 < KLe < 1.5$
- Total quench; $KLe > 1.5$

Figure 2.11 and Equation 2.22 can be condensed to a more compact form over the entire range of displayed results:

$$\frac{u_{te}}{S_L} = 0.88\left(\frac{u'_k}{S_L}\right)(KLe)^{-0.3} \tag{2.24}$$

Following on from, and very similar to, the Abdel-Gayed diagram, in 1988 Borghi confirmed that all flames begin as propagating laminar flames and, when subjected to a turbulent field (charge motion in a combustion chamber) could be sub-divided into different regimes depending on the length and velocity scales of the flame and the turbulence. In Figure 2.12 is the Borghi diagram, which details the differing regions of combustion, based on two non-dimensional parameters: u'/S_L and l_I/δ_L. As stated, all flames begin as laminar flames and these fall into the 'Laminar' area of the Borghi diagram (where $Re_T < 1$). As the flame advances and interacts with the turbulence, the two interacting parameters dictate the flame structure. For the area labelled 'A', the turbulence intensity is so small that the flame thickness (δ_L) is only able to wrinkle the flame front as $\delta_L < l_I$. The next

region is one in which fluctuations of velocity (u') become larger with respect to S_L ($u'/S_L = 1$) thus the flame front begins to ripple and 'corrugate'. This is identified by the label B in Figure 2.12. It is this area that is most susceptible to pockets of unburned gas becoming entrained behind the front. This was further explored by Peters (1986).

The final two regions of the Borghi diagram are concerned with thicker flames, either well distributed with more frequent interactions spread amongst the flame front (Area C of Figure 2.12) or flames which have been modified by turbulence in an unfavourable way (Area D of Figure 2.12). To identify which flames have had their chemical burning times interrupted by fast turnover of eddies in the flame front (relative to the laminar burning time), a ratio between the two must be calculated. This is known as the Damköhler number (Equation 2.25) and when this value is greater than 1 then the flame can be viewed as possessing broken reaction zones. The Damköhler number is one of the most important numbers in engine design and is defined as [1940]:

$$Da = \frac{\tau_T}{\tau_L} = \left(\frac{l_I}{\delta_L}\right)\left(\frac{S_L}{u'}\right) \tag{2.25}$$

This value can be used to help define the reaction time of the mixture. Prior to the work of Borghi, but with much the same result (only from an automotive aspect), Abraham, Williams and Bracco [1985] constructed their "map" of differing regime areas – weak turbulence, reaction sheets and distributed regions were plotted as a function of the Re_T and the Da values (Figure 2.13).

The shaded region of Figure 2.13 is the traditional operating envelope for an SI engine which has been identified as being in the reaction sheet flame region. High speed (the lower right edge) and low load running (lower left edge) give Da and Re_T values below that of the $l_I/\delta_L = 1$ line due to the lower laminar flame speed.

Ultimately the turbulent burning velocity describes the overall influence of the charge motion on the entrainment rate of a given charge at a given pressure

and temperature. The ratio between the turbulent and laminar burning velocity therefore provides an indication of the flame speed ratio, which is a useful metric for comparing the ability of the flow field to increase the rate of unburned mass entrainment.

2.4 Exhaust Gas Recirculation

For the purposes of this work EGR can mean both internal and external methods of recirculating the exhaust gases. Where possible the distinction as to which is being employed will be pointed out but if it is not, EGR can be read as both. In addition 'residuals' will exclusively refer to internal EGR.

2.4.1 Internal and External EGR

External EGR is historically seen as the most common form of recirculating exhaust gases in modern SI engines, mainly due to it being one of the lowest cost options albeit with transient response limitations. Many companies such as Ford [Qi et al., 2011], Fiat [Dimopoulos et al., 2007] and Mitsubishi [Zhao, 1999] have employed external EGR in their SI engines, particularly in the US where stringent NOx emissions legislation has existed for several years. Many, if not all, modern CI engines also utilise external EGR to help control in-cylinder temperature and the particulate-NOx trade-off. The ability for inert exhaust gas to reduce the fuel consumption is primarily due to in-cylinder volume occupation and reduced peak in-cylinder temperatures and heat losses. When exhaust gases are recirculated or retained in the cylinder, they inhabit a volume that previously would have been occupied by fresh charge. As the volume available for fresh charge is reduced by the excess charge trapped in the engine or intake manifold, a wider open throttle with higher in-cylinder and manifold pressures at lower speeds and loads is forced on the system. As a result the pumping losses can be reduced (as indicated in Figure 2.14).

In recent years internal EGR has become much more commonly adopted. Such EGR lessens some of the control issues inherent in using external EGR, thus making transient response easier albeit still with hardware activation limits. Most systems so far entering production have been based upon hydraulically actuated

cam phasers inducing overlap, which typically provide 40-60° crank range [Roberts and Stanglmaier, 1999; Moro, Minelli and Serra., 2001; Kramer and Philips, 2002]. However modern alternatives are beginning to emerge based upon fully variable hydraulic or even electric actuation [Schäfer and Balko, 2007]. Regardless of the mechanism employed, the ability to vary the inlet and exhaust valve events of the SI engine is well-known to facilitate improved compromise between performance, fuel economy and emissions. There are several mechanisms by which a variable valvetrain (VVT) influences fuel consumption:

- Increasing valve overlap, which increases trapped residuals and reduces engine pumping and heat transfer losses (where trapped residual gases occupy part of the cylinder volume and hence allow less vacuum to be used in the inlet systems at part-load)
- Late Inlet Valve Closure (IVC), which further decreases pumping losses by allowing further increased intake pressures (given the piston pushes some of the gas back into the inlet system)
- Late Exhaust Valve Opening (EVO), which can increase expansion work

As a result, fuel economy can typically be improved by up to ~5% over the European drive cycle for example [Cairns, Blaxill and Irlam, 2006]. The choice of optimum VVT strategy is highly dependent on exhaust manifold design, engine compression ratio, cam phasing limits due to valve-to-piston clash, part-load residual dilution tolerance and the importance of Wide Open Throttle (WOT) performance relative to part-load fuel consumption and emissions. A so-called dual-independent VVT strategy (where the timing of the inlet and exhaust valves may be varied independently) offers high overlap potential and reasonable compromise between maximising WOT torque and minimising part-load fuel consumption and emissions [Cairns, Blaxill and Irlam, 2006].

2.4.2 EGR Fuel Economy Effects

When adopting EGR a trade-off exists between fuel economy and engine-out emissions, associated with changing gas temperatures, heat transfer, chemical composition and combustion efficiency. In the study by Cairns, Blaxill and Irlam [2006] the main aim was to seek ways of improving fuel economy by using internal and external EGR at both part and full load. The schematic related to this study is detailed in Figure 2.15. During conventional homogeneous SI operation, small thermal efficiency benefits were ultimately limited by combustion stability due to the slower burning incurred. At part load it was found that the combined internal/external EGR mixture was able to provide ~10% reduction in CO_2 at key sites over the New European Drive Cycle (NEDC).

If IVO was retarded thus raising the residual gas fraction in the cylinder, then there was also a 6% reduction in NOx with a small additional fuel consumption benefit due to more stable combustion (coefficient of variation [COV] of IMEP of 2% compared with 5% without IVO retard). This improvement was postulated to be due to later IVO leading to improved mixing (with the piston further down the bore during valve overlap). At full load the cooled external EGR could be used to help suppress knock, with fuel consumption benefits of ~12% but more notably engine-out HC and CO emissions improvements of up to 80%. The improvement in full-load fuel economy was primarily associated with reduced knocking tendency and hence less full load over-fuelling for exhaust component protection. Such so-called EGR-Boosted operation has been the subject of significant research in recent years [Turner et al., 2009 & 2014; Taylor, Fraser and Wieske, 2010] given the onset of downsized engines, which inevitably spend more time operating at higher engine loads where rich combustion is often incurred (Figure 2.14). This problem is likely to become the focus of more attention if world harmonized type drive cycles come into effect, which should scrutinise a wider range of engine operation.

2.4.3 EGR Emissions Effects

Exhaust gas dilution helps reduce the trapped charge's oxygen concentration giving a proportional reduction in the heat release per unit mass of the mixture. This allows for lower combustion temperatures and, in turn, lower

peak temperatures produce lower NOx. Utilising up to 15-25% EGR allows for a substantial NOx reduction, as seen in Figure 2.16 [Heywood, 1988]. Tullis and Greaves [1996] ran a single cylinder engine at low speed and load which was shown in previous results to be the site at which 15% of the overall NOx emissions were released. By introducing up to 30% EGR and adding a spark timing retardation, they displayed a marked drop in NOx (~60% reduction); however this had to be balanced with a rise in Brake Specific Fuel Consumption (BSFC) and particulates associated with operation upon the combustion stability limit. By altering the injection timings and EGR levels, eventually a balance was struck at 24% EGR with an advanced injection event allowing for an overall 30% reduction in NOx levels with a minor increase in BSFC (around 2.4%). In reality, engine manufacturers tend to leave some "headroom" in combustion stability, which in turn limits fuel consumption benefits normally recorded when mapping EGR. Regardless, the work by Tullis and Greaves arguably demonstrated the ultimate possible reduction in NOx for such an emissions reduction biased part-load calibration. EGR has been previously reported to have little effect on the rates of CO production under stable operation but can cause a rise in unburnt HC levels, primarily associated with lower gas temperatures and reduced combustion efficiency. Regardless, as running EGR allows an engine to operate more effectively in the stoichiometric range; the catalytic convertor has an improved efficiency rate for converting HC and CO in this region as indicated in Figure 2.17. As the combustion stability limit is approached, partial or complete misfire can lead to substantial reduction in combustion efficiency, with potential increase in both CO and unburned hydrocarbons (Heywood, 1988).

2.4.4 Synergy with Alcohol Fuels

For use with alcohol fuels, there are over 30 types of FFV on the market in the USA alone and an estimated 5 million on US roads in 2007. Thus the focus on, and research into, EGR with future fuels will inevitably increase over the next decade. In work published by Gingrich, Alger and Sullivan [2009] the use of EGR in a FFV running gasoline (premium and standard), E50 and E85 (blended with gasoline) was investigated. Alcohol fuels will be discussed in more detail in Chapter 2.5 but alcohol fuels have a higher octane rating and provide lower exhaust gas

temperatures thus they are seen as one potential displacer of gasoline. It is already well known (and extensively laid out so far in this work) that EGR can help inhibit knock and reduce exhaust gas temperatures so the intention was to combine the two to seek gasoline-type performances with drastically lower fuel consumption and emission levels.

With EGR, the effective compression ratio can be increased and ethanol compounds such increase. In Gingrich, Alger and Sullivan's work the R_c for ethanol rose from 9:1 to 11:1. As a result the performance was significantly improved at both full and part load with cooled EGR. This work showed that using EGR allows for more flexibility when designing the engine architecture and with the possibility of variable compression ratio engines in the future, EGR can only help designers further. In addition, the work showed that E85 with EGR could work effectively for improving performance, fuel economy and engine-out emissions.

2.5 Alcohol Fuels

2.5.1 Background and Alcohol Types

The lower carbon alcohols (ethanol and methanol) have the potential to increase engine performance and efficiency over gasoline fuelled levels due to a number of factors including higher latent heat of vaporisation, lower unburned gas temperatures and ultimately improved knock resistance [Brewster, 2007; Turner et al., 2009; Cairns et al., 2009]. This last point in particular makes alcohol fuels a very attractive prospect for downsized SI engines, which are drawing significant global interest at present. Despite differences in burning velocities ultimately it is the higher latent heat of vaporisation that mainly leads to the knock resistance in modern engines [Cairns et al., 2009]. The unique properties of ethanol require careful consideration in engine design. In recent studies [Cowart et al. 1995, Turner et al., 2007] it has been shown that current engine output may be raised by 10-15%, with potential additional gains for dedicated ethanol operation in the future if the power cell design and compression ratio may be fully optimised. However, the low volumetric energy content of the alcohol must be taken into consideration when utilising such fuels. In addition, Kar et al. [2008] investigated the effects that a

gasoline-ethanol blend has on the vaporisation and thermodynamic properties compared to gasoline. It was shown that the blended alcohol fuels exhibit azeotropic tendencies that cause blends with lower ethanol concentrations (0-30%) to evaporate more readily than those with higher ethanol content. Furthermore, with concentrations higher than 85% ethanol, cold starting problems occur due to ethanol's higher latent heat of vaporisation causing induction to occur with a partly-liquidised fuel-air mixture. This has prompted interest in the use of direct-injection to aid cold start performance. For example, Siewart and Groff [1987] discovered they were able to start an engine running neat low carbon alcohols at -29°C by directly injecting a high-pressure stratified charge later in the cycle than usual. While Nakajima, Saiki and Goryozono [2007] found that, when running PFI, deactivating one intake valve could allow for starts at temperatures as low as -10°C. The study also trialled raising the compression ratio from 10.5 to 11.5 to enhance drivability at these lower temperatures to aid in the evaporation of the fuel-air mixture. In addition to such driveability issues, other mechanical upgrades such as material changes to the fuelling system and valve seats must also be considered due to alcohol corrosion and/or detergent effects [Kameoka et al., 2005; Bergström, 2007; Tanaguchi, Yoshida and Tsukasaki, 2007; Galante-Fox et al., 2007].

While many studies have investigated the "lower" carbon alcohols, "higher" carbon alcohols such as pentanol, propanol and butanol have also been proposed for automotive use. In terms of performance, these fuels exhibit a better resistance to water contamination, lower Reid Vapour Pressure and a higher calorific value making the relative fuel consumption better than ethanol based counterparts. Yacoub, Bata and Gautam [1998] investigated the use of several higher carbon alcohol-gasoline fuel blends in a single-cylinder research engine and demonstrated that higher carbon alcohol fuels exhibited a greater resistance to knock when compared to neat gasoline. In addition, aldehyde emissions were much higher than that of gasoline. Previous work [Cairns et al., 2009] studied a high carbon alcohol fuel (butanol) gasoline blend against a low carbon alcohol fuel (ethanol) gasoline blend which have comparable oxygen mass weighting – E10 versus Bu16, both with 3.35% O_2 weighting. These workers concluded that the two fuels exhibited similar

fuel consumption rates and similar spark timings for MBT combustion at part-load. In another study [Malcolm, et al., 2007], a comparison was made between ethanol and butanol splash-blended with iso-octane in a single-cylinder optical research engine with fixed spark timing. The study reported no appreciable difference in terms of combustion characteristics between the three fuels, E25, Bu25 and neat iso-octane, when looking at the optical data produced. A direct comparison of lower carbon alcohol fuels to traditional fuels (both typical gasoline and iso-octane) can be found in Table 2.1 which clearly sets out the benefits and differences. In many applications alcohol fuels are used to blend and dilute petrol to improve performance and reduce emissions without having to make wholesale changes to the power plant.

Property	Iso-octane	Typical Gasoline	Ethanol	Butanol	Hydrogen
Chemical Formula	C_8H_{18}	Varies – up to 150 different chemicals	C_2H_5OH	C_4H_9OH	H_2
Density at Atmospheric Pressure and Temperature (kg/m^3)	0.692	0.72-0.78	0.792	0.81	0.09 (at 0°C)
Lower Heating Value (MJ/kg)	44.3	44.0	26.9	32	120
Stoichiometric AFR	15.13	14.6	9	11.1	34.3
Molecular Weight	114.23	~110	46.07	74.12	2.015
Volumetric Energy Content (MJ/litre)	30.6	31.6	21.2	31.6	0.012
RON	100	95	109	98	130*
Sensitivity (RON minus MON)	0	8-12	18	10	No data
Reid Vapour Pressure (bar)	0.52	1.03	0.18	0.03	-
Latent Heat of Vaporisation (kJ/kg)	308	305	840	430	NA
Auto-ignition Temperature (°C)	No data	260-460	360	314	-
Oxygen Content by Weight (%)	0	0	34.8	21.6	0

Table 2.1: Properties of iso-octane and gasoline compared with two alcohol fuels (ethanol and butanol) and hydrogen [adapted from Heywood, 1988; Turner et al., 2007; Li, Zhao and Brouzos, 2008 and ORNL, 2011]

One issue clear from Table 2.1 is that ethanol has a lower volumetric energy content. As the ethanol content of the fuel rises, the volumetric energy content falls linearly – See Figure 2.18.

2.5.2 Interaction with EGR and other Vehicle Modifications

Kar, Cheng and Ishii [2009] discussed the issue of vaporising the fuels when using PFI. He noted that the maximum vapour pressure was achieved at blends of 20% ethanol. In addition he noted that the enthalpy of vaporisation was not a continuous linear relationship (as had been reported by others) albeit possessing a linear relationship up to around 20% concentration (Figure 2.19). When any hydrocarbon fuel and ethanol mix, they form an azeotrope – a mixture with quite different properties from the two base fuels. Kar, Cheng and Ishii [2009] found that using a higher valve overlap allowed the residual gas temperature to help perform the vaporisation work without reducing the inlet air temperature. This was a phenomenon also reported by Aleferis [2008] who noted that when using PFI E85 the COV of IMEP was higher than that of iso-octane but when moving to DI, while the iso-octane stability remained constant, the E85's rose. This would indicate that the charge cooling effect had encouraged a more unstable burn and that if an engine had a valve overlap with some residual gas backflow then this would pre-heat the charge and aid combustion.

One of the largest challenges faced in adapting the world's fleet for neat alcohol or flex-fuel running are the adaptations that the car will require to efficiently and safely run these new fuel types. It simply is not possible to put high amounts of ethanol fuel into the modern production car and expect it to run both smoothly and with increased efficiency over its entire lifecycle. In 1999 some Japanese fuel suppliers began blending gasoline with 50% alcohol in an attempt to boost profit margins. However, within 18 months consumers were reporting fuel leakage and even fires due to aluminium corrosion [Kameoka et al., 2005]. The materials that may need to be altered on a car (according to Bergström [2007]) are:

- spark plugs
- valves and valve seats
- polymer seals on anything which will be in contact with fuels
- fuel rails, fuel lines and tanks,
- injectors
- pistons

- head material and the crankcase ventilation system

In addition there may need to be engine management system (EMS) changes to the fuel detection system and lambda sensors as well as areas like the cold engine torque limits, boil off points and injection mass flow for the fuels.

The paper referred to earlier by Kameoka et al. [2005] which investigated the Japanese fuel problems ran multiple tests on the material worthiness of standard production parts combined with alcohol fuels. In their testing of forecourt petrol they found what was sold as pure gasoline was in fact often blended with other alcohol fuels such as ethanol, n-propanol, i-propanol, n-butanol and i-butanol. The authors could not ascertain which alcohol had been combined in what quantity so they immersed test pieces in each forecourt fuel and further test pieces into 2 or 3 fuel combinations to examine corrosion levels. Aluminium (the most common metal in an engine's fuelling system) was found to exhibit corrosion in all fuels; in most cases total corrosion had occurred by the end of the 480 hour test cycle. It also found that once the alcohol percentage rose above 35%, aluminium was more likely to corrode than any other metal.

Fuel ID	Chloride (mg/L)	Formate (mg/L)	Acetate (mg/L)	Water (wt. %)
SGS #1	15.4	0.3	1.1	0.7
Delphi #1	17	3	339	1.5
Delphi #2	6.4	4.3	338.7	0.9
Delphi #3	8.4	6.2	235.9	0.8
Delphi #4	1.5	8.1	380	0.8

Table 2.2: E-85 Fuel Contamination Tests [Galante-Fox et al., 2007]

Ethanol in particular is susceptible to contamination making it very corrosive. In 2006, SGS and Delphi (independently) tested various commercially available E85 fuels for contaminates and the results are reproduced in Table 2.2. These are designed to show the worst case scenarios for the forecourt purchaser but demonstrate the need for tight controls in the manufacturing of biofuels to avoid contamination. In the 2007 study from which Table 2.2 is taken, Galante-Fox et al. tested E85's corrosivity when contaminated with water, chloride or organic

acids (these are typical ethanol contaminants) and what effect this had on PFI durability. While ethanol itself is not corrosive, it is hygroscopic meaning it readily absorbs water which makes it susceptible to contamination with any soluble and corrosive salts in said water. After testing 17 different samples of E85 with varying chloride content and CIC levels (Corrosion Inhibitor C – formed from Imidazolines), The authors found that if no CIC is present then chloride levels greater than 3.5 ppm can cause serious corrosion. At 5ppm of chloride, it requires CIC levels of 5 pounds per 1000 barrels (ptb) can achieve B+ NACE rating, as dictated by the NACE TM0172-2001 experimental standard [NACE, 2001]. Above this 5ppm level the NACE rating will be even higher, even with up to 20 ptb of CIC blended, the maximum allowed for this test. Again, this reinforces the need to protect alcohol fuels to prevent contamination and any spoiling.

With regards to integrating alcohol fuels into the mainstream market, a study from Brazil was undertaken by Nakajima, Saiki and Goryozono [2007] running Honda's Brazilian-sold Civic FFV which could operate on a variety of fuels from E20 to E100. In addition to the smaller alterations mentioned above the study ran a dual fuel system. In this the main fuel tank was used for normal FFV operation and a secondary tank was filled with only E22 Gasohol, used purely for start-up. The reason for the secondary tank is the lower saturated vapour pressure of ethanol fuel which can reduce startability - see Figure 2.20. This lower vapour pressure is also related to a lower theoretical AFR (Table 2.1) meaning that the necessary vapour pressure needed to reach stoichiometry won't occur until 41°C higher than gasoline, reducing startability. It was found that the engine had good drivability at low temperatures with the one intake valve deactivate, even as low as -10°C. When the intake valve was reactivated, results showed misfires at high loads soon after start-up (Figure 2.21 a&b). With only one valve, the velocity of the air-fuel mixture rises so the ability for the fuel to be vaporised increases and thus the engine can run at a higher speed.

2.5.3 Performance Characteristics

While alcohol fuels are seen to be a strong avenue of research it is a widely held belief that the first generation of biofuels are largely ineffective for wholesale

replacement and are something of a niche, only for FFVs. By only focussing on the second generation, can alcohol fuels become a fuel source in their own right? Until such time as second generation fuels are ready for distribution, engines powered via ethanol or methanol blends must increase in efficiency to compensate for the short comings of the first-generation fuels such as if the crop is not farmed correctly, the full benefits will not be seen. As it stands in the US if all $1.23x10^{8}$ hectares of arable land were given over to the growth of biofuels (regardless of whether or not the land is suitable) the supply would not satisfy current US gasoline usage. Even harvesting palm oil, the biofuel with the biggest yield of litre per hectare, would only produce $5.85x10^{11}$ litres, just $0.4x10^{11}$ litres over the US yearly usage in 2007 [Cheng, 2011]. In addition wheat straw and rapeseed ethanol used 45% and 40% respectively of the UK arable land assigned to biofuel yet only supplied 5% of the UK energy demand in 2001. These numbers improve to 10% and 15% if the fuel is derived from sugar-beet or wood [Woods and Bauen, 2003]. So far it has been shown that basic efficiency is improved by running alcohol fuels purely due to the reduced gas and charge temperatures and the higher flame speeds (compared to gasoline). The result is a reduced heat loss, improved efficiency, lower exhaust temperatures and therefore a higher overall output [Brewster, 2007]. In fact by operating an engine with M85, the maximum power can increase by 8% and the torque of the engine will increase proportional to the increase in the methanol content of the fuel as in Figure 2.22 [Suga and Hamazaki, 1992].

In Table 2.1 the key benefits are laid out for running alcohol fuels. These collaborate to allow ethanol and methanol the potential to increase engine performance over gasoline. The higher octane numbers also provide greater knock resistance. Traditionally in an engine, the desire is to run at MBT but when burning gasoline the spark advance is sometimes dictated by the DBL. This forces manufacturers to run with a spark timing of -1° of DBL at lower speeds, where knock is more likely. Using ethanol, however, this restriction is less prevalent and knock was rarely encountered so oftentimes MBT timing can be employed [Brewster, 2007].

The ability for the alcohol fuels to burn with greater efficiency is linked to the Reid Vapour Pressure (RVP), a measure of a fuel's volatility. While the chemical formulae of alcohol fuels are consistent, the RVP value can vary from market to market. Suga and Hamazaki [1992] ran a back to back performance test of two identical FFVs, one with gasoline, the other running M85. However, the author varied the RVP of the M85 from 0.62 (traditionally the type sold in warm climates) to an RVP of 0.85 (declared here as 'winter grade' fuel). It was noted that the lower grade of RVP impacted the start-ability in cold conditions while both grades exhibited excessive fuel tank pressure levels.

As described earlier, alcohol fuels are consistent in their chemical makeup (though not always in construction) compared to gasoline, which can be a melting pot of formulae, including having a vastly reduced carbon count compared with the average gasoline sample. It is this that lends to the higher latent heat of vaporisation and the knock resistance [Cairns et al., 2009]. Cairns et al. continued to investigate using 3 varied blends of ethanol (and one of butanol) in a downsized engine to measure the effect on BSFC c.f. gasoline. At a constant speed of 2000 RPM and a load increase from 2 to 4 bar (thus simulating the effective 50% downsizing of the engine) very little change was noted BSFC levels when compared with the gasoline's performance (Figure 2.23). However, maintaining a fixed load and doubling the speed produced more varied results compared to the gasoline baseline case (Figure 2.24). BSFC dropped relative to the octane number for 'standard' fuels and the ethanol fuels mimicked that trend whilst remaining ~0.5% ahead at all times. This study then continued on to look at the NEDC operation of an alcohol-fuelled vehicle. Running both DI and a downsized engine with gasoline fuelling there was an overall 17% reduction in fuel consumption against the baseline. When the NEDC test was repeated for ethanol fuels, the consumption rate rose. This is to be expected as alcohol fuels have a much lower calorific value and volumetric energy content than gasoline. In fact, the rate at which the consumption rose is proportional to the calorific value of the fuel – e.g. E85 has a calorific value 32% lower than that of 98RON and the fuel consumption rates were ~30% higher.

Heat release rates are usually slowed by use of blended alcohol fuels. Brewster [2007] found the 10-50% MFB rates for ethanol to be quicker than that of gasoline at identical spark timing. Alcohol's quicker, cooler burn was researched by Suga and Hamazaki in 1992 who logged piston temperatures at WOT and found that the piston top-round temperature was 23°C cooler running M85 compared to gasoline. In addition, the surface temperatures were much lower even though the engine power increased, some 25°C less for the same conditions running gasoline.

2.5.4 Emissions Effects

Part of the drive to use biofuels as either a total substitute for gasoline or as an additive is to see emissions (in particular, carbon emissions) fall. Many governments have set in place directives that pledge to reduce carbon emissions to below that of an historical date (for example the UK government has, in line with others in the Kyoto Protocol, have pledged to reduced GHG emissions to 80% of the 2008 levels by 2050), though whether this is achievable legislation by those governments or not remains to be seen [DECC, 2011]. Indeed with ethanol, one can offset the CO_2 impact during combustion by producing it from products such as biomass and one particular type of methanol can be synthesised directly from CO_2 in the atmosphere [Turner et al., 2007].

2.5.4.1 Nitrogen oxides (NOx)

Varde and Manoharan [2009] looked at multiple EGR amounts and the effect on NOx levels in a four-cylinder, PFI FFV. Running E85, NOx levels were between 1 and 2 g/kW-hr lower than gasoline over a range of speed and load points. As the NOx levels are related to the burnt gas temperatures this is to be expected due to the lower combustion temperatures and slower burn rates of alcohol fuels. Upon the introduction of EGR, the burnt gas temperature fell further still; halved when running 15% EGR (it is key to note that the EGR was maintained at 21°C throughout the test). This drop in NOx emissions is independent of load and speed (Figure 2.25) and is present in both low and high concentration blends of ethanol [Wallner and Frazee, 2010]. However, Al-Farayedhi, Al-Dawood and Gandhidasan [2000] and Turner et al. [2011] both found that for blends below 10%

ethanol concentration, the emissions were reduced c.f. gasoline but beyond that ethanol content then the NOx rates would rise.

2.5.4.2 Carbon Monoxide

As the alcohol content rises some workers have reported that the CO levels drop as shown in Figure 2.26. Studies put this relationship between CO emission levels and the alcohol content in fuels down to the improved combustion resulting from the hydroxyl bond in the fuel [Karman, 2003; Wallner and Frazee, 2010]. This is backed up by Al-Farayedhi, Al-Dawood and Gandhidasan [2000] who found that CO levels dropped in all fuel blends unless running lean fuelling.

To say that all alcohol fuels behave identically is as incorrect as to say that all gasolines perform consistently. In a 1996 paper by Kremer, Jardim and Maia the authors studied the impact of differing ethanol production methods on the emissions. NOx and HC emissions exhibited little-to-no change for the four blends tested but CO emissions rose 10 and 45 per cent using ethanol synthesised from natural gas c.f. gasoline, while ethanol created from coal produced 29 to 58% more CO and corn ethanol between 12 and 31%, dependant on the engine size. These increases are due to the fact that synthesised alcohols carry less oxygen (Table 2.1).

2.5.4.3 Unburnt Hydrocarbons (uHC)

HC emissions tend to follow the same trend as NOx emissions. As the content in alcohol increases, the uHC emissions reduce. Again the oxygen content is thought to be a contributor to this fact and this is independent of load and speed (Figure 2.27) [Karman, 2003; Wallner and Frazee, 2010].

2.5.4.4 Unregulated Emissions

While lower gas temperatures provide a drop in NOx values, as the flame temperature reduces the catalyst it takes longer to heat up to the required temperature for efficient running, so the CO, HC and aldehyde emissions will rise (though the former two are likely to be below current gasoline levels). However E85 combustion produces nearly three times as much aldehyde emissions as gasoline (Figure 2.28). By diluting the charge with exhaust gases the gap becomes more pronounced between the gasoline and E85 aldehyde levels, therefore it can be seen

that the higher the EGR rates, the lower the combustion temperatures and thus the higher the aldehyde levels [Varde and Manoharan, 2009].

It is these currently unregulated toxins (like formaldehyde, acetaldehyde and acrolein) that could be the future environmental and health dangers in using biofuels. When using ethanol, formaldehyde levels show a minor increase with the highest readings at low loads and speeds [Wallner and Frazee, 2010]. While running the LA-4 drive cycle it was found that the majority of the aldehyde emissions released by a vehicle occur before the catalyst has time to reach operating temperature (as shown in Figure 2.29). Hence it is important to locate the catalyst as close as is safe to the exhaust manifold to ensure rapid light-off [Suga and Hamazaki, 1992]. It was also been previously noted that as a methanol fuelled vehicle ages and its mileage rises, the aldehyde emissions may rise due to increased combustion chamber deposits [Tsukasaki et al., 1990].

2.5.4.5 Emissions After-Treatment

Many of the studies presented above are largely focussed around the engine-out emissions taken from exhaust runners in a test cell. However all modern automobiles possess after-treatment devices such as three way catalytic convertors (TWC) for gasoline operation and diesel oxidation catalysts (DOC) and selective catalytic reduction filter (SCRF) for diesel operations. In addition diesel engines usually employ a particulate filter, while much discussion is currently taking place around the transferring of this technology to gasoline cars to meet tightening emissions standards.

Stansfield et al. [2012] looked at a range of ethanol and butanol fuels in an SI engine with a TWC. When comparing low blends of ethanol to the baseline fuels the TWC was able to reach 50% efficiency (dubbed “cat light-off stage”) in a similar timeframe while the higher blend of ethanol (E85) incurred a large time penalty in light-off, particularly impacting HC emission rates. Turner et al. [2012] also looked at the TWC when installed on an FFV and concluded that there was no significant risk of failure in the after-treatment system due to the higher corrosivity of ethanol and methanol fuels.

Maunula and Kinnunen [2009] compared biodiesel to diesel in a conventional diesel engine to assess the impact of the alcohol content on the TWC. They found that over the NEDC there was no great damage to the TWC due to alcohol fuelling and that no changes were required to any of the after-treatment system when operating under 20% ethanol content. When moving to higher ethanol blends (E85), the authors found that by tailoring the zeolites inherent in the TWC then the higher HC emissions reported in the study by Stansfield et al. [2012] could be countered. Further investigation identified that the best construction of gas trap was one of platinum/rhodium. The regeneration and conversion efficiencies remained good c.f. the baseline fuel when the TWC was artificially aged.

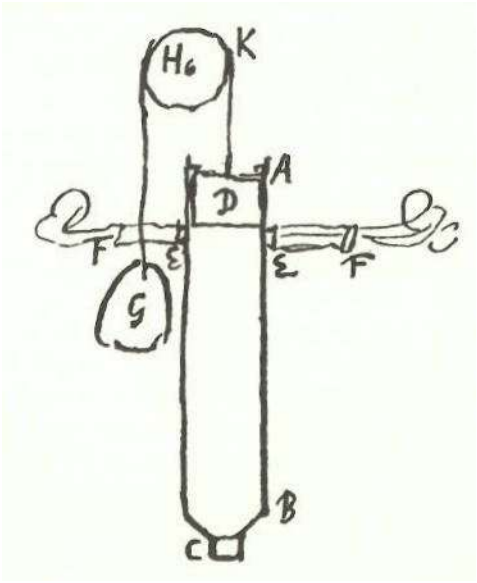

Figure 2.1 – Diagram of the Huygens engine [Taken from Cummins Jr., 1976].

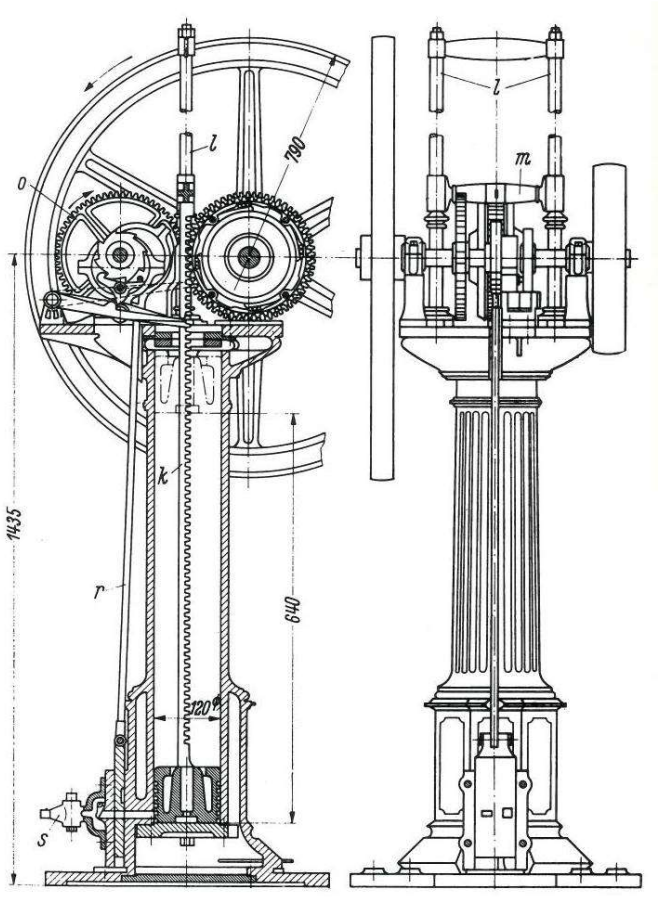

Figure 2.2 – Diagram of the second atmospheric engine developed by Nikolaus Otto in 1876 [Taken from Cummins Jr., 1989].

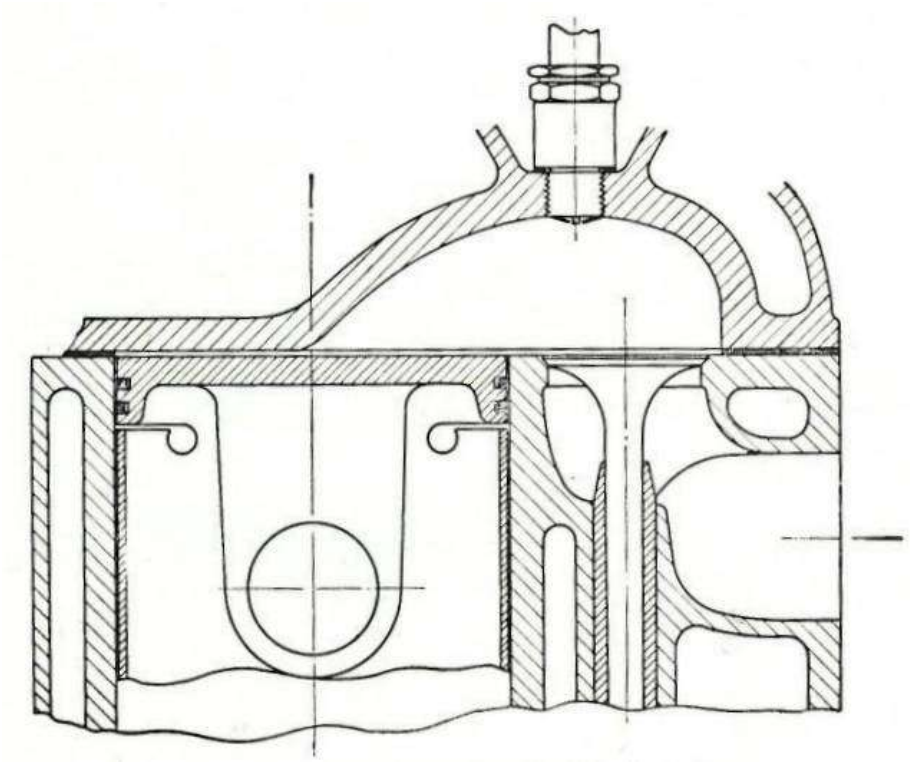

Figure 2.3 – Cross-section of the turbulent head developed by Harry Ricardo in 1920 [Ricardo, 1968].

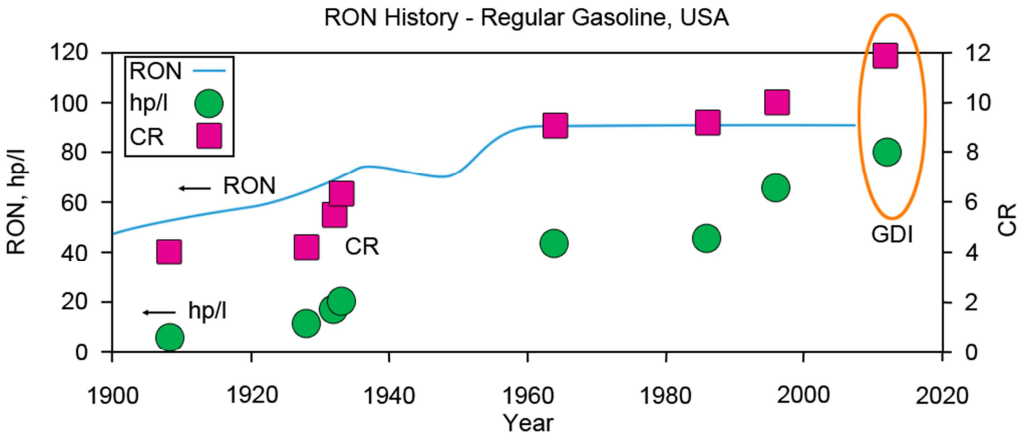

Figure 2.4 – The steady development of both the octane number of fuel and the compression ratio over time. [Adapted from McCarthy, 2011].

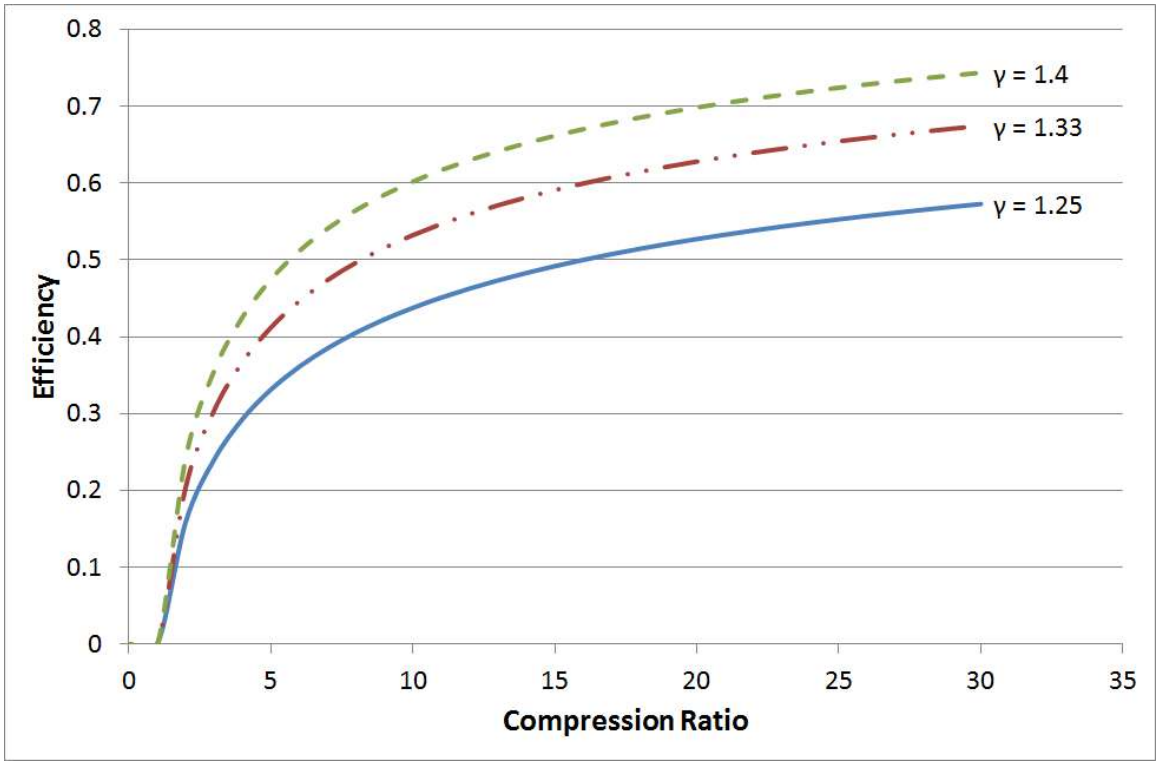

Figure 2.5 – Thermal Efficiency as a function of the compression ratio for differing gamma values where $\gamma = c_p/c_v$.

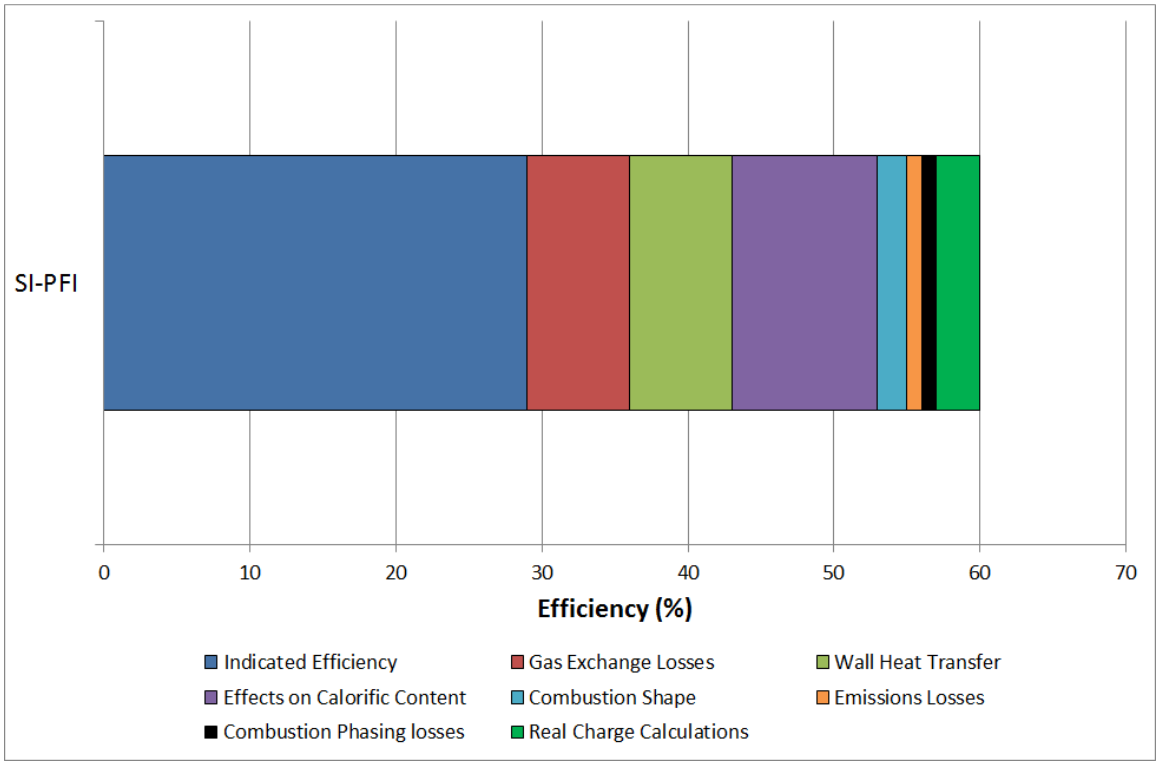

Figure 2.6 – Thermodynamic split of losses compared to the ideal constant-volume cycle at 2000 RPM and 3 bar Net MEP [Adapted from Kulzer et al., 2006].

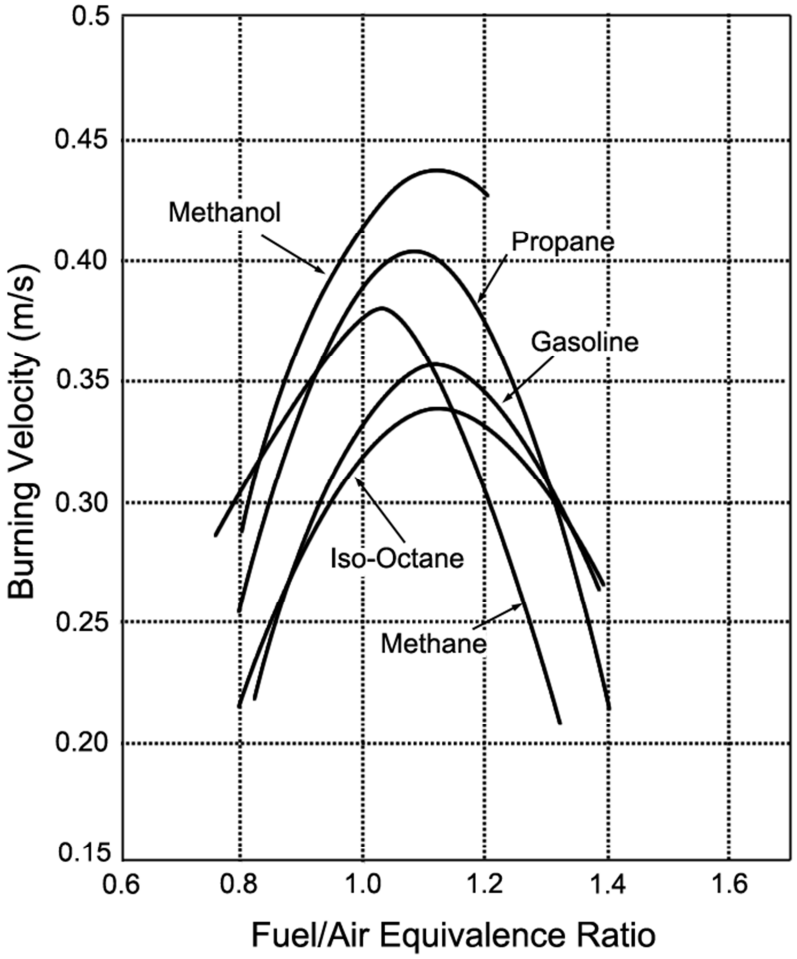

Figure 2.7 – The laminar burning velocity for several fuels as a function of the equivalence ratio [Adapted from Metghalchi & Keck, 1980 & 1982].

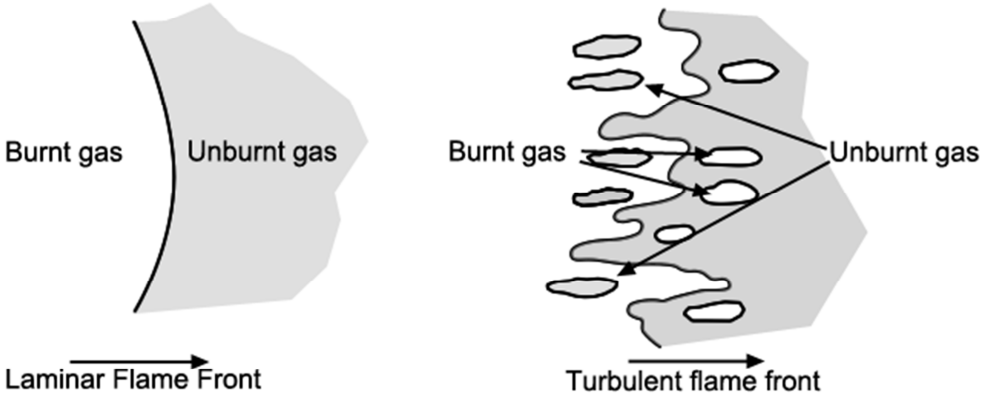

Figure 2.8 – Comparison between laminar and turbulent burning flame fronts for a pre-mixed composition [Adapted from Stone, 1992].

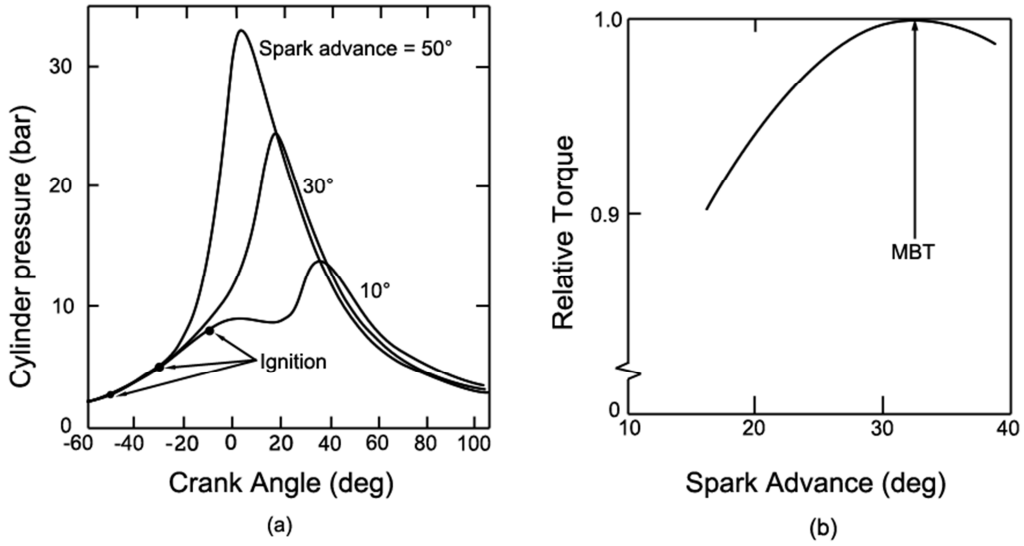

Figure 2.9 – (a) Cylinder Pressure vs crank angle for three distinct spark timings (over advanced, MBT and retarded); (b) Effect of spark advance on the brake torque highlighting MBT for a given engine [adapted from Amann, 1985].

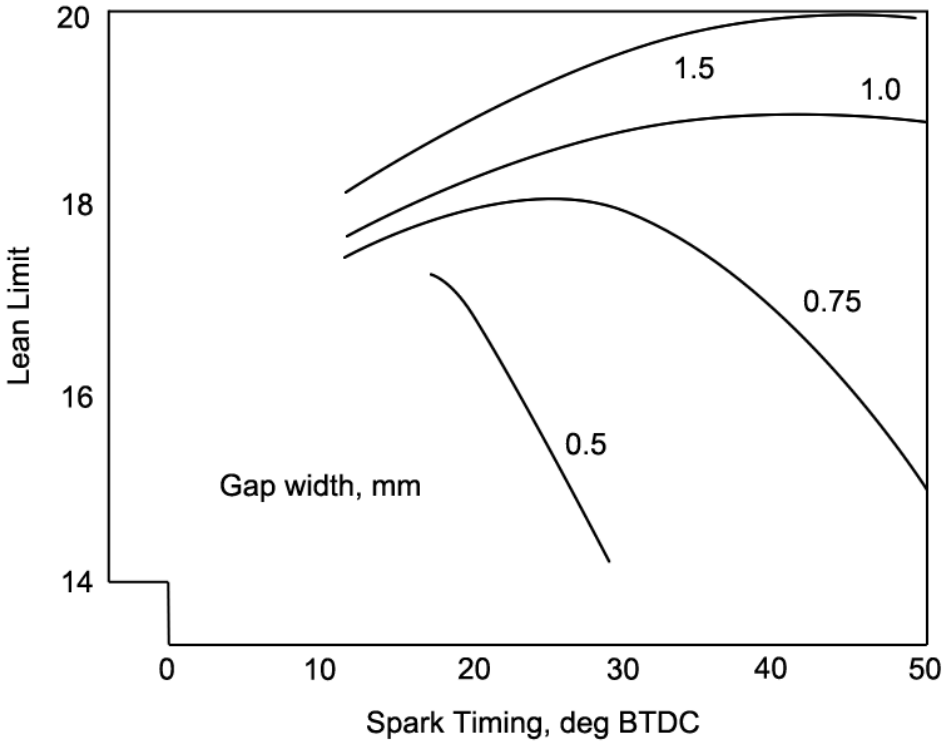

Figure 2.10 – The effects spark plug gap width on the AFR at the lean limit point. [adapted from Heywood, 1988].

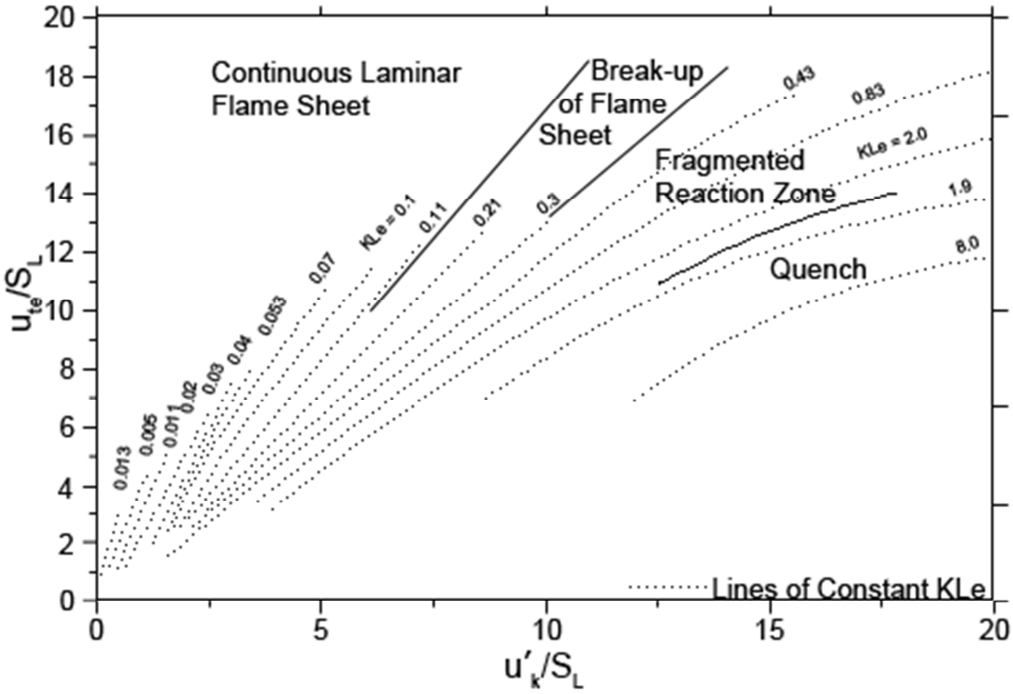

Figure 2.11 – General correlation of turbulent burning velocities in terms of dimensionless groups [adapted from Abdel-Gayed, Al-Khishali and Bradley, 1984].

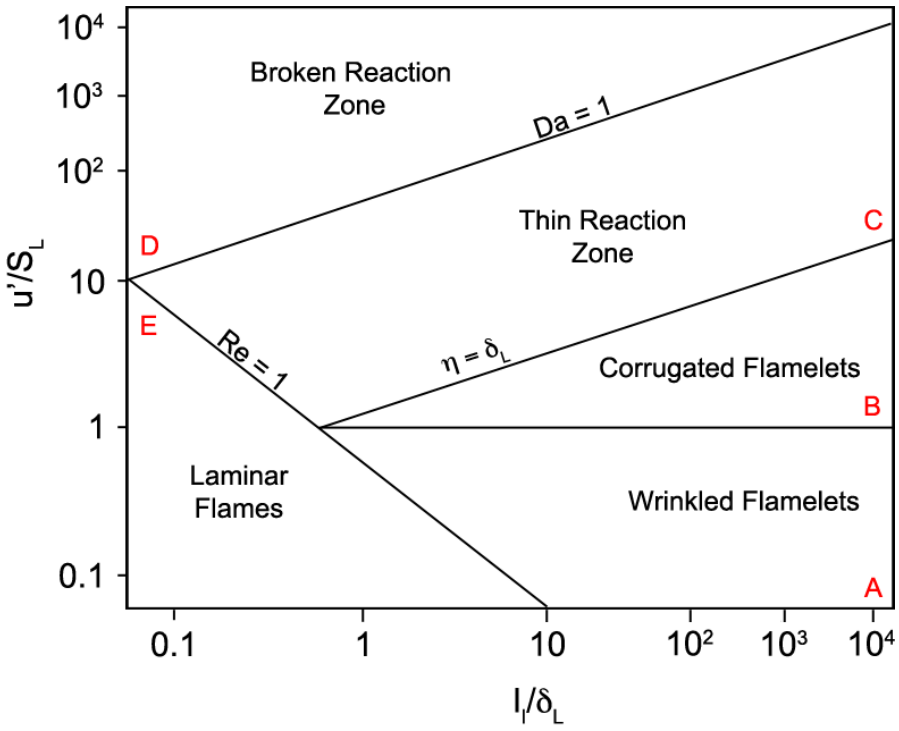

Figure 2.12 – Borghi diagram showing the different regimes of turbulent premixed flames [Peters, 1986; Borghi, 1988].

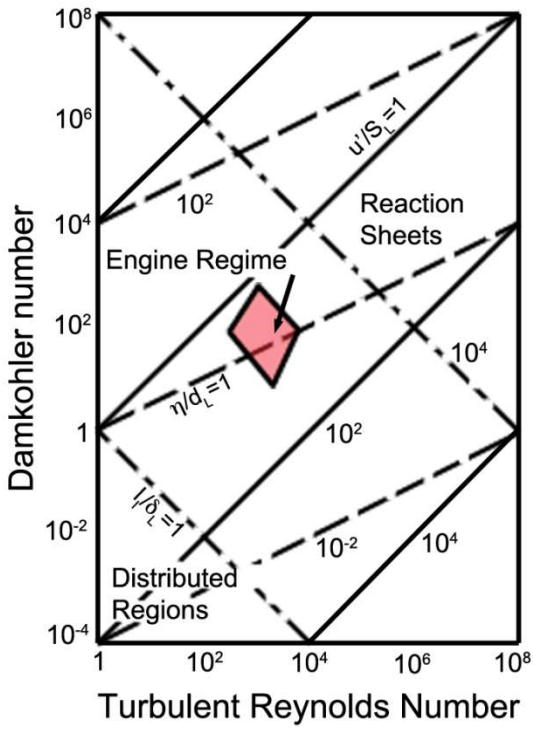

Figure 2.13 – Various turbulent flame regimes in an engine on a graph of the Damköhler number versus the turbulent Reynolds number [Abraham, Williams and Bracco, 1985].

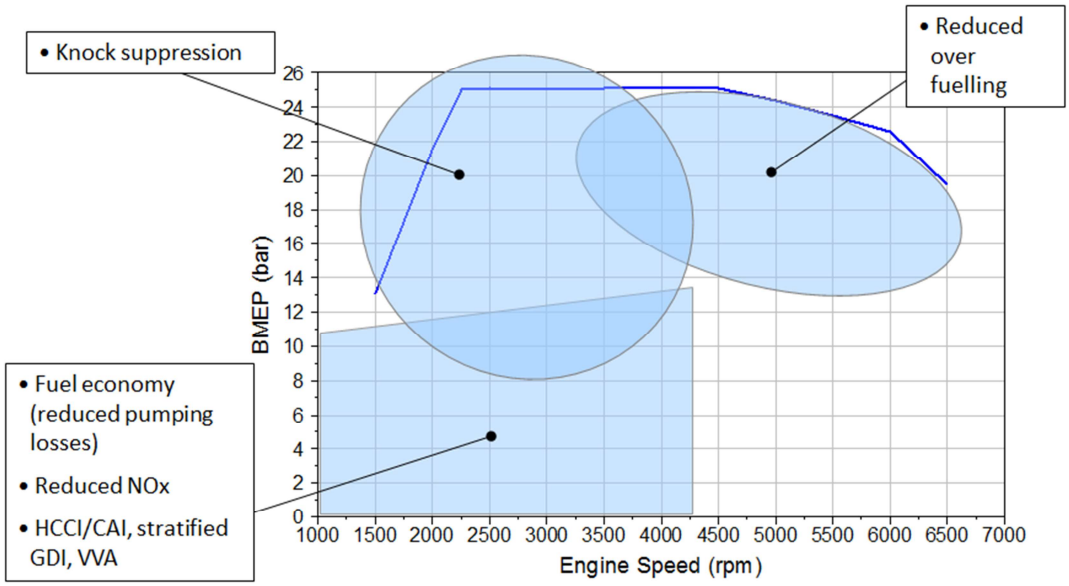

Figure 2.14 – A BMEP trace of an advanced downsized engine showing three key areas where EGR would be employed [Moxey et al., 2012].

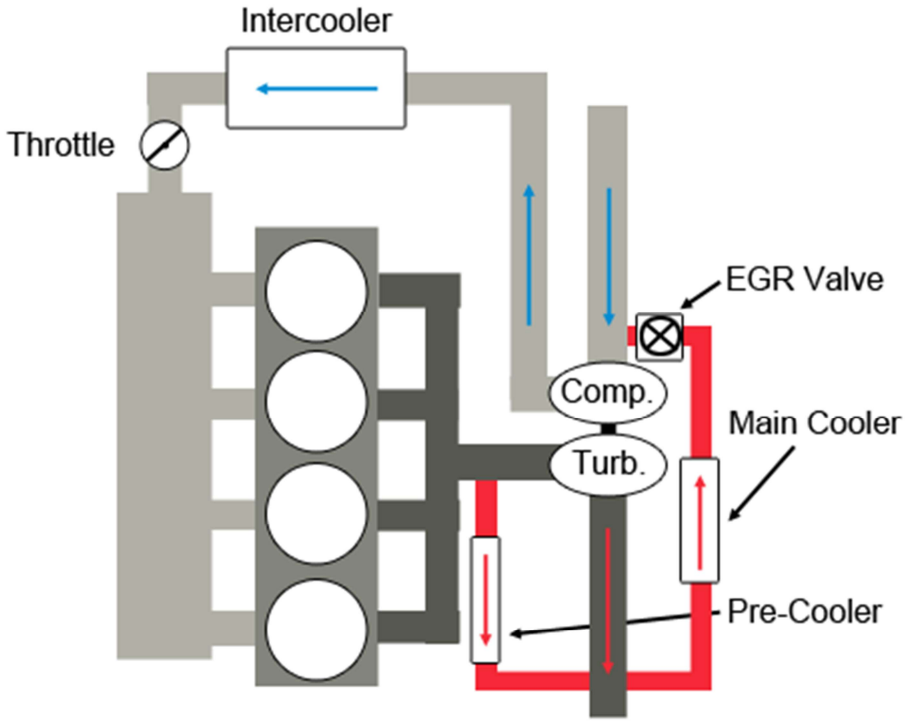

Figure 2.15 – Example of the external EGR routing employed by Cairns, Blaxill and Irlam [2006].

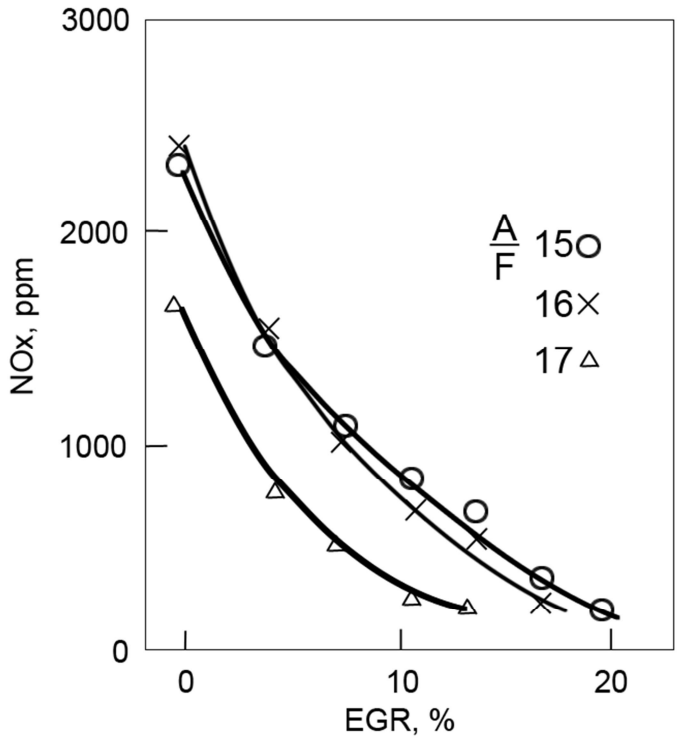

Figure 2.16 – NOx emissions in ppm against an increasing amount of EGR [Heywood, 1988].

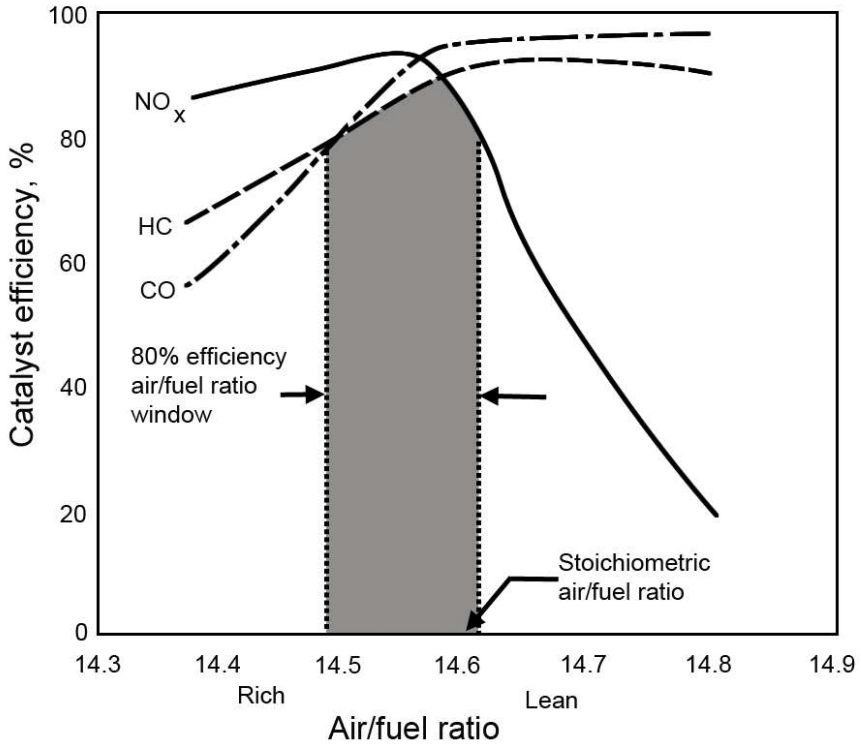

Figure 2.17 – Conversion efficiency for NO, CO and HC for a three-way catalyst as a function of the AFR [Heywood, 1988].

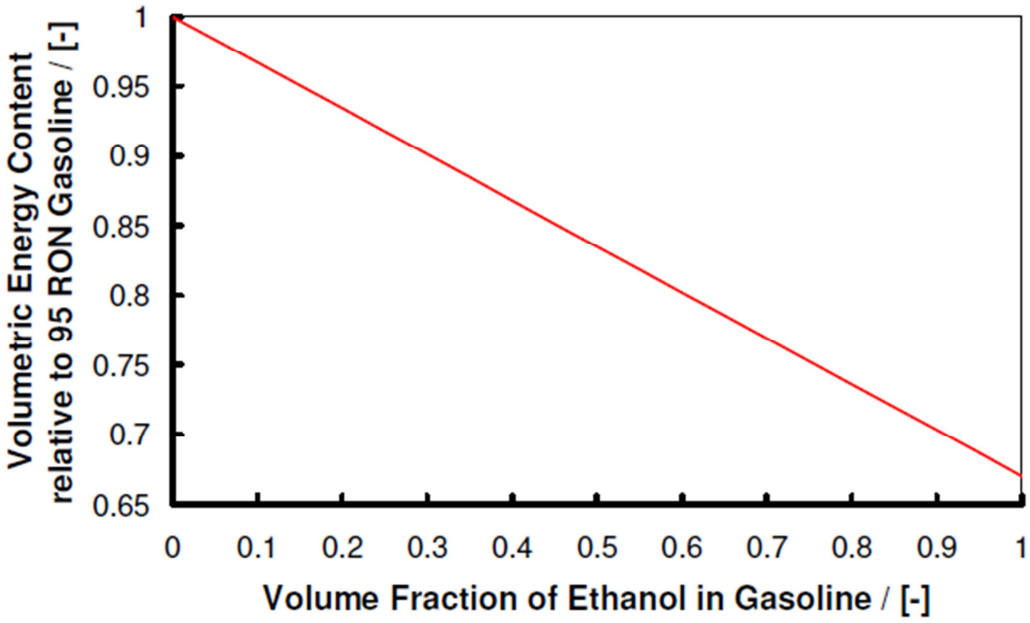

Figure 2.18 – The volumetric energy content of ethanol gasoline blends displaying the fact that as the ethanol content rises, the energy content falls in a linear fashion [Turner et al., 2007].

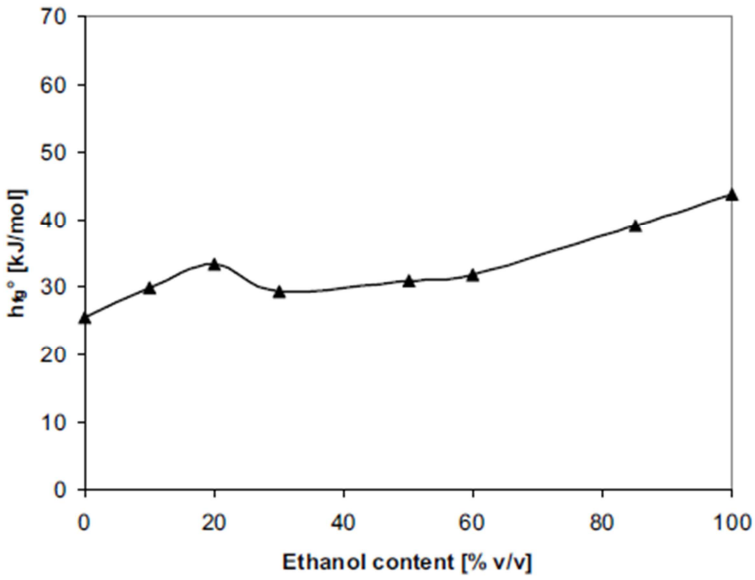

Figure 2.19 – Experimental values of the enthalpy of vaporisation of a fuel mixture for increasing ethanol content [Kar et al., 2008].

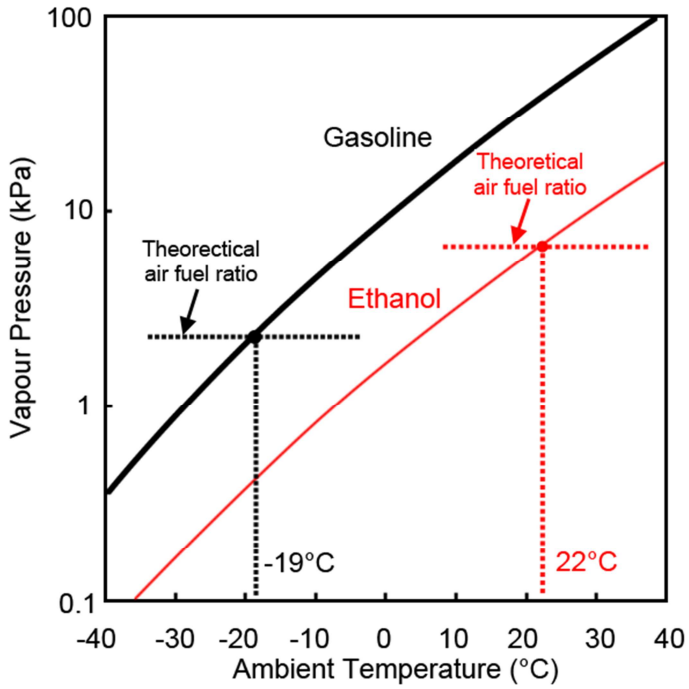

Figure 2.20 – Comparing the vapour pressure of both gasoline and ethanol and effect temperature has on the theoretical AFR [Nakajima, Saiki and Goryozono, 2007].

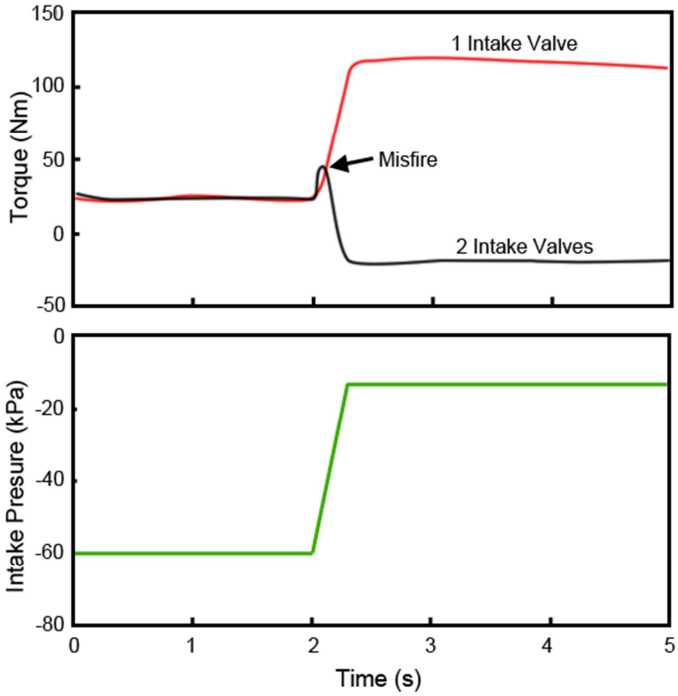

Figure 2.21 – a) Torque curve for both single and dual intake valves over time and b) the pressure curve showing the load increase to cause the misfire [Nakajima , Saiki and Goryozono, 2007].

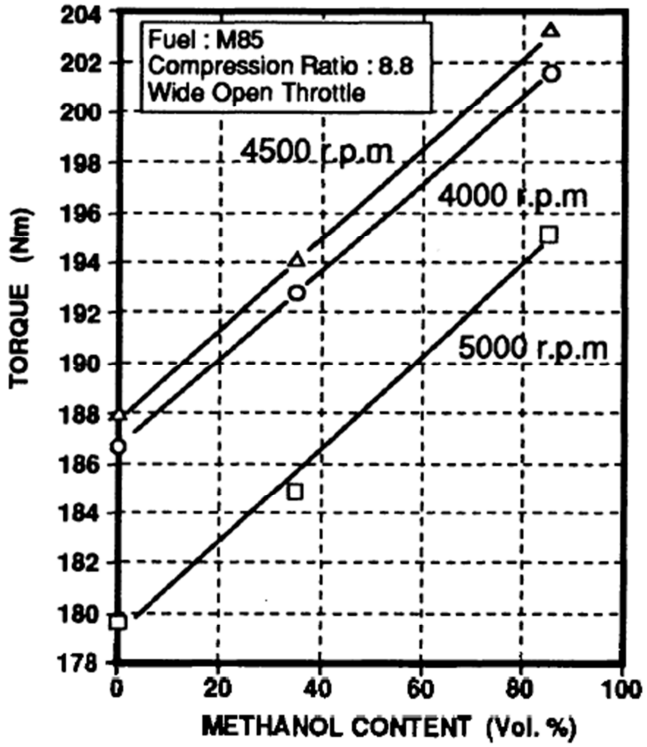

Figure 2.22 – Engine torque at varying speeds with increasing methanol content (by percentage) [Suga and Hamazaki, 1992].

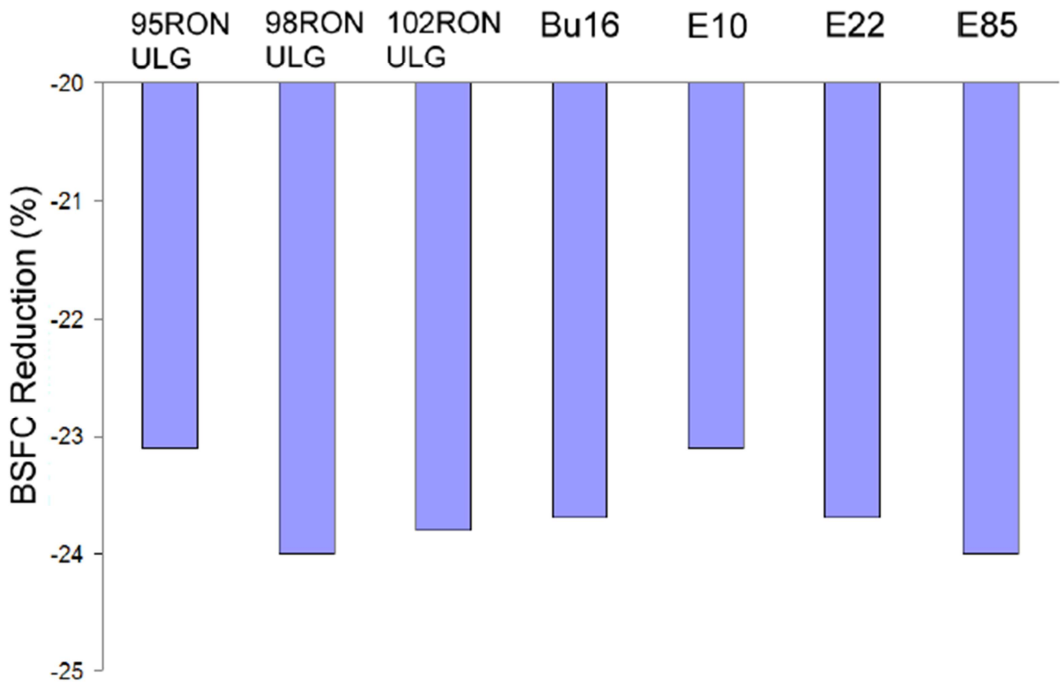

Figure 2.23 – BSFC reductions as the engine load rises from 2 bar to 4 bar at 2000RPM indicating performance of the fuels while downsizing [Cairns et al., 2009].

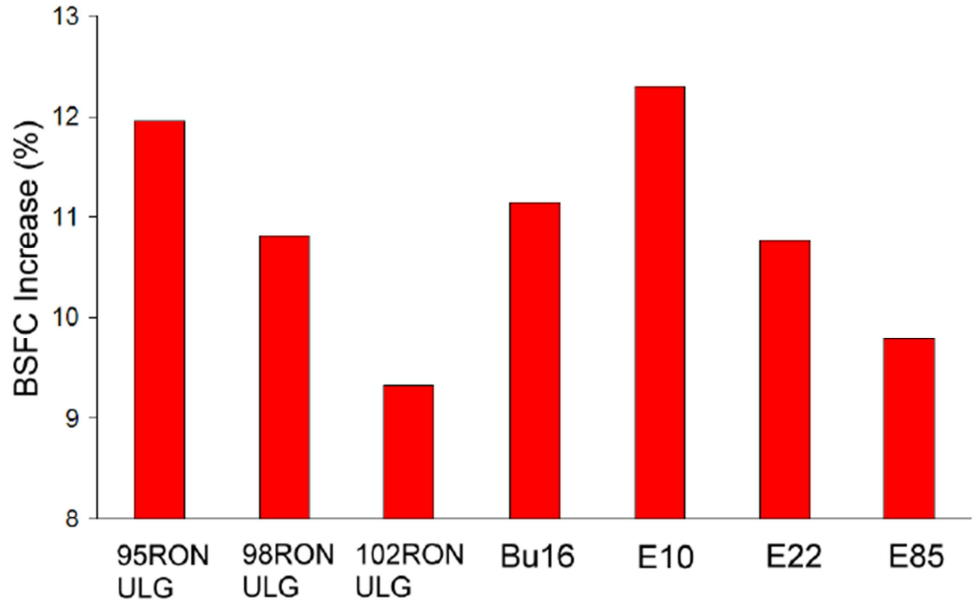

Figure 2.24 – The rise in BSFC as the engine speed rises from 2000RPM to 4000RPM at 2 bar BMEP, also showing the cost of downsizing [Cairns et al., 2009].

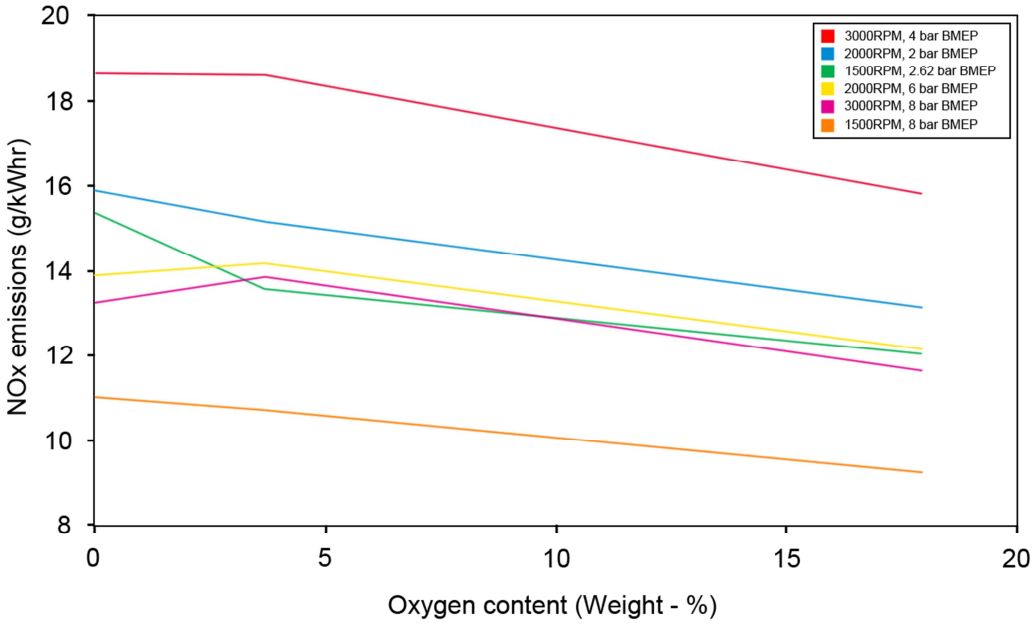

Figure 2.25 – NOx emissions for ethanol blends at differing speeds and loads showing that NOx emissions in alcohol combustions are not dependent on speed or load [adapted from Wallner and Frazee, 2010].

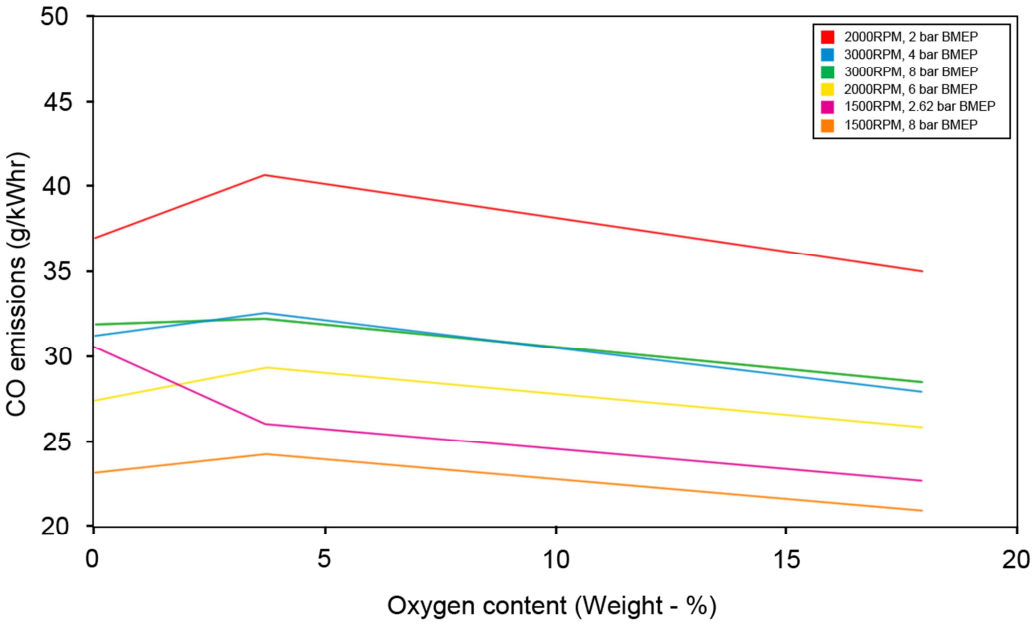

Figure 2.26 – CO emissions for ethanol blends at differing speeds and loads [adapted from Wallner and Frazee, 2010].

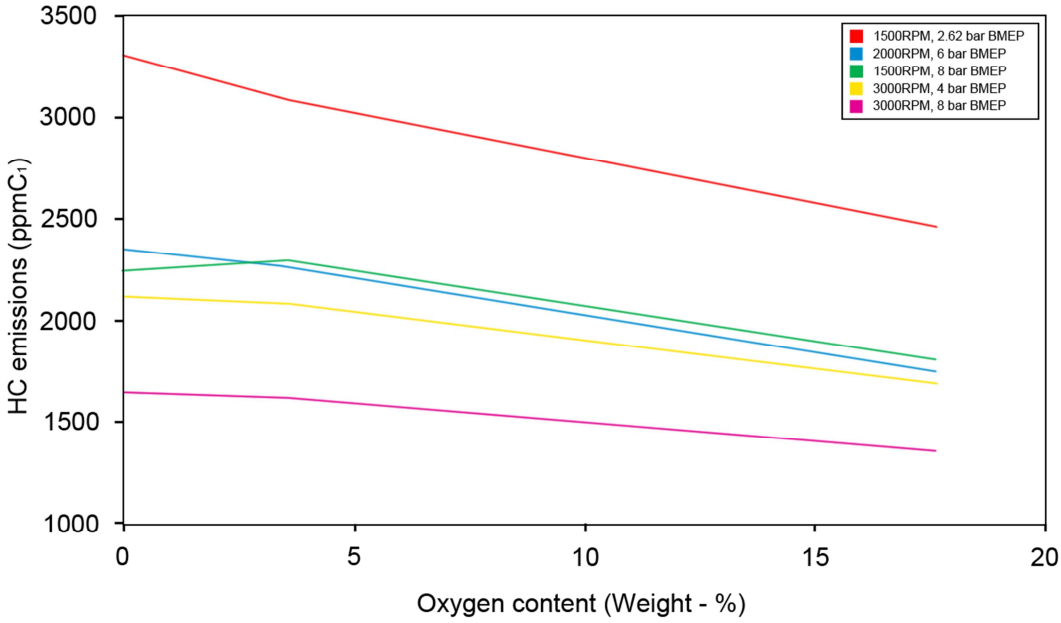

Figure 2.27 - HC emissions for ethanol blends at differing speeds and loads showing that HC emissions in alcohol combustions are not dependent on speed or load [adapted from Wallner and Frazee, 2010].

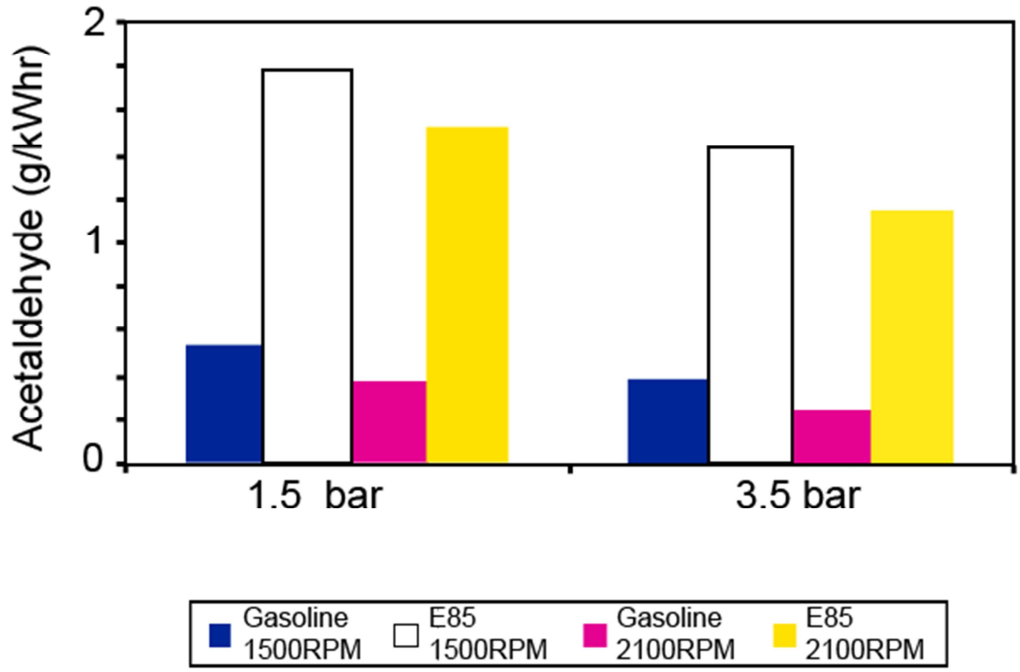

Figure 2.28 – The acetaldehyde levels for gasoline and ethanol at differing speeds showing the much higher levels of emission from ethanol than from gasoline [adapted from Varde and Manoharan, 2009].

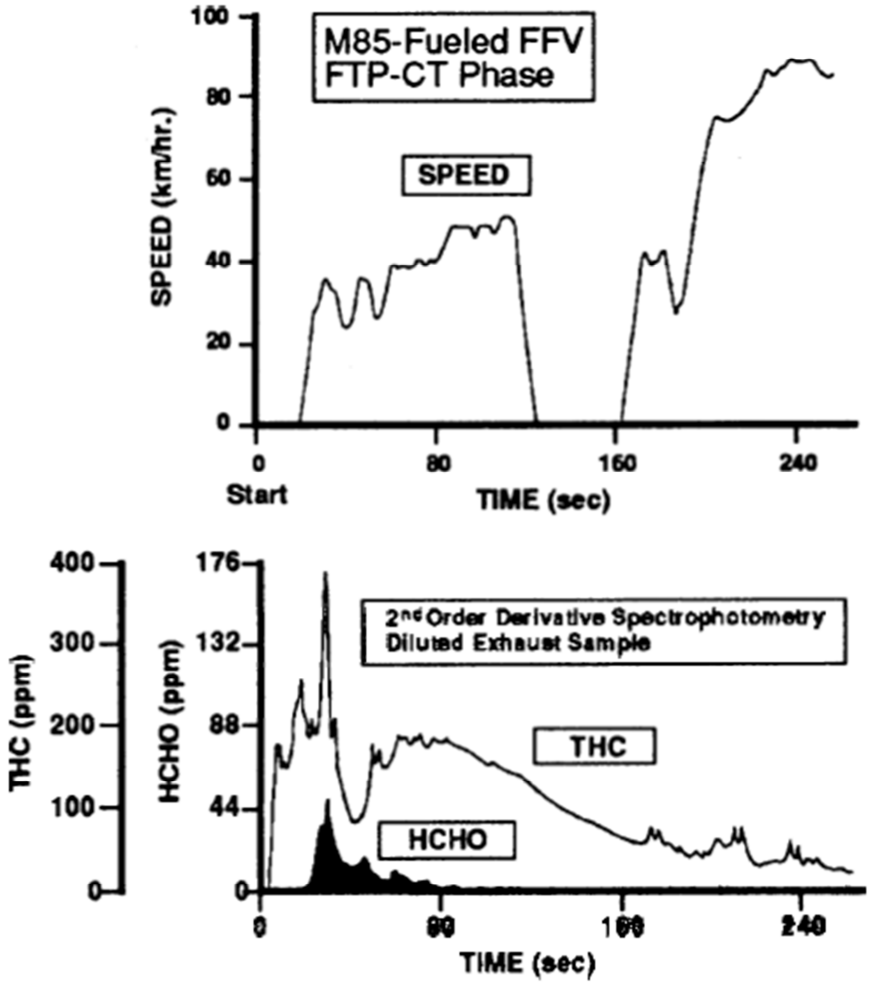

Figure 2.29 – Aldehyde emissions over the LA-4 cycle for an M85 fuelled Honda FFV [Suga and Hamazaki, 1992].

Chapter 3

Experimental Facilities and Diagnostics

3.1 Introduction

The engine used in this study was a Lister Petter TS-1, originally produced for a diesel canal-boat powertrain (as illustrated in Figure 3.1) but employed here with a fully redesigned cylinder head. This new head allowed for full-bore overhead optical access and the use of a more typical SI engine compression ratio of 8.4:1. Despite these changes the bottom of the engine itself was almost entirely unchanged from the piston down, with the main exception of the addition of some key instrumentation as discussed in more detail below.

3.2 Lister TS-1 Assembly

3.2.1 Research Engine Background

The Lister engine was originally used at Brunel University London for diesel experiments, later extending into novel HCCI and EGR entrainment combustion studies [Zhao, Hu and Ladommatos, 1999; Peng, Zhao and Ladommatos, 2003; Abu-Jrai et al., 2006; Tsolakis et al., 2007 & 2007; Bai et al., 2009]. The unit was first modified for SI combustion by Williams (2002), albeit remaining somewhat unconventional in nature due to the full bore overhead optical capability via the pancake-shaped combustion chamber and deep pockets for three side poppet valves.

3.2.2 Basic Engine Geometry

The Lister Petter TS-1 possesses a single 0.6 litre capacity cylinder with a bore of 95mm and stroke of 89mm, with the original air-cooled liner providing a suitable body upon which to mount the optical head. Overall, the redesigned unit could be considered to offer a relatively robust platform, with recent reverse

engineering analysis and validation proving the current unit to be capable of withstanding in-cylinder gas pressures of up to 150 bar [Dingle, 2014].

The desire was to construct an engine that would allow for full-bore optical access while still providing accurate data which would be as close to a conventional automotive engine due to a high tumble port layout of horizontal orientation. The employed design uses poppet valves installed in the side of the combustion chamber, shrouded by valve pockets. Figure 3.2a shows the final design of the head from above. Clearly visible are the two inlet valves (coloured blue) and the two exhaust valves (coloured red). As this project involved low light imaging and bespoke optical parts that dictated simple shapes, the combustion chamber was flat-roofed and the piston had a flat crown. With this design a compromise existed between maintaining adequate compression ratio and avoiding valve-to-piston clash while using realistic valve duration. In the current work a clearance height of 9 mm and pocket depth of 5 mm provided a geometric compression ratio of 8.4:1.

Similar optical research engines exist elsewhere [Hall and Bracco, 1987; Hicks et al., 1994] but these engines use ported valves which do not produce the in-cylinder flow characteristics typically experienced in modern production engines. While more details about the optical capture methods are provided later, it is key to note that not only is there full-bore access via the Fused Silica window (Corning 7980 HPFS, hereafter often referred to as the ‘glass’ or ‘window’) inserted into the head, but the design also allowed for partial side optical access; potentially for a laser sheet setup in future work. These side windows can be seen directly above and below the bore in Figure 3.2a, highlighted green. A full schematic of the engine control system is shown in Figure 3.3. The full list of the redesigned engine geometry is found in Table 3.1.

Parameter	Value
Bore (mm)	95
Stroke (mm)	89
Swept Volume (cc)	631
Clearance Height (mm)	9
Geometric Compression Ratio	8.4:1
Exhaust Duration (deg. CA)	230
Exhaust MOP (°bTDC)	105
Exhaust Valve Lift (mm)	5
Standard Valve Overlap (deg. CA)	25
Intake Duration (deg. CA)	230
Inlet MOP (°aTDC)	100
Inlet Valve Lift (mm)	5
Con-Rod Length (mm)	165.16

Table 3.1: Basic redesigned Lister-Petter TS-1 Geometry

3.2.3 Ignition

To ensure the fullest optical access was enabled, the spark plug was mounted in the side wall of the engine. Early work by the current author investigated embedding a central plug into the optical window but this proved difficult to adequately seal at the operating in-cylinder pressures experienced during this work. The side-mounted spark-plug diameter also limited the minimum clearance height possible so it was decided that an NGK ER9EH 8mm spark plug (traditionally used in a Honda VRF400 motorbike) would be employed, which had the lowest profile of the readily available plugs in the marketplace. This was placed into the cylinder wall between the uppermost exhaust valve and the top side window, flush with the underside of the main window (purple disc in Figure 3.2a). The plug was attached to a Bosch P100T ignition coil taken from an MY2005 Ford Mondeo. A comparison between the side-mounted spark plug and a centrally mounted plug (embedded in a metal blank window) can be found in Chapter 5.2.2.

3.2.4 Ports and Valvetrain

The cylinder head was constructed from a single block of aluminium and the various ports and tappings were machined into it (with final spark erosion of the valve pockets). This resulted in several limitations to the port runner design. Traditionally, to aid better premixing of the fuel and air mixture, the inlet runner would be curved. However the manufacturing method available limited the possible designs to straight ports. To aid the mixing as best as possible, a compromise was made in which the ports were designed with a tight angle and tapered runner design (Figure 3.2b).

The diameter of the valve seat and face was limited by the low clearance height available between the piston crown and the bottom of the window. In a study by Dingle [2014] a relationship between the diameter of the valve head, the choked engine speed and the geometric compression ratio was found that resulted in valves of 22mm diameter being deemed the optimum for this engine. This diameter matched those installed in the Fiat Multijet diesel which enabled running costs to be controlled due to ease of supply. Each of the valve seats required a counter-bore to be machined into the head for secure placement. These were spark-eroded into the already-machined head prior to assembly. During this process however, one of the exhaust valve counter-bores was accidentally displaced by 2mm. To repair the damage would have been difficult and costly (both in time and money) so the decision was made to install a blanking plate across the port (flush with the port entrance), with the engine thereafter operated with two active intake valves and one active exhaust. Again this limitation should be noted but was still considered acceptable for the part-load operation intended within this work.

With fixed valve timing, as employed within this work, a compromise must be struck between the overlap period and the engine speeds and loads. When an engine is in a vehicle at idle a retarded IVO is advantageous as it allows for a lower residual gas fraction and thus a most complete burn in the following cycle. However when moving to higher speed operation, this same valve timing can cause excessive knock and high temperatures forcing the EMS to advance the spark timing to 1°

before the DBL therefore losing potential performance. However, if IVO was advanced at the higher speeds this would encourage better intake charge flow as the drop in in-cylinder pressure due to the exhausting of the burnt gases would draw in the fresh charge. This would raise the volumetric efficiency and increased the power and torque outputs as the exhausting charge is performing greater work in inducting the charge. For this set of experiments, the valve timing was selected to give ideal scavenging and induction at 1500RPM so the valve timing was set to 230° duration (ramp end to ramp end) and the overlap was initially set to 10°, symmetrical about TDC to replicate the modern SI engine when running at the lower speeds to be used in this work. This was later altered with a final valve lift duration retained at 230° with a 5mm lift and 25° overlap asymmetrical about TDC, with the exhaust cam being 5° further retarded. When overlap durations were experimented with later in the work, the exhaust valve timing was altered while the inlet valve timing was retained. The lower lift was also deemed acceptable as the engine was well below the choked flow condition at the speeds and loads examined [Dingle, 2014].

As the window was installed in the chamber roof, this forced the entire valvetrain system to the side walls. In the end the two valve events (intake and exhaust) were split into two separate diametrically opposed direct acting camshafts. A 30mm wide simple pulley and toothed (or synchronous) belt system linked the two cylinder head camshafts to the crankshaft via two 28-tooth taper-lock pulleys (visible in Figures 3.4 and 3.5) fitted to the relevant shafts which could be removed to allow for valve timing changes. The inlet camshaft had an Encoder Technology EB58 shaft encoder coupled to it with which to record all DAQ data. A further discussion of which data streams were logged can be found in Chapter 3.5.

3.3 Optical Head Assembly

3.3.1 Window Material and Installation

To see not only the rate of the flame's propagation throughout the cylinder, but also its structure and burn dynamics, it is vital that the fullest optical access be

achieved. Such ability to observe the flame is not new. For example, Glyde [1930] was able to experiment with a line of miniature windows in the head to allowing a limited view of the combustion event. This optical restriction was due mostly to manufacturing processes of the time – it was impossible to make a glass window sufficiently strong enough to withstand the in-cylinder pressures of the combustion event. Today, however, specialist cutting and shaping technology is more readily available to manufacture and machine a window large enough to provide full bore access but strong enough to withstand high pressure combustion.

As already stated, the window used for the overhead optical access was constructed of Corning 7890 HPFS silica, a high purity, synthetic amorphous silicon dioxide material manufactured by flame deposition. Such material possesses very low thermal expansion characteristics. With a bore of 95mm (giving an area of 7088mm^2) and a 15 MPa peak combustion pressure that the engine experienced, the window would have to withstand a maximum force of 106kN and thus the employed clamping method needed to be able to retain the window in the head against this force without overloading the delicate glass.

Initially the window was lowered directly into the head's viewing recess by hand, with a ring gasket on the lower shoulder, and was then clamped down from the top via eight retaining bolts (Figure 3.6). However it was soon discovered that this led to an expansion of the compressed ring gasket which then impinged upon the window's shoulder or caused the window to sit at an angle, thus creating additional localised stress. A solution was found whereby, instead of the window being 'loose', the window was bonded into an aluminium shoe with a small clearance for high temperature silica and two Elring Klinger C4400 soft cut gaskets to be used to provide a cushioning layer between the window and metal (Figure 3.7). It was this shoe which would be handled and have the stresses of clamping placed upon it. This also made the window easier to work with as when using the window 'loose' the author had to be very careful so as not to damage any of the square edges so vital for correct sealing of the engine – a task made more difficult when the average window temperature shortly after running was, at the least, 90°C. Not shown in Figure 3.7 is the silicon sealant between the window and the

shoe that not only acted as an adhesive agent securing the window in, but also helped cushion the glass. This approach proved highly successful, with no window failures throughout.

3.3.2 Other optical opportunities

To obtain laser sheet access through the side windows, two windows could be inserted and bonded into the head in the recesses provided (highlighted green in Figure 3.2a). Due to time constraints, this was not implemented during this work but the capabilities exist for future work and the ability to obtain 3D flow data and planar laser sheet images would be recommended for fuller understanding of some of the effects discussed later on.

3.3.3 Testing and Shakedown

Prior to running the optical setup, numerous test runs of the engine were completed with a metal window blank and the side mounted spark plug installed to ensure that the engine assembly was robust and also operating with the appropriate thermodynamic characteristics. Results from these tests are analysed in Chapters 5.2.1 and 5.2.2.

For the very first optically captured cycles, the engine was motored at 700 RPM. This speed was chosen due to concerns that above this, the 45° mirror above the cylinder (for directing light from the bore) would vibrate; as would the breadboard upon which was the high-speed camera. This oscillation could cause inaccuracies in data capture and, in extreme cases, could damage the imaging equipment. Later on the vibration was eliminated by moving both the breadboard and the mirrors' support legs off the large engine base mounting plate and bolting them directly to the concrete lab floor.

3.4 Mixture

Daily measurements of ambient temperature and pressure were taken from a thermocouple in the test cell and a calibrated barometer in the laboratory respectively. This allowed for the best ambient control possible and allowed the user to identify where combustion errors could become apparent due to cooler ambient conditions.

3.4.1 Airflow

The initial concept design for this work included the capability of running boosted intake air fed from a stationary compressor in an adjacent room (thus simulating a supercharger). This compressor was to be shared with the university's wind tunnel facility but was not utilised in the end, albeit the system and capability remains. The throttle was situated at the head of the plenum and initially was that of a 40mm diameter drive-by-wire Bosch DV-E5 body, more commonly found in the MY2010 VW Golf. However, it was found that this gave too little sensitivity in throttle control. Consequently a mechanically actuated AT Power throttle of 24mm diameter was adopted (identical to that being used by the Brunel University Formula Student team in 2010/11). This throttle incorporated two throttle position sensors (TPS) providing measurements of the throttle configuration to the ECU. Figure 3.8 shows a schematic of the intake system.

Downstream of the intake throttle the airflow entered an intake plenum. The 50 litre plenum was designed to allow the intake air to collect and to reduce any pressure waves that could occur, particularly at lower engine speeds where excessive time between breathing events in a single cylinder engine can cause difficulties in maintaining a constant vacuum. In this plenum, the temperature and pressure of the gas were logged. There was also a drain on the underside of the plenum to remove any water accumulation from the potentially boosted air or from potential external EGR fittings.

The airflow passed out of the plenum and into a 2kW Secomak 571/4 Process Heater (in the foreground of the image in Figure 3.8) which was able to heat the air to a desired constant temperature. From there the flow entered the final stage of the inlet system where the PFI introduced the fuel into the intake manifold, with the fuel jets targeting the back of the intake valves as described by Dingle (2014). The temperature of the inlet air was controlled via a closed loop temperature regulator attached to the heater. In both heated and ambient modes, the temperature was logged using a k-type thermocouple.

3.4.2 EGR System

Originally the project called for using external EGR (hence the port fitting on the plenum) but due to both naturally-occurring high residual levels within the engine and project time constraints this plan was deemed inappropriate. It was noted that with the deactivated exhaust valve, the trapped residual levels were sufficient to provide in the region of up 15% EGR. A valve overlap sweep was carried out to determine the best starting point for the engine and in later experiments the timing would be altered to achieve variable EGR levels.

3.4.3 Fuel Supply

In this work, the focus was on future fuels and their effect on the flame propagation and combustion rate. During initial shakedown work, commercial gasoline was used for all baseline tests (unless stated otherwise) but for experimental work the baseline changed to iso-octane in order to reduce sooty combustion associated with liquid gasoline “pooling” in the intake valve seats and fouling the window. All fuels followed the same route to the engine in that they were drawn from a 5 litre reservoir via a pump and filter system which pressurised the fuel rail to 3 bar (Figure 3.9). At the end of the tract the fuel was then sprayed into the inlet manifold onto the back of the valves via a Bosch EV6 PFI. This type of injector possessed twin sprayjets and had a maximum mass flow rate of 349 g/min at 380 kPa fuel rail pressure.

The fuel/air mixture concentration was monitored using a Bosch LSU 4.9 UEGO (Universal Exhaust Gas Oxygen) lambda sensor in the exhaust tract connected to an ETAS LA4 Lambda meter that was simultaneously logged on the data acquisition system (DAQ). By observing the LA4 read-out the operator could vary the fuel-air mixture via the MBE ECU software to achieve the desired lambda. The Lambda meter had a number of variables – H:C ratio, O:C ratio and AFR for stoichiometric combustion. These could be altered to produce an accurate lambda value depending on the fuel type and the desired mixture concentration (Table 3.2). The UEGO was a planar dual oxygen pump cell which supplied a monotonic signal of between -2 and 3 mA depending on the lambda level (lambda of 1 equals 0mA) It ran with a limiting pressure of 4 bar and a limiting operating temperature of 930°C

and possessed an operating lambda range between 0.65 and air. The measured error for the sensor demonstrated that at 1 bar there was 0% error ranging up to 15% at 2 bar. The LA4 received the mA signal from the LSU 4.9 and converted the data into a read-out on the display. Both items had been tested for mechanical and thermal shock, though Bosch had warned against sudden high thermal shock.

Fuel type	H:C Ratio	O:C Ratio	AFR of Stoichiometric Combustion
Gasoline	1.850	0	14.7
Iso-Octane	2.5	0	15.13
E10	2.55	0.05	14.517
E15	2.575	0.075	14.211
E20	2.6	0.1	13.904
E30	2.65	0.15	13.291
E40	2.7	0.2	12.68
Ethanol (E100)	3.001	0.5	9
BU16	2.5	0.04	14.485
BU32	2.5	0.08	13.840

Table 3.2 Fuel properties entered into the ETAS Lambda meter for all fuel blends used [Heywood, 1988; ORNL, 2011 and Coryton, 2013]

For running alcohol fuels, the system required adaptation as the rubber fuel lines would eventually fail due to the corrosive nature of the fuel blends. These lines were replaced by stainless steel lines and the pumps monitored for signs of corrosion or failure. In addition, two different injectors (alcohol & non-alcohol) were used to avoid contamination. Details of the test fuels used are shown in Tables 2.1 & 3.2.

3.5 Control and Diagnostics

In the chapter below the various methods of logging data will be discussed. All the equipment referred to below is shown in a schematic layout, in tandem with the engine, in Figure 3.3. Much of the data was recorded using individual sensors which relayed information back, via a dual-combination of National Instruments USB DAQ cards, to a computer running bespoke Brunel University data acquisition

software, herein referred to as “Yantech” (Figure 3.10a). Within this software the last 100 cycles were displayed for the instantaneous IMEP as well as the mean of the last 100 cycles for key variables including IMEP, COV of IMEP, CA50, head and temperatures and the heat release rate.

Two DAQ cards were employed for this work: a high sample rate card and a low sample rate card (National Instruments USB-6353 and USB-6210 respectively). The high sample card had 32 analogue channels and a maximum sample rate of 2MS/s which sampled data with every increment of the digital shaft encoder, attached to the camshaft. The low sample card only ran at 3Hz and was used purely to log the temperature data and the lambda reading. These were logged via the low-speed DAQ as they are only required logging once in every cycle. The data from the two cards was unified and exported when the ‘Save’ button was toggled in the Yantech GUI.

3.5.1 Engine and Dynamometer

The engine was coupled to a 10kW motor-and-absorb dynamometer which was controlled from a panel adjacent to the door of the cell. Later in this project, a remote control panel was installed allowing the user to operate the engine while sitting beside the DAQ computers and the ignition/injection control board. The engine speed and torque measurements obtained from this dynamometer were recorded via the DAQ software and displayed on the MBE ECU software.

3.5.2 Ignition and Injection Control Board

The engine was largely controlled using commercial engine mapping hardware and software; specifically MBE Easimap Version 6 software (Figure 3.10b) connected to a MBE 959 CPU. This ECU used the crankshaft speed and cam position signals supplied by the various sensors (detailed later) to calibrate the results accurately. From this software the operator could change the spark timing, injection duration and start of injection as well as other parameters that were not varied during this work. The throttle aperture was adjusted via a mechanical linkage cable with the throttle position relayed to the Easimap software via the TPS. With regards to actions like PFI injection, spark initiation and DI injection (with the latter

not used here), the timing and duration settings were applied on the MBE software but did not become “live” until the user activated the relevant switch on the ECU switch panel. Also on this board were the ECU main power and the E-kill switch (red button in the centre). It is important to note here that during early setup work the claimed timings of the injection and spark were confirmed to be sufficiently accurate (error < 2° crank) via high speed logging synchronised to the in-cylinder pressure data.

3.5.3 High-Speed Camera Timing

The MEMRECAM fx 6000 digital high-speed video camera, fitted with a complimentary metal-oxide semiconductor (CMOS) sensor, was used throughout the optical work. When the camera was triggered, the system would instantly place a mark on the captured data sheets to allow for the user to unify both the optical and thermodynamic results, cycle for cycle, at a later date.

The camera was coupled to a DRS Hadland Model ISL3-11 image intensifier, an electro-optical device that transfers low level light images into visible quantities of light in a single wavelength. Due to its role of boosting the available light from the combustion region, care had to be taken to protect the photocathode and phosphor screens inside the device. The laboratory lights were extinguished before powering up the intensifier, with only a small light source by the PC used for illuminating the workstation. This ensured that only the combustion light would enter the intensifier-camera coupling’s aperture. After a sweep of intensity settings from 40% gain to 60% gain (See Chapter 4.7.1), it was decided that an intensifier gain of 60% would be the chosen setting for all imaging work. This was found to be the lowest setting at which combustion flames could be viewed in totality without being too dim for detection and the highest setting the user was prepared to utilise for fear of damaging the intensifier.

3.5.4 Pressure Logging

There were two points at which the system pressure was logged. The first of which was the pressure in the intake plenum which obtained the inlet air pressure. The pressure here was logged via a GEMS 1200 series pressure sensor attached to

the side of the plenum, consisting of a steel tube inside of which was a thick rubber diaphragm that deflected relative to the pressure in the plenum. This deflection was detected by a chemical vapour deposition (CVD) sensor coupled to an application specific integrated circuit (AISC) chip that processed the information and emitted a current relative to the pressure. From here the data was relayed to the DAQ and logged. Due to the steel tubing, the transducer was insulated against voltage spikes, electrical noise and static. Thus the transducer was capable of withstanding 20 times the force of gravity in terms of shock and 5-2000 Hz peak-to-peak vibration. In addition the transducer was capable of withstanding pressures from a perfect vacuum to 400 bar and had a safe operating temperature range of -20 to 125°C with a claimed 2% error at high temperatures and 0.2% signal drift per year [GEMS, 2011].

The second pressure sensor provided the in-cylinder pressure measurement. Due to the limited space in the cylinder, a small diameter, non-water-cooled pressure transducer was required (AVL GH14DK piezoelectric). Being a piezoelectric sensor this used the effect of an electrical charge created by the internal crystals (in this case gallium orthophosphate crystals) whilst they experienced load due to the in-cylinder pressure. The body of the sensor was embedded in the cylinder wall between the side window and the bottom exhaust valve in Figure 3.2a. This sensor could endure up to 300 bar (with an overload capacity of 350 bar) and a temperature of 400°C, adequate for the low load conditions and the temperature limits imposed by running an aluminium head. In addition the sensor was reported to have a cyclical temperature drift of ±0.7°C when running at 9 bar IMEP and was protected against vibration (with an acceleration sensitivity of 0.0005 bar/g and could withstand around 2000 times the force of gravity). This sensor had been specifically designed for knocking applications, yet was accurate enough to provide the precision measurements needed for accurate heat release rate analysis [AVL, 2013]. In early setup work the "thermodynamic loss angle" was fixed to 1° CA by recording the motoring pressure data at fixed speed (1200 RPM) and WOT conditions. Such a loss angle was based upon a "typical" SI engine value as recommended by AVL. Ideally the actual loss

angle would be measured under dynamic conditions using a capacitive probe; however such an instrument was not available. In reality the loss angle could also potentially vary with engine operating conditions but again this was considered beyond the scope of the work. Otherwise the in-cylinder pressure data "pegging" was performed via the "Yantech" software by computing the polytropic index during part of the compression stroke and extrapolating the curve to provide an estimate of absolute pressure at IVC. An ideal pegging would involve measuring the absolute pressure via a suitably accurate piezo-resistive transducer mounted in the liner wall [Cairns, 2001] but again this was not available.

3.5.5 Temperature Logging

The monitoring of temperatures is another parameter vital for both analysis and safety. In this project there were three main temperature probe locations: a rapid gas sampler port in the head, the DI tip, and exhaust bridge. The intake temperature was also logged. For this early shakedown work it was decided that only the in-cylinder and exhaust bridge temperatures would be used due to a limit on the data recording available from the early encoder and DAQ combination.

Figure 3.5 shows the location of the thermocouples used to read the temperature. These k-type thermocouples were made from two different metals which produce a voltage depending on the temperature gradient between the two materials – here the materials were chromel (90% nickel and 10% chromium) and alumel (95% nickel, 2% aluminium, 2% manganese and 1% silicon). The ones used in this work were RS manufactured k-type thermocouples that were capable of reading between 0 and 1100°C with a sensitivity of 41 µV/°C.

3.5.6 Speed and Crank Angle Measurement

The method used to measure the speed of the engine is one adapted from the design used by Williams [2006]. A 36-toothed metal plate was attached to the flywheel with a notch in the outer circumference and a variable reluctance (VR) sensor placed at the base of the flywheel. As the notch intersected the magnetic field of the sensor, a magnetic flux was created inducing a proportional voltage which could be converted into a wavelength for analysis. This wavelength was then

relayed to the ECU and thus a measurement of the engine's speed and the TDC location was noted (from referring to the position of the plate). While this type of sensor is inexpensive and can operate in high temperatures (up to 300°C) and vibrations (ideal for engine diagnostics), it does require some additional signal processing circuitry.

To measure the crank angle position for the engine controller, a second, smaller 36-toothed wheel was fitted to the exhaust camshaft and a Hall effect sensor was used to determine the orientation of the wheel, this is visible on the top left of Figure 3.4. Similar to the VR sensor, the Hall effect used a varied voltage output responding from a magnetic field. The Hall sensor itself was relatively more expensive than the VR but the output signal was processed by the transducer itself (or the required electronics were supplied with the sensor) which eliminated the cost difference. The Hall sensor can also detect much slower speeds than the VR, giving rotational information from high-speed to zero-speed ensuring the data logger didn't lose count of the location when the shaft rotated slowly – idling or low speeds.

Measuring the crank angle from the camshaft does have inherent issues, partly because the camshaft speed is half that of the crankshaft but also because the cams were linked to the crank via a cam belt which was subject to torsional vibrations. In addition the belt could stretch and break as it aged (though this was not observed during the lifetime of this work). The error in spark and fuel injection timing was proven to be less the 2° CA and this was considered acceptable based upon prior experience of crank angle based encoder error relative to MBE spark timings [Cairns, Blaxill and Irlam, 2006].

3.5.7 Crank Angle Encoder

The encoder that was originally supplied at the inception of this project was limited to supplying data once every half crank-angle degree. So as to ensure the most precise value of data per crank angle possible was achieved, the decision was made to switch to an encoder with a higher resolution: 2880 samples per revolution. Sourced from Encoder Technology, it was mounted to the inlet camshaft

allowing for data to be recorded with a resolution of 4 samples per crank angle. Upon removing and refitting the encoder, the author had to make sure that it was aligned properly and a custom tool was made to locate the encoder in such a way that it was mounted in the same position it was removed so that the readings taken were accurate. There were inherent errors of around 2° in the fitting of the encoder to the camshaft rather than to the crankshaft due to the torsional vibration that impacts upon the cam belt and the play in the cam lobes on the valve stem but this compromise was judged to be necessary due to the cost and time delays that would come from altering the crank housing to attach the encoder. This error was measured by simply rocking the camshaft and measuring the angular displacement of the intake camshaft. Subsequent results could have been impacted by excessive phase shift in the pressure trace or injection and ignition timings could have been excessively mistimed but in the early setup work several average IMEP logs were obtained to confirm that no error in average IMEP was occurring due to this positioning (error < 1%).

3.5.8 Testing Procedure

Upon entering the test cell every day, initial checks were made to the fuel lines to ensure that they were still all connected tightly and that no visible perishing or leakages had occurred to the fuel lines, a known issue with alcohol fuels [Kameoka et al., 2005; Bergström, 2007; Galante-Fox et al., 2007]. Once that had been completed, the dynamometer power supply was activated as was the ECU power supply. After a diagnostic system warm-up period, the Easimap software was launched on the lab computer, the in-cylinder pressure amplifier activated and the DAQ powered up. The lambda sensor was also activated and the calibration settings (HC, OC and AF ratios – Table 3.2) were checked to ensure they were set correctly for the fuel in use. The fuel level was also checked to ensure that there was enough for the day's running.

The final set-up check was to remove the window from the engine. This was done by unfastening the retaining bolts and turning the engine over by hand. If the engine was sealing properly then the window would be slowly forced out of the top of the engine. With this done and the window removed, a visual inspection of the

combustion chamber was carried out to check for any foreign bodies or deposits in the chamber or any damage to the engine that may have occurred in the previous day's running. The window was then checked for any damage and cleaned if required. With all checks passed, the window was slotted back into the head and the retaining bolts fastened tight. Before the engine could be motored, the throttle was moved between WOT and fully closed to see that the TPS was still transmitting correctly. The desired spark and fuel timings were then entered into the ECU and the engine motored to 1500 RPM.

When motoring, it was important to check that the engine was sealing correctly and that there were no air leaks around the overhead window, side windows or any other known potential leak paths. This check could be done audibly, listening for leaks, but was also done via the pressure trace in the Yantech GUI. Once this had been completed the fuel pumps were charged (this was done as late as possible to preserve the pump's lifespan). When the fuel pressure had reached 4 bar, the fuel supply and ignition switch could be activated and combustion running could begin. Every day the same operating point was tested and performance verified – 4 bar IMEP, 1500 RPM and MBT spark timing and stoichiometric fuelling set for the relevant fuel type. Once the engine was up to temperature the data was logged and compared to the daily checkpoint datasheet. This gave a good point for continuity and allowed for comparison between each day's running to ensure that there had been no shift in the baseline data for each fuel.

After the daily check was completed satisfactorily, the engine was run up from ambient conditions in this stoichiometric combustion state until the exhaust temperature reached 130°C. The engine was then turned off and the exhaust allowed to cool down. This process repeated until the head temperature reached 90°C. Once this temperature had been reached, the engine was shut down to allow the head to cool to base temperatures of 85°C and the exhaust to 90°C with a margin of error of 1°C. While the engine was cooling, the high-speed camera and intensifier were turned on. The camera was set to 8000 fps and the intensifier set to 60% gain (already established as the optimum intensifier setting as described

later in Chapter 4.7.1). The camera's remote control was then positioned ready by the lab computer. Once the temperatures had cooled to 85°C and 90°C respectively, the engine was re-started, with the desired spark, fuelling and throttle settings run until the head temperature reached 90°C (this usually coincided with the exhaust reaching 130°C – dependant on the fuel type and concentration), again with a 1°C margin of error, at which point the camera was triggered to capture the images and Yantech was triggered saving the last 100 cycles. This was done so as to ensure temperature consistency with the air-cooled engine.

Once all data had been captured, the fuel and spark were shut off and the engine and fuel pumps stopped. The engine was then left to cool to the base temperatures before the next set of results could be captured.

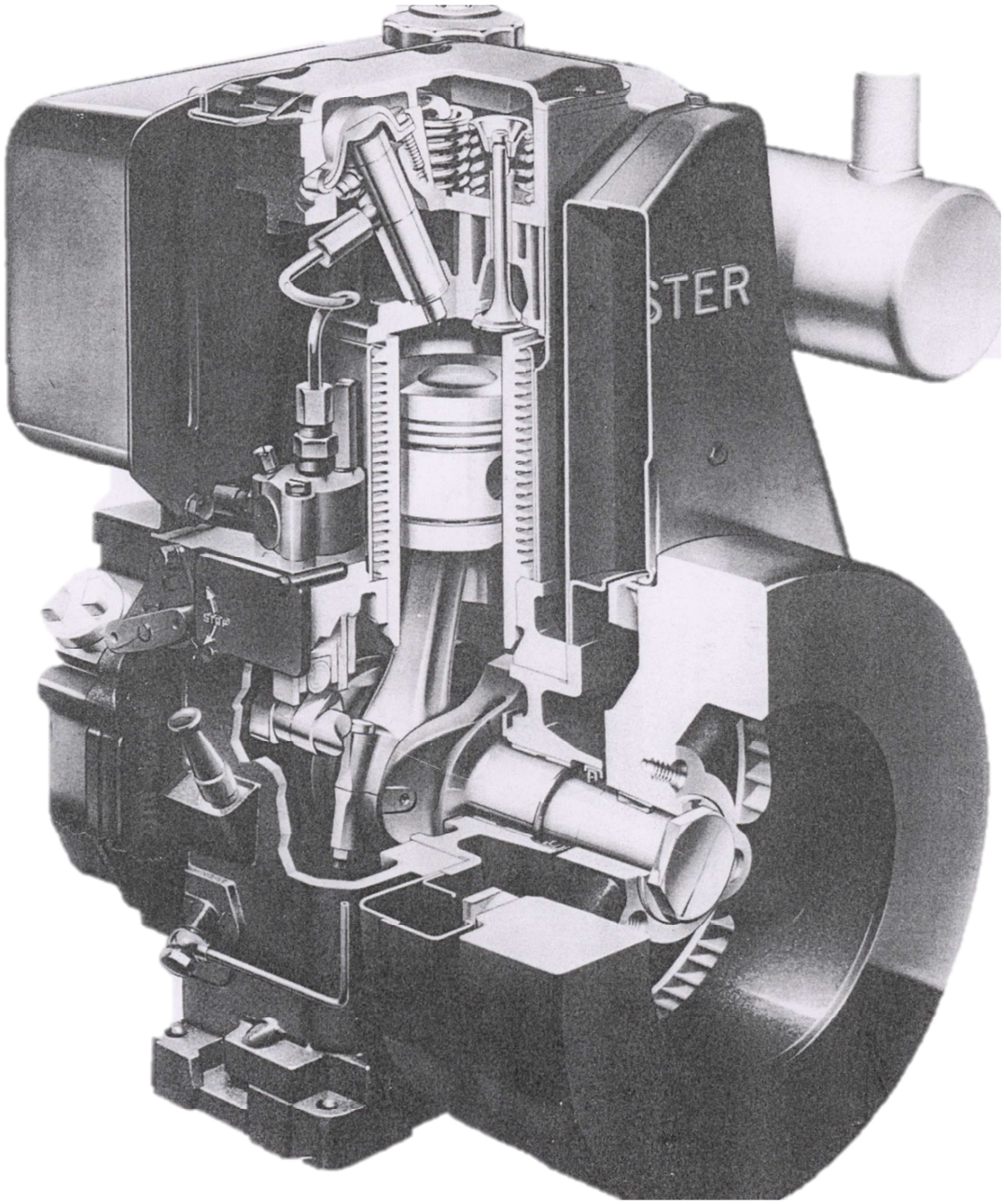

Figure 3.1 – A Lister TS-1 engine with a cut-away to display the single cylinder.

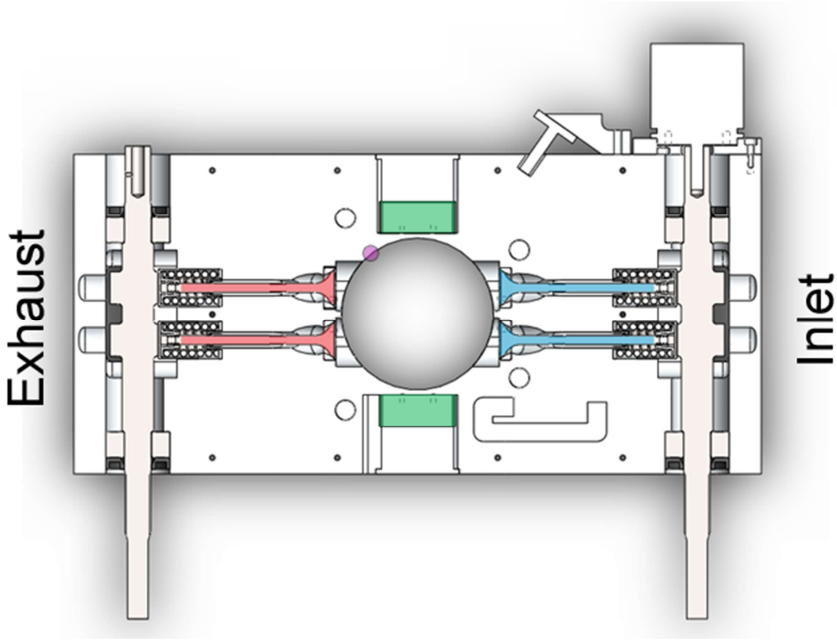

Figure 3.2 – **a.** Overhead view of the re-designed Lister head with the inlet valves shown in blue, the exhaust valves shown in red, the side windows in green and spark location identified in purple.

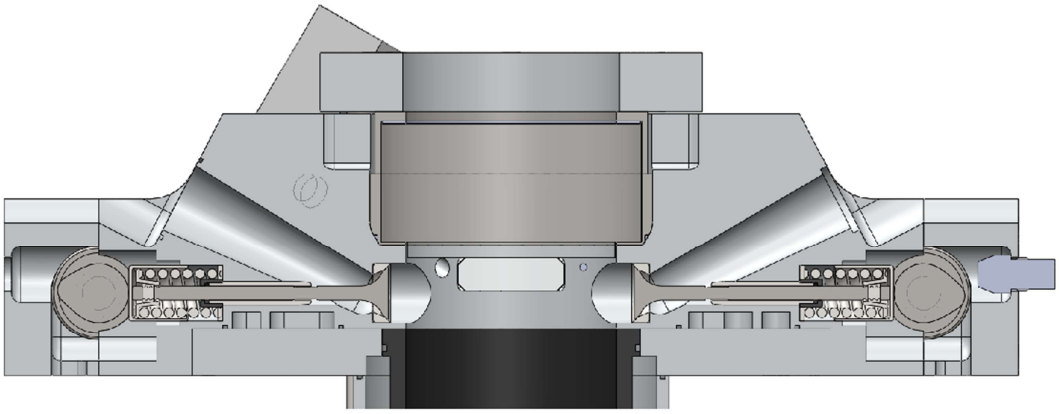

Figure 3.2 b. A cross-sectional view of the engine showing the inlet and exhaust port geometry.

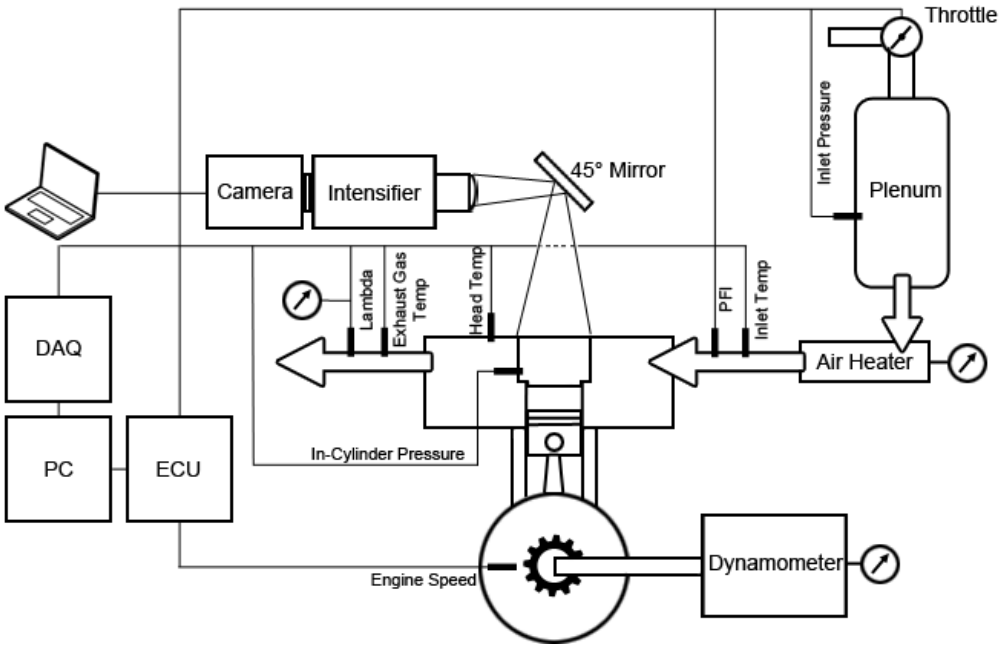

Figure 3.3 – Schematic of the experimental engine control, image capture and data acquisition systems.

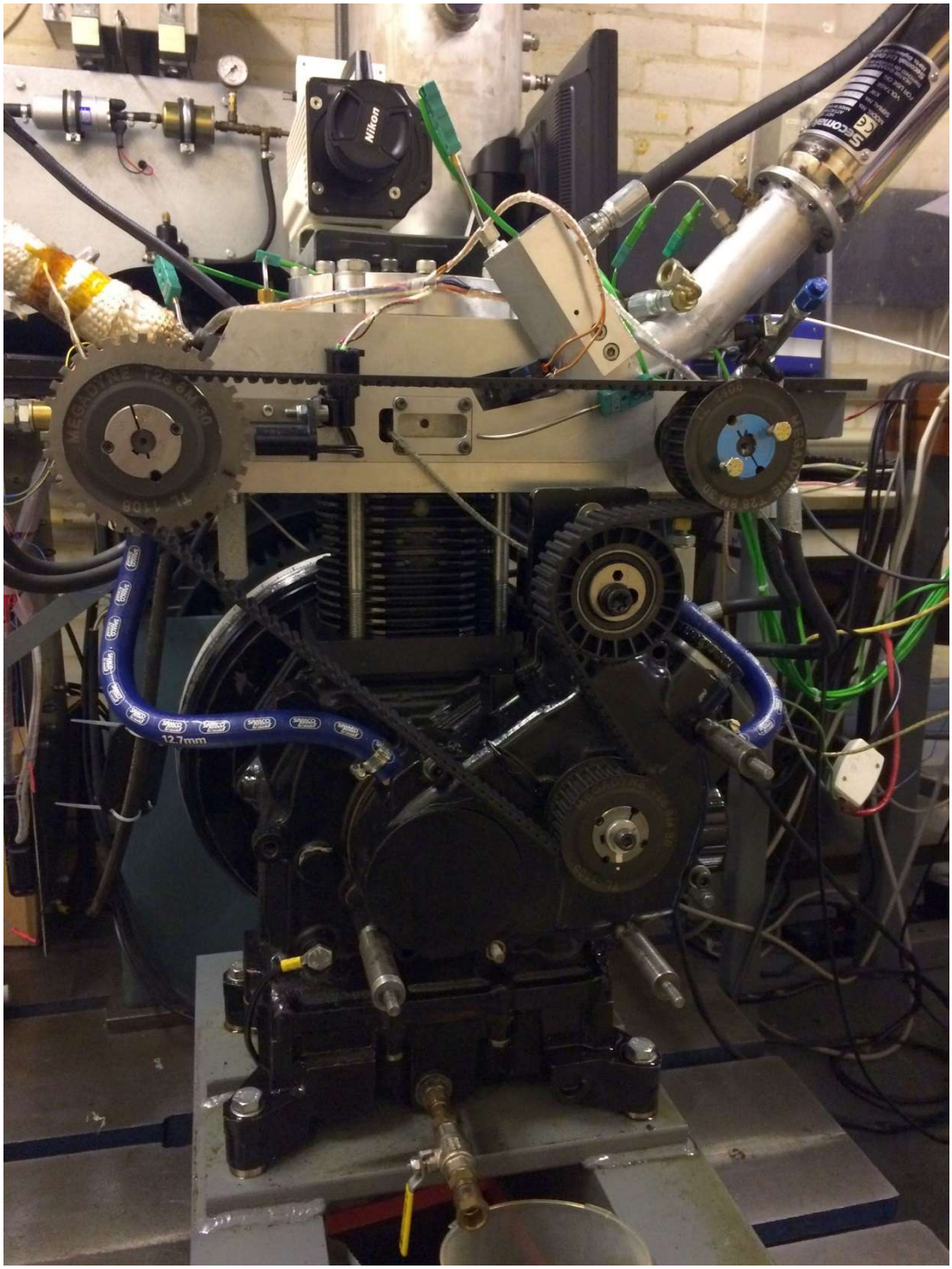

Figure 3.4 – An image of the engine showing the belt and pulley arrangement with the intake cam on the right of the image and exhaust on the left. The belt is driven off a pulley connected to the crankshaft via a toothed gear.

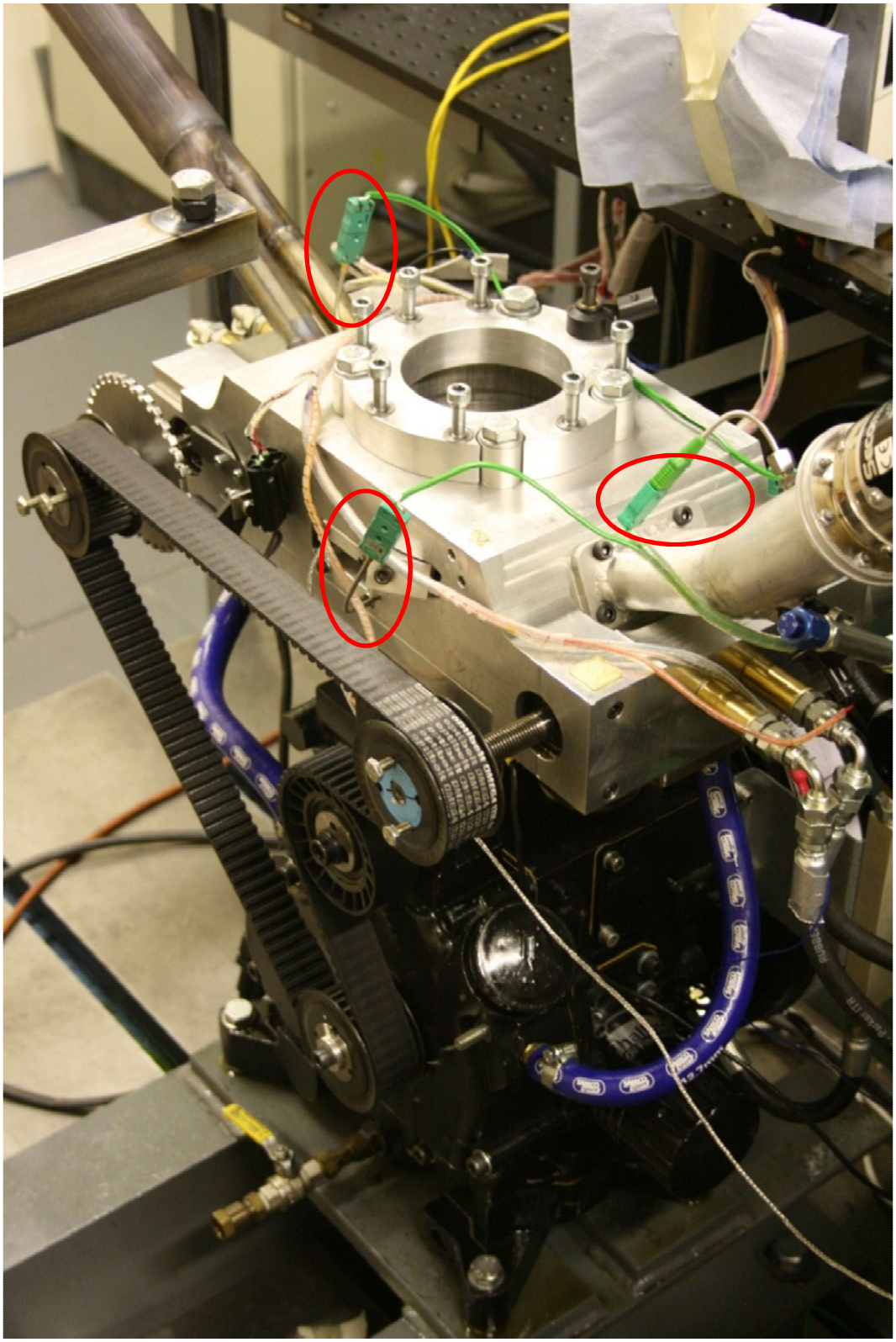

Figure 3.5 – An image of the engine showing the locations of the thermocouples for temperature logging with the belt and pulley arrangement in the foreground.

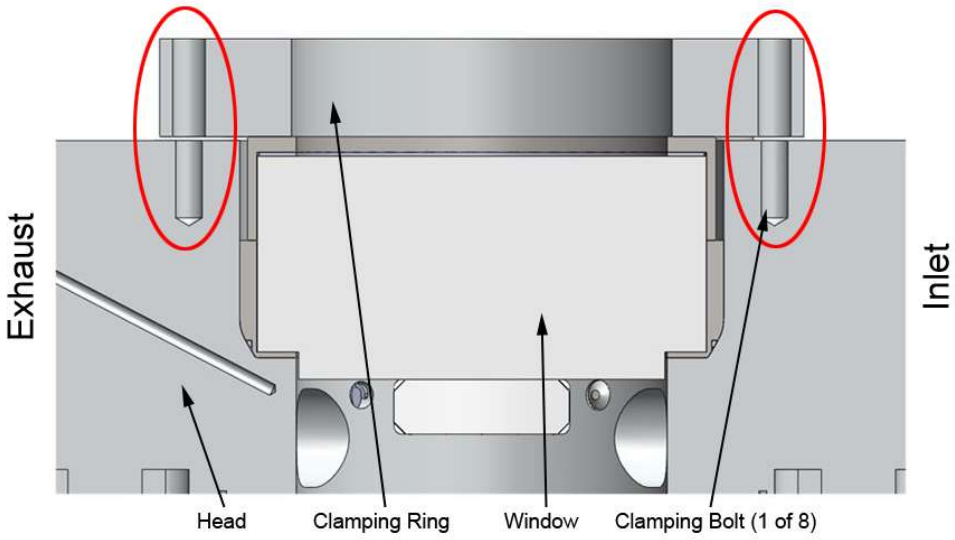

Figure 3.6 – Cross-sectional view of the cylinder head, looking from the bottom of Figure 3.2a with the inlet on the right. Circled in red are two of the eight clamping bolts.

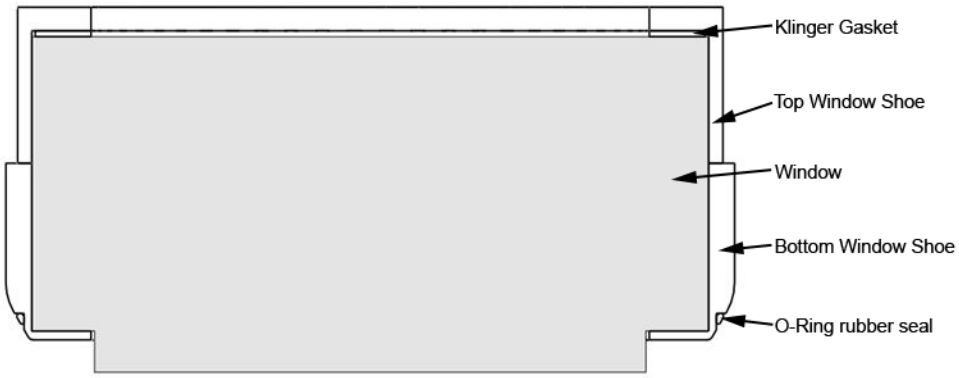

Figure 3.7 – A breakout from the above cross-section showing the window and its clamping shoe.

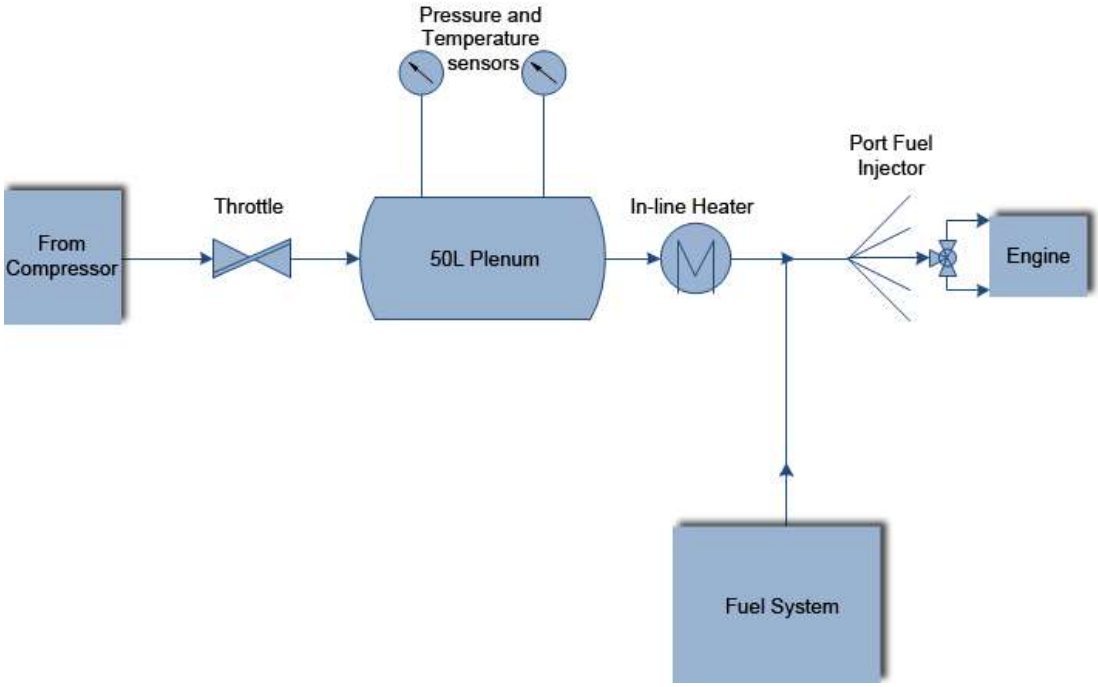

Figure 3.8 – A schematic diagram of the engine's intake system indicating the passage of air through the throttle, plenum and heater before being mixed with the fuel.

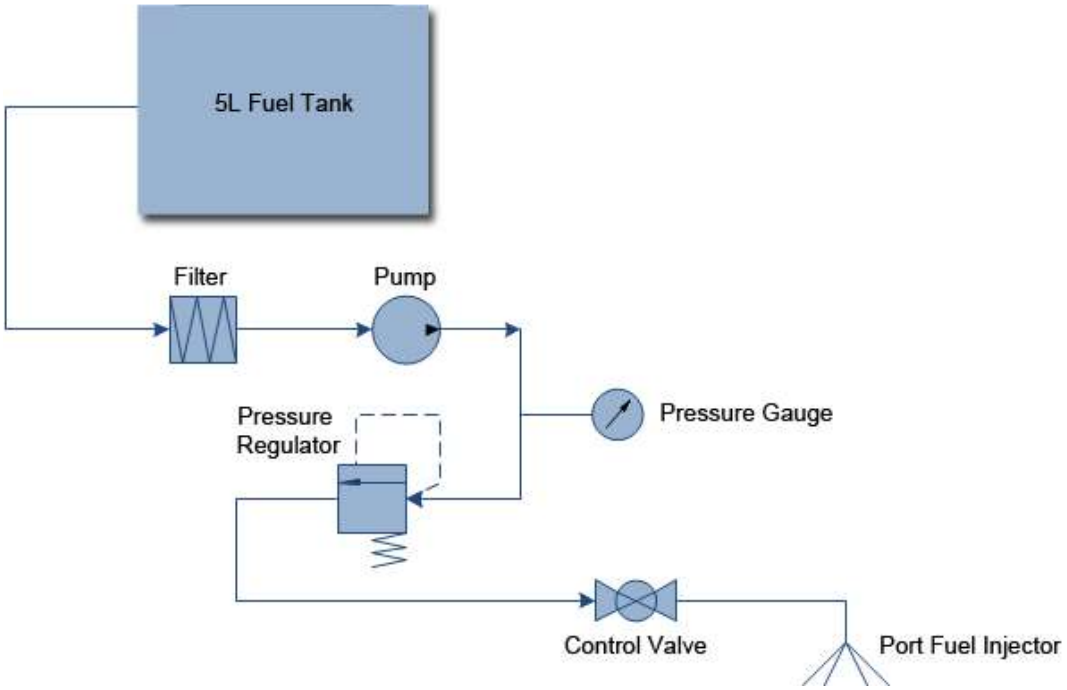

Figure 3.9 – A schematic diagram of the engine's fuelling system. The 5L fuel tank leading to fuel pump and filter before being injected into the intake manifold.

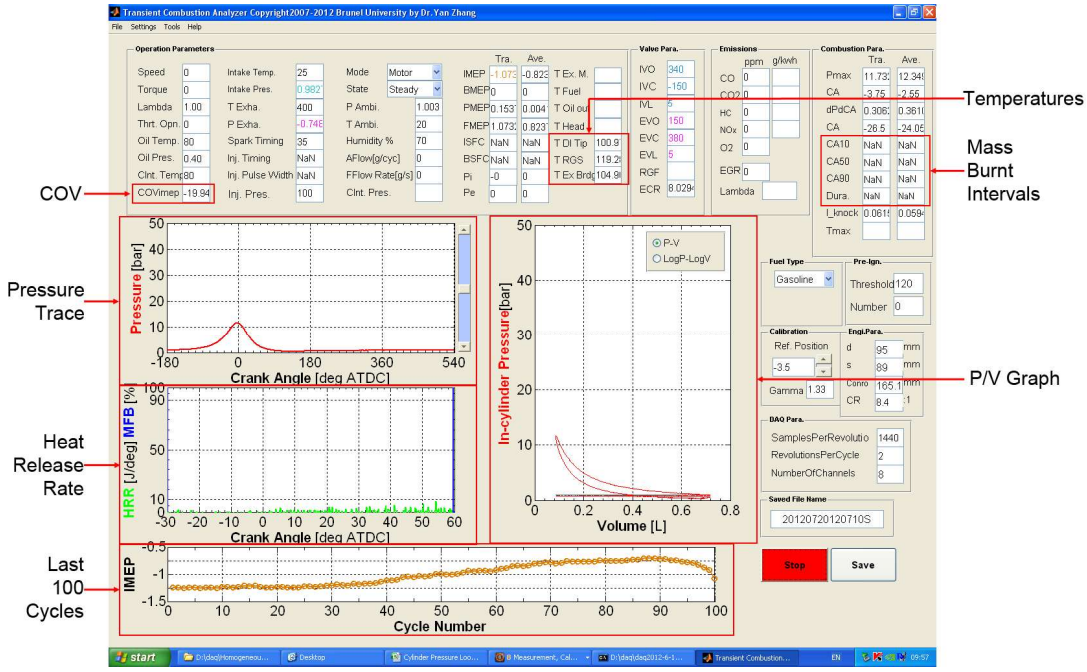

(a)

(b)

Figure 3.10 – Screenshot of the data acquisition software. Figure 3.9 a is 'YanTech' GUI, a Brunel University, in-house software allowing for interaction with the DAQ card. Figure 3.9 b is the MBE Easimap 6 GUI for controlling the ECU and dictating spark timing and fuel duration as well as displaying the TPS information.

Chapter 4

Flame Imaging Techniques & Analysis

4.1 Introduction

Over the last few decades optical in-cylinder diagnostic techniques have become an integral part of the automotive engine research and development process. Of particular note has been considerable use of these methods to optimise the delivery (spray and distribution) and combustion using DI in both SI and CI units, which involves the complex interaction between the incoming fuel and in-cylinder flow [Yang, Zhao and Megaritis, 2009]. However, even in the context of an ideal homogeneous mixed charge, the processes involved during combustion remain far from fully understood.

The interaction of the flame with the in-cylinder flow is random, highly complex and has been shown to evolve during flame propagation. For example, Cairns & Sheppard [2000] showed how the flow may initially determine the overall shape of the flame but the propagating flame itself may then, in turn, directly impact the flow ahead, with evidence of the flame "pinching" and accelerating the unburnt gases due to local burned gas expansion effects. In addition to such complex phenomena, other limitations to the present theoretical understanding of the combustion process exist. This includes laminar and turbulent flame instabilities, which remain ill-defined and continue to impede the reliability of any laminar and turbulent burning velocity correlations across all likely engine conditions [Gillespie et al., 2000]. As a result of these and other such issues, the availability of direct optical access within the combustion chamber remains crucial to engine research and development.

The first recorded evidence of the use of optical viewing windows dates back to the 1930's, where authors including Glyde [1930] and Withrow and Boyd [1931] sought to achieve maximum visualisation of the combustion process within the limits of the manufacturing processes available to them. Due to a lack of

suitable windows able to both view the full bore and withstand the high combustion pressures, Glyde used six miniature windows across the cylinder head. It was discovered that, while viewing these windows through a slit in a revolving disc, a bright yellow flash appeared in all of the windows at once but only once a normal flame had traversed the chamber, indicating a high level of remaining entrained unburnt gases being consumed.

In 1931, Withrow and Boyd connected such windows to form a single slit and recorded the outcome onto a revolving drum camera. In the following years, Withrow would then work with Rassweiler to further implement a quartz circular window allowing full bore access to the cylinder [1936]. This facility provided the first recorded evidence of a flame steadily propagating outward from the spark as a textured front and was captured using a high-speed motion camera. From such work Rassweiler and Withrow were able to show a correlation between flame geometry and the in-cylinder pressure development. Following on from such seminal work, in 1960 Frank Bowditch developed his eponymous extended piston design, which consisted of a long hollow shaft being mounted to the original piston and an optical crown being attached to the piston as illustrated in Figure 4.1. The shaft and bore had an elongated slot cut within the side wall which allowed a mirror to be placed at 45° inside the base of the extension. The piston would run up and down around the fixed mirror which would direct light up and through a window set into the piston crown (usually of quartz construction, sometimes sapphire for higher strength). The Bowditch setup therefore offers the ability to easily fit a production multi-cylinder head to a single cylinder bottom end with optical access via the piston. The key advantage of such a system was ability to gain good optical access (usually up to ~70% area of the bore) to the centre of the combustion chamber of a modern pent-roof engine while retaining more realistic breathing and flow.

As imaging technology advanced, the ability to see combustion in ever smaller timeframes was possible and with that it became possible to see the crucial early burning process from the spark kernel. Keck [1982] and Gatowski, Heywood and Deleplace [1984] observed, via schlieren photographs, that early in the spark

event the flame front possessed a 'wrinkled' structure dividing the burnt and unburnt charge. Smith [1982] used a laser scattering process in which the density profile of the flame was captured via a beam of laser light passing through it which then became scattered by the gas particles. From this an oscillogram of the varying intensity of the scattered light was obtained (and therefore the varying density of the gas at a point which Smith used to identify the flame front). Figure 4.2a corresponds to a section of the advancing flame front (motion from right to left) as it is intersected by the laser and scatters light particles due to density gradients between the burnt and unburnt charge. Figure 4.2b is a graphic representation of what the oscillogram displays. The right-hand peak in the trace denoted that a pocket of unburnt charge had become enveloped behind the flame front, caught in between two of the eddies which have curled together but not yet caused the pocket to ignite.

Smith's paper also concluded that engine speed affected the degree of 'wrinkling' of the flame front. Figure 4.3 shows a collection of propagating flame images all at identical crank angle locations with varying engine speed. As the speed of the engine increases, the wrinkling becomes more pronounced and the likelihood grows that more and more pockets of unburnt charge will become entrained behind the flame front. In more recent years it is now well known that such increase in wrinkling is the result of increasing the turbulence intensity with higher engine speeds [Gillespie, 1998]. In each slate the piston speed is noted in the bottom right. This was calculated from the stroke and the engine speed noted in the top right. This provides a good comparison between the engine Smith [1982] used and the one employed in this study – the piston speed that will be used for all experiments in this work will be 4.45m/s. Obviously the charge and fluid motion of each engine is different but the steady increase in turbulence intensity typified by Smith will mean that at the higher piston speed of this work the turbulence can be deemed to be at least in-line with traditional pent-roofed SI engines.

4.2 Natural Light Flame Imaging

Natural light imaging is a form of visualisation that uses only the light from the combustion process itself. Since the creation of the optical engine, this has

been the most common method of imaging until the 1980s when researchers began to develop tools such as Planar Laser Induced Fluorescence (PLIF) which is explained in more detail in Chapter 4.4.2. The aforementioned work by Rassweiler and Withrow [1936, 1938] using natural light can be considered to be highly advanced for the time, as they used a high-speed camera recording at 5000 frames per second (fps), resolved to 2.4 crank angle degrees per image to capture the progression of the flame across the cylinder. It was from this the authors were able to formulate their well-known method of calculating the mass fraction burnt. With the cylinder pressure already known via an array of probes in the cylinder walls and the total combustion volume of the chamber also known the authors would project photos of the flame against a plaster cast of the complete chamber. The unburnt section was then removed from the cast and the remainder weighed. To calculate the mass fraction accurately it was known that the in-cylinder pressure change (ΔP) is a combination of the pressure rise due to combustion (ΔP_c) and the pressure change due to the variance of the combustion chamber's volume (ΔP_v) due to the motion of the piston:

$$\Delta P = \Delta P_c + \Delta P_v \tag{4.1}$$

If the expansion or compression strokes are constant then the pressure and volume at the start and the end of each crank angle interval can be related by:

$$P_1 V_1^n = P_2 V_2^n \tag{4.2}$$

So to calculate the mass fraction burnt at the end of the *n*th interval:

$$\frac{m_{b(n)}}{m_{b(total)}} = \frac{\sum_0^n \Delta P_c}{\sum_0^N \Delta P_c} \tag{4.3}$$

where N is the total number of crank angle intervals. This is still a widely used method and is reliable on a qualitative basis (Beretta, Rashidi and Keck, 1983). However, on a quantitative basis the technique must be treated with caution as the

effects of irreversibilities such as heat transfer and mass blowby cannot be directly taken into account.

Natural light imaging cannot only be used to visualise the progress of flames as they traverse the cylinder but also to analyse the combustion products. As the flame spreads, specific molecules become raised to an excited state via exothermic reactions. Subsequently these molecules then decay back to equilibrium energy levels resulting in the emission of a photon (Figure 4.4), released in wavelengths depending on their chemical structure, whose radiation is much stronger than normal thermal radiation and therefore easier to detect. The capture and analysis of this is often referred to as Chemiluminescence. Table 4.1 shows the photon emissions wavelength groupings that differing chemical compounds display.

Methane CH (nm)	Hydroxide OH (nm)	Formaldehyde CH_2O (nm)	Carbon Dioxide CO_2 (μm)	C_2 (nm)	Aldehyde CHO (nm)
314 387-389 431	302-309	368 384 395 412-457	2.69-2.77 4.25-4.3	470-474 516 558-563	320, 330 330, 340 355, 360 380, 385

Table 4.1 - Emission peaks of key combustion species in IC engine [Yang, Zhao and Megaritis, 2009]

Rassweiler and Withrow [1938] showed that a flame front during the knocking cycle released photons that indicated methane, C_2 and hydroxide combustion products. Work carried out by Chomiak [1972] attempted to match these emissions rates from the flame front to the Kolmogorov scale from which a relationship with the turbulent flame scale could be found. He stated that the smallest highly luminous objects inside the combustion region would have a size of 1.5mm, which corresponds to the Kolmogorov microscale in said region.

The topic of cool flame combustion has been studied for a number of years and holds extra relevance for a thesis such as this involving ethanol-based

combustion. Cool flame combustion typically occurs between 600K and 800K and is a major contributing factor in auto-ignition. For example, Dec and Espey [1998] were able to show that auto-ignition was more prevalent when photon emissions were emitted at ~430nm. From this work it was clear that these emissions were from a cool flame and that it was largely made up of formaldehyde and methane. This flame chemistry is then engulfed and replaced, after the combustion, by the soot combustion spectra at 310nm, which displays a strong hydroxide presence.

Yang, Zhao and Megaritis [2009] confirmed this with a study of the effects of injection timings of Controlled Auto-Ignition (CAI) combustion. They too found that in a cool flame, a higher wavelength photon is emitted (here it was an aldehyde photon) which is quickly overtaken by hydroxide species in the combustion towards the end of the cool flame. This hydroxide radical becomes stronger and brighter during the main heat release. As the OH radical is a major chemical intermediate of combustion it is usually a good approximate indicator of the flame front when hot flame combustion occurs and is the target of many PLIF methods [Tanaka & Tabata, 1994; Zhao, Peng and Ma, 2004].

This use of the OH radical as a flame front marker is one of the biggest challenges with natural light imaging. To find the exact front of the flame is dependent on finding the UV light emitted from the hydroxide elements. In cool-flame combustion it is highly likely that this will not be as evident; Srinivasan and Saravanan [2010] have demonstrated that ethanol possesses low light intensity combustion due to the much cooler combustion temperatures. In using a natural light method of measurement, the user is reliant on the emissions from combustion itself to indicate the flame front. With OH radicals being emitted as UV light the user will struggle to view the advancing flame using just an ICCD camera. To improve the likelihood of seeing the flame front, the use of either an image intensifier or a suitable external light source of chamber illumination will help differentiate between the burnt and unburnt regions due to the difference in density. This use of an external light source can be known as schlieren (derived from the German ‘schliere’, which translates as streak or flow-mark).

4.3 Schlieren & Shadowgraph Flame Imaging

Schlieren is a technique that was first developed by Toepler in 1864 in an attempt to detect streaks in optical glasses. This was advanced and adapted for further research by Mach, who used it to photograph supersonic jet flows in Prague in the late 1880s [Settles, 2001]. Schlieren was not used in automotive applications until shortly after the Second World War by scientists like Male [1949] who used the system to detect auto-ignition in the cylinder. Ultimately this field owes a great deal to the work of Smith [1982] who advanced understanding of in-cylinder visualisation by passing a light source (in this case, a laser beam) through the cylinder and photographing the resulting images as shown in Figure 4.3. This use of a laser is now widely adopted for capturing schlieren or shadowgraph images [Smith, 1982; König and Sheppard, 1990; Pickett, Kook and Williams, 2009]. While both shadowgraph and schlieren have near identical setups; there are some important differences between them. Both will report density changes in the flow field, however schlieren is more sensitive to the first derivation of density due to the use of a knife-edge or aperture in the flow field (as seen in Figure 4.5) [Zhao and Ladommatos, 2001]. This filtering device is designed to reduce light noise from entering the image plane thus leading to clearer and better contrasted images than would be achieved with shadowgraph. Shadowgraph has its own advantages however, as it is less reliant on high quality optics and labour intensive precision alignment. In addition, if using a double-pass setup for schlieren the returned light can fluctuate due to piston rock, particularly around the edge which is a crucial analysis zone on a side-spark project such as this. Therefore successfully using an aperture (as in schlieren) would be difficult.

4.3.1 Profile

While laser light illumination allows for greater and more accurate imaging using lasers as coherent light sources carries inherent problems. The first being laser speckle, which are locations of random intensity light across the profile of the laser caused by the interference of multiple waves of the same frequency but different phases and amplitudes. Figure 4.6 shows an image captured using a standard D-SLR camera of an HeNe laser (633nm) profile. By looking closely at the

pattern in the profile it is clear to see areas of local maxima and minima with regards to the intensity of the beam. This phenomenon will greatly affect the image produced and an uneven profile will alter the ability to correctly analyse the flame. In addition, most lasers have a Gaussian distribution profile. This causes the intensity of the beam to be heavily focussed towards the centre of the beam's profile and to lessen as it spreads out to the sides. Shown in Figure 4.7, this profile means that nearly 80% of the beam's intensity is focused within half of the diameter. Therefore the resulting image will not have adequate illumination around the edges of the beam and will be too bright or over-exposed in the centre making accurate analysis difficult, another potential source of inaccuracy for a project such as this looking at side-spark combustion

One method to correct this is to insert a disc of ground glass in front of the laser beam to diffuse the profile. However, when the ground glass was trialled it was found that the returning beam's signal was inadequate in intensity. The grit ratings of the glass present a fine balancing act of transmittance and diffusion, a 1500 grit glass will provide a higher transmittance while 220 grit glass will create a greater amount of diffusion at the expense of transmission (Figure 4.8). Upon testing three different ground glass sets (1500, 600, 200) in the engine cell with the lights extinguished (as would occur during experimentation), it was found that the transmission ranged from 80% to ~50% of the total beam but all glass tested showed a severe impact on the beam's final intensity and that after a distance of about a metre the beam was too highly scattered to transmit results with any clarity.

4.3.2 Distinctions between Methods

Both shadowgraph and schlieren are widely used methods for detecting knock due to their sensitivity to changes in field density. As the refractive index may vary over the flame profile, due either to the propagation of the front or the mixing of the burned and unburned gases, this can result in two very different density areas. If the refractive index gradient is normal to the light rays that are being passed though the test area, then the rays will be deflected in a particular pattern as light particles travel more slowly where the index is larger. This deflection is a

measure of the first derivation of density and is the key definition of schlieren imaging [Zhao and Ladommatos, 2001]. A standard schlieren setup is seen in Figure 4.5. As the light passes through the work area, it refracts off in multiple directions thus leaving an imprint in the beam's profile which can then be recorded via a high-speed camera. Prior to the beam reaching the camera it usually passes through a knife-edge (or adjustable aperture) to partially block some of the scattered light from reaching the eventual destination. While this will make the resulting image dimmer, it is needed as the beam will become distorted and unfocussed while passing through the flow, it is this that will allow for clearer and more focussed images.

However, if the index gradient varies across the field (for example in turbulent flame structures) then the deflection of adjacent rays will alter so that they converge (or diverge) giving increased (or decreased) illumination on the screen or camera lens. These changes are known as the "direct shadow method" or shadowgraph, as worked on by Dvorak in 1880 [Settles, 2001]. As stated earlier, this differs from schlieren in that it has no knife-edge cut-off and does not provide a 'focused' image. It is also very sensitive to piston rock and motion. Figure 4.9 shows a standard shadowgraph setup. The lens L1 expands the beam to a diameter equal to or greater than that of the required work area. The beam is then re-collimated by lens L2, passed through the test section and then focused back down by a third lens, L3. Some setups will then either use a final lens, L4, to pull the image straight onto a translucent screen that is then filmed with a high-speed camera or will simply position the camera lens to act as lens L4.

As both schlieren and shadowgraph have a high sensitivity to density changes they are ideal for the study of both flame development and initiation and are not seen as *alternatives* to each other, more *variations* each with their own advantages over the other in a specified field or state, as noted in Table 4.2.

4.4 Laser Sheet Flame Imaging

In addition to schlieren and shadowgraph another laser method exists for optically capturing flame propagation through the charge. These were not trialled

within this thesis but perhaps could be implemented in future work. Laser sheet has benefits over schlieren/shadowgraph in that whereas they are only able to generate information directly along a defined line of sight, laser sheet can illuminate a plane in the charge thus giving spatially resolved information with a good temporal resolution. Indeed, a study by Hicks et al. [1994] utilised four separate sheets of four differing wavelengths (Figure 4.10) to provide as much information about the processes in the cylinder as possible. As combustion imaging is always a balancing act between spatial and temporal resolution types, this 'middle ground' of the laser sheet is seen by some as the better form of imaging [Kurada, Rankin and Sridhar, 1993]. In reality, the analysis of laser sheet images pertains to a two-dimensional slice of the reaction front whereas the aforementioned chemiluminescence and schlieren techniques are more closely related to the leading edge of the flame. The following sections will discuss, briefly, two more common methods of laser light imaging

4.4.1 Mie Scatter

This is the simplest of the laser sheet methods to implement and analyse. Mie scattering involves passing a light source through the field of study from which the particles of light become scattered. These are then captured on a standard high-speed camera. The term 'scatter' refers to the interaction of the electromagnetic radiation between the laser light and the "seeded" charge. If there is no energy exchange between the particles of the light and the particles of the mixture, then all light scatters. Once this happens there are generally two types of scatter: elastic and inelastic. Elastic scatter occurs when the frequency of the scattered light is equal to that of the laser light entering the field. Mie scattering is an elastic scattering whereby the diameter of the scattering particle (d) is greater than or equal to the wavelength (λ) of the laser light. One advantage of the Mie scatter system is that, unlike other systems, it does not require a particular power rating of light source or specialised ICCD, enabling setup costs to be kept low. However the light only scatters when the particles in the charge are large enough, in the order of 0.5µm for visible light, to disrupt the flow of light waves [Zhao and

Ladommatos, 2001]. With regards to the type and pattern of scattering, there are two forms of diffraction that will occur from the seed particle.

In both events the light is scattered in a pattern (as shown in Figure 4.11) which shows that the majority of the light scattered is returned to its source. The easiest angle to record optically from is 90° from the initial flow direction directly over the cylinder head or below the piston crown (depending on imaging setup), which is where many researchers install their optics. In the previously mentioned experiment led by Hicks in 1994, the four different laser sheets of different wavelengths were all captured by a single camera (Figure 4.10). Gillespie et al. [2000] took the work further by sending a pulsing (~20 kHz) copper vapour laser through a slow rotating mirror to create a 'swinging sheet'. This provided 25 simultaneous sheets giving either a three-dimensional flame front or gathering several multi-sheet images in a single combustion event. Though the information gathered was collected from a spherical bomb chamber and the technique difficult to implement it is none the less a valuable, advanced tool potentially allowing three-dimensional reconstruction of the flame.

4.4.2 Planar Laser Induced Fluorescence (PLIF)

PLIF is similar to Mie scattering in its set-up in that it produces a two-dimensional flame visualisation. This can be used to determine many things about the state of the charge: flow patterns, species concentration, temperature, pressure and velocity [Lozano, Yip and Hanson, 1992]. The in-cylinder charge is illuminated by a laser that has been formed into a sheet, which is passed into the engine via an optical window – usually situated as a 'collar' between the cylinder liner and the head or as two windows at the side of the head allowing the sheet to pass through the head itself (Figure 3.2). The laser sheet is usually pulsed and tuned to a chosen wavelength that will react with a specific tracer in the inducted mixture. This tracer can be a naturally-occurring product of combustion (aldehydes or OH radicals) or it can be a dopant, artificially inserted into the mixture [Hanson, Seitzman and Paul, 1990].

A portion of the molecules in the tracer will absorb the energy of the laser and become excited, decay and then release a photon of light energy which can be recorded on an ICCD or similar device. One potential issue with PLIF being so similar to Mie scatter is that Mie scattering can occur at the same time, causing interference and over-powering the PLIF signal. This is largely dependent on the dopant types and laser used. While PLIF gives a good flame front definition it can be time-consuming to implement. The energy required for the high-powered lasers can reduce the effective data captured to one image per cycle. As already discussed in Chapter 4.2, any fluorescence can be hard to accurately image and it can be difficult to interpret the signals correctly. PLIF can also be affected by any temperature and pressure fluctuations. Finally, PLIF requires a very particular type of laser which is dependent on the dopant selected. Some dopants work better with one laser and some with another; marrying the two together is the key to a successful experiment.

4.5 Comparison of Imaging Methods

To determine which method is most suitable for the imaging required in this work, a table of the positive and negative points from all five methods was drawn up, shown below as Table 4.2.

Method	Positives	Negatives
Natural Light/ Chemiluminescence	• Low in complexity to setup • Relatively inexpensive • Good measure of heat release fluctuations, both temporally and spatially • Alerts users to knocking regions • Allows user to spot species formation to analyse the chemical balance of the charge • Can visualise not only combustion, but 'cool-flame' combustion due to the emergence of a CHO radical	• Difficulties with identifying three dimensional structures • Signals must be interpreted carefully to ensure accuracy in assessment of emissions spectra • May not detect the flame front of cooler flames – particularly ethanol • Can be hard to detect all species due to varying wavelengths and with the spectrum of emissions being beyond visible light • Requires an image intensifier or an artificially boosted image – especially for alcohol fuels with less luminous flames

Schlieren	• Very good contrast, especially compared to shadowgraph • Works with both laser and white visible light (like LEDs) • Due to its sensitivity to density changes, is suitable for detecting knock and for visualising the initiation and propagation of the flame • Provides an in-focus image, unlike shadowgraph	• Can only generate information along the line of sight of the light source • Not able to see mixing clearly • If the flow is in three-dimensions the results can be misleading and the user is unable to integrate spatially throughout the flow • Requires the knife edge to be precisely placed • Requires a laser light source which could have a poor beam distribution • Double-pass can be very difficult to setup
Shadowgraph	• Lower quality equipment required compared to schlieren – therefore lowering expense • Works with both laser and white laser light • Due to its sensitivity to density changes, is great for detecting knock and visualising the initiation and propagation of the flame	• Can only generate information integrated along the line of sight of the laser • Difficulties with identifying three dimensional structures • Unable to integrate spatially throughout the flow • Double-pass can be difficult to setup • Requires a laser light source which could have a poor beam distribution • Sensitive to piston motion meaning lower accuracy around bore perimeter

Laser Sheet	**Mie Scatter**	• Can use any light source • Can use any type of camera (ICCD or high-speed) • Very strong signal • Clear distinction between the total burnt and unburnt gases • Good balance of spatially and temporal resolutions	• Unable to function with droplets less than 0.5µm in size because of its second order size dependence • Usually restricted to two dimensional (though swinging sheet techniques can be used to increase complexity)
	PLIF	• Very simple to set-up • Very high contrast as it is able to ignore irrelevant light scatters • Good balance of spatial and temporal resolutions	• Difficult to interpret signals • Must have an ICCD camera, thus raising costs • Requires a high-powered laser • Time-resolved images can take a long time to process, reducing the amount of optical work that can be completed in a day • Requires use of a dopant which may influence the in-cylinder mixture properties (such as the evaporation and the burn rates) • Requires a UV source to fluoresce the dopant

Table 4.2: Comparison of the major methods of visualising flame propagation in the cylinder [Zhao and Ladommatos, 2001; Nori and Seitzmann, 2008]

As a result of the technologies available and the accuracy level required, the method of flame imaging chosen on this project was natural light imaging. Murad [2006] made a comparison between two-dimensional flame imaging using natural light and schlieren and found that, metrics such as flame radius development and

shape factor were unaffected by the choice of technique provided the natural light emission was sufficient.

4.6 Flame Image Processing

To aid the processing of the images a certain amount of automation must be introduced. While this code itself will be discussed in greater detail in Chapter 5.4, a brief overview may be found below.

Once the video file had been deconstructed into individual frames, with a resolution of one frame every 1.15° crank angle, these were then processed via in-house MATLAB coded software. This analysed the pixel density of the image and assigned each a value between 0 and 1 as set by a pre-defined threshold value. The resulting image contained only white regions (pixels under that assigned value) and black regions (pixels over that assigned value). While the value requires initial calibration for each fuel concentration or equivalence ratio data set, this code saves time overall. From this binary image the program could identify the flame edge and the area of the black pixels, thus the area of the flame was calculated. The code then outputs not only the binary image of the flame for visual analysis but it produced a spreadsheet of the flame speed, area, radius, wrinkle and shape. More information on this code and its results can be found in Chapter 5.4.

4.7 Experimental Procedure

Originally this project was due to utilise both shadowgraph and natural light imaging but as the work evolved to focus more on the thermodynamic aspects of alcohol fuels and residual gases, the high specification requirements from the optical side of the work lessened. Both setups were tested and attempted but, as will be shown in Chapters 5 and 6, only natural light was used, which was considered an acceptable compromise given the observations by Murad [2006] in a similar full bore optical SI engine.

An NAC MEMRECAM fx 6000 high speed video camera coupled to a DRS Hadland Model ILS3-11 image intensifier was used to record all optical data for this experiment. The camera was triggered at the same time as the DAQ to record images simultaneously with the pressure and temperature data. The camera was

set to record at 8000 fps at a resolution of 512 x 308 pixels (3 pixels per mm) meaning that the time-resolved images acquired would be at 1.15° crank angles per image. While the desire will always be to capture the images 1:1 with the engine speed, this frame speed chosen was the quickest one available which still allowed full-bore optical capture at a resolution that allowed for early flame development to be identified accurately. Shown in Figure 4.12 is an example of a typical image output of the combustion process (note the TDC light on the right of the image).

The engine cell (shown in Figure 4.13) shows the engine with the optical head in place but also the camera and image intensifier secured to an optical table. A mirror positioned at 45° allowed the camera to capture images using only the natural light emitted from combustion. While pressure data for 300 thermodynamic cycles was obtained with each run, only 50 imaged cycles were obtained. This was due to the inherent data storage capacity issues and time-consuming nature of the optical imaging process. Figure 4.14 is a graph detailing the cumulative percentage error in COV of IMEP between the cycles, showing that as the amount of data captured increased, the variation between a cycle and those before it is reduced and that outliers were less likely to skew results. The error at 50 cycles was considered an acceptable compromise and it should be noted that several other authors have also shown that obtaining 50 optical cycles is sufficient to pick up key differences in flame development [Cairns & Sheppard, 2000; Aleiferis et al., 2008].

4.7.1 Intensifier Sweep

At the start of the work it was deemed crucial to evaluate the sensitivity of the mean flame propagation parameters to the intensifier setting. The images from the camera alone would be too dim for accurate analysis to be performed especially under lean conditions. The DRS intensifier (described in Chapter 3.5.3) was coupled to the camera and connected in such a way that when the camera's trigger was activated that, the intensifier's shutter opened. The purpose of this work was to ascertain the ideal light gain setting for the intensifier to be set at. Too low an intensifier gain setting and the flame still would not be clear enough; too high and the photocathode and phosphor screens in the device would be damaged due to excess light entering the shutter and effectively damaging the intensifier cells.

It was decided that three gain intensity settings should be tested. Previous users of the intensifier had advised not exceeding 60% gain in a darkened room (to avoid intensifier damage), so this formed the upper limit. Gain settings of 40% and 50% were selected for the remaining test points. Tests were carried out at 1500 RPM, stoichiometric iso-octane with MBT spark timing at 4 bar IMEP. In addition, the tests were repeated at a lean combustion site using iso-octane fuel (where the 4 bar IMEP lean limit was found to be $\lambda = 1.22$) at the same speed and load. It was expected that, while stoichiometric fuelling would show little major distinction between cases, the imaging of lean combustion would be hampered due to the dimmer nature of lean burn flames thus demonstrating the lowest gain setting with which accurate results could be obtained.

When analysing this flame data there are two parameters to observe and calculate. First is to look at the maximum flame radius achieved. Due to the spark being situated at the side of the cylinder walls, the ideal maximum radius is that of the full bore diameter (95mm) - however there will be some fluctuations in the precision of this value due to sight lines from aligning the optical equipment. The second key area of attention is the early flame development. With combustion, much of the flame's behaviour and motion during its propagation is established in the early milliseconds after the spark event. If this early motion and light emission is not adequately captured by the camera then the true reasons for the resulting flame motion will not be available.

In the stoichiometric intensifier sweep, the flame radius results show that all three gain settings resulted in the camera being able to identify a near-full radius (Figure 4.15), though 60% gain was the closest to the actual maximum flame radius. However, earlier in the flame development, with the intensifier gain set to 40% the camera was unable to visualise the early flame's progression until 15° after the spark event. This inability to identify the early flame is also apparent from the flame speed trace in Figure 4.16. The apparent flame speed is calculated using the change in distance (radius) over the time step between images and is equal to the sum of the turbulent entrainment velocity and the velocity at which the unburned gas is pushed away by compression due to piston motion and the expanding burned gas.

So while this is ‘flame speed’, it can also be viewed as ‘flame radius growth rate’ – thus any failure to accurately identify the flame radius from its initial kernel can lead to sudden and erroneous jumps in the flame speed, which can be more pronounced when using flame imaging techniques influenced by three-dimensional effects.

With the intensifier set to 40% gain, the results would indicate that the flame never reaches full bore, stopping some 10mm prior to the bore’s full radius and that the flame speeds exceeded 50m/s. In truth, the speed is closer to 28m/s maximum. As such, 40% gain was ruled out as a viable setting. Looking at Figure 4.17 a full visual comparison of the three stoichiometric fuelled cycles is shown. The three cycles chosen were the closest optical cycles to the numerical mean cycle’s PMax and APMax. The intervals were spaced 5° crank angles apart, with the first images being 9° after the spark event. In the images captured using a gain of 40%, the already dim combustion is not boosted enough by the intensifier to be adequately imaged by the camera and as a result, the processing software was unable to identify the flame until 10° before TDC (some 19° after the spark). By comparison, with the intensifier set to both 50% and 60% the camera was able to detect and capture combustion from early on – though the flame size and shape is different for both.

Analysing the lean combustion results (Figure 4.18), the conclusion that 40% is an inadequate setting was reinforced, as with the dimmer combustion profile the ICCD can only detect a flame with a maximum radius of 42mm, under half the actual bore diameter. When the intensifier gain was increased to 50% this identified radius is improved, showing 60mm as the full burn radius. As for early flame development, again 40% and 50% intensifier settings failed to identify the flame growth until 26° and 10° after spark respectively.

Once again these failures to track the flame radius growth accurately carry over to the flame speed results – Figure 4.19 – with the fastest speeds being shown as occurring post-TDC, when much of the flame has traversed the cylinder, thus producing sudden flame speeds in the region of 30m/s. In Figure 4.20, as with

Figure 4.17, the optical cycles closest to the numerical mean cycles have been selected for each gain setting to aid comparison. Even though these three gain settings are essentially imaging the same combustion event and the flame profile and pattern should be roughly similar (allowing for minor cyclical variation), there is no flame at all in the 40% gain images. As for the images taken at 60%, while the flame is still harder to identify than those from stoichiometric combustion (as is typical of lean combustion) the imaged flame was a complete advancing kernel as would be expected. With ethanol having a dimmer burn than iso-octane or gasoline [Srinivasan and Saravanan, 2010] the aim of this brief experiment was to identify the intensifier setting that would allow the camera to record the combustion data as accurately as possible, while avoiding over-powering the intensifier. Thus 60% was chosen to be the intensifier setting but it is important to note this was at the mercy of the 60% cap. Ideally, in the lean case, a higher setting would have been tested to confirm the satisfactory performance at 60% and it can be seen that some small error remains in the maximum flame radius recorded.

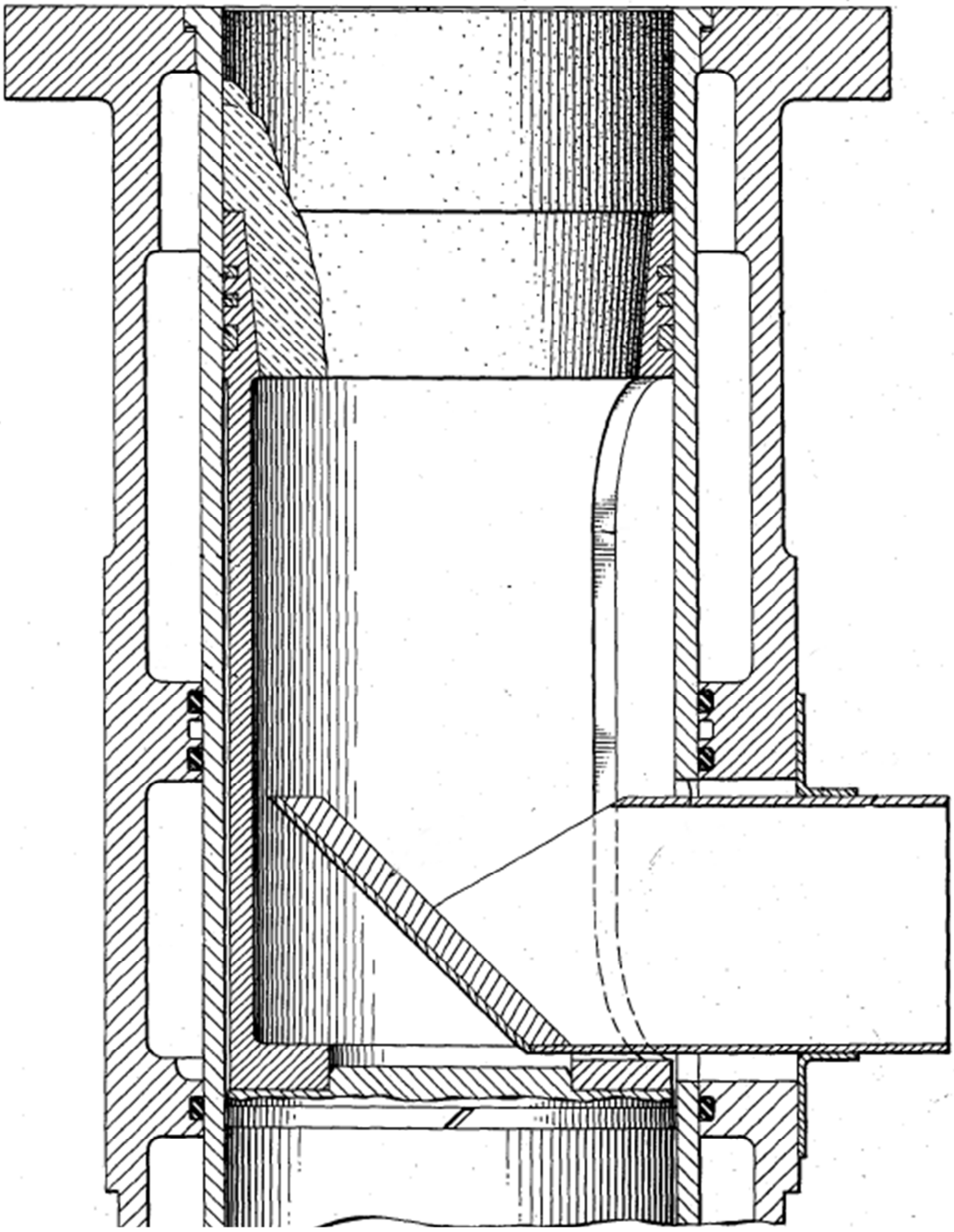

Figure 4.1 – The design for the Bowditch piston as taken from the US Patent filed for invention [Bowditch 1960].

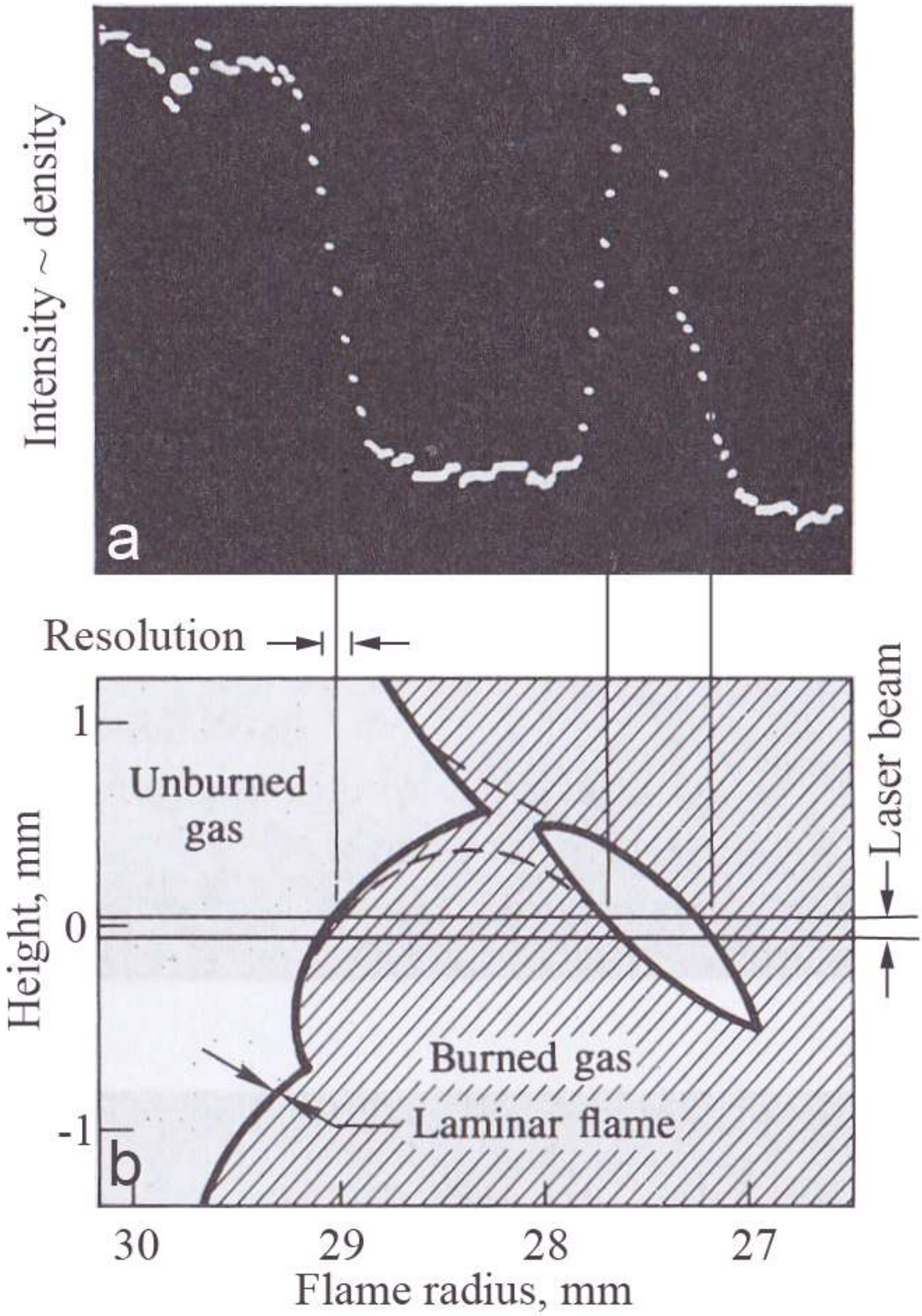

Figure 4.2 – Smith's captured density profile in a) an oscillogram output of the intensity of the light scattered from the laser beam as a function of the distance through the flame and b) a schematic of the oscillogram's display clearly showing a pocket of unburnt gas 'trapped' behind the flame front [Smith, 1982].

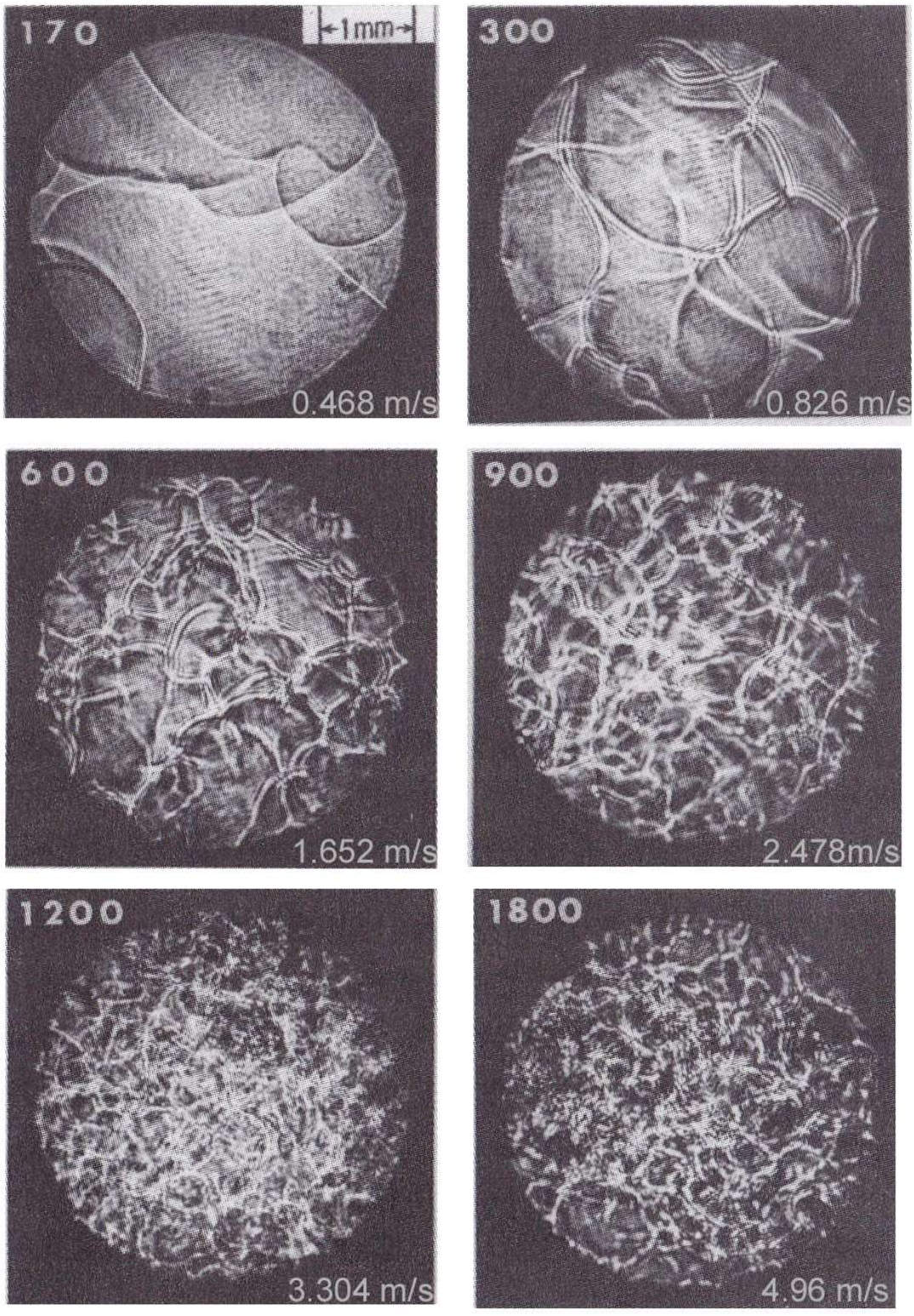

Figure 4.3 – Shadowgraph images of flames propagating towards the camera at differing engine speeds, the speed in RPM is noted in the top left hand corner of the slates with the piston speed noted in the bottom right [Smith, 1982].

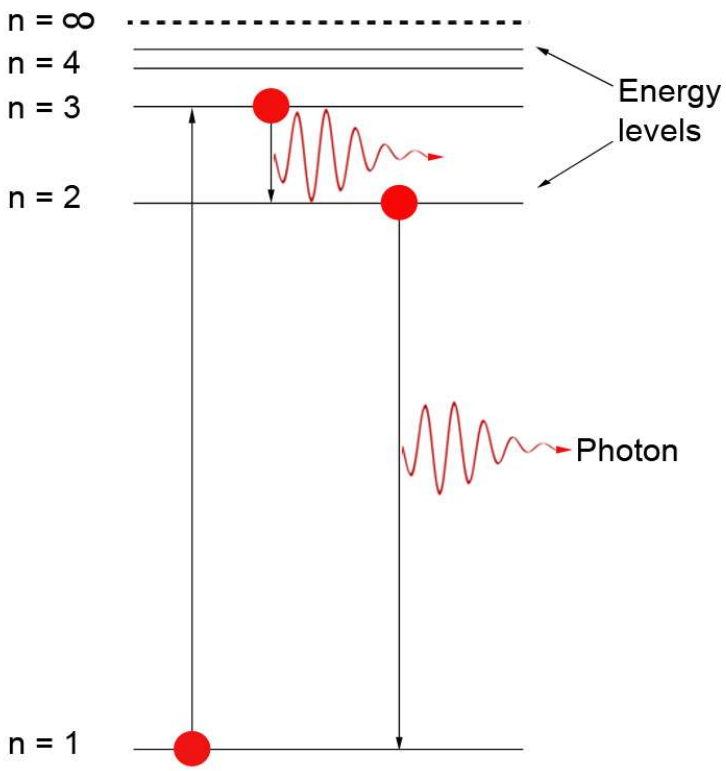

Figure 4.4 – Molecules becoming excited by exothermic reactions which raise them to an excited state. Their decay then produces a photon.

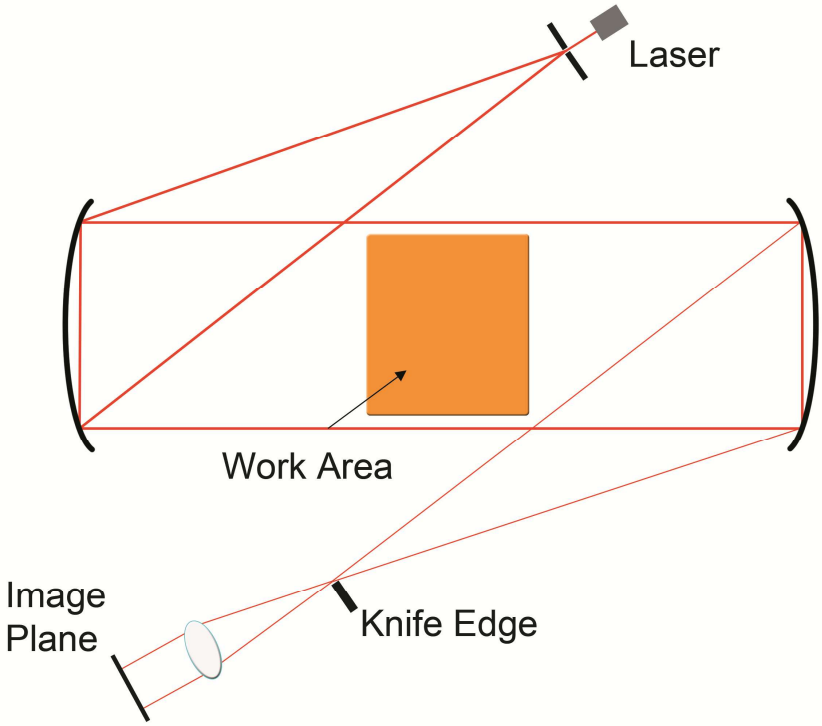

Figure 4.5 – Typical schlieren setup with concave mirrors and a knife edge to clean up the resulting image and remove shadowing [Adapted from Zhao and Ladommatos, 2001].

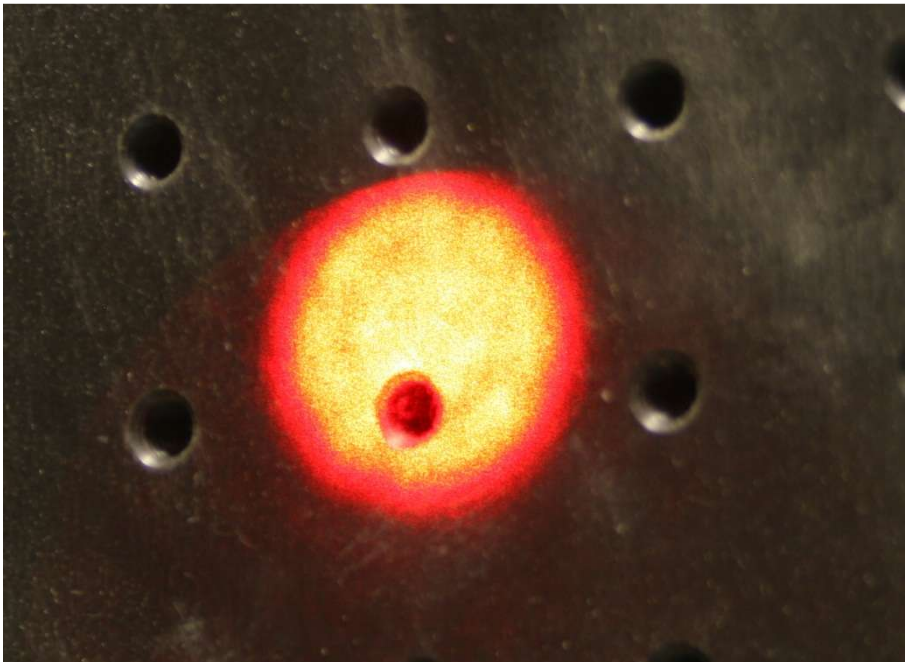

Figure 4.6 – Image of a laser profile displaying laser speckle issues.

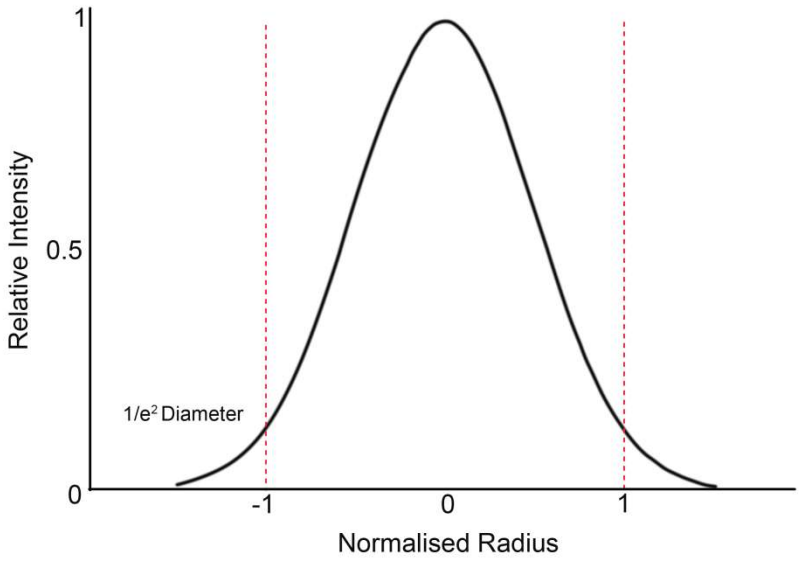

Figure 4.7 – Gaussian intensity distribution of a typical HeNe laser.

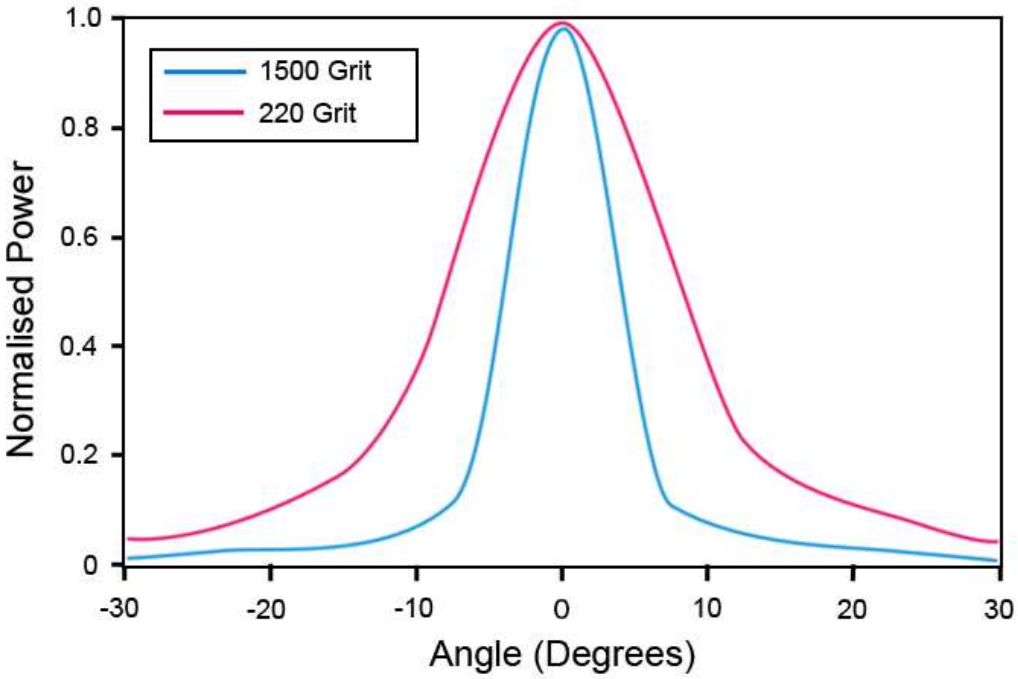

Figure 4.8 – A graph displaying the diffuser transmission for the two grades of ground glass trialled in this work displaying differing angles. From this it is clear that the 220 grit gives greater diffusion and the 1500 has a better transmittance [Thorlabs website, Accessed 15th July 2012].

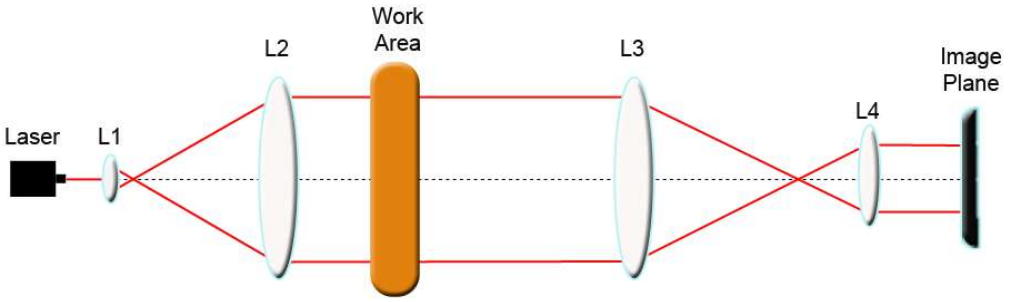

Figure 4.9 – Recollimated shadowgraph setup [Adapted from Zhao and Ladommatos, 2001].

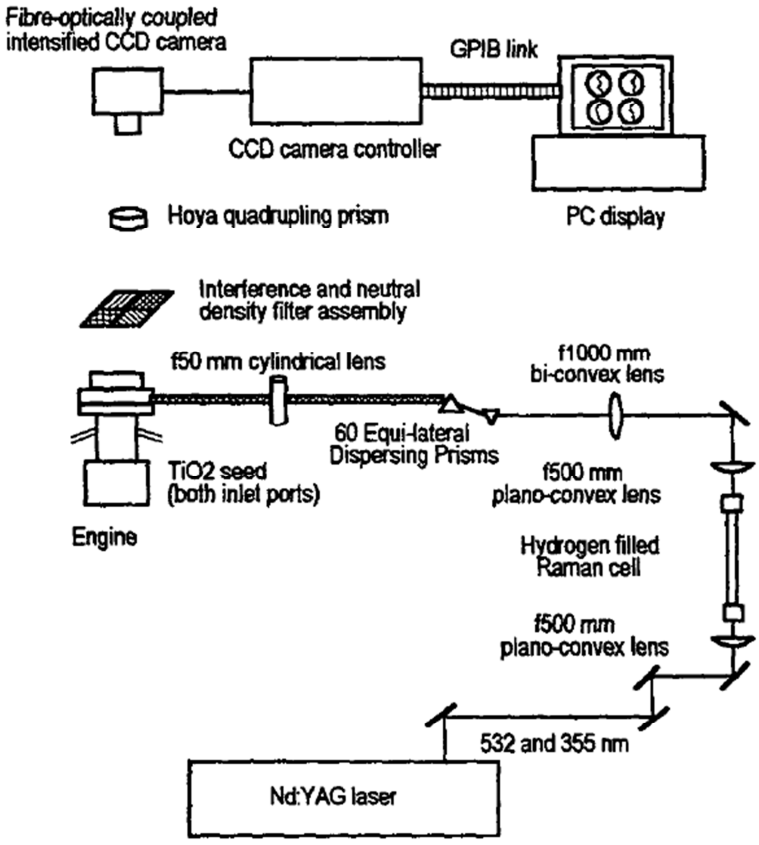

Figure 4.10 – The multiple laser sheet setup used by Hicks et al. [1994] to provide a three dimensional imaging data supply.

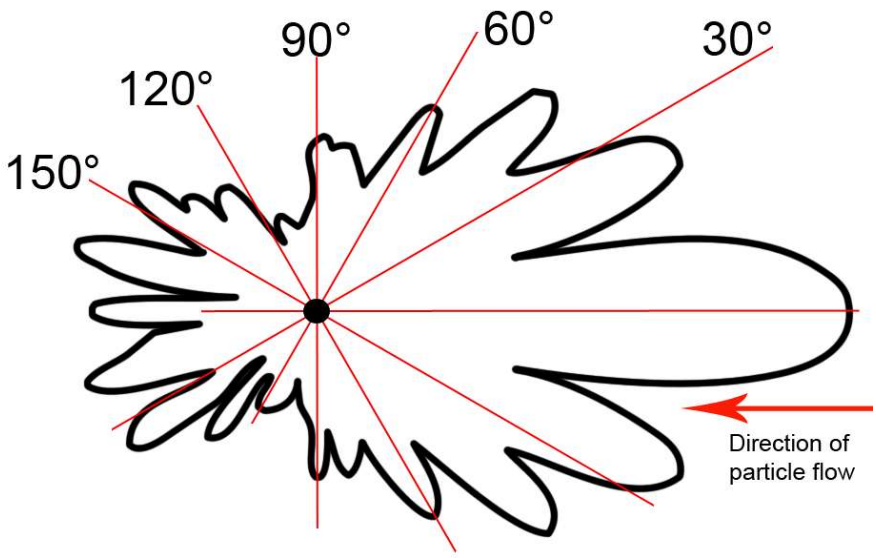

Figure 4.11 – The calculated angular distribution of the light intensity scattered by a sphere [adapted from Cairns, 2001].

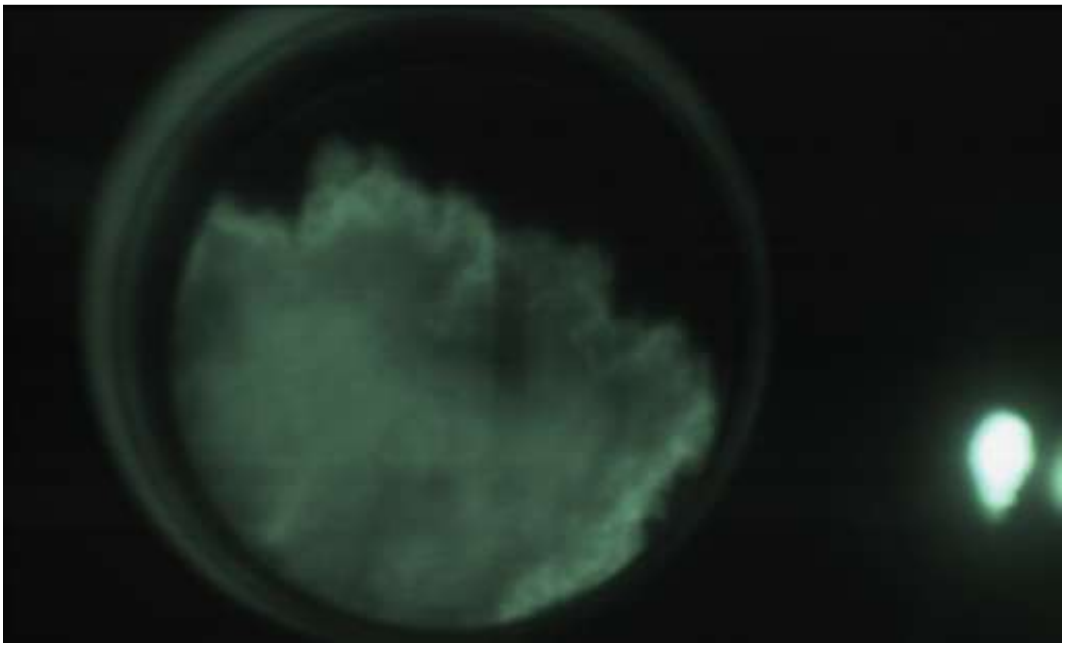

Figure 4.12 - Graphic detailing a standard image captured during combustion. The bore is evident from the 'halo' of light around it with the propagating flame clear in the centre. The burst of light on the right-hand side is to indicate TDC.

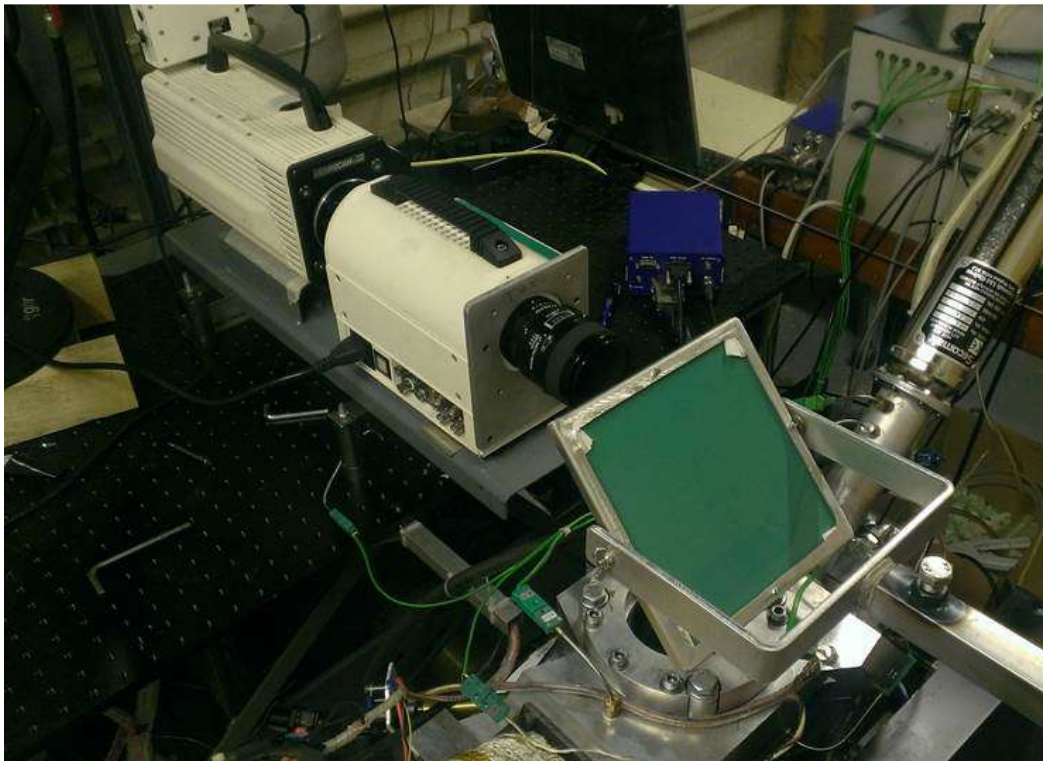

Figure 4.13 – Photograph of the natural light imaging setup for this experiment showing the NAC MEMRECAM fx6000 joined to a DRS Hadland Intensifier position directly in front of the engine and aligned with the 45° mirror.

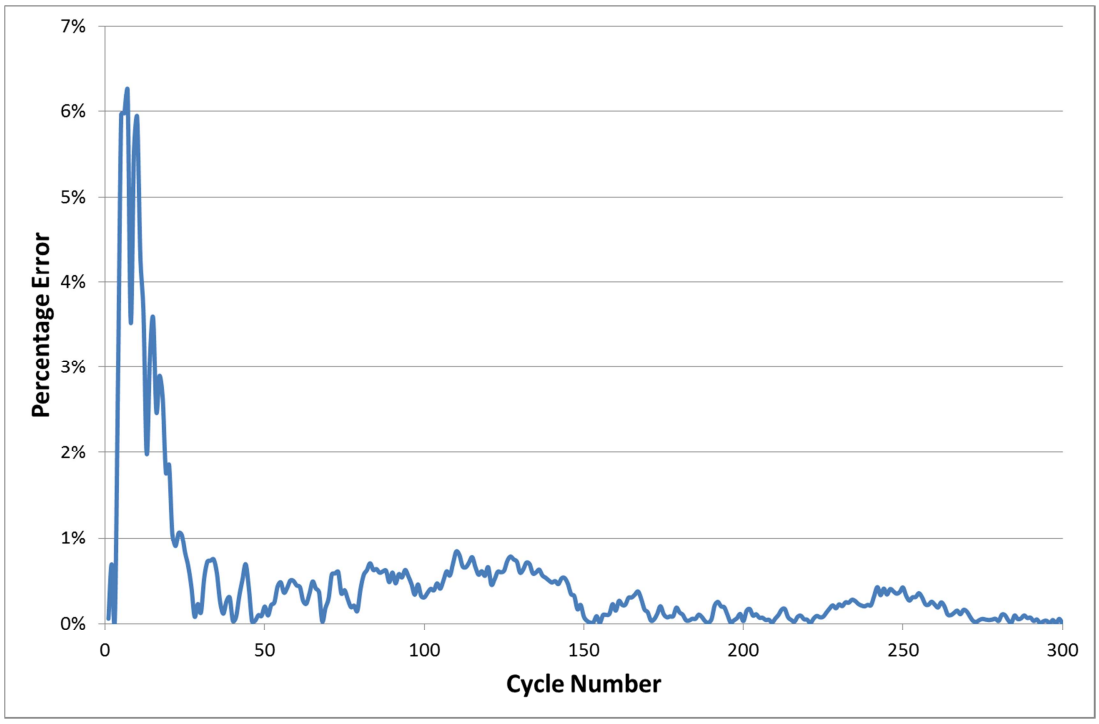

Figure 4.14 – The cumulative percentage error in COV of IMEP over the 300 cycles captured.

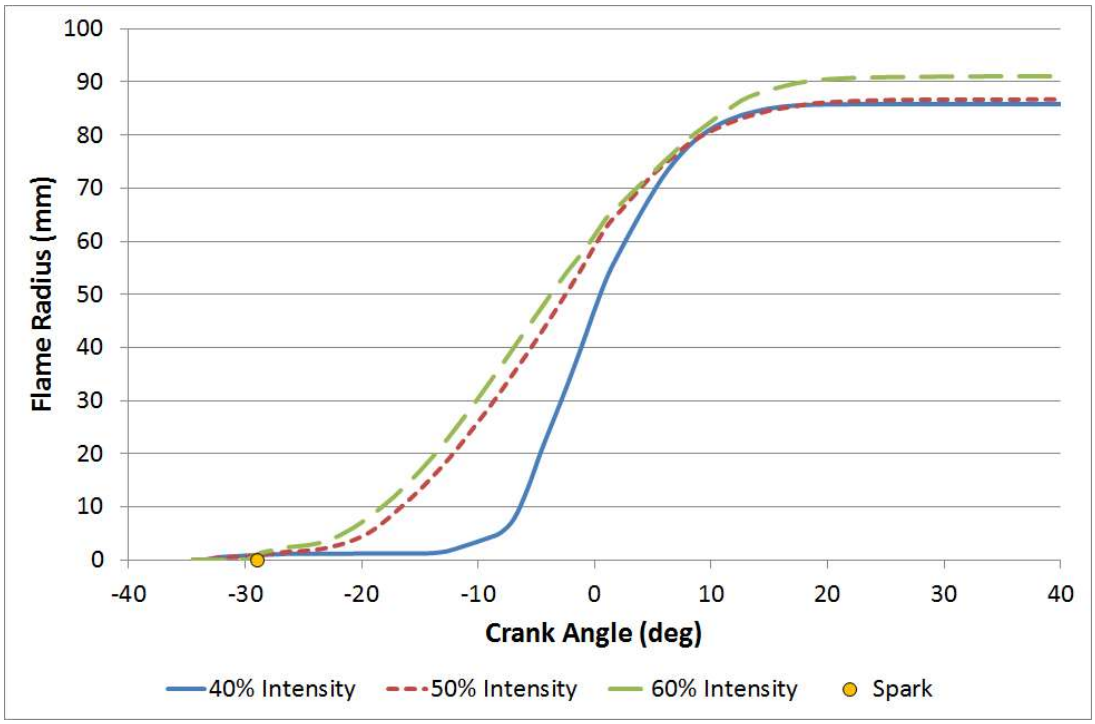

Figure 4.15 – Flame radii for the three light intensity settings for the image intensifier. The spark is located at 29° bTDC for stoichiometric, MBT combustion at 1500 RPM.

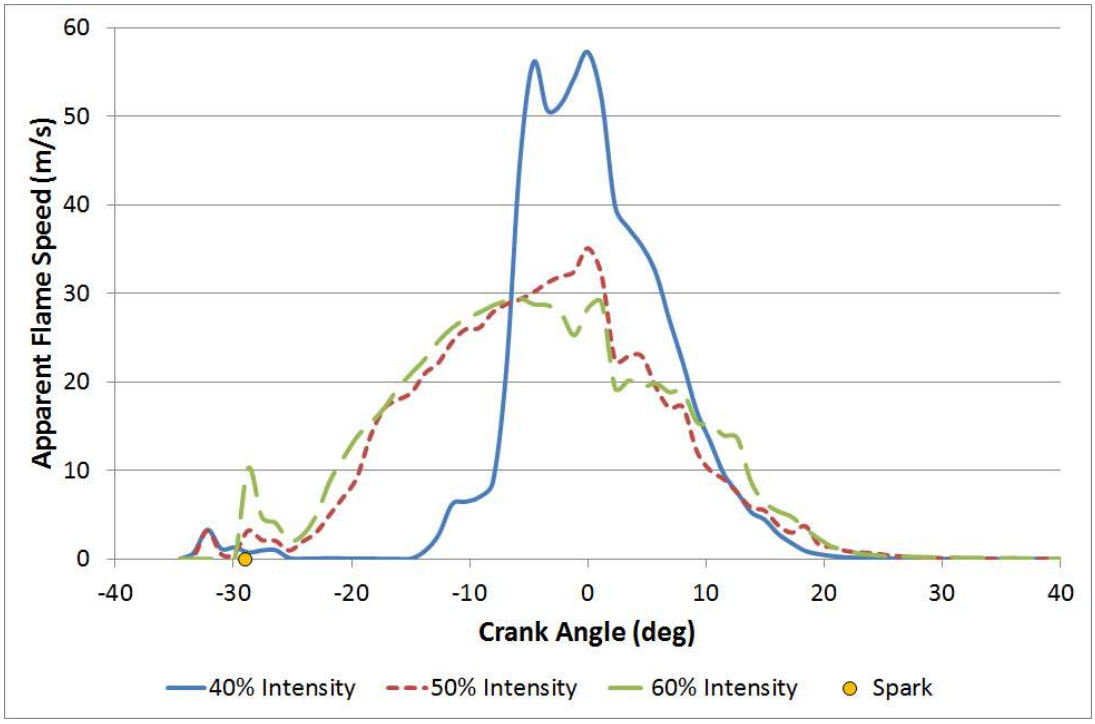

Figure 4.16 – Apparent flame speeds for the three light intensity settings for the image intensifier.

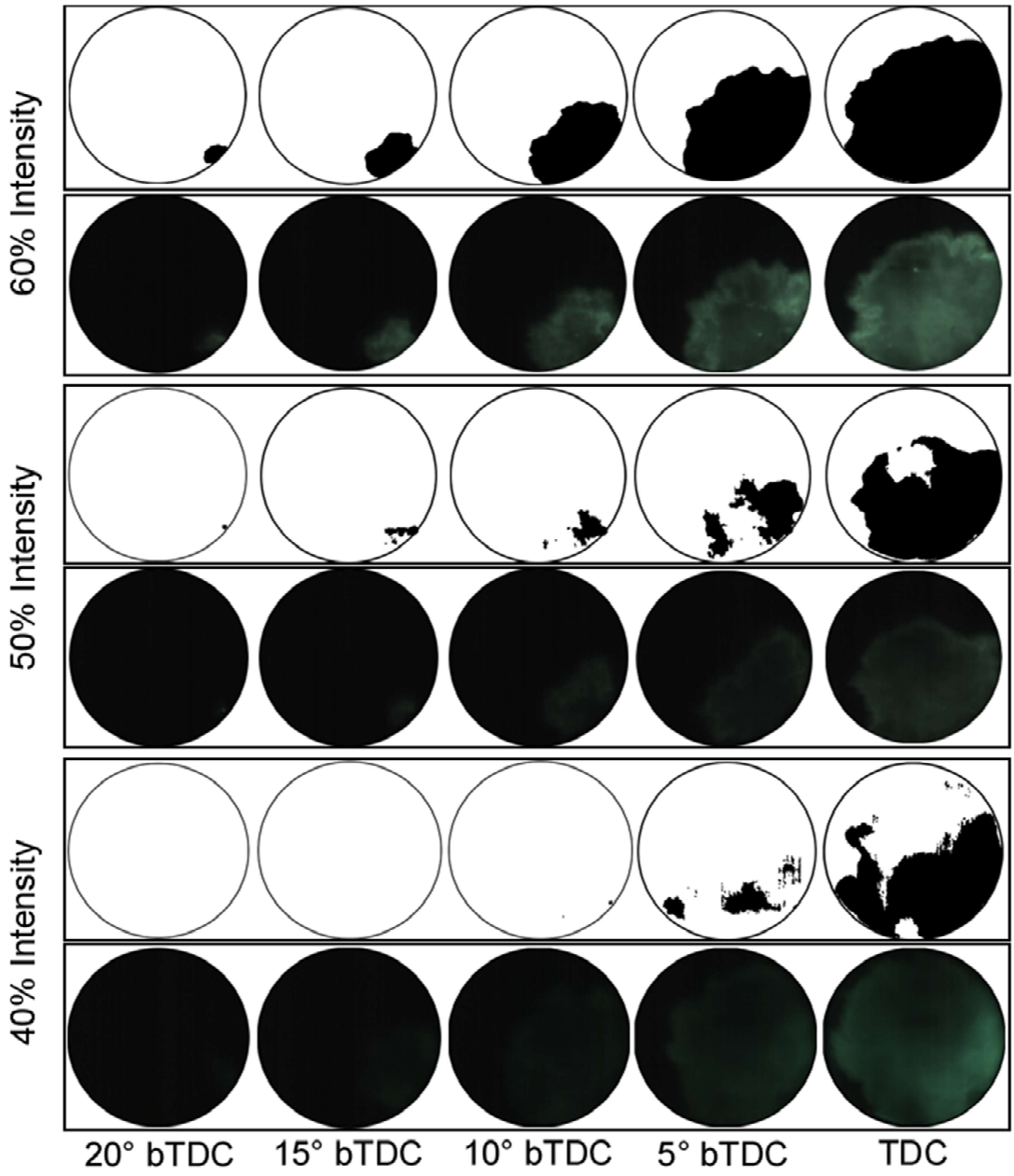

Figure 4.17 – Side by side comparison of images for the three intensity settings running stoichiometric fuelling at 5° intervals, beginning 9° after the spark event. The cycles chosen were so because they are closest in PMax and APMax to the mean cycle.

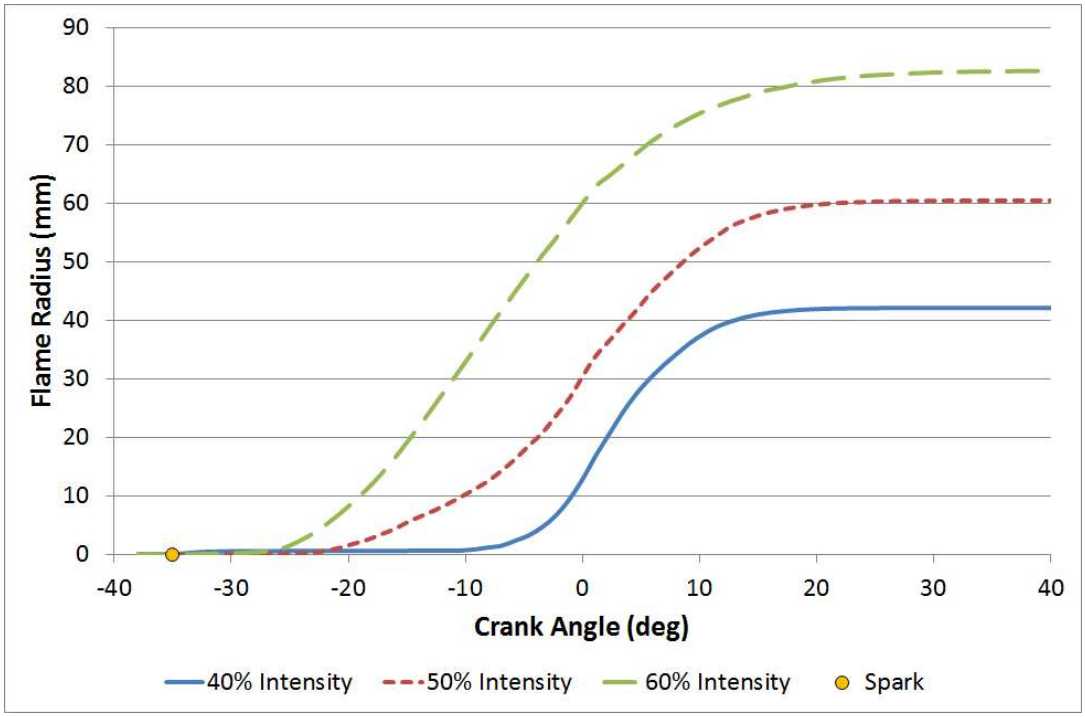

Figure 4.18 - Flame radii for the three light intensity settings for the image intensifier. The spark is identified at 35° bTDC for lean (λ=1.22), MBT combustion at 1500 RPM.

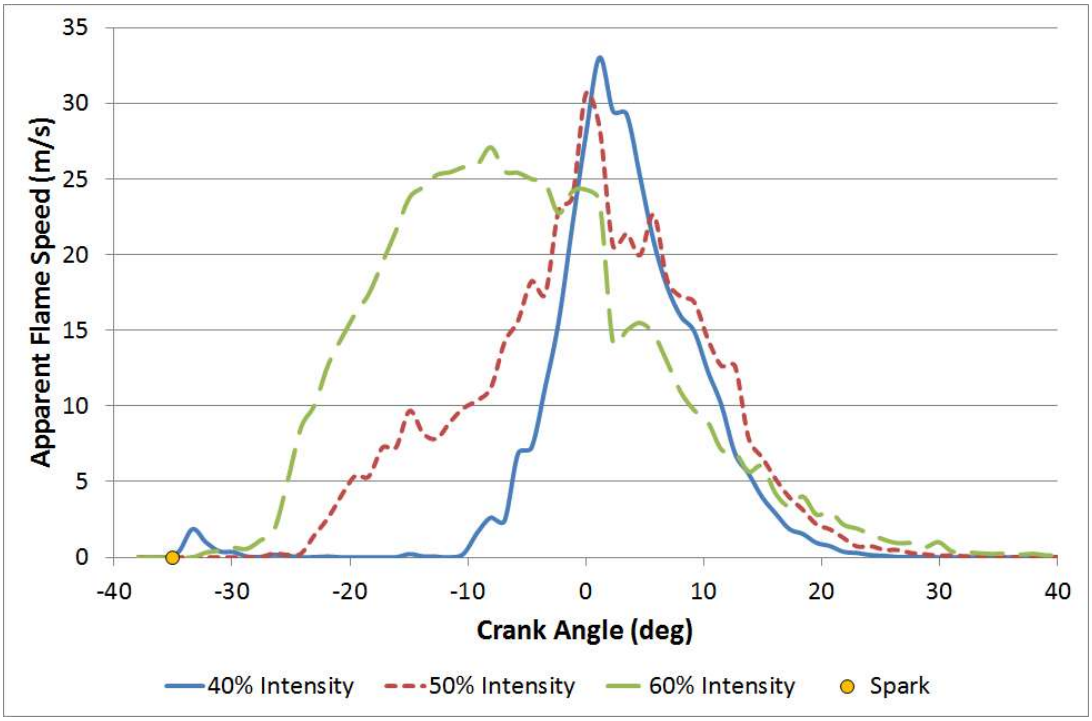

Figure 4.19 - Flame speeds for the three light intensity settings for the image intensifier.

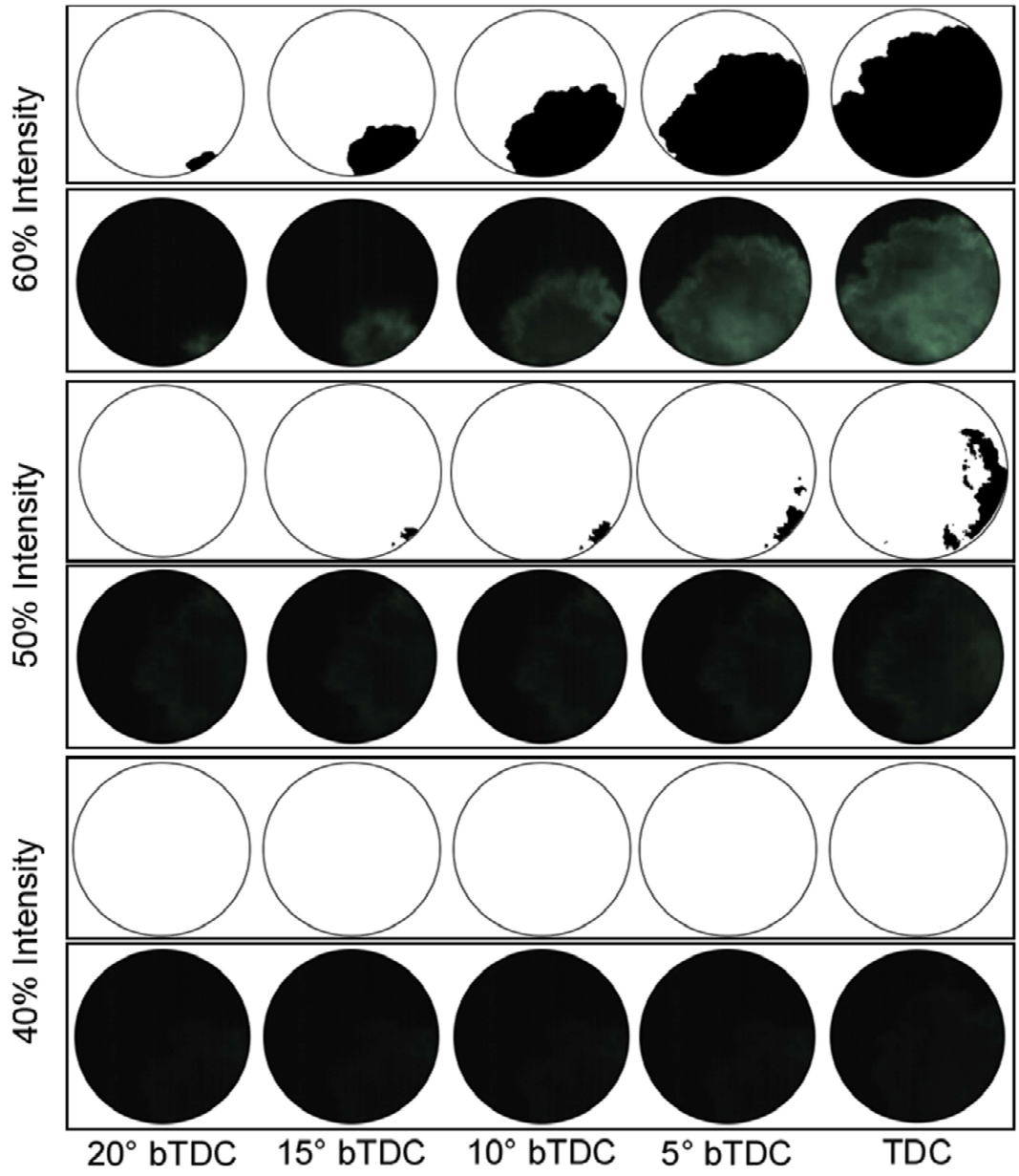

Figure 4.20 - Side by side comparison of images for the three intensity settings running lean limit fuelling (λ=1.22) at 5° intervals, beginning 9° after the spark event. The cycles chosen were so because they are closest in PMax and APMax to the mean cycle.

Chapter 5

Optical & Thermodynamic Data Processing

5.1 Introduction

For accurate analysis of the thermodynamic and optical data being obtained in the lab, a number of processes were devised to allow for accurate comparison between different fuels and setups. Set out below is a collection of these methods describing the way in which optical data was processed for flame radius, speed, shape and wrinkling analysis. Also described is the experimental characterisation of the engine's thermodynamic performance and validation of a one-dimensional thermodynamic model of the unit. A comparison of two methods of analysing the amount of charge combusted at any given crank angle is also provided.

5.2 Engine Characterisation

Before work can begin capturing results for analysis, the engine must go through two rigorous processes: shakedown and validation. In the shakedown process the engine was run for long periods of time to allow the author to test the engine under normal operating conditions for the first time and then operate a sweep of temperatures, spark timings and injection durations (exploring the limits of the engine). Once the shakedown process was completed satisfactorily then the validation work was undertaken. It is during such work that a user can ascertain if the results have been skewed by what is known as the 'Observer Effect' wherein by observing an event changes the way in which an event occurs. In this early work, one main concern was to find out if inserting a silica window into the cylinder head affected the indicated heat release results when compared to a full metal setup. For all tests carried out, both in validation and in the results section, the decision was made to capture 300 thermodynamic cycles to allow for cycle-to-cycle variation to be accounted for in a manner in-line with standard industry practice for SI engines.

5.2.1 Glass versus Metal

In the following set of experiments the engine was first motored, then fired with both the optical window and a metal blank in the window bay. This allowed for comparison between the two material types to investigate what trade-offs (if any) existed when running an optical window.

5.2.1.1 Motored

Figure 5.1 shows the mean motored pressure running WOT at 1500 RPM. PMax reached for the metal blank was 13.27 bar and for glass, 13.34 bar. This small difference was likely to be due to the heat retention properties of the silica leading to reduced gas heat losses, with higher gas temperatures and pressures. As already stated, the material of the window was Corning silica which possesses a Heat Transfer Coefficient (HTC) of 1.3 $Wm^{-2}K^{-1}$, whereas the aluminium window blank has an HTC approximately 100 times greater (125 $Wm^{-2}K^{-1}$) meaning the glass will act as an insulator. In Figure 5.1 there exists a secondary peak located at the point at which the exhaust valve was opening. As previously described in Chapter 3, due to complications in the manufacturing process of the head, the first exhaust valve (from the top, when looking at Figure 3.2a) had been sealed and did not aid the scavenging process. As such, when the exhaust process was taking place, the bulk of residual gasses were ejected out of the single valve, with increased internal EGR likely to occur due to throttling effects.

Set out in Figure 5.2 it can be seen that the temperature in both the cylinder head and in the bridge of the exhaust were higher for the silica window due to the heat retention, as expected. These higher temperatures are likely to affect the burn rate and could cause the engine to overheat more readily.

5.2.1.2 Combustion

The next process to be completed in the validation process was the running of the two cylinder head window materials with stoichiometric combustion. All tests were conducted using iso-octane with identical fuelling durations. The results of the tests are shown in Figure 5.3 where the mean pressure traces are compared. There are three traces – one for glass mapped to MBT (29°bTDC), another for metal

also running the same fixed spark timing to investigate how glass truly impacts upon combustion and a final trace for metal mapped to its own MBT spark timing (31°bTDC). Once again the glass pressure trace is higher than that of both the metal traces – further evidence of the increased heat retention with the silica. Figure 5.4 sets out the temperatures of the head and the exhaust bridge where it is plain that the glass, again, causes higher chamber temperatures than those with a metal window. The hotter chamber results in a hotter charge which in turn results in a faster flame and lowered duration as seen in Figure 5.5.

The hotter initial charge also goes some way to aiding the spark timing as, to achieve MBT while running glass; the spark must be advanced by three degrees compared to that of running metal. This means that use of the metal blank with glass spark timing will cause slower and less ideal combustion. Both the early combustion period and the time required to reach 90% MFB are retarded compared with either the glass or MBT metal results.

In Figure 5.6 both the net IMEP and the COV of IMEP can be seen. The IMEP values are all within a tenth of each other showing that, while combustion is quicker in the optical configuration, there is no adverse effect on the output of the engine. Looking at the stability of combustion the glass provides a more stable event even when the spark timing has been adjusted for MBT. Potentially the higher temperatures and marginally quicker burning with the glass running results in less time being available for the flow to distort the flame.

5.2.2 Central versus Side Spark

In a conventional SI engine the spark plug would be situated in the centre (or as near as possible to the centre) of the bore, embedded in the cylinder head. This is done so as to give the spark kernel 360° in which to more freely propagate without wall contact and to reduce the combustion duration with a view to lessening the likelihood of quenching or excessive flame stretch. In this work, however, the desire was to have full-bore optical access via the cylinder head. Thus the plug is situated in the side wall of the cylinder, as demonstrated in Figure 3.2a.

In theory this will double the distance that the flame has to travel which may significantly influence the combustion duration (for a given flow field).

To analyse the effect of this, the two locations were compared: one plug situated in the side spark location (flush with the base of the metal window blank), the other embedded in the window blank, emerging 1.5mm into the chamber. Both locations used the same coil (Bosch P100T) and plug type (NGK ER9EH with an 8mm diameter). In addition, both locations used stoichiometric iso-octane and were mapped for MBT. The central spark plug was also operated at the MBT timing of the side plug in an attempt to further qualify differences in performance as indicated in Table 5.1 below.

Spark Location	Spark Timing (°bTDC)	MBT or Fixed Spark?
Central Spark	31	Fixed
Central Spark	25	MBT
Side Spark	31	MBT

Table 5.1 – The plug locations and their spark timings

In Figure 5.7 the mean pressure traces of the three engine setups are compared. As is the intention with mapping for MBT, both the central MBT and side MBT operations exhibited a CA50 time of 8-10° aTDC, resulting in an APMax of ~14-16° aTDC. Also seen in the traces is that the MBT mapped central spark plug produces slightly higher PMax values, most likely due to the geometrical differences creating a longer combustion event with more time for heat transfer to occur in the side ignition case. The trace for the central spark running the "fixed" spark timing shows an over-advanced burn, with an APMax of 8°aTDC. While the PMax value itself is much higher than that of the two other cases, much of that output will be wasted pushing against a rising piston (Figure 5.9).

In Figure 5.8 the head and exhaust temperatures are set out for the three cases. When looking at the temperature for the exhaust bridge, the value for the side-mounted plug is much higher than that of the two centrally-mounted plugs. While slight variations in the head temperature at the start of testing could account for some variation, it is more likely that the side ignition case results in higher heat

losses, with the flame kernel in contact with the walls from the onset and longer combustion duration observed. These higher heat losses are also visible when comparing the in-cylinder pressure traces of the MBT cases, with side ignition producing a marginally lower PMax. In the central ignition case a larger proportion of the flame kernel area will be free to advance without such side wall contact. In Figure 5.9 the load and stability of each of the three cases is set out, showing that there is little variation in stability between the two locations when each is timed for MBT, but that the COV rises dramatically when using the fixed spark timing in the central location. This variation also impacts the phasing of the combustion (Figure 5.10) with incorrect timing leading combustion away from MBT. The poorer stability is also indicated in Figure 5.10 comparing CA50 and the IMEP values, as the data points for the side-mounted plug are largely clustered together, while the centrally-mounted plug has several outliers with lower output and late combustion. The burn durations are shown in Figure 5.11. As expected the combustion durations for the two centrally-mounted plugs are quicker than for that of the side-mounted plug, even with the central fixed spark timing being so poorly optimised. This is largely due to basic geometry: the flame front propagating from the side-mounted plug has to travel twice as far as the central plug, with the flow potentially having more time to distort the kernel also.

This difference in burn speeds can be seen in Figure 5.12 where the mass fraction burned profiles are displayed. Here the two MBT-mapped curves are quite similar in burn duration until around a quarter of the charge is burnt at which point the flame front in the cylinder for the central spark case will be well established and already has a fair radius, speeding in all directions; however the flame front for the side spark will only still be relatively small and potentially experiencing higher heat transfer and larger scale distortion (for a given radius). Due to the bigger distance the flame has to travel and this increased heat transfer with potentially increased flame front distortion, longer combustion duration is experienced. Centrally mounted spark results demonstrate that this is the best configuration for the engine but an optimally mapped side spark can produce valid results within a few percent of the central results with similar combustion stability.

5.2.3 Ethanol versus Iso-Octane with Variable Spark

Following on from the work above, efforts were made to investigate what effect the fuel type had on combustion when operating with differing spark locations. As with the earlier work, NGK spark plugs were situated in the centre of the metal window blank and the side wall, adjacent to the exhaust valves. Both spark plugs were in the chamber at the same time, with the ignition coil switched between the two. The spark was set to 31° bTDC and 25° bTDC for the side and central spark respectively for either fuel and the throttle was set to WOT with the fuel rate set to achieve λ=1.

As with the earlier work, the PMax value for the central spark location is higher than using side but in addition ethanol presents a higher PMax value than iso-octane for both spark locations (Figure 5.13). The gap is more pronounced (~1 bar) for the central spark location due in part to the higher laminar burning velocity of ethanol [Gülder , 1982] while the PMax delta between the fuels at side ignition is just over 0.1 of a bar greater in ethanol's favour. In Figure 5.14, the differences in wall temperature between the fuels and locations are set out. Again, the side spark location leads to a longer combustion which is related to the doubling of the distance a propagating flame must cover (with the aforementioned impact upon wall contact/heat transfer rates). It can also be seen that ethanol combustion resulted in marginally lower wall temperatures, which may have been related to differences in gas temperatures (due to charge cooling) and a marginally faster burn resulting in reduced wall heat transfer losses during the power stroke. Such differences will be returned to later on in Chapter 6.

Set out in Figure 5.15 are corresponding values of net IMEP and COV of IMEP. With regards to the IMEP, both the fuels running side ignition had similar COV of IMEP values while ethanol running central spark demonstrated a worse COV compared to iso-octane. It is possible that due to the cooler surface temperatures inherent with the short duration combustion, the ethanol-air mixture struggled to fully evaporate and thus suffered in comparison with iso-octane. Finally, looking at the combustion duration and 10%, 50% and 90% duration locations, again it is clear that central spark is a quicker method of combustion than side spark (Figure 5.16).

5.2.4 Valve Overlap and Timing

An overlap duration of 25° was chosen, based on a typical SI setting [Cairns, 2006]. Further investigation into the impact of a sweep in overlap amounts will be studied in Chapter 6.4.

5.2.5 Pressure and Volume Curves

Presented in Figures 5.17 and 5.18 are log P/log V diagrams for both the fired and motored pressure traces from the engine. Each of the four strokes is labelled in Figure 5.18. The fired traces are taken from the mean pressure trace over the 300 cycles against the volume matched to every quarter crank angle degree. The motored traces are an average of 100 cycles matched to volume at the same crank angle resolution. In Figure 5.18 the two traces show the motoring pressure cycle with iso-octane injection (but no spark) and without any fuel injection. On Figure 5.17 the inlet valve closing and the exhaust valve opening have been identified. Looking at the IVC event, there is some noise on the trace indicating that as the valves close they produce vibration through the head and this is picked up by the in-cylinder pressure transducer. Here is a point where noise could affect the results, but as the event is taking place at 145° bTDC then it is unlikely to have any serious consequences on the heat release analysis. Using data presented in these graphs, the effective compression ratio and polytropic indices were calculated for compression and expansion, which are provided in Table 5.2. As expected the effective compression ratio is slightly lower than the geometric compression ratio (7.6 to 8.4 respectively). The polytropic index for compression is in-line with those expected of a standard spark-ignition engine at λ=1 and indicate adequate sealing [Heywood, 1988].

Parameter	Value
Effective Compression Ratio	7.6:1
Polytropic Index during Compression Stroke (Fuel & Air)	1.31
Polytropic Index during Compression Stroke (Air Only)	1.375
Polytropic Index during Expansion Stroke (Fuel & Air)	1.39
Polytropic Index during Expansion Stroke (Air Only)	1.48

Table 5.2 – Calculated values for compression ratio and polytropic index

5.3 Cyclic Variation, Sample Size and Cycle Selection

Cyclic variation can be defined as fluctuations in engine performance from one cycle to the next in spite of constant engine control settings. Young [1981] noted that if the cyclic variation was eliminated, then the power output of an engine could be improved by ~10% and there would be a sizeable drop in emissions. This work was bolstered by Lyon [1986] who identified a potential ~6% improvement in the fuel consumption rates if cyclic variations were eliminated. This is not to say that variation between the cycles is always a detrimental quality. As each cycle varies it allows a user to monitor for misfires or knock and adjust accordingly. If variation was eliminated then either all the cycles would auto-ignite (potentially leading to run-away knock which is likely to destroy the engine) or none of the cycles would knock.

The cause of these variations can be traced back to the very start of combustion and are numerous. At the moment of induction the dissipation rate of turbulence, flow separation in the intake ports, excessive bulk air motion or inlet pressure waves can impact on the turbulence intensity, which in turn can influence flame front wrinkling, increasing variation. Ma et al. [1996] found that by increasing the inducted flow's turbulence intensity then the variation between cycles would rise as well. As the ignition occurs, the formation of the mixture in the spark-gap will set the scene for the rest of the combustion process. If there are variations in the state of the fuel (liquid or vapour), incomplete mixing of the charge or any excessive exhaust gas residuals present then this will affect the way the flame initially propagates from the spark plug [Suyabodha, Pennycott and Brace, 2013]. The duration and energy of the spark event can alter the flame development rate. Indeed, variation has been found to increase as a result of any factor that elongates the combustion duration. Running a lean combustion will result in a very long, slow flame meaning that the turbulent eddies have increased time to distort and stretch the flame surface. This will increase the likelihood of partial or complete misfires and will certainly increase the variation between cycles.

While one can rely on the rate of heat release (or mass fraction burned) and the in-cylinder pressure trace to identify cyclical variation, one other immediate

indicator of variation is the IMEP, a useful relative performance measure for engine designers as it allows them to compare the output of engines of different sizes. It is also the output of the engine that is experienced by the driver when he/she puts their foot on the throttle. When the COV of IMEP is too severe then the driver will begin to notice and must respond accordingly. The COV of IMEP should never exceed 5-10% and for many experimental labs, including this one, the aim is to keep it below 5%. To combat this variation, experiments can be repeated and averaged to find the numerical mean and then to identify those cycles closest to that mean. Care must be taken to obtain enough data to give accurate results that are indicative of the trend in data. In Figure 5.19 the decreasing trend indicates that as the amount of captured cycles grows, the percentage error between that cycle and those that have been previously begins to even out and outliers are less likely to skew results dramatically. It is for this reason that when obtaining thermodynamic data 300 cycles will be the desired number of cycles to gather.

Once the experimental requirements have been established a comparison of data can be made. Figure 5.20 shows 300 combustion cycles taken for the same fuelling and spark settings used in Figure 5.19. These have been collated together in to one pressure graph (Figure 5.21 shows a cropped version of the same plot). On to these 300 traces the ‘arithmetic mean cycle’ has been superimposed. Also added in Figure 5.21 are the arithmetic ‘slow’ and ‘fast’ cycles – these are cycles that are two standard deviations above and below the numerical mean which have been determined in this work to give appropriate boundaries for identifying the fastest and the slowest cycles. Over the 300 cycles the spread between the fast and the slow cycles is quite broad, demonstrating the effect of even mild cyclic variation. As the pressure in the cylinder increases during compression, the 300 cycles are roughly uniform and follow a similar line in the rate of pressure rise. This indicates good sealing and compression over the entire data set, meaning that no cycles need be excluded due to any extraordinary leakage or misfiring. As mentioned previously, the point at which the flame’s initial burning speed and shape are set is just after the spark event. This being iso-octane at MBT timing and stoichiometric fuelling, the spark event occurs at 29 degrees before TDC – this is clearer in Figure

5.23. At this event, the cycles begin to diverge due to spatial and/or temporal variations in ignition, flow, charge state, charge homogeneity, residual content and/or mixture strength.

With regards to cycle selection, to use all 300 thermodynamic cycles (or all 50 imaged cycles) would lead to result smoothing and individual variations in pressure build-up or combustion durations being misrepresented. In Figure 5.22 the arithmetic mean cycle has been extracted and the three cycles with the closest PMax value to that of the mean cycle have been identified. While these cycles possess values that are the closest to the PMax of the mean cycle, this figure clearly demonstrates that no cycle will ever match the arithmetic mean. The entirely random and chaotic motion/mixing in the cylinder ensure that perfect continuity is impossible. All that can be hoped for from an experiment is a low percentage of fluctuation. This method of using the peak in-cylinder pressure value about which to base cycle selection is well used in literature [Cairns, 2001; Abdi Aghdam, 2003; Hattrell, 2007]

This variation in burning speeds and cylinder pressures is more noticeable when an optical study is made. In Figure 5.24 the three cycles identified as closest to the arithmetic mean are compared at set crank angle intervals. From this it is clear that, although the three cycles are running under identical fuelling, temperature and spark timing conditions, the speed at which the flame propagates across the cylinder differs greatly from cycle to cycle. It is also possible to see differences in the way in which the flame propagates from the spark plug. In Cycle 49 the flame propagates both up and down the cylinder wall from the plug, with the flame edges curling back on themselves to create a flame with a ‘divot’ in the centre, in line with where the spark plug is situated, as if it is a valley pointing back to its source. This is unlike that of Cycles 157 and 165 who both have a flame that resembles a kernel expanding in a roughly uniform shape from the plug. These flow variations are at least partially associated with varying charge motion in the cylinder during combustion. Ultimately it is possible to produce similar pressure development from quite different flame propagation events.

5.4 Image Capture Method

For the most part this work focussed upon the effect of various fuel compounds on burn speeds and the relationship between these fuels and residual gas fraction. As already discussed briefly in Chapter 4, this included thermodynamic and optical observations. When the thermodynamic work was completed there was an opportunity to revisit sites of interest and to optically capture them to ascertain in greater detail the effect of the fuel on the turbulent flame propagation events.

The availability of optical engine data provides the opportunity to better understand the causes and effects of varying flame propagation events on the pressure development and hence ultimately engine output. To do this, the engine cell was set up as in Figure 4.13. A mirror was positioned over the optical cylinder head and angled so that the high-speed camera (set up at 90° to the engine) was able to record the resulting combustion. The image's light intensity would be enhanced prior to recording on the ICCD. Once this had been done the images were processed as described below and then the desired information could be determined and results extrapolated from this.

5.4.1 Flame Image Processing

As discussed previously all flame images for this project were captured using a MEMRECAM fx 6000 and a DRS Hadland Image Intensifier. The images were stored on the internal memory of the camera as a concurrent video file. These were then downloaded as TIFF files where each image represented 125 μs (or 1.15 crank angles degrees). As each data point requires 50 individual cycles to be imaged (to reduce cyclic variation impacts) this means that each point could result in up to 15,000 images, which would make individual analysis between setup and fuel effects near impossible. Thus a process was created to batch process the images to allow for effective and quick analysis, while ensuring accuracy and continuity.

To do this a MATLAB code was written that would be able to compute the mean flame radius as it propagates, thus giving a mean flame speed. In addition the code could also calculate the perimeter length of the flame front, the 'shape factor' of the flame as well as the level of 'wrinkle' experienced. With these pieces of

information it was then possible to determine the effects of both bulk and local distortion on the flame propagation event. However some caution was required with respect to quantifying flame wrinkling given the limitations of the natural light imaging technique adopted.

Once the code had run, the image was then inverted to provide black flames on a white surround to be used in all literature. This is purely an aesthetic requirement as it allows one to easily 'read' the image on the page (demonstrated in Figure 5.25).

5.4.2 Flame Image Read

The first segment of the code used the *imread* function of the MATLAB command library to import the digital images. This was performed by the user instructing the code to open the first image in the folder which contained the images for analysis. As the code ran through the processes and completed, it returns to the head of the code to select the next image until all have been processed. Once imported, the images were stored in the MATLAB workspace and were stored in matrices that are the same size as the image (pixel by pixel).

5.4.3 Noise Suppression & Masking

As evident in Figure 5.25 the initial image captured from the engine shows not only the flame kernel but also several elements of light pollution including reflecting light from the inside edges of the window and the TDC light probe which may affect the accuracy of the results. Firstly the image under analysis had a 'background image' subtracted from it. This was an image made of several points in a cycle overlaid on top of each other and common noises can be isolated leaving only the foreground (the bore).

The second stage was to apply a mask to crop out the cylinder wall noise (the 'halo' in Figure 5.25) and leave only the flame itself for analysis. This was accomplished by applying a binary matrix to isolate the bore and thus divide the image into ones and zeros, each representing the area inside the mask and outside the mask respectively. This had to be manually placed at the beginning of each processing run to account for camera movement or size of the bore in the image

(Figure 5.26). To aid in this mask creation, the code was able to select the image with the highest luminosity from the set to allow the user the best chance of placing the mask correctly. It was also here that the ratio of the image to the real-world dimensions is created. This aided the correct calculation of the various analysis figures later (radius, area, etc.). Here the ratio was set as 1:2.922.

5.4.4 Image Binarisation

This stage is represented in the middle image of Figure 5.25. The code changed the image from RGB to black and white, where each pixel is represented by either a one or a zero, depending on it being white (of flame) or black (of unburnt gas). This binarisation has two stages:

- Greyscaling – The RGB image was turned to greyscale, transforming each region of the coloured image into shades of grey. This was vital as many binarisation codes require a thresholding value that decides which pixel is part of the flame or not and this value can accept only greyscale inputs. In MATLAB, grayscaling of the image is done by eliminating the hue and saturation information while retaining the luminance.
- Application of the binarisation algorithm: The algorithm used initially was a threshold finding technique which depends on certain criteria. The one employed here was the Otsu method as it offered very accurate distinction between the flame and the bore with the least processing time.

The aim of this section of the code was to maximise the differentiation of the two regions (burnt and unburnt) making it easier to separate the two, so the pixels of the image were divided into two classes depending on the intensity value and the spread between them could be minimised with a calculated threshold value, which was easily done by the code.

One issue however with the threshold value method was that it judges the pixel to be flame or not purely via the intensity of the pixel and was not able to ‘see’ the relationship between the pixels. Sometimes regions of the flame that a human being would identify as part of the flame possibly curled back on itself or an anomaly on the image (sooty build up), MATLAB would identify incorrectly as part

of the flame or part of the background. These errors were more prevalent in lean burn combustion or dimmer combustion from alcohol combustion. Figure 5.27 sets out two images, the first is the original flame image that was imported by the code and the second shows the resulting black and white image. It is clear from this that the Otsu method was unable to fully identify that the region around a black zone on the image (damage to the photocathode by a previous user) was inside the flame front and should be included in the black and white image.

To avoid this issue with the dimmer areas of the flame, a different thresholding method was applied *in addition* to the Otsu method. This secondary method was the triangle method [Zack et al., 1977]. This uses a graphical representation of the frequency of the pixel intensities of the image from white to black (Figure 5.28). If the top of the trace is connected by a line to the furthest end of the scale (the 'black' end), this creates a rudimentary triangle. The 'triangle value' is the distance between this line and the trace.

The triangle method would, however, tend to over-inflate the flame, displaying the flame as having reached full bore burn when in reality the flame was a few millimetres from completion. This was the reason as to why both methods were employed together: they provided accurate results with an averaged flame that was neither over-inflated nor lacking in detail.

5.4.5 Calculations

Once the binarisation had taken place, the next stage of the code was to extract various items of data that would aid in accurate analysis of the flame including the flame area, speed, radius, perimeter and flame centroid.

The centroid was identified by locating the point at which a centre of mass would be situated were the flame a solid object. So for a finite set of pixels (P_x) throughout the image, the centroid is:

$$C = \frac{\sum P_x}{k} \tag{5.1}$$

where k is the number of pixels selected in the image and $P_x = (x_i, y_i)$ represents the Euclidean co-ordinates of the pixels. Once this centroid had been identified all other calculations could be taken from here.

5.4.6 Flame Radius

This is one of the most important computed values of the flame analysis as from this many other values can be derived. Therefore obtaining the flame radius with the highest level of accuracy is key.

The code used the best-fit circle method, an idea originally proposed by Keck [1982], and used numerous times in literature [Berretta, Rashidi and Keck, 1983; Bradley, Lau and Lawes, 1992; Gillespie et al., 2000 and Bradley et al., 2003] to obtain the radius. This method seeks to find the flame's centre and radius by affixing a circle to the image. This is done so that the amount of unburnt charge encompassed by the circle is equal to the amount of burnt charge.

This best-fit circle can be calculated by solving a non-linear, least-squares problem, in order to minimise the sum of the squares of the distances:

$$d_i^2 = (\|z - x_i\| - r)^2 \tag{5.2}$$

where d_i is the distance between a point (x_i) and the centre of the best-fit circle (z) which possesses a radius of r. If $u = (z_1, z_2, r)^T$, this means that $\tilde{u}$ needs to be determined so that:

$$\sum_{i=1}^{m} d_i(u)^2 = min \tag{5.3}$$

Here the Jacobian, defined by the partial derivatives $\frac{\partial d_i(u)}{\partial u_j}$ is given by:

$$J(u) = \begin{pmatrix} \frac{u_1 - x_{11}}{\sqrt{(u_1 - x_{11})^2 + (u_2 - x_{12})^2}} & \frac{u_2 - x_{12}}{\sqrt{(u_1 - x_{11})^2 + (u_2 - x_{12})^2}} & -1 \\ \vdots & \vdots & \vdots \\ \frac{u_1 - x_{m1}}{\sqrt{(u_1 - x_{m1})^2 + (u_2 - x_{m2})^2}} & \frac{u_2 - x_{2m}}{\sqrt{(u_1 - x_{m1})^2 + (u_2 - x_{m2})^2}} & -1 \end{pmatrix} \quad (5.4)$$

From this, using the Gauss-Newton method, the best-fit circle could be iteratively computed around a set of given points [Gander, Golub and Strebel, 1994]. If those points are the flame front data, then the calculated circle would equal one with a radius identical to that of the flame radius. Figure 5.29 shows both the best-fit circle (red) and the flame perimeter (white) for an individual image in a cycle.

5.4.7 Flame Speed and Shape Factor

This value is also vital to the analysis of the flame development and the effects that charge motion or residual gas levels can have on a combustion event. As stated earlier, the flame speed is the expansion rate of the flame's radius over a set time frame – in reality it can be viewed as the radius growth rate. The time interval to analyse the two radii over was selected to be the interval between two flame images. As the camera was set to 8000 fps, this results in an interval of 125 µs. The difference between the two best-fit circle's radii could then be used to determine the speed.

The flame front analysis can be further enhanced by quantifying the developing flame front's distortion. This is referred to as the shape factor [Buran, 1998; Gillespie, 1998; Cairns, 2001] and is defined as the ratio of the perimeter of the flame contour (P_c) to the perimeter of a circle whose radius is equal to that of the flame at a given crank angle (usually the radius of the best-fit circle, P_r):

$$SF = \frac{P_c}{P_r} \quad (5.5)$$

The perimeter of the flame contour was calculated via the commercially available photo-editing software Photoshop. Batch processing of the black and white images would entail importing the TIFF file, selecting the flame area and using the *Measure* tool within Photoshop to produce a count of the perimeter pixels of the flame shape. Once this perimeter length had been converted to millimetres it became P_c and could be used in conjunction with the earlier calculated P_r to produce the shape factor (as dictated in Equation 5.5).

5.5 Heat Release Analysis

5.5.1 Rate of Heat Release/Rassweiler and Withrow

As discussed in Chapter 2.3.4, the maximum power and torque available from an engine can only be accessed if the spark timing is situated so that the flame will have burnt 50% of its charge by the time combustion reaches between 8° and 10° aTDC. This is related to the way in which the propagating flame releases energy as it sweeps across the cylinder. The two methods of heat release proposed below are to be assessed against each other and a decision made as to which method produces the most accurate and acceptable results for this work.

The first method, described by Heywood [1988], assumes that combustion occurs over a finite time frame. Figure 5.30 shows a basic, theoretical pressure trace and heat release curve from an Otto cycle with the burn duration identified. The finite burn duration ($\Delta\theta$) spans from the start of combustion (θ_b) to the end (θ_e). The formula governing the energy in a system over small crank angle duration is expressed by:

$$dU = \partial Q - \partial W \tag{5.6}$$

where dU is the energy change (defined as $dU = mc_v\Delta T$), ∂Q is the partial heat release over that time frame and ∂W is the partial work (defined as $\partial W = PdV$). If these formulas are inserted then Equation 5.6 now reads as:

$$mc_v\Delta T = \partial Q - PdV \tag{5.7}$$

Since $PV = mRT$, Equation 5.7 can be rearranged to read:

$$m\Delta T = \frac{1}{R}(PdV + VdP) \tag{5.8}$$

and

$$\Delta U = \frac{c_v}{R}(PdV + VdP) \tag{5.9}$$

Equation 5.7 now can become:

$$\partial Q - PdV = \frac{c_v}{R}(PdV - VdP) \tag{5.10}$$

which can be reduced further to read:

$$\frac{\partial Q}{d\theta} - \left(1 - \frac{c_v}{R}\right)P\frac{dV}{d\theta} = \frac{c_v}{R}V\frac{dP}{d\theta} \tag{5.11}$$

Finally, as $R = c_p - c_v$ and $\gamma = c_p/c_v$ we can define these terms together as:

$$\frac{c_v}{R} = \frac{1}{\gamma - 1} \tag{5.12}$$

and when Equation 5.12 is combined with Equation 5.11 this leads to an equation for calculating the rate of heat release from an engine (Equation 5.13).

$$\frac{\partial Q}{d\theta} = \frac{1}{\gamma - 1}V\frac{dP}{d\theta} + \frac{\gamma}{\gamma - 1}P\frac{dV}{d\theta} \tag{5.13}$$

The analysis using this method is based on comparing the rate of change of pressure in the chamber during a fired cycle to that from a motored cycle with fuel injection. With the change in volume a known amount the net heat release for both

fired and motored cycles is calculated and the motored heat release data is subtracted from the fired to provide only the heat released due to combustion. In essence this is the ratio of the cumulative heat release to the total heat release in the event. While it may not take into account the differences in temperature between the burnt and unburnt, Yeliana et al. [2008] showed that this Rassweiler and Withrow method produced comparable mass fraction burnt curves as both the single-zone and two-zone models while being easier to solve.

5.5.1.1 Signal Filtering

In order to accurately use the data from the heat release formula there needs to be an amount of signal filtering to reduce the noise. Two methods were employed and tested with the aim of reducing some of the noise associated with data capture (electrical interference, vibration and shock, etc.) without compromising the information. The first method is to increase the crank angle interval over which the pressure and volume are measured. Figures 5.31 and 5.32 show that as the interval between crank angles is increased, the noise is reduced while the shape of the curve remains intact. As is clear from this diagram, there is a large amount of noise (vibration) occurring when the inlet valve closes. While this is not a key area of combustion analysis, any noise should be reduced where possible. Thus 5° interval filtering alone will not be sufficient.

The next method trialled requires use of a box filter. This is done by, instead of using each data point as it is, every point becomes an average of those around it; the larger the averaging 'box', the higher the level of filtering. Figures 5.33 and 5.34 show that as the box filter is increased the noise is reduced further with little deformation of the trace. In order to improve the filtering without altering the shape too much it was decided to use both the box and interval filters together – as shown in Figure 5.35. In Figure 5.35 the region shown is that of the desired APMax of MBT, an area of vital importance to the combustion analysis. The 2-stage filter provides excellent filtering over the raw data and a good shape compared to the two separate filters. While it appears in Figure 5.35 that the rate of heat release is subject to phase shift as the interval and box filters are applied separately, a study of the data shows that the maximum mass fraction burned value occurs at the

same crank angle for the raw data, both filters and also when both filters are combined. Where there is some difference is the reduction of that maximum value but this is to be expected when the variation in the trace is smoothed. As will be detailed further below, the ROHR function does have inherent complexities that the simplified Wiebe function avoids.

5.5.2 Wiebe Function

Another simpler method exists for calculating the heat release in an engine over the cycle. This is the Wiebe function. While the Rate of Heat Release requires detailed knowledge of the rate of pressure change, the Wiebe formula relies on the location of the just three key regions in the combustion cycle that are defined as the flame development process ($\Delta\theta_d$), the rapid burn angle ($\Delta\theta_b$) and the overall burn angle ($\Delta\theta_o$). These are all displayed in Figure 5.36 [Heywood, 1988]. Thus an accurate estimate can be calculated from the spark location and burn duration. Ultimately, if accurate in-cylinder pressure data is available then the Wiebe function can be used to accurately calculate heat release.

The flame development process has been discussed in Chapter 2.3.4. Here the same 10% MFB (CA10), 50% MFB (CA50) and 90% MFB (CA90) definitions will be used. In the CA10 region there is usually very little noticeable heat release from the charge. The heat release rate is affected by mixture state, composition around the plug and the charge motion.

The next stage is the rapid-burn angle where much of the useful energy in the fuel is expended as the flame front spreads to the cylinder walls. This too is affected by turbulence in the charge as this may speed up or slow down the burn rate. The bulk of the charge is consumed by the combustion here; traditionally up to 90% of the charge will have been burnt by the time this stage is complete – this 10-90% MFB period is referred to as the combustion duration.

The final stage is one in which the remaining charge is burnt off. This region can prove difficult to calculate correctly due to the complex nature of the interactions of the flame with the walls.

These flame development definitions seem fairly arbitrary but vital as they are required for the Wiebe function which is defined below:

$$x_b = 1 - exp\left[-a\left(\frac{\theta - \theta_s}{\Delta\theta_t}\right)^{m+1}\right] \quad (5.14)$$

where $\Delta\theta_t$ is the total duration of combustion, x_b is the mass fraction burnt, θ_s is the start of combustion and a & m are adjustable parameters used to smooth the curve to match reality.

5.5.3 Wiebe Function vs. Rate of Heat Release

Ultimately the ROHR calculations are usually calculated via stand-alone analysis codes that fail to appropriately account for irreversibilities such as in-cylinder heat transfer and mass blowby. The advantage offered by the Wiebe function is simplicity and high accuracy when linked with one-dimensional codes that can deal with such losses. This is provided accurate in-cylinder pressure data is still available; ultimately the Wiebe function is only as accurate as the data provided and cannot be described as predictive. In the current work it was therefore decided to adopt such a one-dimensional simulation approach as described in more detail below.

5.6 Thermodynamic Analysis

Thermodynamic combustion models can be deemed to be either “forward” or “reverse” analysis of an engine. In forward mode, models are used to predict engine behaviour and can be used by researchers to simulate what they may expect to happen to a system without the expense of running the physical experiment. In a reverse mode model, the simulation uses empirical data to validate, and expand upon, the original data – for example supplying heat release data, gas temperatures or residual gas levels. In addition, thermodynamic models can be referred to as either “one-dimensional”, possessing no flow modelling, operating on a single plane normal to the flow and using a simplified description of the physical and chemical processes occurring in the chamber – usually the Wiebe function; or “multi-dimensional” in which some flow characteristics are known having been obtained

via CFD or similar flow modelling which provides a greater understanding of the air/fuel mixing and subsequent combustion in three dimensions about the chamber.

The method of analysis to be used in this work is one-dimensional, reverse mode. One reason for this is because a fully validated model of the charge motion does not exist for this engine, another is due to the expense and physical difficulty involved with attempting to measure the burnt and unburnt gas temperatures needed for laminar burning velocity calculations it was decided that using the commercial simulation software, Ricardo WAVE to model the engine and extract the required data would allow for characterising engine operation without the need for high–end processing and time-intensive computations. At its core is an engineering code that is designed to analyse the dynamics of the pressure waves, mass flows and duct/flow interactions.

5.6.1 Basic Model

The WAVE modelling library allows for users to build a network of ducts, junctions and orifices leading to and from the combustion cylinder. Once the model is constructed the geometric data can be aligned to the various modelled parts and the operating parameters can be set in place. In Figure 5.37 a screenshot of the WAVE GUI shows the 'Elements' library of engine parts on the left of the window with which to construct the model. The engine used in this study is shown in the centre of the graphical display on the right of the image. Inside the Elements library the user can specify the fuel to be used, control the iteration process of the solver or add/create library parts for use in the model. Parts are added via a drag-drop system and linked by automatically created ducting. This ducting initially is created with zero dimensions requiring the user to go back and manually add them in.

5.6.2 Inlet and Exhaust

In Figure 5.38 is a closer view of the model to be solved in WAVE with the inlet and exhaust systems inside the areas marked 1 and 3 respectively. All real-world dimensions from the two systems must be logged and entered correctly into the program for an accurate model to be formulated. WAVE uses a basic four-

stroke intake and exhaust process to model the residual gas percentage in the cylinder. In the inlet system the first library item is the 'Ambient' condition (here referred to as 'Plenum') which is where the starting ambient pressure and temperature are recorded. Also in the intake system is the fuel injector ("Injector1") which requires geometric information on its positioning in the inlet track and the desired ratio of fuel to air. Because the plenum is situated after the throttle, no throttle has been added to the model.

The third area in Figure 5.38 indicates the exhaust duct. As discussed earlier in this chapter, one of the exhaust valves in the engine had been deactivated, inducing high residual gas levels in the chamber. To ensure that the model is as accurate as can be, there is only one exhaust runner coming from the engine. It is important to note that none of the ducts are to scale in the GUI. The final duct ("duct 2") is in fact over 5000mm long and represents the exhaust duct reaching up to the ceiling of the cell, expelling the gas out of the lab.

5.6.3 In-Cylinder Modelling

Accurate modelling of the inlet and exhaust systems is vital to the successful validation of the WAVE model but the information surrounding the cylinder and engine block are equally important for obvious reasons. Pictured in Area 2 of Figure 5.38 the orange cylinder is mounted to a standard engine crankcase. There are 3 valves (as in the actual engine) and these are noted as inlet or exhaust by the colour – blue for inlet and red for exhaust.

The basic data that need to be entered can be done so in the 'Engine General Panel' (Figure 5.39). Variables and parameters such like the bore, stroke, compression ratio, the con-rod length and the clearance height must be defined. The most efficient method of modelling the engine is to sweep from inlet to exhaust, as the inducted charge would, altering and calibrating data as you go. The interaction between the inlet manifold and the cylinder an important part of the model simulation. If the valves are situated too low in the cylinder, are too small or if the valve lift profile or discharge coefficients don't match that of the real engine then the two sets of results will never align. Shown in Figure 5.40 is the dialog box

for the valve lift profile. In this work, because the engine was custom built, a spread-sheet of valve lift position to crank angle already existed, thus this could be transferred into the cells on the left of the dialog box. Here also a user can specify the amount of lash or bounce in the valves and move the profile in the cycle. This stage was repeated for the exhaust profile.

To finish the geometric definition of the cylinder head, the flow versus the valve lift had to be specified. As no calibrated flow model exists for this engine, the existing data was used as a benchmark and the model's discharge coefficient altered until the simulated data began to align with the empirical data. It was vital to get the forward and reverse discharge coefficients correct in relation to the pressure data. Under ideal circumstances these coefficients would have been determined on a cylinder head flow rig but this was considered to be outside the scope of the current work.

The final element that requires attention in the panel is that of the combustion profile itself. In Figure 5.41 is the 'Combustion' menu of the 'Engine General Panel'. Here the user can select from several combustion profiles. In this work the SI Wiebe function will be used. The data required is the crank angle of the 50% MFB point, the combustion duration and the Wiebe exponent (a from Equation 5.14). Once these are fed into the system, then a Wiebe curve is produced for the combustion to follow. The standard SI Wiebe function was deemed sufficiently accurate for iso-octane and gasoline combustion but when moving to ethanol, WAVE struggled to match the early and late burn times. In this instance, the user chose a multi-component Wiebe function defined by any three crank angles and the mass fraction burned at those angles, thus allowing for greater control over the burn profile that, experimentally, may differ from WAVE's calculation for whatever reason.

The engine cylinder used in this work is the standard WAVE model engine cylinder. This allows for a good deal of customisation with some accurate assumptions also included. However it does not account for blowby, one of the biggest sources of lost compression or combustion pressure. The only way to

calculate this in Ricardo WAVE is to use an 'IRIS' cylinder which allows for a very large amount of geometric customisation. With this very complex model however there are some restrictions (presumably to aid the solver) – the IRIS cylinder would not allow a side-valve, flat-roof SI engine to be modelled. Thus the standard engine cylinder was used and a work around was devised to account for blow-by (discussed further below).

5.6.4 Model Validation

The main two sources of information for model validation are the MFB curve and the in-cylinder pressure trace. As the curve has been specified in the SI Wiebe dialog box, it is expected to conform to the data it was supplied. Upon checking, this was found to be the case. However, when the in-cylinder pressure trace (shown in blue in Figure 5.42) was superimposed onto the empirical data (pink trace) it was clear that the WAVE model was not correct. While the compression/combustion stroke shows an equal pressure rise between the two models, when the engine data reaches TDC, the pressure begins to peak and then fall during the expansion stroke. The simulated model however continues to rise in pressure, showing a PMax of 26.6 bar (while APMax remains close to the experimental data). This was a clear indicator that the absence of blowby was creating an unrealistic peak in-cylinder pressure.

It was assumed that the blowby of the engine was between 12% and 18% of the mass charge inducted, thus the intake plenum's pressure was altered iteratively to below that of the experimentally measured data to simulate a blowby model. At each modelling iteration the pressure trace was compared to the pressure trace, PMax and APMax values of the empirical data. As the amount of "blowby" increased the PMax and compression curve reduced and aligned with that of the experimental data at 15% blowby, beyond this the PMax value was lower and the compression curve was too shallow. In Figure 5.43 the in-cylinder pressure trace from a simulation with 15% "blowby" is shown with the original experimental data overlaid. Here, the compression/combustion stroke shows near parallel traces between the two models, but the lower pressure at IVC of the simulation is clear. At PMax however the two converge and as Table 5.3 shows the PMax values are near

identical. While this is a deviation from the 'real-world' scenario, it was decided that as the peak pressure amount and location are so close in value that this was sufficient for validating the model. Thus the "blowby" model could now be used to determine unburnt gas temperatures needed for calculating the laminar burning velocity and the residual gas levels which would aid analysis of the valve overlap cases. Several other users have noticed the need to lower the inlet pressure to tune a simulated model to match real-world results [Browning, 1991; Cairns, 2001].

	IMEP (bar)	PMax (bar)	APMax (°CA)
Mean Experimental Data	3.95	22.25	17.06
Simulation without blowby	5.37	26.6	16.6
Simulation with blowby	4.2	21.9	16.39

Table 5.3 – Power and Pressure for the mean experimental data and two WAVE models for validation

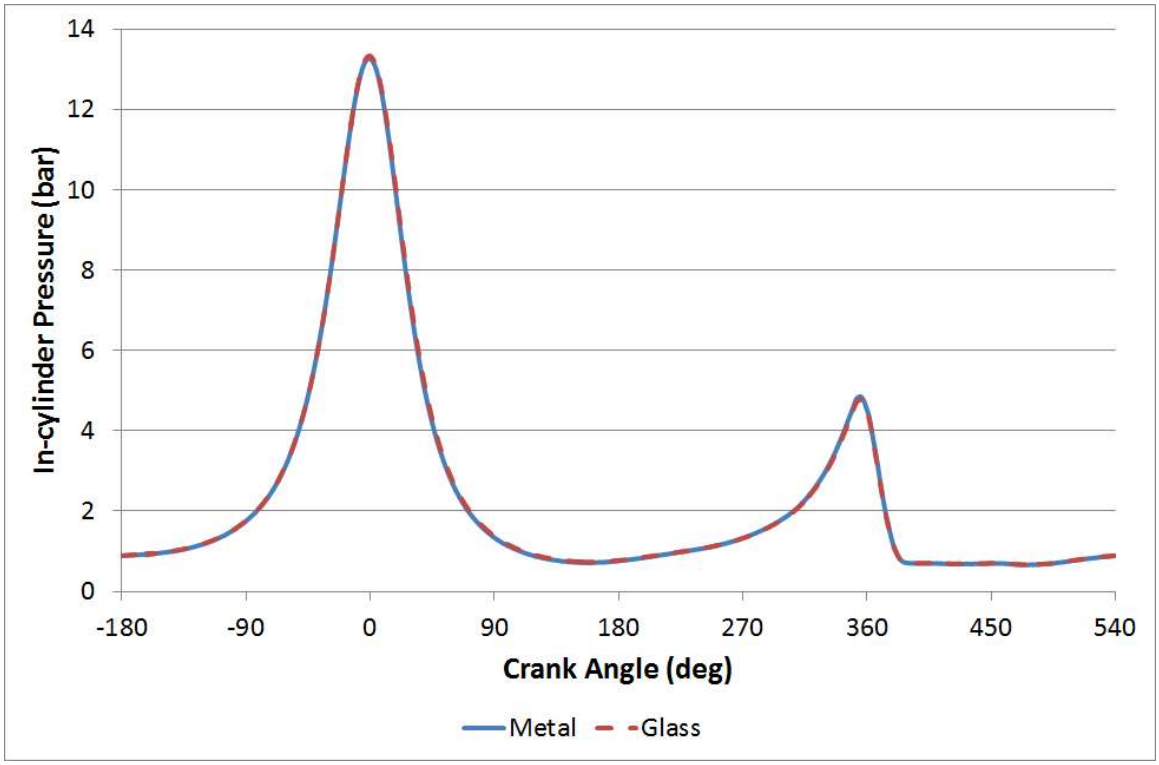

Figure 5.1 –The motored in-cylinder pressure for both glass and metal windows.

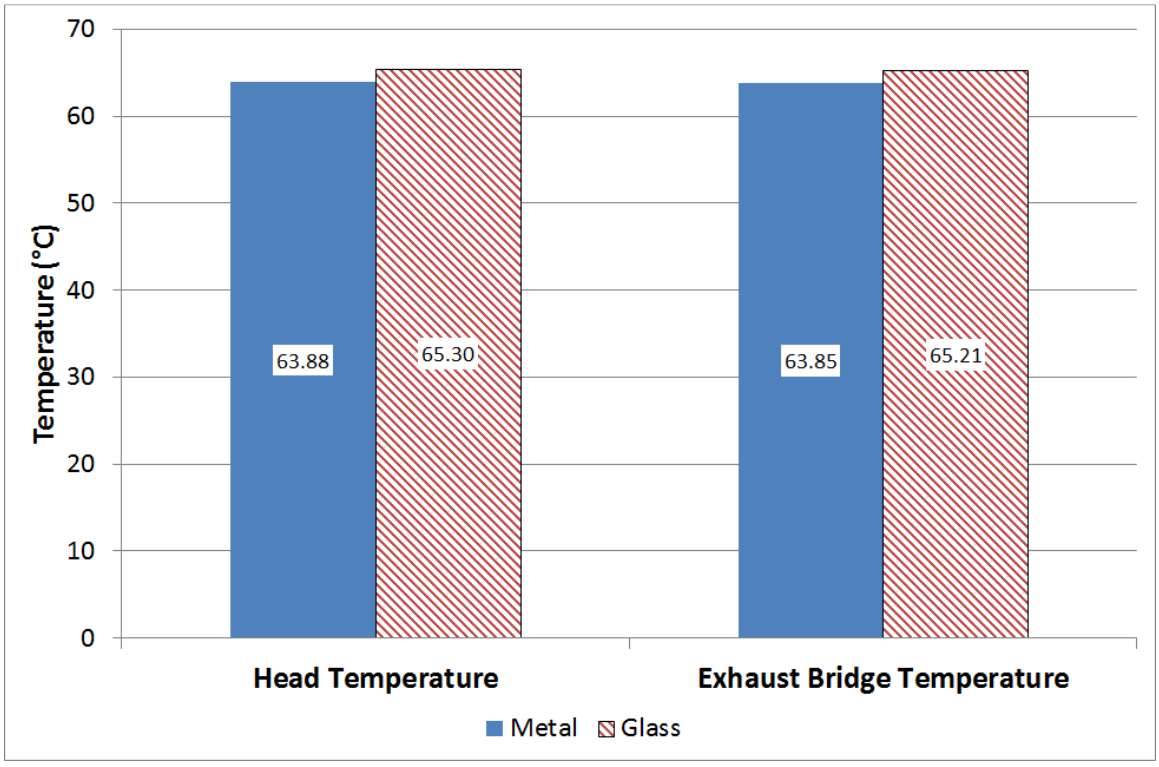

Figure 5.2 –The temperatures in the head and the exhaust bridge for both the glass and metal windows (motoring only).

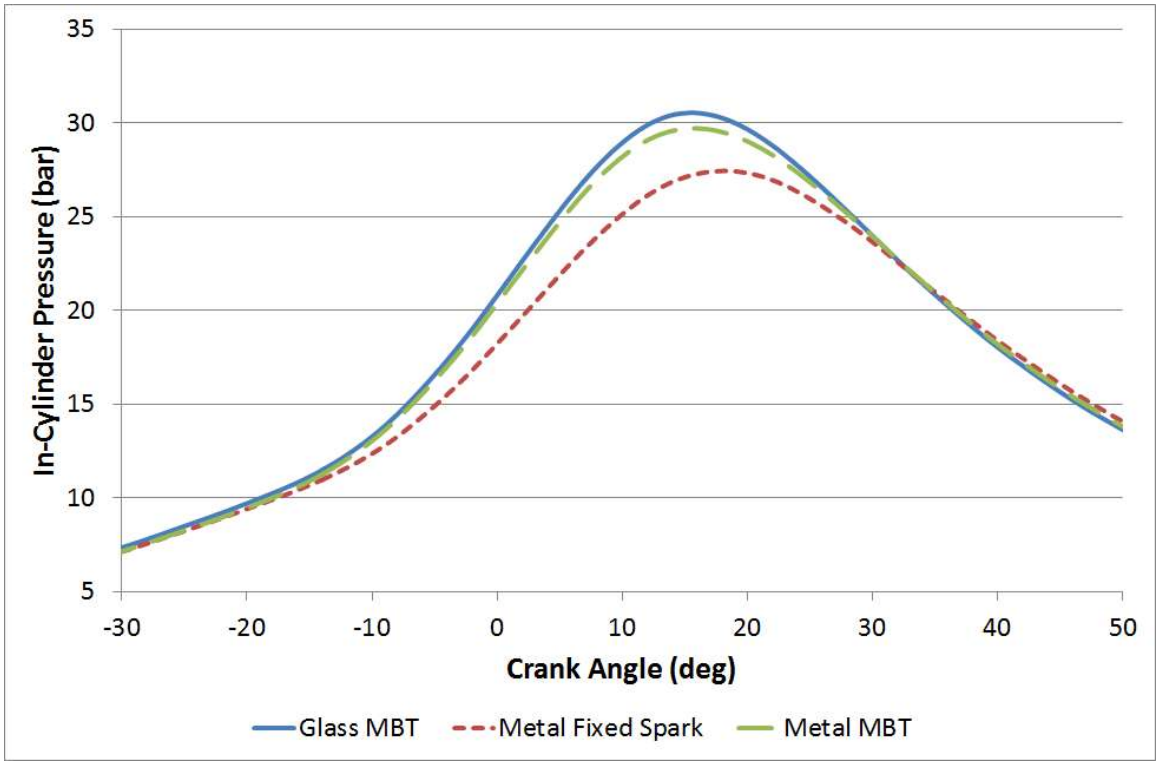

Figure 5.3 – Comparison of the combustion pressure traces for the differing window material and spark timing combinations.

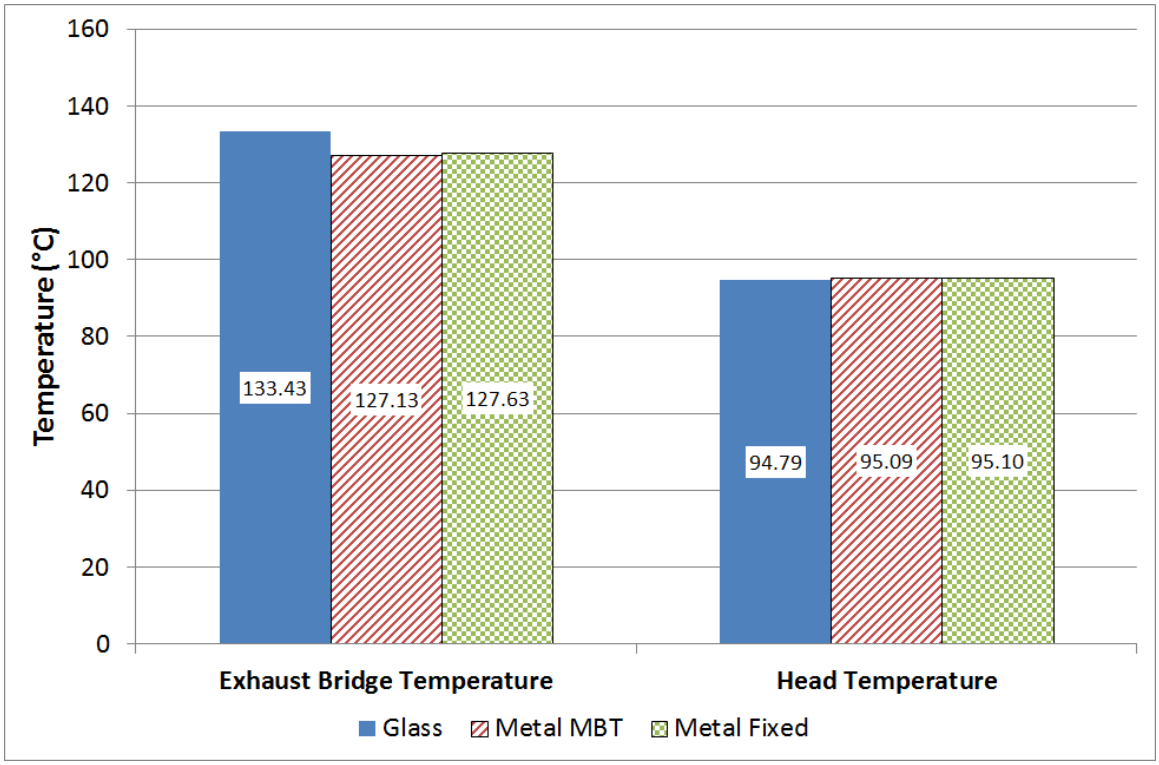

Figure 5.4 – A side-by-side comparison of the temperatures in the head and exhaust bridge for the differing window material and spark timing combinations.

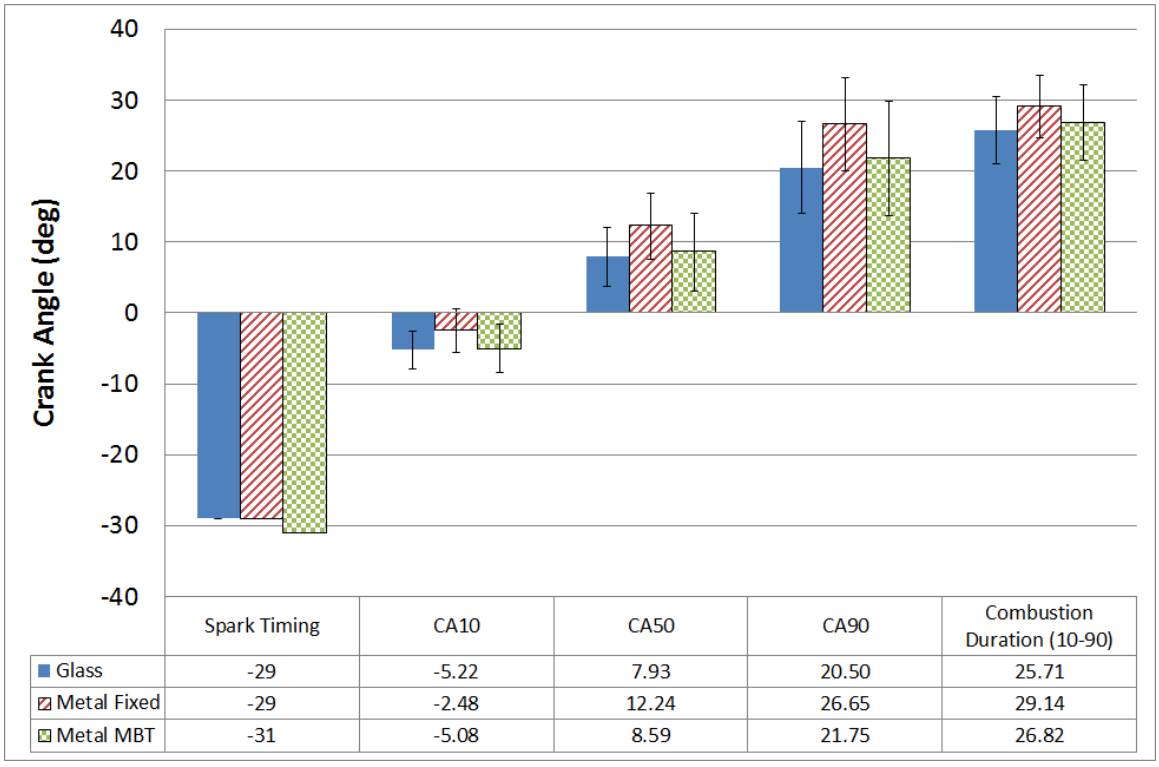

	Spark Timing	CA10	CA50	CA90	Combustion Duration (10-90)
Glass	-29	-5.22	7.93	20.50	25.71
Metal Fixed	-29	-2.48	12.24	26.65	29.14
Metal MBT	-31	-5.08	8.59	21.75	26.82

Figure 5.5 – The spark timings and burn durations of the three differing window material and spark timing combinations.

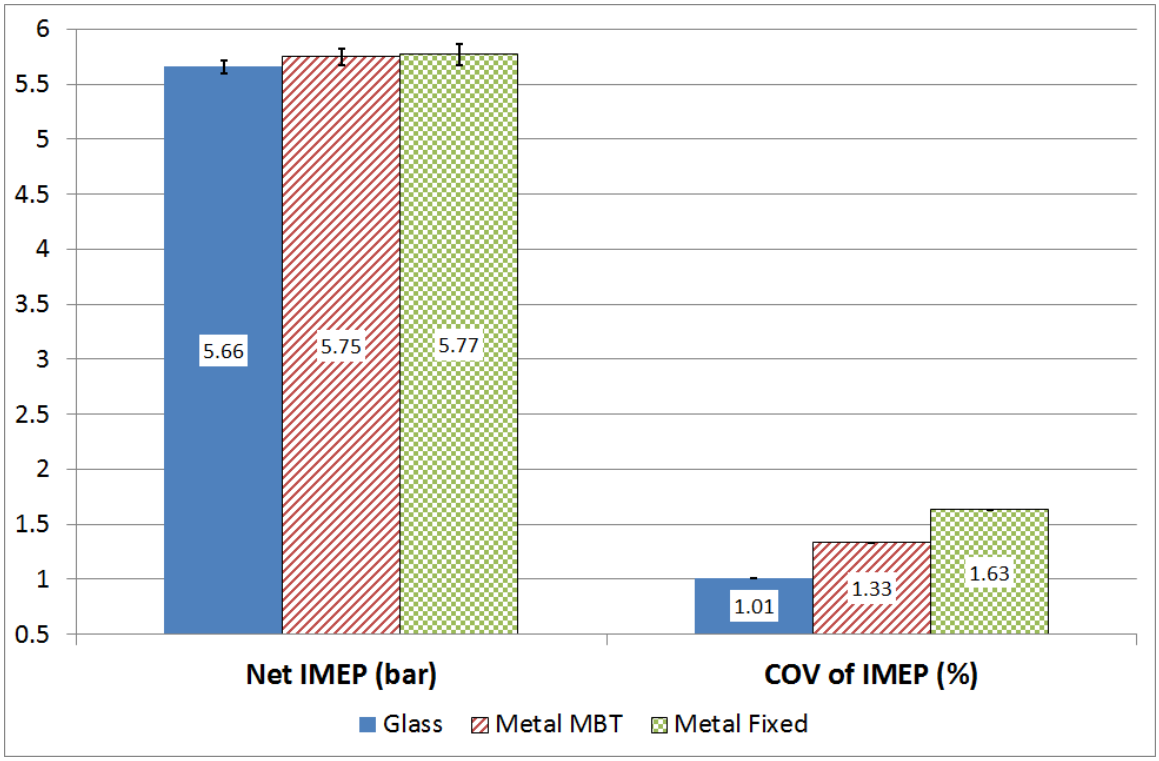

Figure 5.6 – The net IMEP and stability for the differing window material and spark timing combinations.

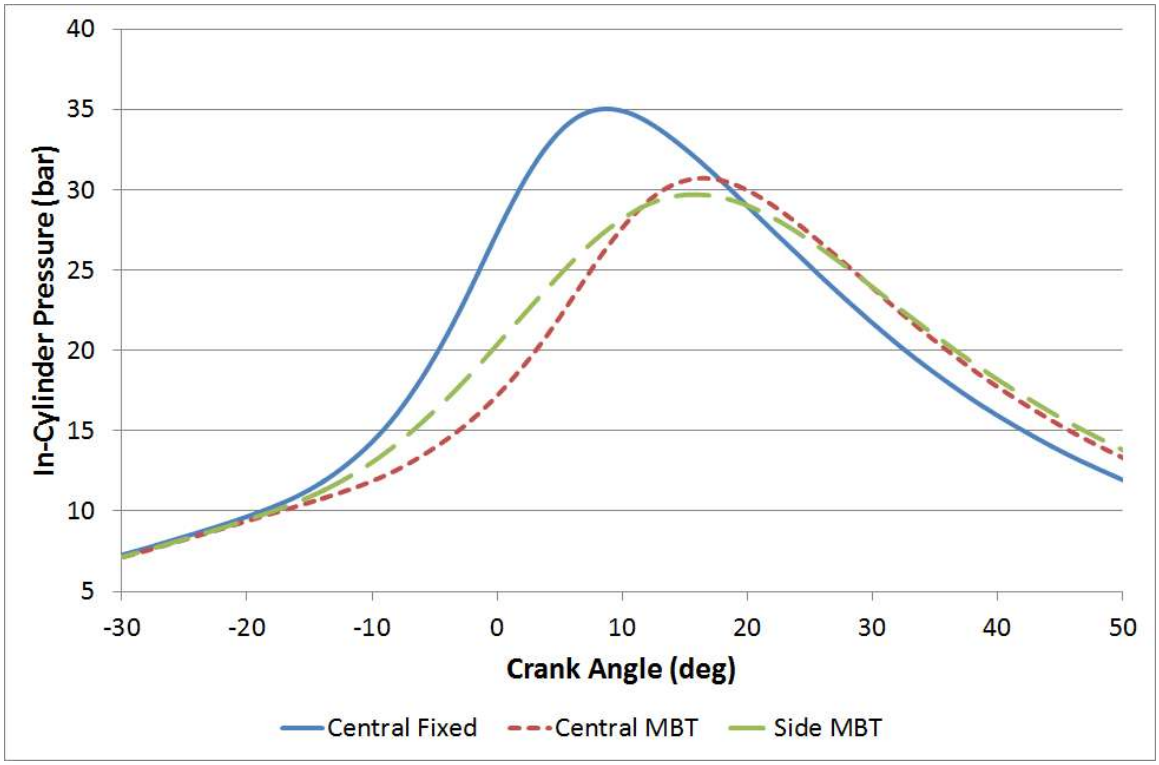

Figure 5.7 – In-cylinder pressure traces for the spark locations and timings.

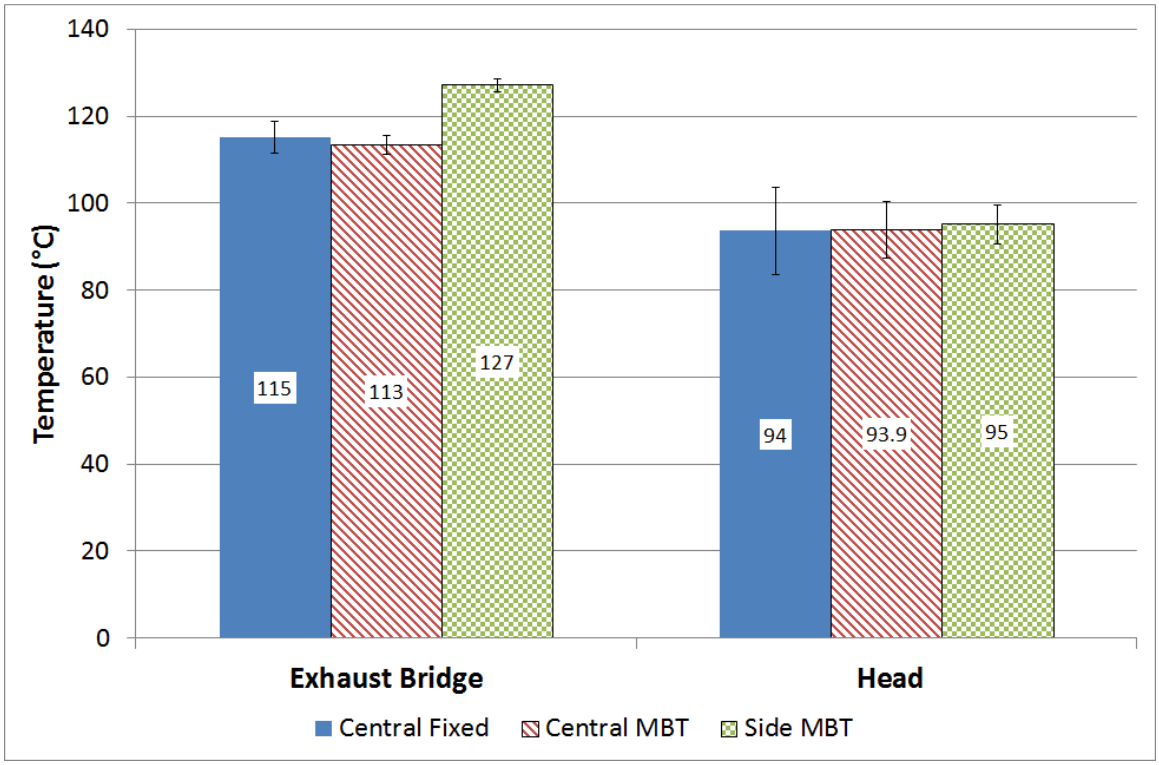

Figure 5.8 – Head and exhaust bridge temperatures for the spark locations and timings.

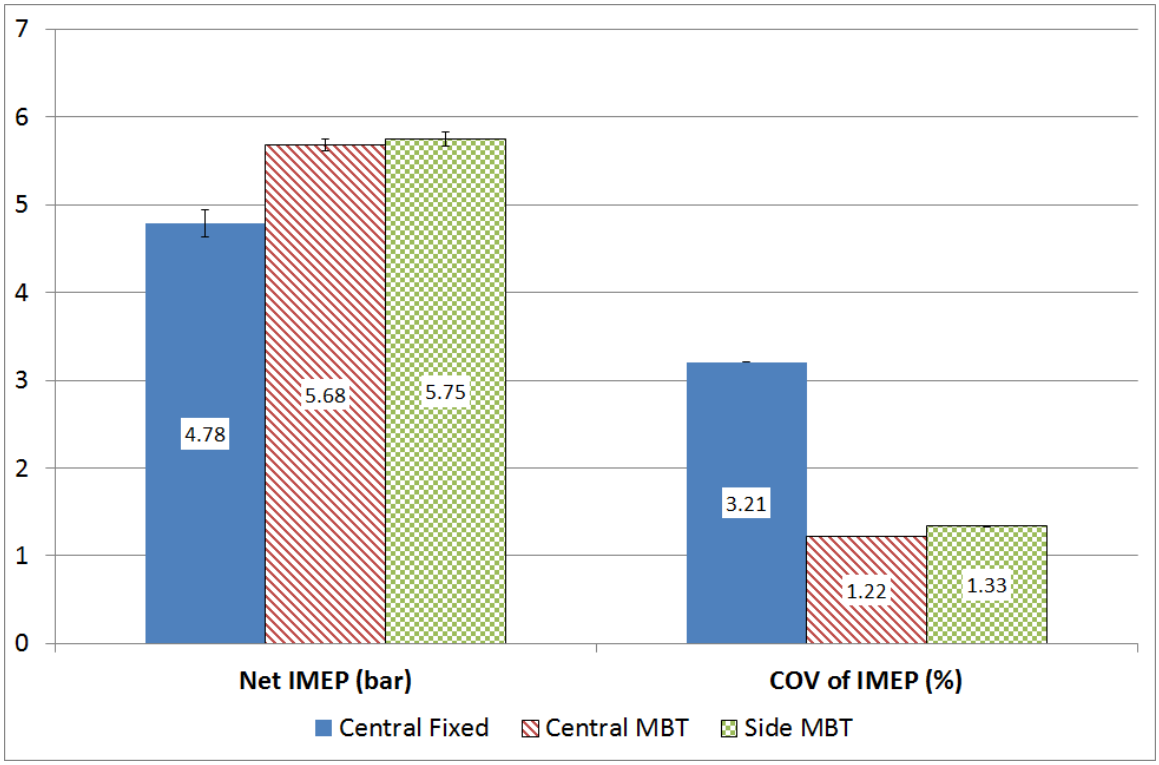

Figure 5.9 – Net IMEP and stability for each of the spark locations and timings.

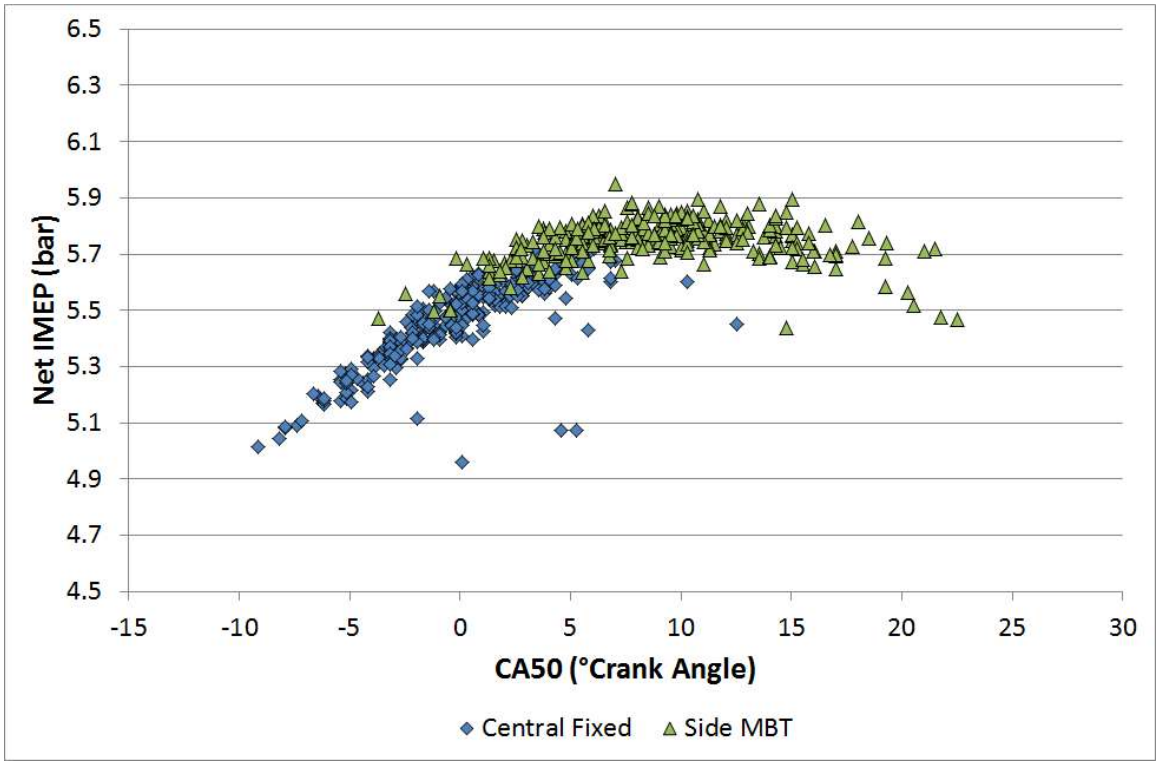

Figure 5.10 – IMEP vs CA50 for identical spark timings at both central and side locations.

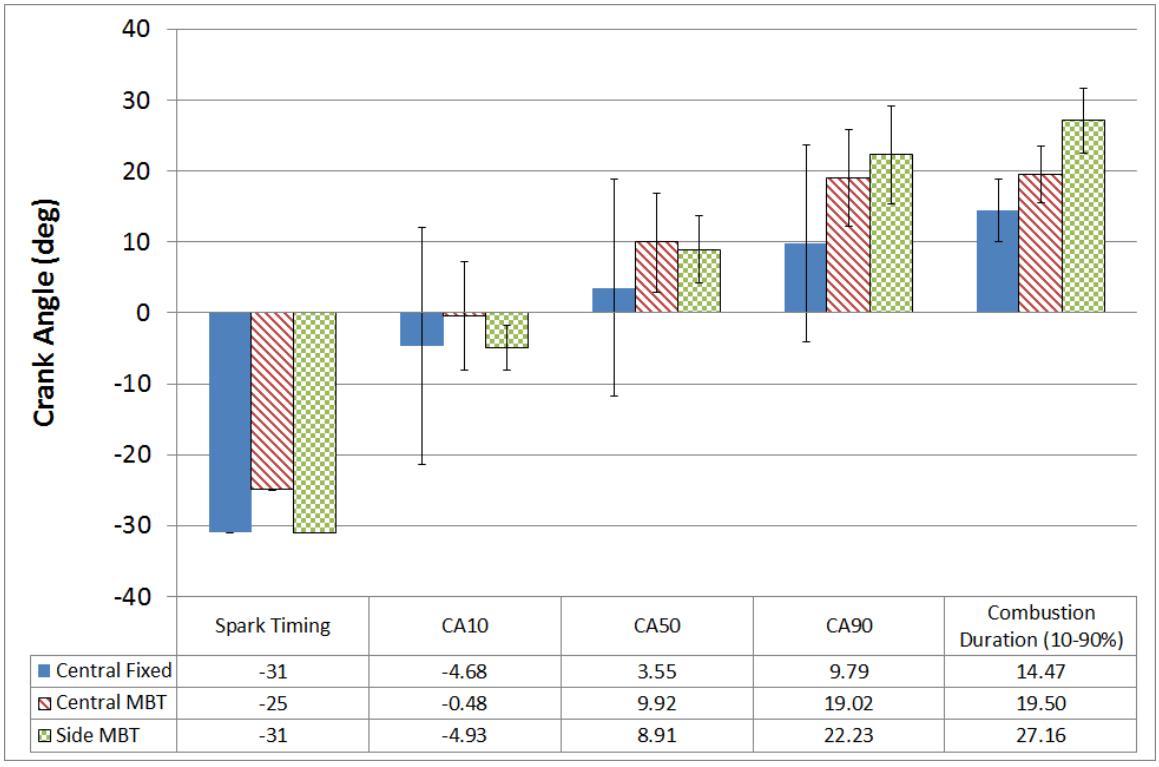

	Spark Timing	CA10	CA50	CA90	Combustion Duration (10-90%)
Central Fixed	-31	-4.68	3.55	9.79	14.47
Central MBT	-25	-0.48	9.92	19.02	19.50
Side MBT	-31	-4.93	8.91	22.23	27.16

Figure 5.11 – Spark and combustion timings for each of the spark locations and timings.

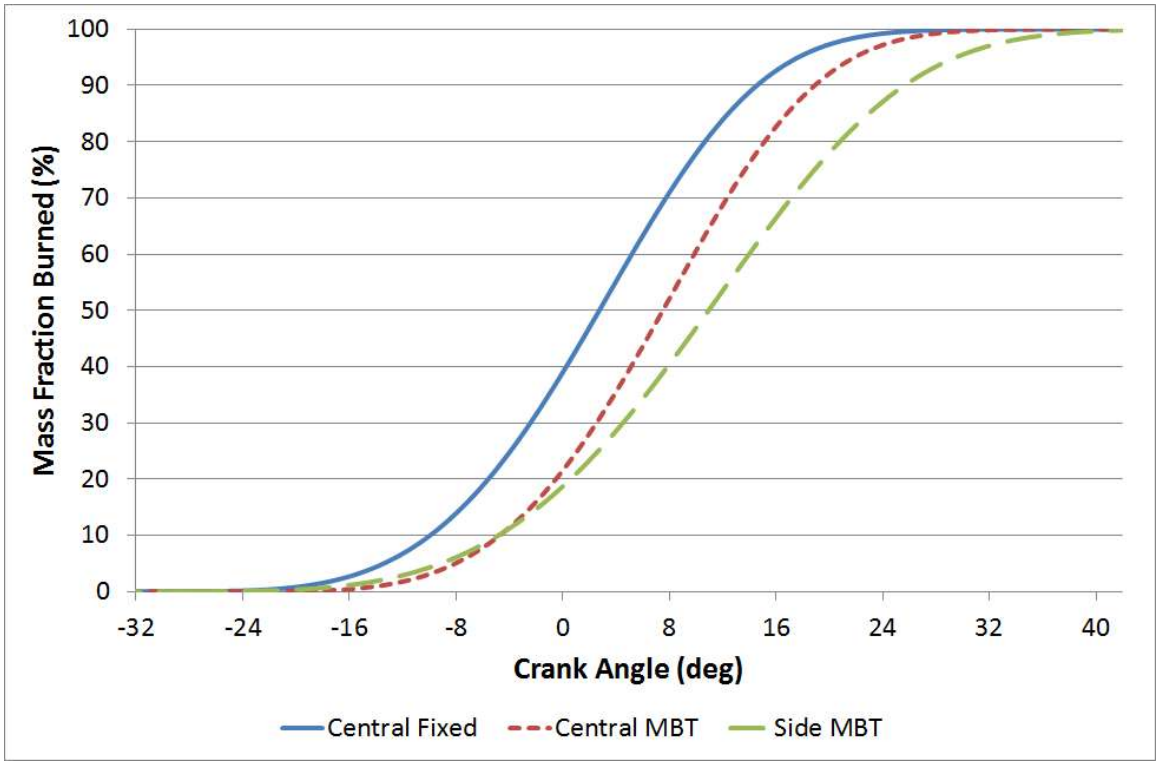

Figure 5.12 – Mass fraction burned curves for each of the spark locations and timings.

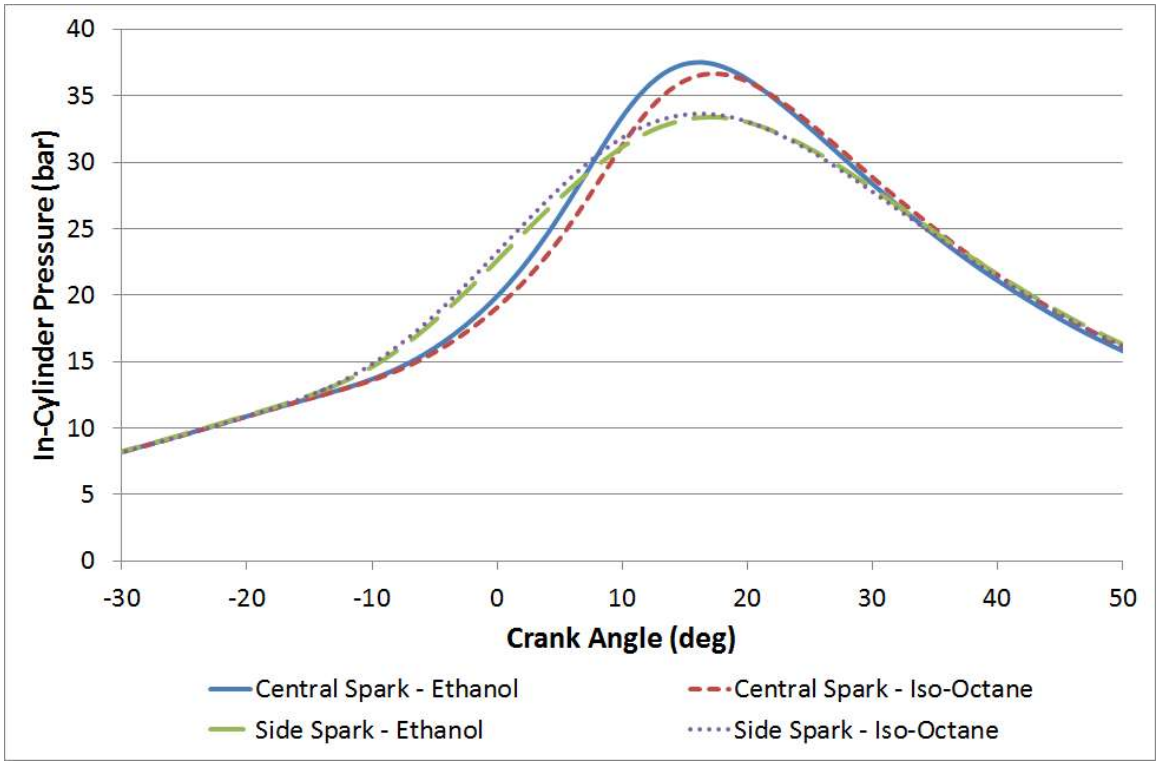

Figure 5.13 – In-cylinder pressure traces for the two fuels and spark plug locations.

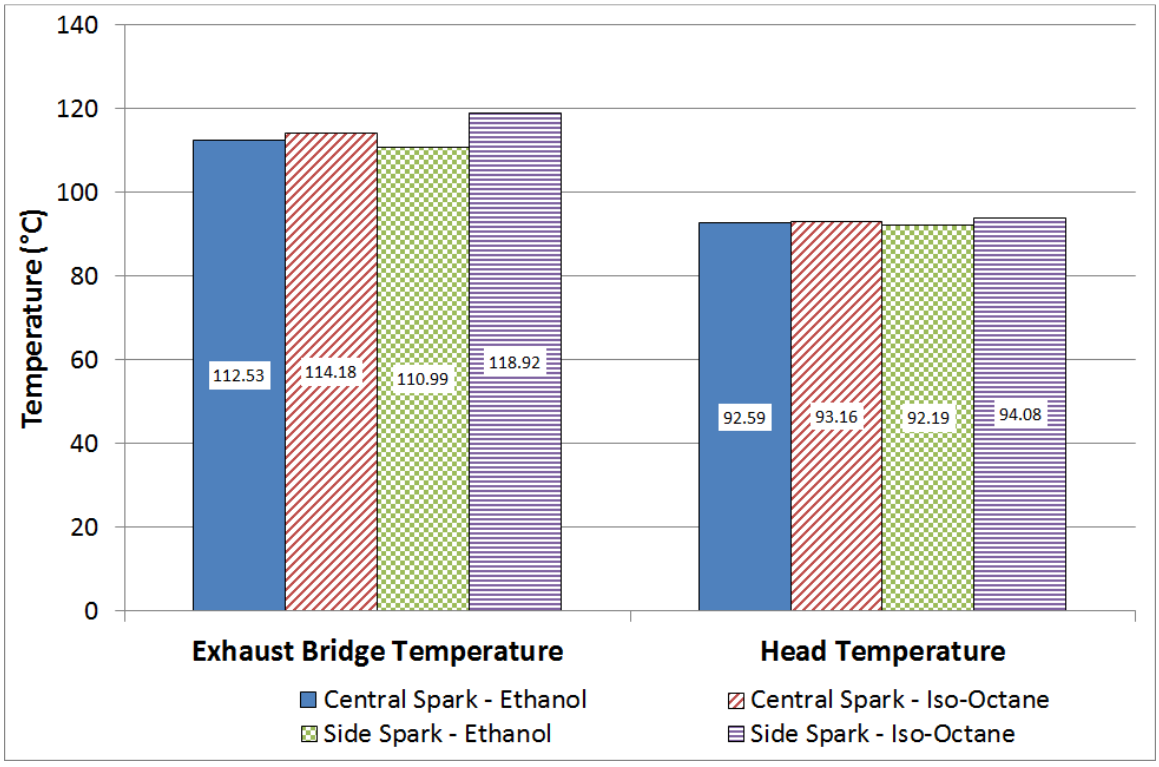

Figure 5.14 – Head and exhaust bridge temperatures for the two fuels and spark plug locations.

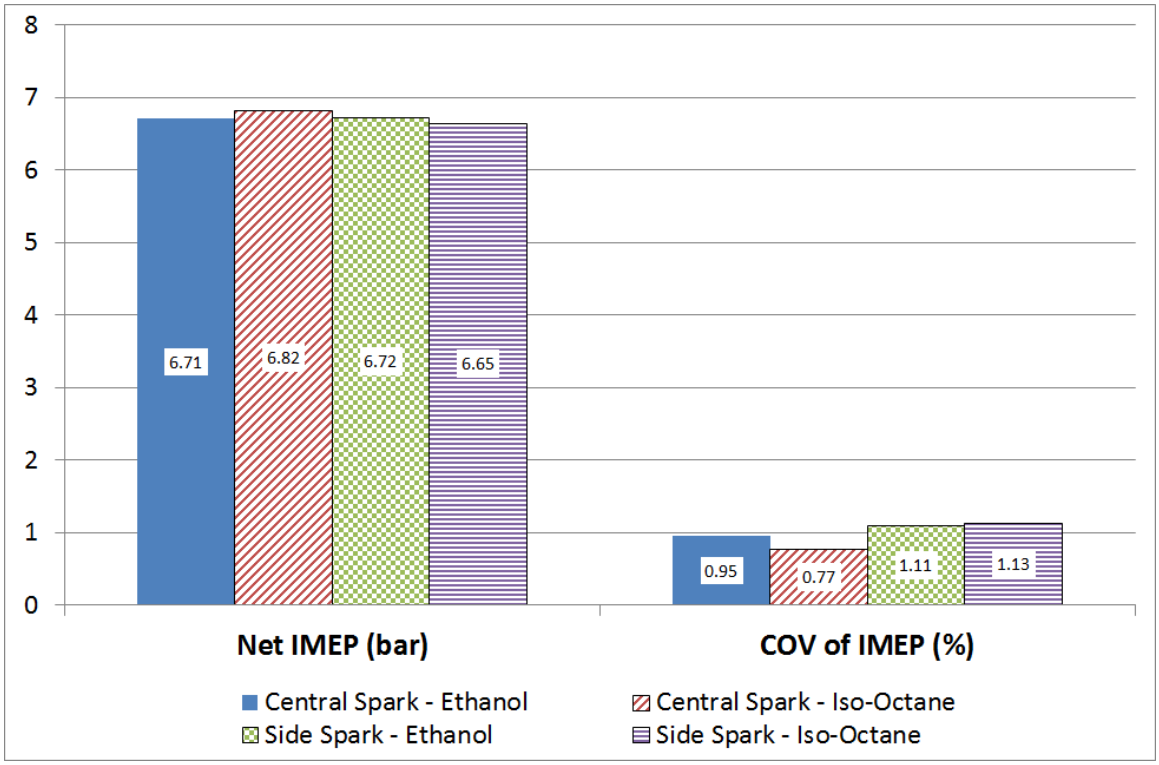

Figure 5.15 – Net IMEP and stability for the two fuels and spark plug locations.

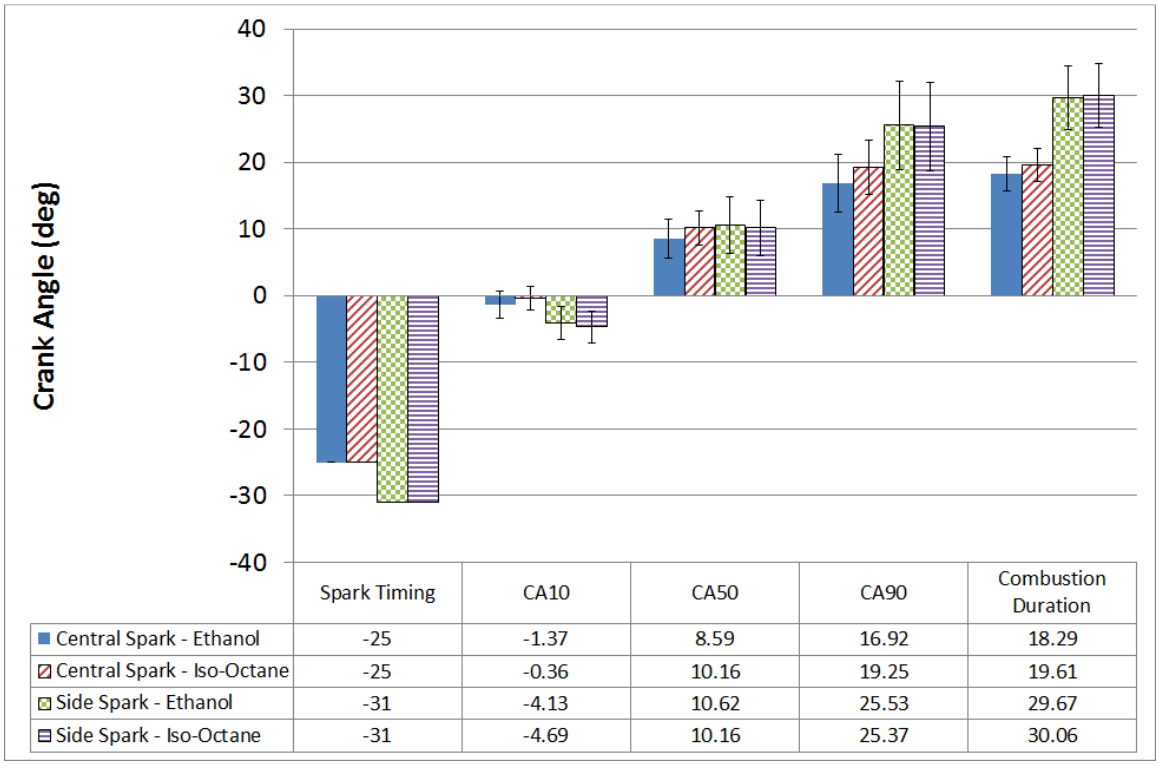

	Spark Timing	CA10	CA50	CA90	Combustion Duration
Central Spark - Ethanol	-25	-1.37	8.59	16.92	18.29
Central Spark - Iso-Octane	-25	-0.36	10.16	19.25	19.61
Side Spark - Ethanol	-31	-4.13	10.62	25.53	29.67
Side Spark - Iso-Octane	-31	-4.69	10.16	25.37	30.06

Figure 5.16 – Spark and combustion timings for the two fuels and spark plug locations.

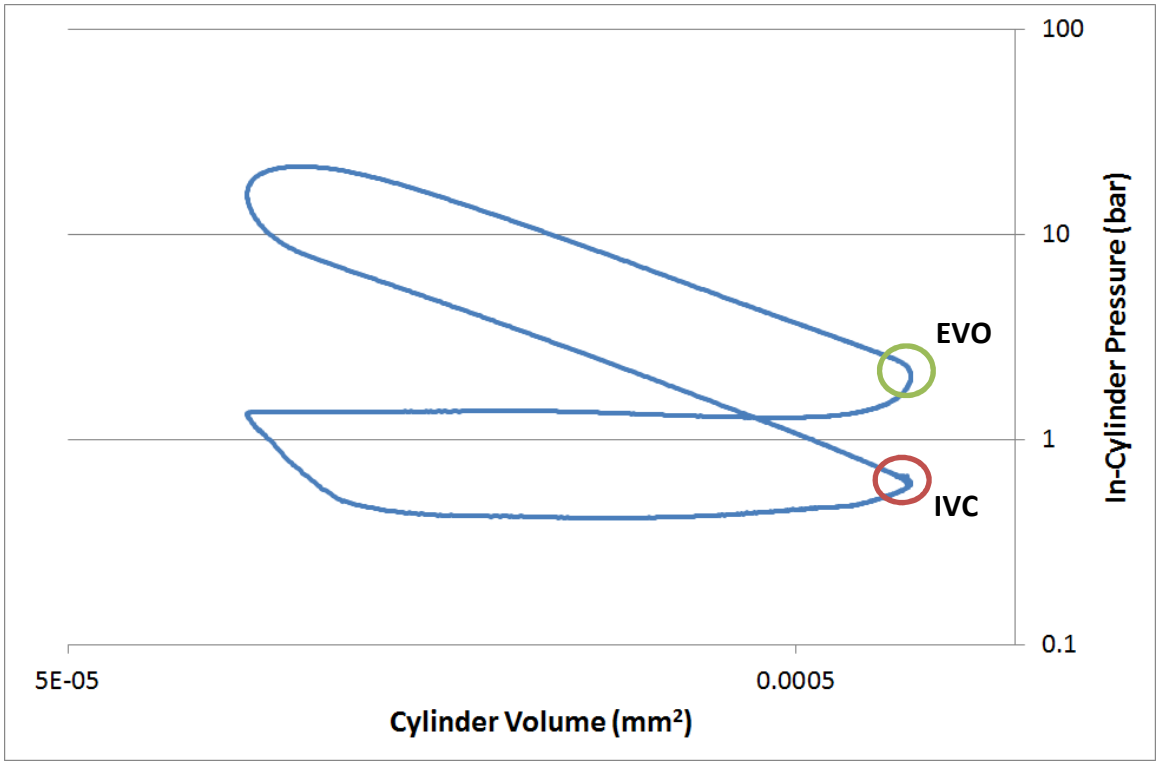

Figure 5.17 – Log Pressure/Log Volume for the mean iso-octane cycle with combustion.

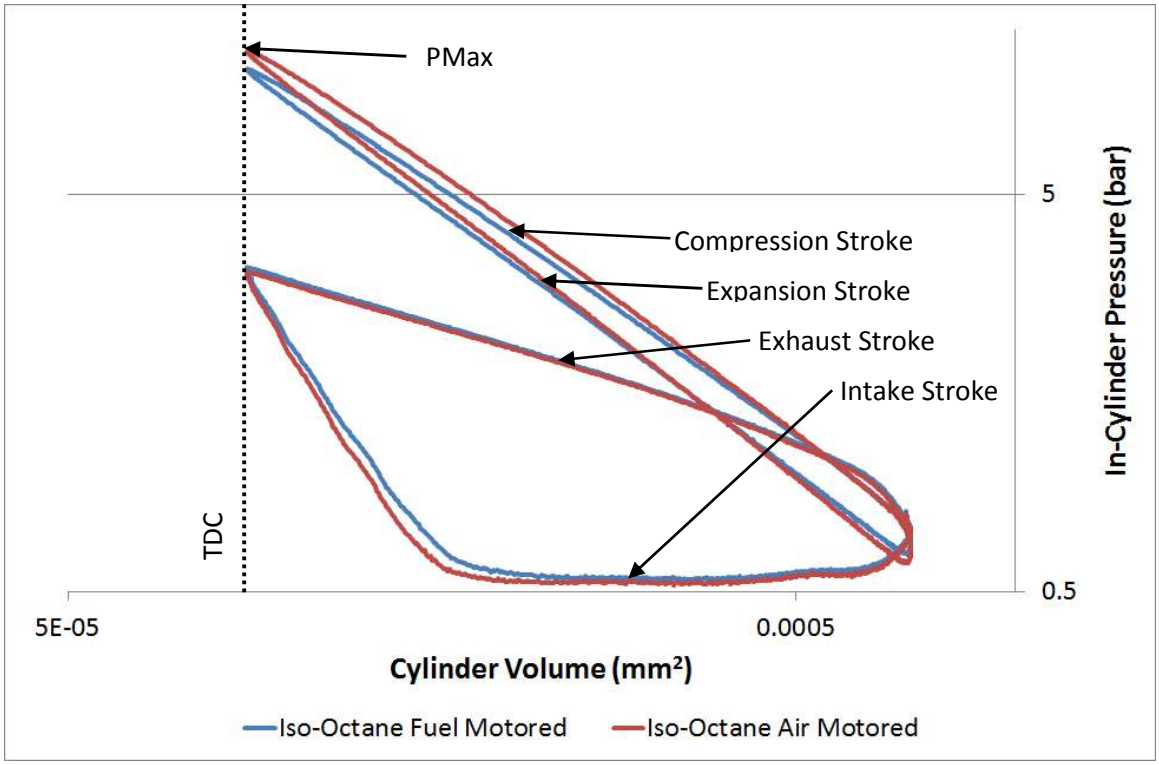

Figure 5.18 – Comparison of the two motored cycles – one with iso-octane injected, the other without.

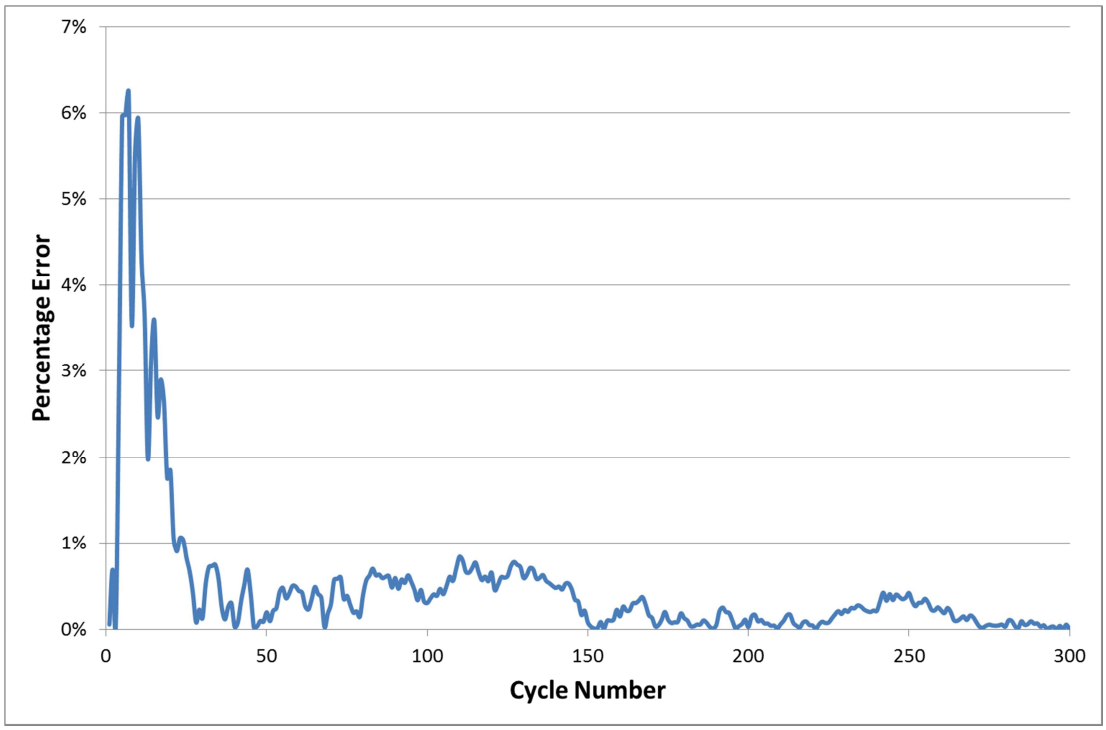

Figure 5.19 – The cumulative percentage error indicating the reducing of COV of IMEP over 300 cycles.

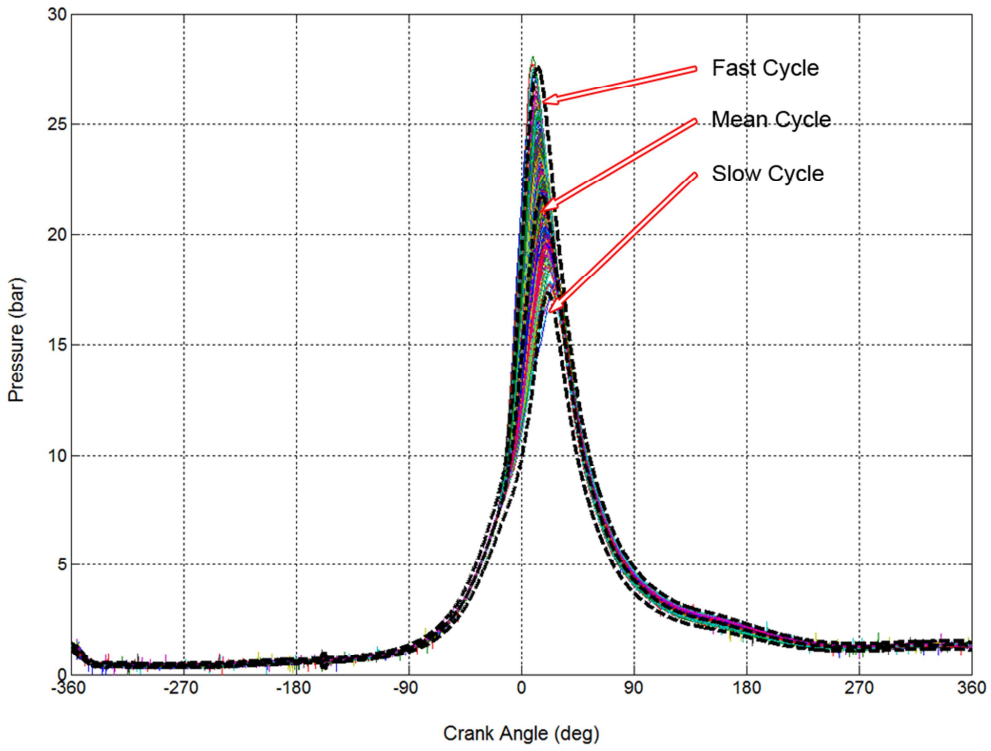

Figure 5.20 – All 300 cycles displayed together with the arithmetic mean cycle, fast cycle and slow cycle superimposed on top.

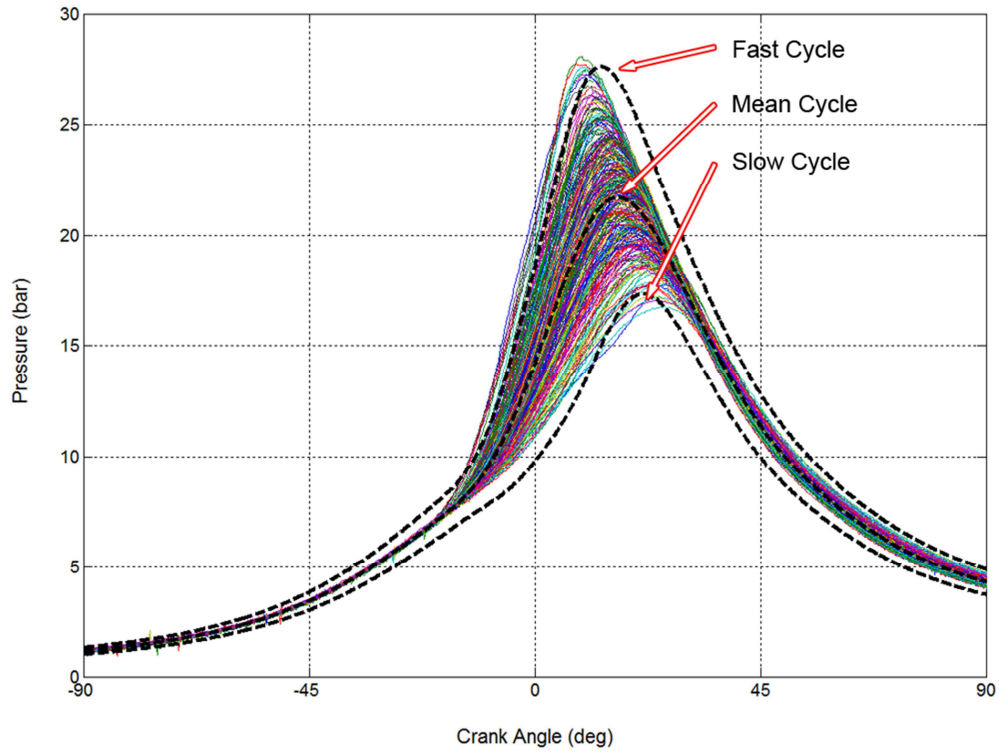

Figure 5.21 – A cropped version of Figure 5.20 allowing for better understanding of the variation between different cycles after the spark.

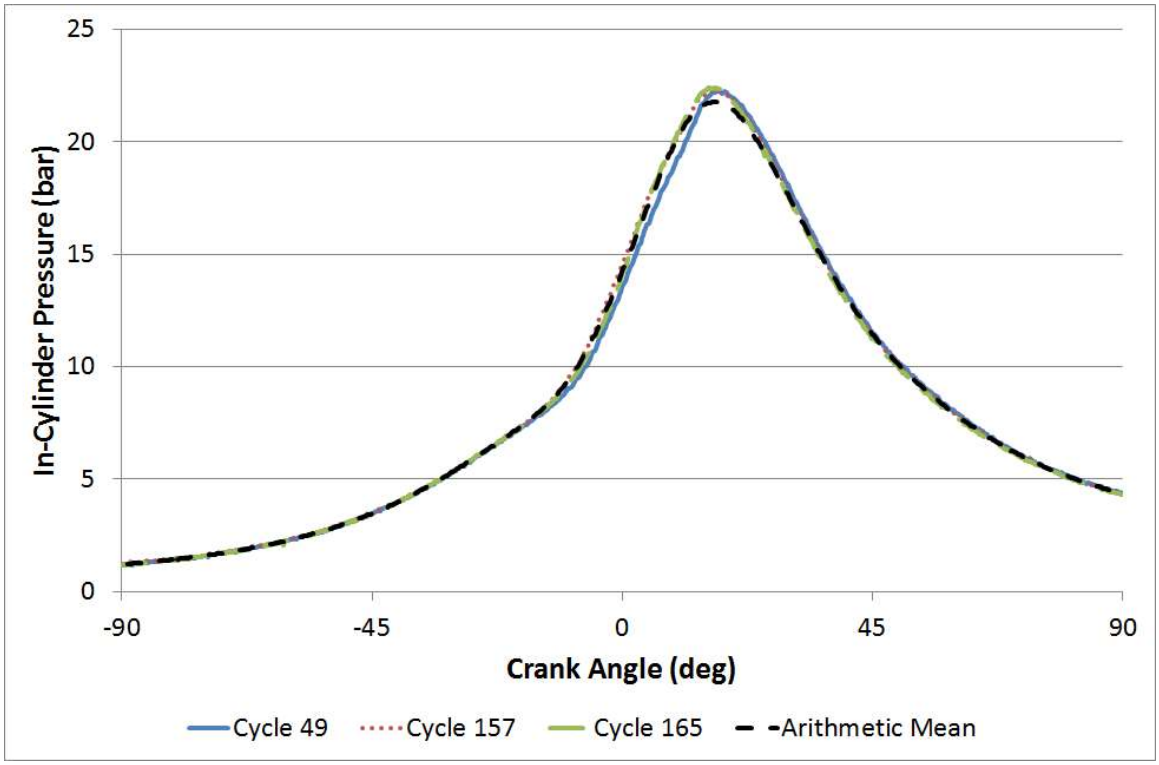

Figure 5.22 – The arithmetic mean cycle with its three closest cycles indicating that achieving the 'optimum mean' cycle is impossible.

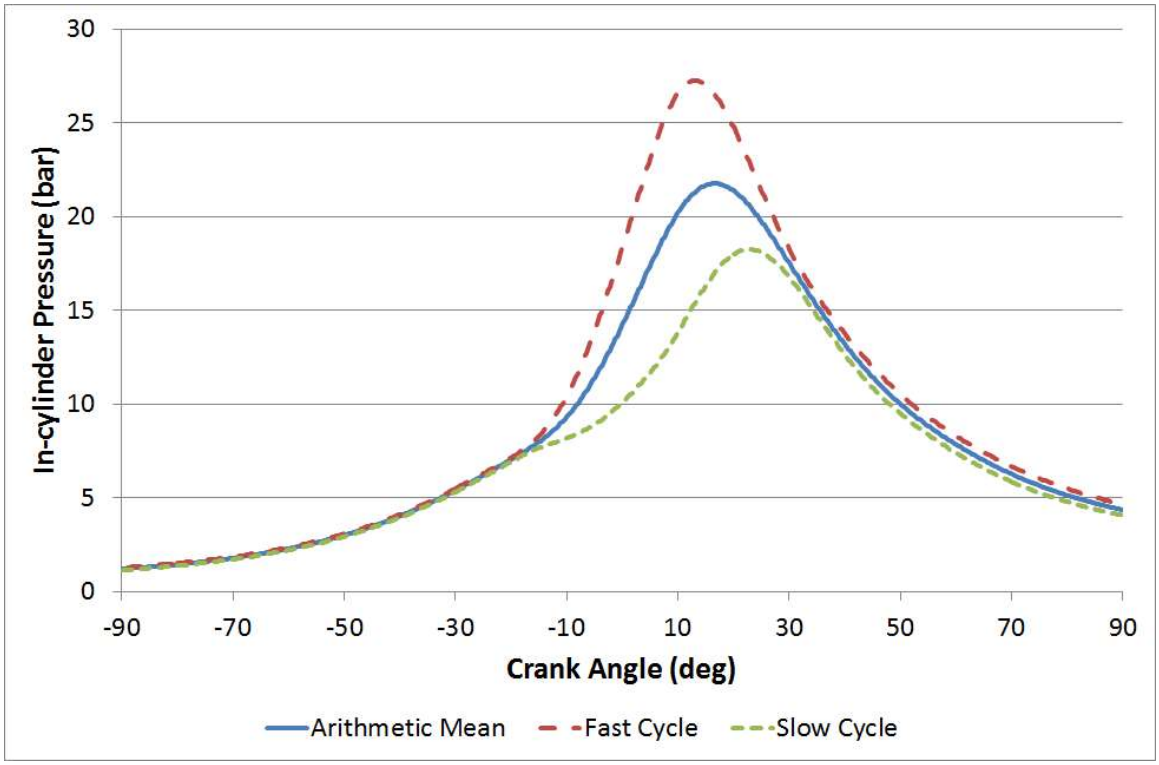

Figure 5.23 – The arithmetic mean cycle with the theoretical fastest and slowest cycles.

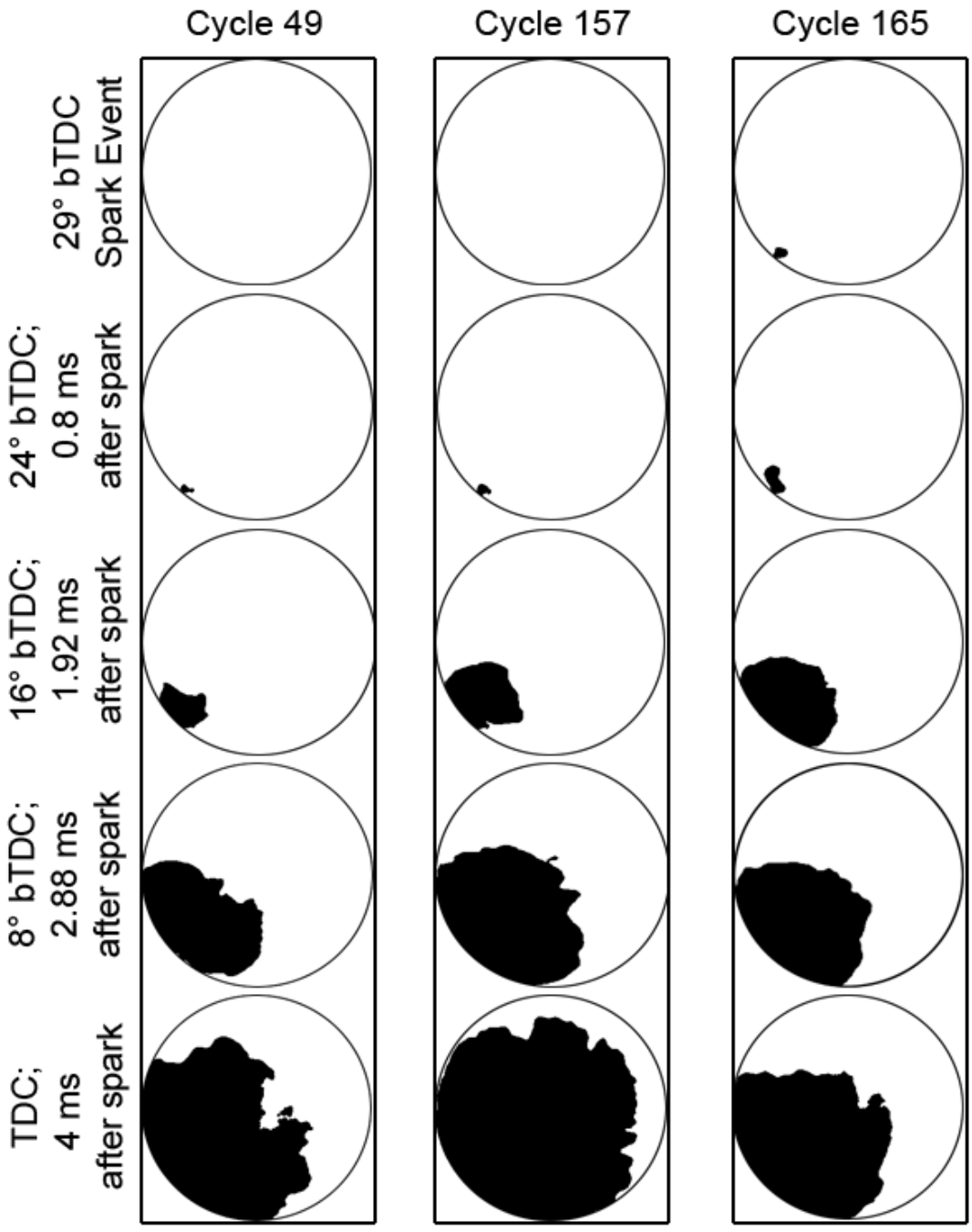

Figure 5.24 – The three cycles closest to the arithmetic mean.

Figure 5.25 – Varying steps of image analysis shown together for the same initial image: Initial image taken with ICCD, mask-filtered binary image and the final inverted white-on-black arrangement (left to right).

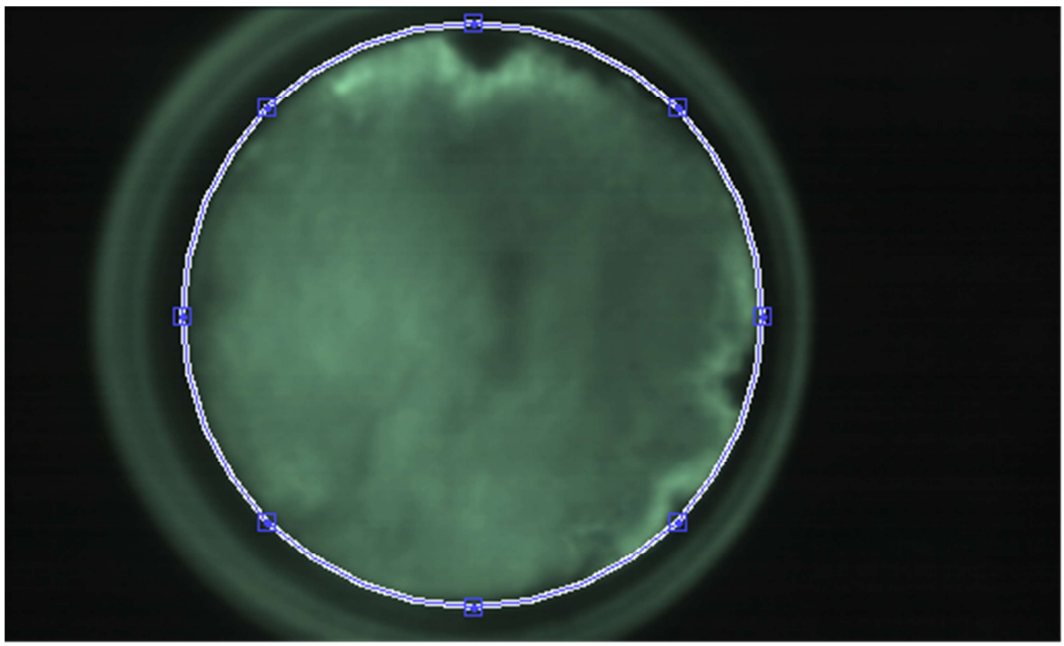

Figure 5.26 – Application of the masking tool in MATLAB to designate the area of the bore.

Figure 5.27 – Example of the issue involved with using the Otsu method of binarisation.

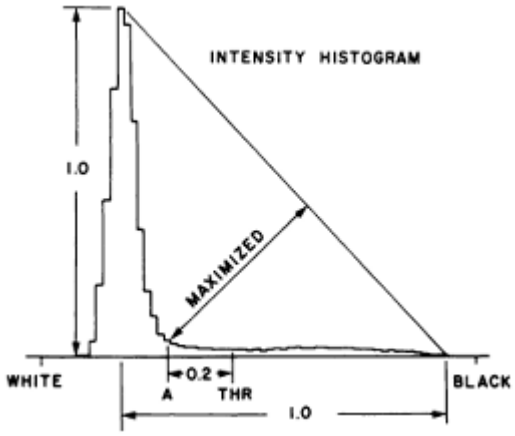

Figure 5.28 – Identification of the triangle region to be used in the triangle value method of binarisation [Zack, 1977].

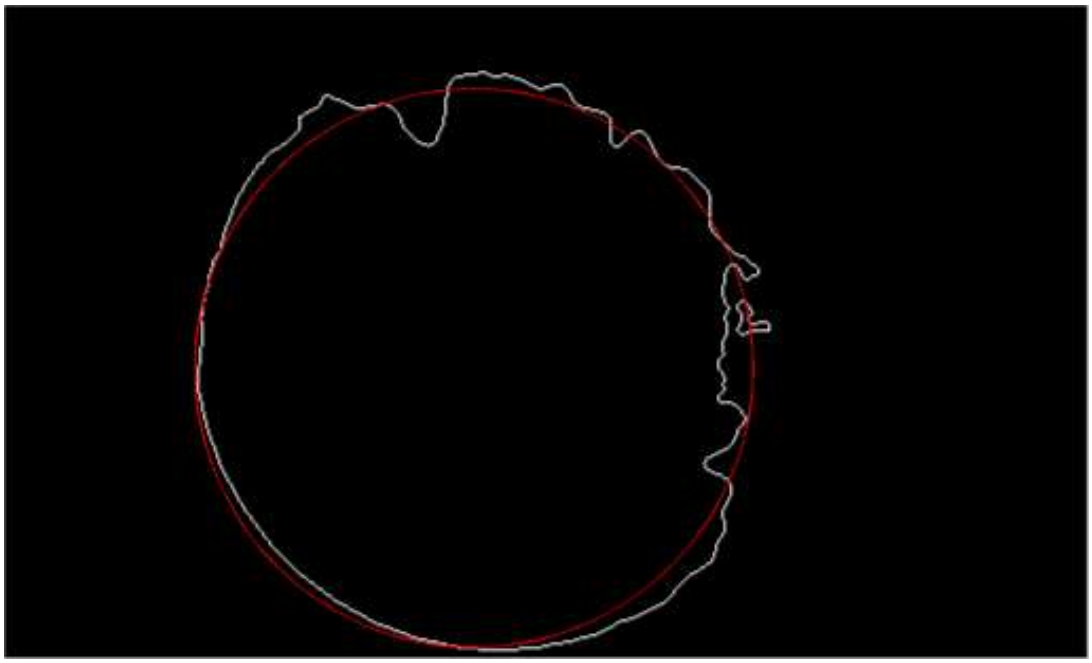

Figure 5.29 – The best-fit circle (red) superimposed on to the flame contour.

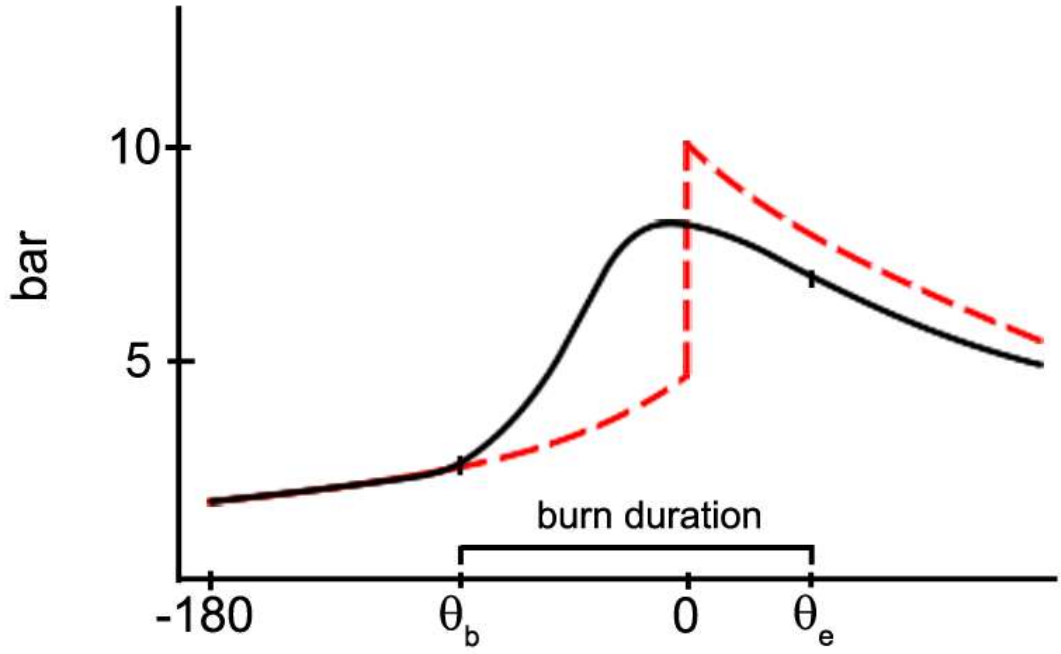

Figure 5.30 – Diagram of a basic low energy pressure trace (black) and the heat release function (red) with the burn duration identified [Adapted from Kirkpatrick, 2006].

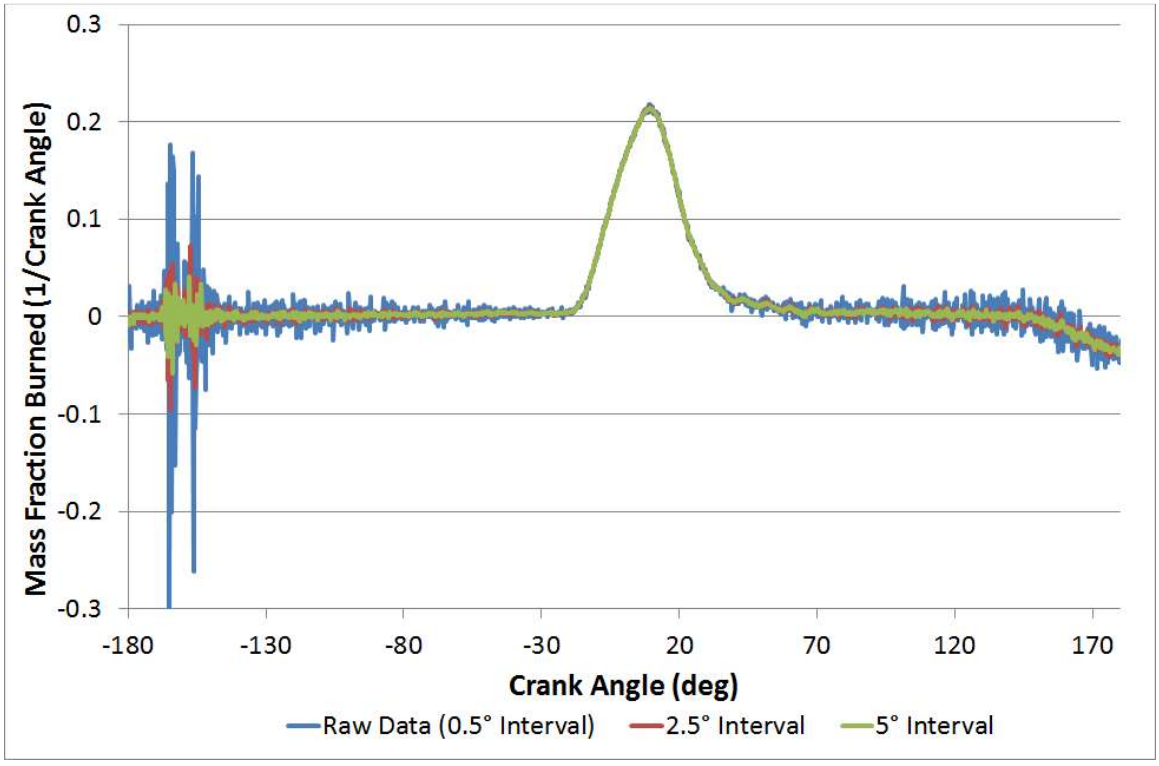

Figure 5.31 – A graph showing the effect of varying the differential interval size when calculating using the ROHR method.

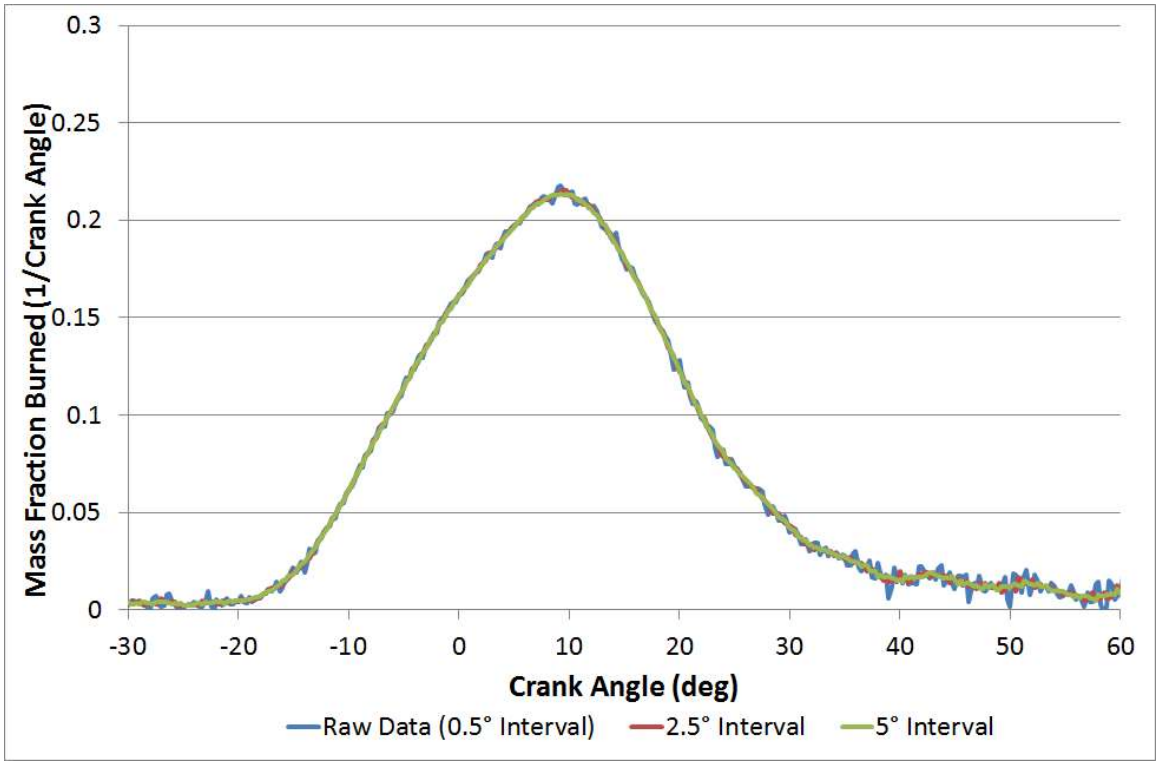

Figure 5.32 – Cropped version of Figure 5.31 showing greater detail of the combustion event.

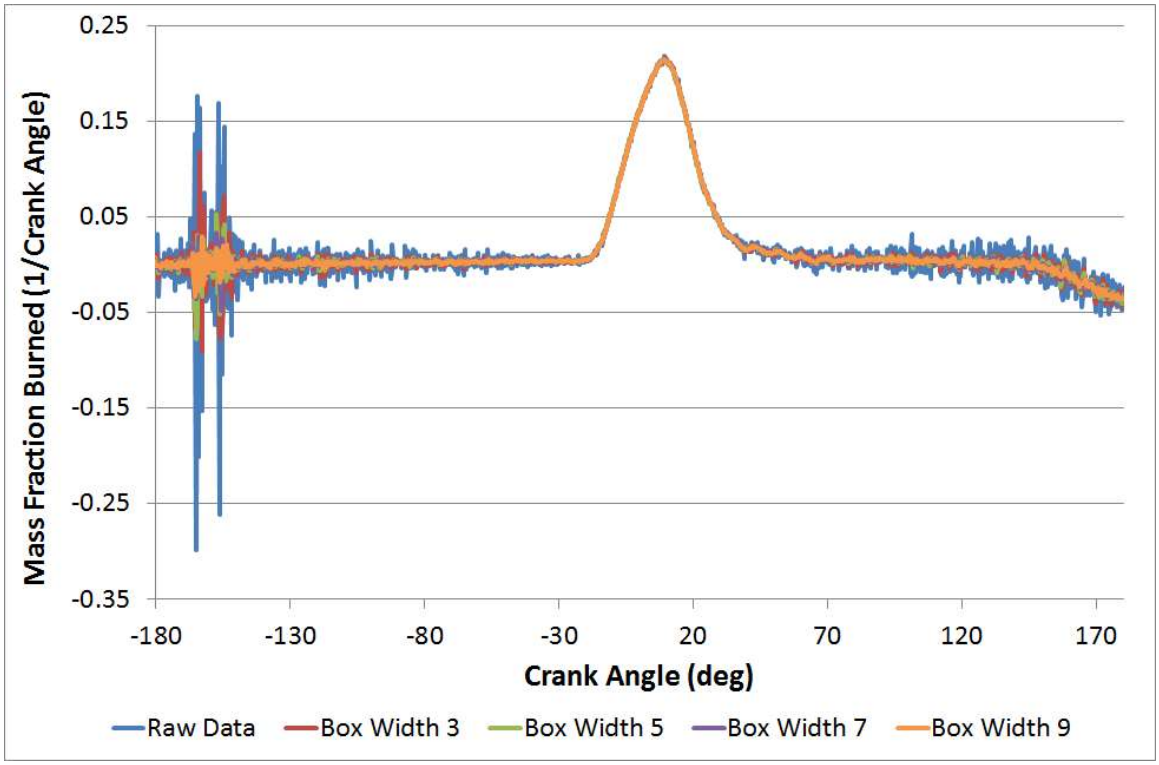

Figure 5.33 - A graph showing the effect of varying box filter width for calculating using the ROHR method.

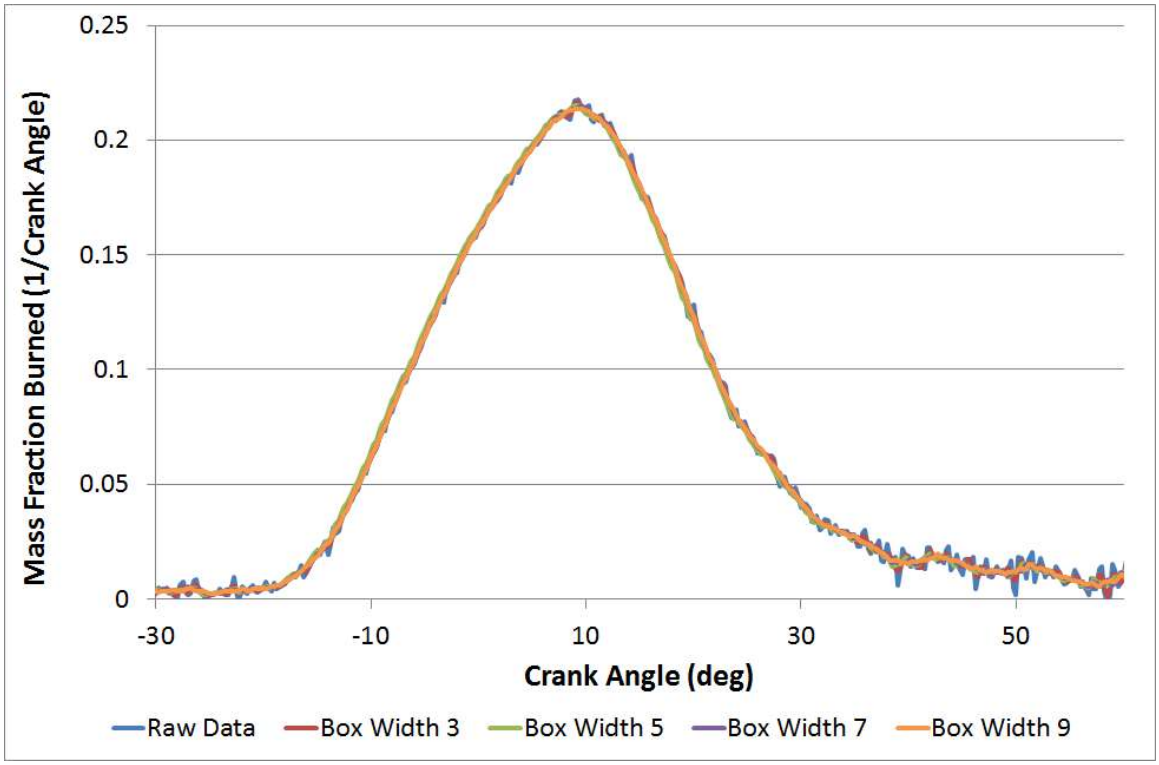

Figure 5.34 – A cropped version of Figure 5.33 showing greater detail of the combustion event.

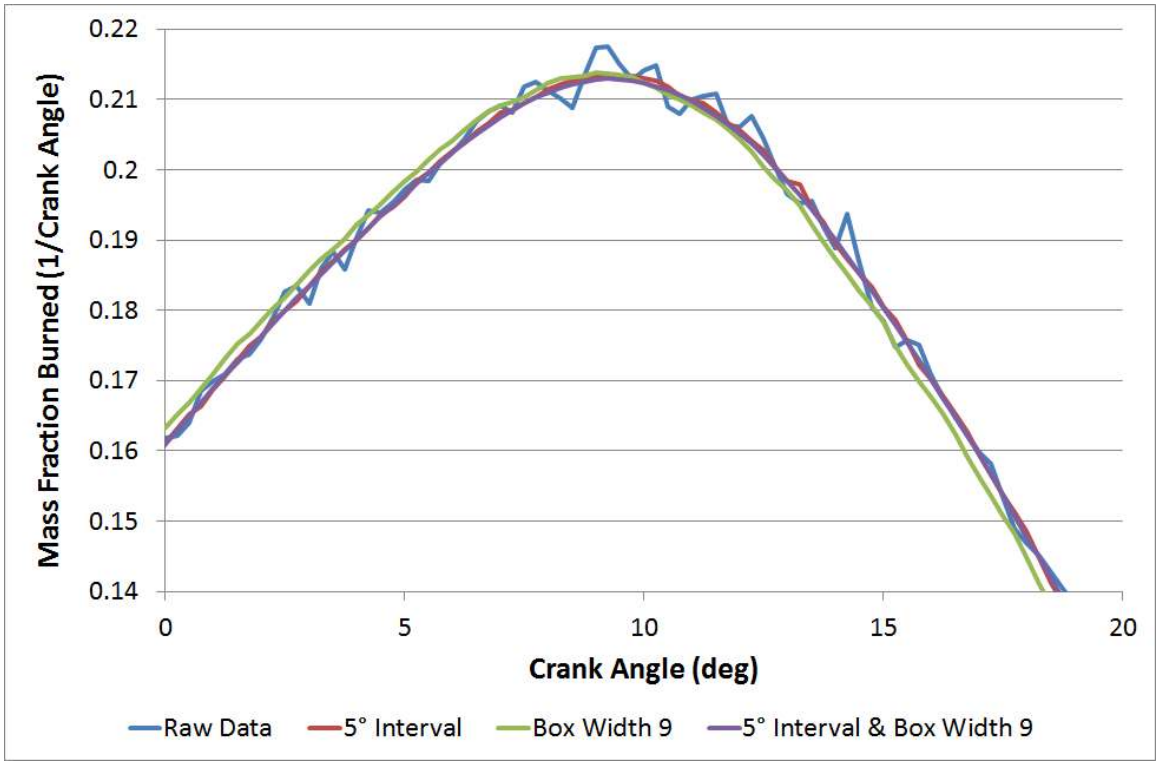

Figure 5.35 – Comparing the raw data, the maximum interval filter used, the maximum box width used and the 2-stage combination filter for calculating using the ROHR method.

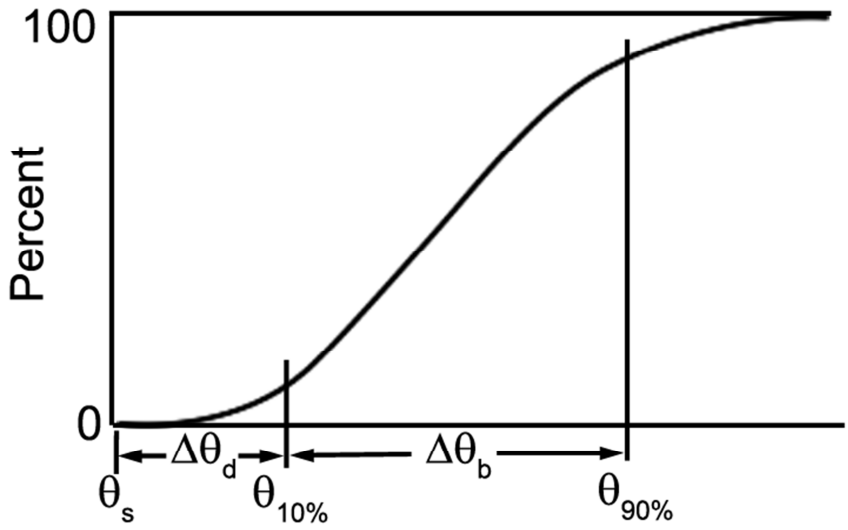

Figure 5.36 – Definition of the flame-development angle ($\Delta\theta_d$) and the rapid-burning angle ($\Delta\theta_b$) set over a mass fraction burnt curve [Adapted from Heywood, 1988].

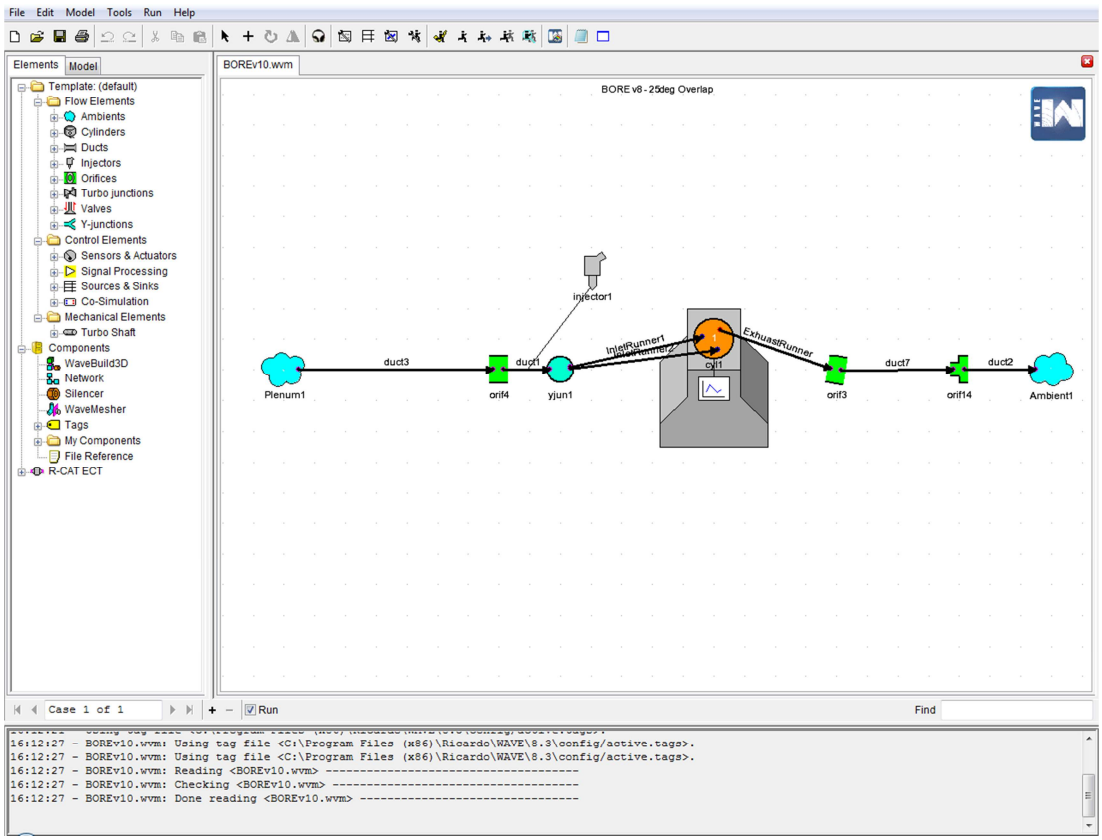

Figure 5.37 – Ricardo WAVE's GUI with the 'Elements' library files on the left side and the model in the centre of the graphical display on the right.

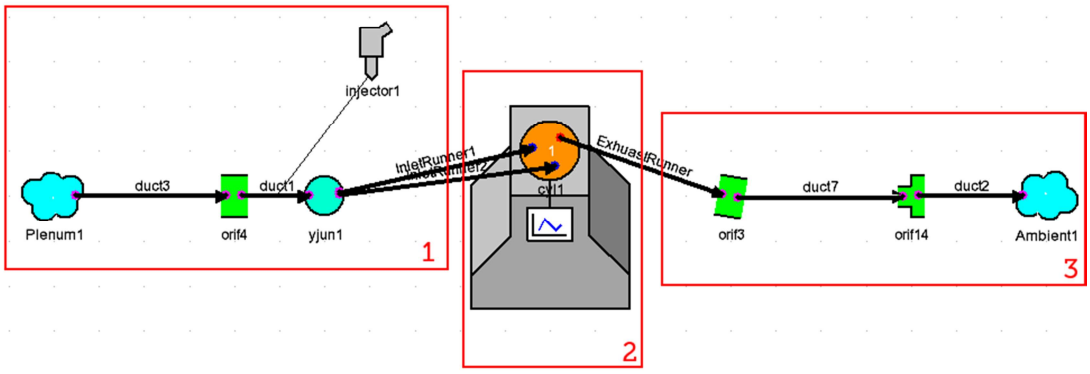

Figure 5.38 – The thermodynamic model used for this work. Detailed in Box 1 are the inlet manifold, runners and the fuel injector, in Box 2 is the combustion chamber and engine block and in Box 3 is the exhaust runner.

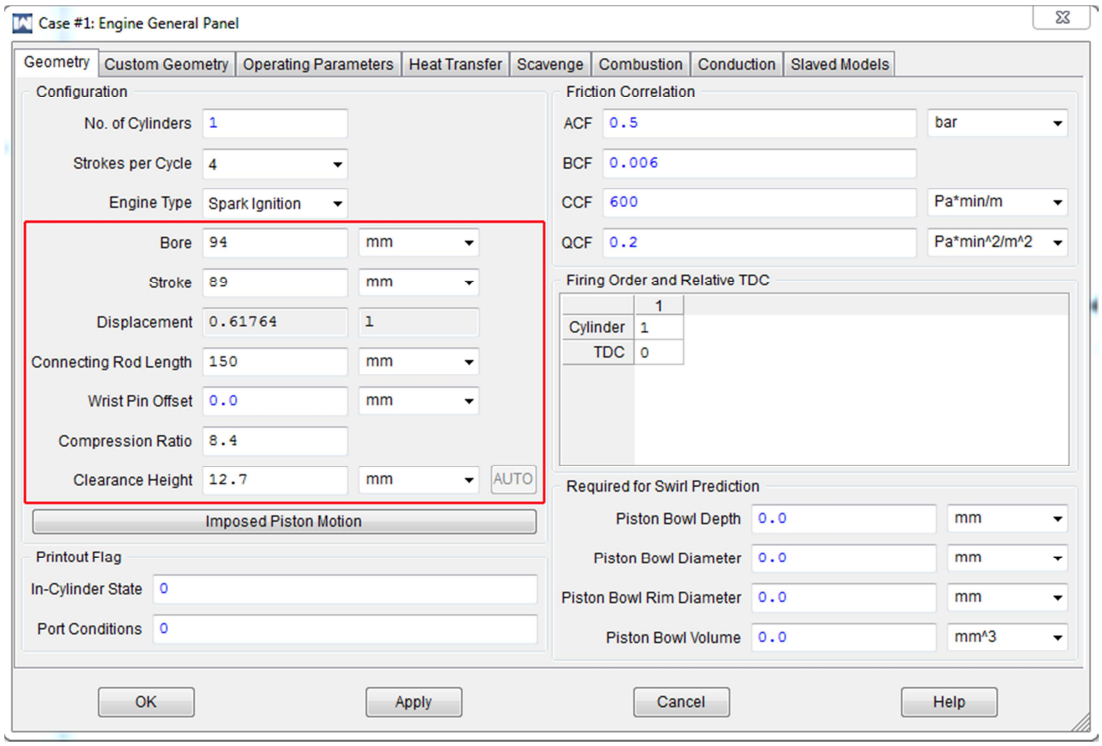

Figure 5.39 – The Engine General Panel in Ricardo WAVE where key engine geometry is entered

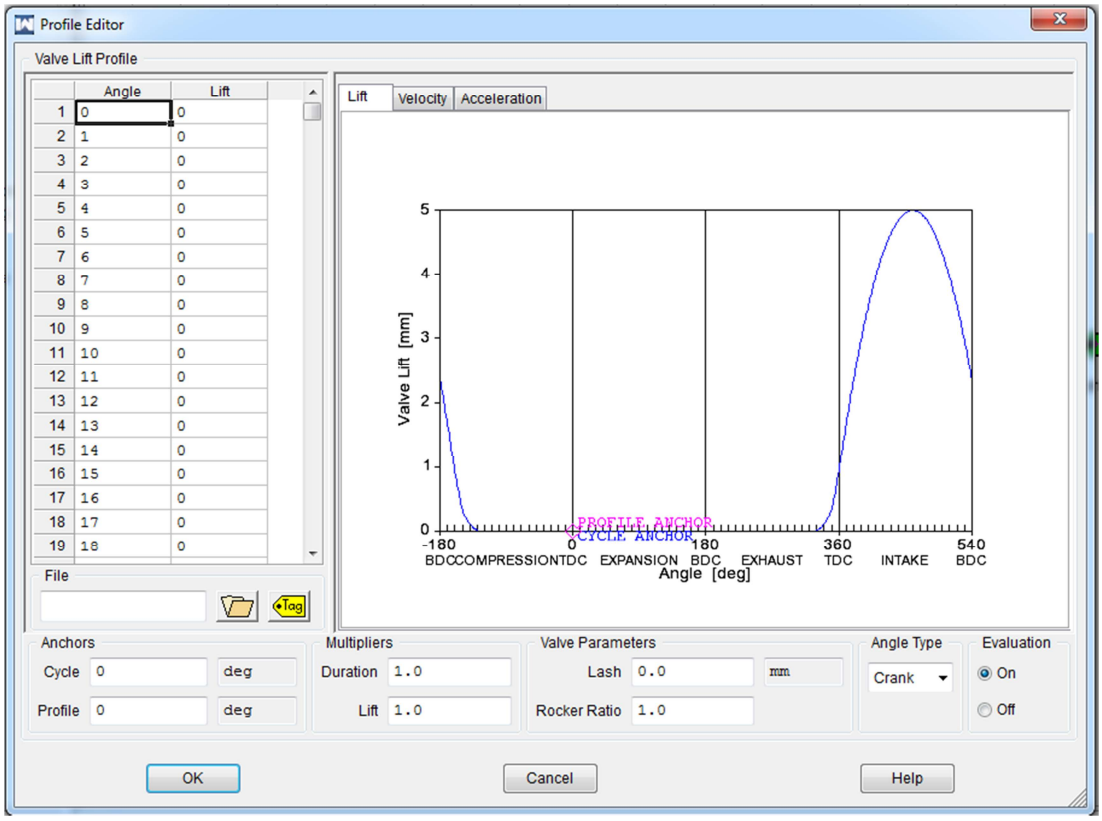

Figure 5.40 – The inlet valve lift profile dialog box in Ricardo WAVE.

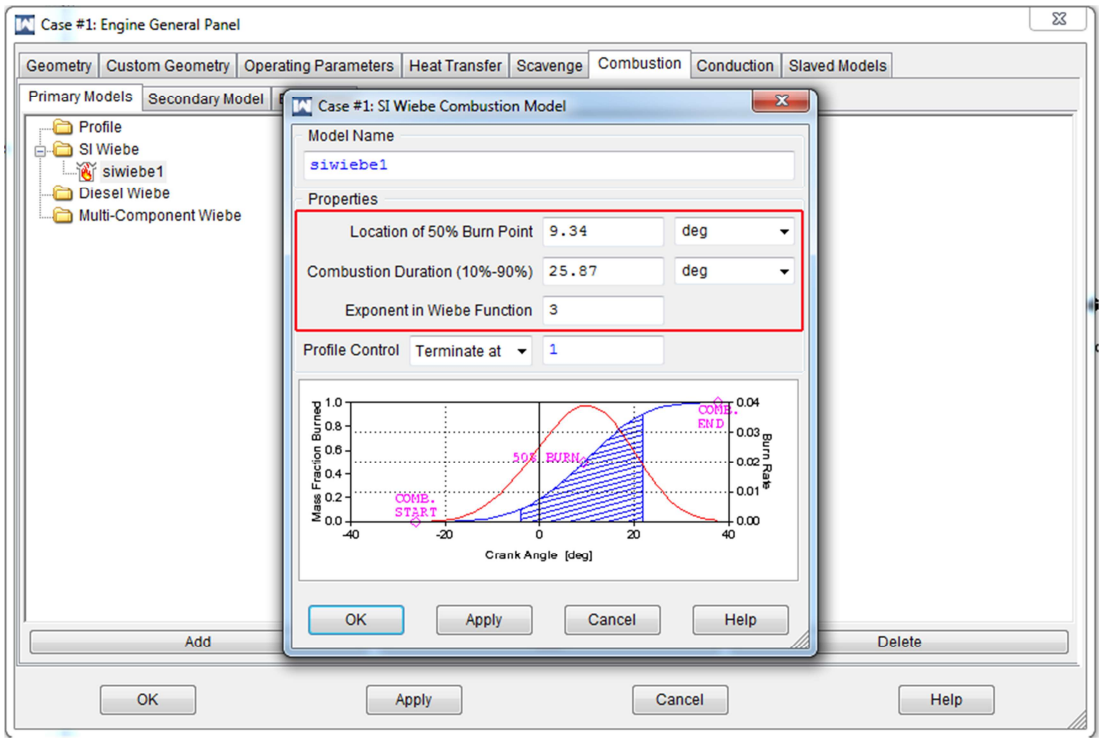

Figure 5.41 – Ricardo WAVE Combustion panel where several models can be chosen from and customised to fit real-world data

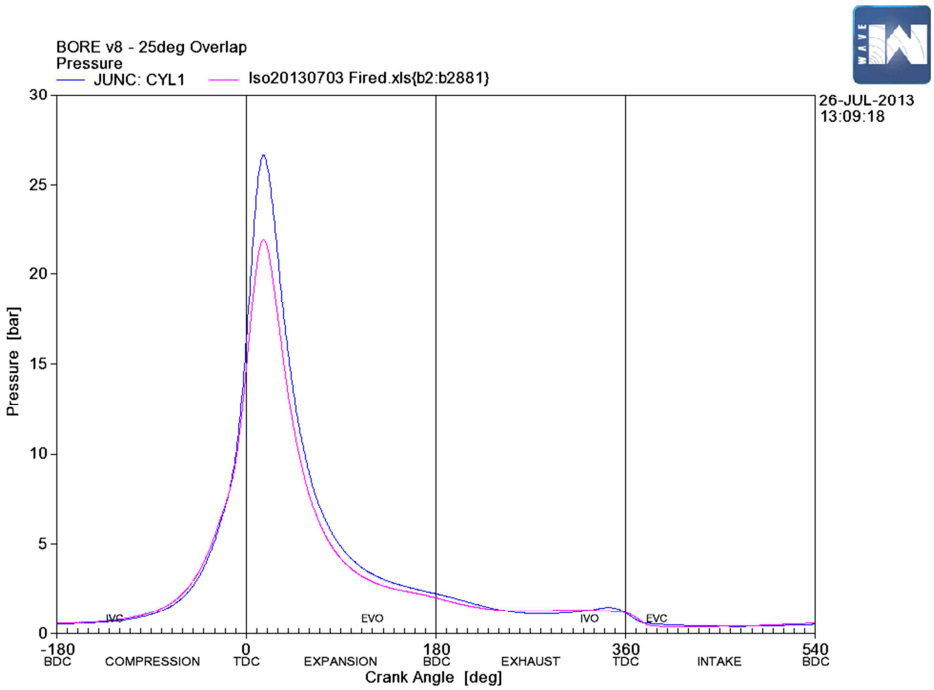

Figure 5.42 – WAVE's in-cylinder pressure trace superimposed with the experimental data. This model was run without any blowby modelling. The pink trace is real world data, the blue trace is computer simulated data.

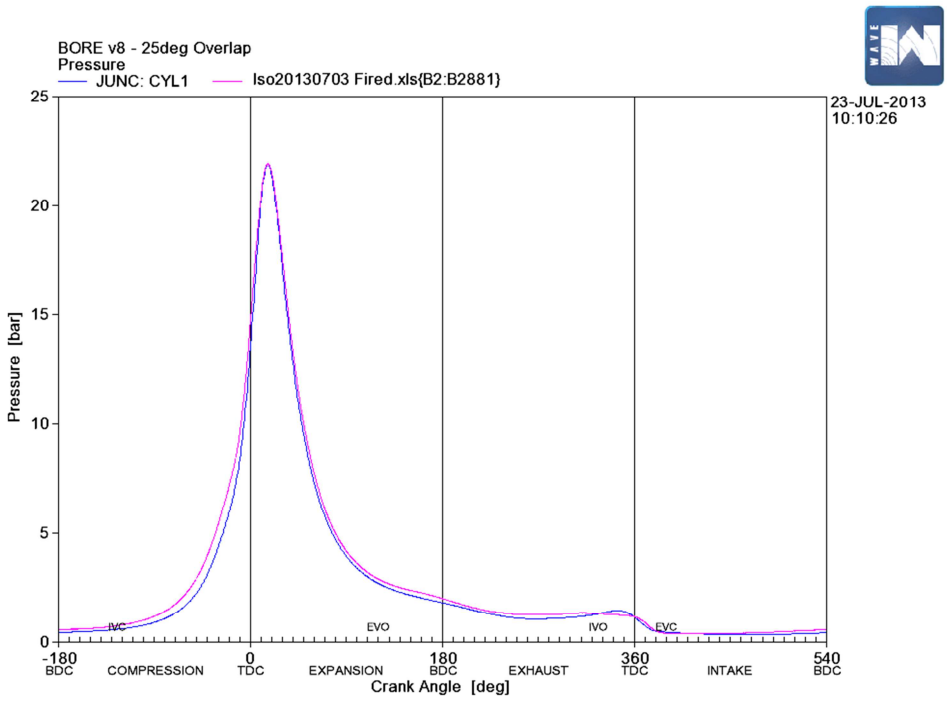

Figure 5.43 – WAVE's in-cylinder pressure trace superimposed with the experimental data. This model was run with an assumed 15% blowby. The pink trace is real world data, the blue trace is computer simulated data.

Chapter 6

Results and Analysis

6.1 Introduction

Presented in this chapter is an in-depth analysis of the thermodynamic and optical data obtained during this work. The main aim of the study was to improve fundamental understanding of the combustion characteristics of isooctane-alcohol blended fuels in terms of both mean and variable observations. Initially, comparisons were made between the 'baseline fuels' – iso-octane, gasoline, ethanol and an isooctane-ethanol fuel blend, E10. Preliminary experiments looked at the thermodynamic and optical data produced from the experimental engine. Cyclically-resolved flame images were generated and various processing methods allowed for quantification of the flame development. Data such as the mass fraction burned, in-cylinder pressure and the COV of IMEP could be extracted from the thermodynamic data; while the flame images were processed to supply the mean flame radius, apparent flame speed, laminar burning velocity, and the level and severity of any distortion of the flame. Engine-out emissions measurements were not considered due to the optical setup and impact of the glass on heat transfer. The general effects of such fuels on emissions were discussed previously in Chapter 2.

Presented in Table 6.1 is a list of some of the main properties of the four baseline fuels. Due to the OH bond at the end of the alcohol chain, the alcohol based fuels require a lower amount of inducted air to combust, thus possess a lower stoichiometric air/fuel ratio. The lower heating value is the amount of heat released from combusting a kilogram of each fuel and then returning those products to 150°C. Table 6.1 shows that ethanol is a little over sixty per cent of the value of iso-octane, meaning that to produce an output equivalent to that of iso-octane, ~30% higher mass of fuel is required. This effect is demonstrated by the increased injection durations.

	Iso-Octane	Ethanol	Gasoline	Butanol
Chemical Formula	C_8H_{18}	C_2H_5OH	$C_nH_{1.87n}$	C_4H_9OH
Density at 1 bar and 21°C (kg/l)	0.69	0.79	0.74	0.81
Lower Heating Value (MJ/kg)	44.3	26.8	44	32
Stoichiometric AFR	15.1	9	14.7	11.1
Latent Heat of Vaporisation (kJ/kg)	308	840	305	430
Reid Vapour Pressure (bar)	0.52	0.18	1.03	0.03
Injection Duration (ms)	13.55	18	13.35	13.99
Oxygen Content by Weight (%)	0	34.8	0	21.6
Volumetric Energy Content (MJ/l)	30.6	21.2	31.6	29.2
RON	100	107	97	98
MON	100	89	85	88

Table 6.1 Fuel properties of the four baseline fuels [Heywood, 1988; Cairns et al., 2009; Broustail et al., 2011; ORNL, 2011; Coryton, 2013]

Ethanol has a higher octane number than iso-octane (and gasoline), primarily associated with the higher latent heat leading to a charge cooling effect, with slightly faster burning also reported to aid knock prevention in some cases [Cairns et al., 2009]. Knocking combustion was considered to be beyond the scope of the current optical work, but such effects should be noted due to the synergy of such fuel with modern downsized engines possessing increased requirements for high octane ratings. The primary goal of the current work was to evaluate the differences in burning rate. Due to the combustion stability limits imposed by iso-octane, the lean limit was set to a lambda of 1.22 with the 'rich' fuelled combustion at a lambda of 0.78.

In this chapter the results of the experimental data will be analysed and discussed with an aim of understanding the fundamental influence of both high and low ethanol content on homogenous turbulent SI combustion when compared to traditional gasoline fuel. In the first instance a comparison will be made between the 'mean cycle' combustion for the four baseline fuels when running a) identical spark timings and then b) MBT timings. Both the thermodynamic and optical data have been used to understand the differences between the combustion characteristics of the four fuels at the varying spark timing and fuelling conditions. In addition a comparative study of ethanol and butanol iso-octane blends was undertaken (with the alcohol content equivalent on an oxygen mass weighting basis).

Also reported within this chapter is an investigation of the causes of cyclic variation, with focus on the impact of both the fuel type and the flow on combustion. In addition to the engine geometry listed in Table 3.1, all tests were undertaken using the fixed test conditions listed in Table 6.2 (unless otherwise specified later on). The inlet temperature setting was elevated slightly above atmospheric via the intake heater to avoid repeatability issues associated with changing daily atmospheric conditions (while still considered to allow study of combustion with typical port fuel injection fuel preparation effects incurred). Finally, a study will be presented into the effects of increased valve overlap between the intake and exhaust ports on iso-octane and ethanol fuels.

Parameter (unit)	Value
Engine Speed (RPM)	1500
Net IMEP (bar)	4
Relative AFR (λ)	1
Maximum COV of IMEP (%)	5
Inlet Pressure (bar)	0.66
Spark Timing (°bTDC)	24
Inlet Air Temperature (°C)	37
Exhaust Bridge Temperature (°C)	130
Engine Head Temperature (°C)	94

Table 6.2 – Engine Operating Parameters

6.2 Optical Fuels Comparison

6.2.1 Fixed versus MBT Spark Timing (λ=1)

During initial tests a comparison was made between fixed and MBT spark timing. The objective was to quantify any differences in burning from a fixed initiation crank angle, which arguably allows for easier extraction of fuel property effects on combustion, with the timing fixed to 24° bTDC as previously indicated in Table 6.2 However, for direct "real world" comparison the performance with the correct MBT setting for each fuel was also evaluated. A comparison of the MBT spark timings is provided in Table 6.3 below. The comparative pressure traces are set out in Figure 6.1 while the associated indicated load and combustion stability for these fixed spark and MBT cases are illustrated in Figure 6.2.

Fuel Type	Spark Timing (°bTDC)
Iso-Octane	29
Ethanol	24
Gasoline	24.7
E10	24.7

Table 6.3 MBT Spark Timings

Set out in Figure 6.3 are key timings extracted from the computed mass fraction burned profiles for each of the fixed spark timing cases. Overall the gasoline resulted in marginally faster burning than all other fuels. The slower

burning of iso-octane c.f. pump gasoline was in good agreement with previous observations elsewhere [Aleiferis et al., 2008; Cairns et al., 2010]. Interestingly, the E10 case was the worst performer, but the differences are small and the overall effect on mean pressure development was negligible when expressed in terms of IMEP and combustion stability. From these results it was generally concluded that fixed spark timing would be adequate in terms of engine calibration for maintaining both load and stability at this part-load site with the range of fuels studied. This observation is in good agreement with prior work in a modern multi-cylinder SI engine, where engine emissions effects were also studied [Cairns et al., 2009].

Shown in Figure 6.4 are details of the mean flame radii development for the fixed and MBT spark cases. Interestingly, clear differences in flame development were noted with the fixed spark timing, with apparent slowest flame growth of the E10 fuel in line with the above thermodynamic observations. When MBT timing was adopted the mean rates of flame development were very similar. Such differences in mean turbulent flame growth are noteworthy but can still be considered negligible in practical terms of attaining similar mean in-cylinder pressure development under the fixed speed and part load conditions examined. This flame radii data was obtained from the natural light flame imaged cycles, each of these imaged intervals was then layered to provide a series of contour plots for each fuel (Figure 6.5). While flame shape will be discussed in further detail later, Figure 6.5 allows for an objective comparison between the selected mean cycles for the different fuels, showing reasonable distortion from a smooth semi-spherical shape in all cases regardless of the fuel type.

6.2.2 Cyclic Variation Effects (Fixed Spark, λ=1)

Set out in Figure 6.6 is a comparison of the in-cylinder pressure data for the mean, fastest and slowest cycles for each fuel under fixed spark timing. Here the small differences observed above in the mean turbulent flame development become more pronounced, where the slower burning E10 and iso-octane cases presented wider bands of in-cylinder pressure development (in terms of the observed range of APMax rather than examining such deviation in the broader terms of COV of IMEP). The relatively narrow spread for the pure ethanol case

indicates differences in pressure development between high and low ethanol content fuels cannot simply be directly associated with differences in key physical properties between fuels such as latent heat (and any associated impact on charge preparation) or calorific value (which would have been most pronounced in the pure ethanol case). Indirect effects such as differences in charge homogeneity and/or thermodynamic state as well as differences in fuel chemistry and flame development may also be dominant.

Charge homogeneity effects were considered to be beyond the scope of the current work. In order to examine the influence of charge state, the reverse mode thermodynamic simulation was adopted for the iso-octane and pure ethanol mean cycle cases. By matching the measured and computed in-cylinder pressure data, the predictions of unburned gas temperature shown in Figure 6.7 were produced (together with a temperature profile for gasoline which has been included to show the close agreement with the iso-octane case). Subsequently these predictions, along with the measured in-cylinder pressure data for the mean cycles, could be used to predict the laminar burning velocity for each case via empirical correlations produced previously by Gülder [1982]. Some caution is required as these velocity correlations did not take into account any variation in exhaust gas residual quantity or quality. In addition the correlations extrapolate a relatively limited original experimental data set to engine-like pressures and temperatures. Nonetheless, when considering the predicted values shown in Figure 6.8 in a qualitative manner, it can be seen that faster burning would be expected in the pure ethanol case, despite the lower initial starting temperature in the chamber due to the thermodynamic properties and charge state incurred with this fuel.

Set out in Figure 6.9 are values of apparent turbulent flame speed for the iso-octane, ethanol and E10 cases derived directly from the flame images for each of the mean cycles selected. The apparent flame speed is equal to the sum of the turbulent entrainment velocity and the velocity at which the unburned gas is pushed away by compression due to piston motion and the expanding burned gas. The ethanol case exhibits the fastest rate of flame development from the onset,

with increasing turbulent flame speed becoming even more pronounced during the flame propagation event until the wall was approached.

Shown in Figure 6.10 are corresponding computations of shape factor for the mean cycle cases. The slower burning fuels were subjected to the turbulent spectrum for a longer period of time, which resulted in increased distortion of the mean flame shape but only as the larger scales of turbulence were encroached towards the end of the propagation event. The observation of increased bulk flame distortion leading to slower burning insinuates any benefits of a larger enflamed area due to such distortion were outweighed by the detrimental effects of flame stretch. This may be associated with a near-horizontal orientation of the intake port in this engine leading to high tumble rates and turbulence intensity, which must be quantified in future work. Nonetheless, the results help highlight the knock-on effect of faster initial laminar-like burning.

During transition toward a fully developed state the flame can only be wrinkled by scales of turbulence smaller than the flame itself; larger scales merely serve to convect and distort the flame rather than directly improving enflamed area [Gillespie et al., 2000]. If the initial flame develops more quickly (primarily due to faster chemistry) it follows that more of the turbulent spectrum will become available more quickly to aid flame wrinkling and improve the rate of unburned mass entrainment into the flame. Such physical effects have been shown to be brought about by the faster initial chemical reaction rates with high ethanol content fuels in SI engines, but become amplified as the turbulent spectrum is faster encroached. While the chemical differences are often cited, such physical interactions have been widely overlooked within recent literature relating to ethanol use in modern SI engines.

6.2.3 Air-to-Fuel Ratio Effects (MBT)

Studies by, for example, Metghalchi and Keck [1980 & 1982] demonstrated the variable nature of a flame's velocity and its dependency on the air-fuel ratio (AFR) for differing fuel compounds (see Figure 2.7 in Chapter 2). For most of the fuels studied, the maximum burning velocity was identified as being situated just

rich of stoichiometric (λ~0.9), with the richer mixture associated with dissociation during combustion. However, excess fuelling inherently leads to a significant reduction in thermal and combustion efficiencies, with a steep rise in unburned hydrocarbon and CO emissions. Conversely, the adoption of excess air operation in an SI engine may allow reduced pumping losses and higher thermal efficiency via raised ratio of specific heats but is usually limited by emissions of NOx. At increased dilution levels NOx may reduce due to falling peak temperatures, however under global homogeneous conditions the combustion will become unstable, misfires will occur more readily and drivability is impeded. Due to further dropping gas pressures and temperatures, this problem becomes even more pronounced at lower loads where the pumping losses are at the highest levels. Nonetheless, over-fuelling is often used at higher loads to reduce exhaust gas temperatures whereas significant interest still remains in lean burn combustion for improved thermal efficiency. Hence study of the effects of varied fuelling levels was considered warranted. In the currently reported work the lean limit was identified as being the point at which the COV of IMEP approached the acceptable limit of 5%. Rich operation was also investigated, with the fuelling lambda level set to mirror the numerical offset from stoichiometric for the lean cases. The corresponding MBT spark timings are listed in Table 6.4.

Fuel Type	Spark Timing (°bTDC)
Iso-Octane Lean (λ = 1.22)	35
Iso-Octane Stoichiometric	29
Iso-Octane Rich (λ = 0.88)	24
Ethanol Lean (λ = 1.22)	28.4
Ethanol Stoichiometric	24
Ethanol Rich (λ = 0.88)	23.7

Table 6.4 Spark Timings of the two fuel sets at each fuel mixture

Set out in Figure 6.11 are the values for load and combustion stability. While the load is taken directly from the optical cycle whose pressure development was closest to the mean, the COV is taken from an average of the 300 recorded cycles. Shown in Figure 6.12 are the key timings extracted from the computed mass

fraction burned profiles for each of the relative AFR cases. In agreement with Gülder's [1982] observations, the rich cases incurred the shortest combustion duration, predominately due to faster chemistry despite the lower ratio for specific heats. Under lean conditions the higher ratio of specific heats will lead to higher unburned gas temperatures upon ignition, however overall a much slower combustion event occurs.

Using the reverse-mode thermodynamic analysis tool, Ricardo WAVE (discussed in Chapter 5), a more in-depth study was undertaken into the conditions inside the chamber during combustion for each air-fuel ratio mixture. The resulting data is presented in Figures 6.13 to 6.16. Under rich conditions the higher charge mass (Figure 6.13) and slightly higher gamma value (Figure 6.14) when running ethanol resulted in a reduced difference in temperature between the two fuels during the compression stroke, with the ethanol temperature during compression nearer that of isooctane. As the mixture strength is reduced, the differences in mass and gamma between the two fuels are reduced. This leads to a relatively lower gas temperature for ethanol upon ignition (Figure 6.15). In spite of this lower gas temperature, ethanol exhibits a faster burning rate. This observation is in good agreement with the recent observations of Beeckman et al. [2009 & 2010], who undertook computations of laminar burning velocity for both fuels (Figure 6.17). However, the results appear to be contradictory to the experimental correlations produced by Gülder, set out in Figure 6.18. The Gülder correlations are more widely cited when considering ethanol effects [Heywood, 1988; Cairns et al. 2009 & 2010]. This helps to highlight the caution that is required when relying upon laminar burning correlations obtained under limited test conditions, which often exclude real engine phenomena (such as residual gas and flame stretch effects) and are extrapolated up to realistic engine temperatures and pressures.

The scatter in existing laminar burning velocity correlations is highlighted in Figure 6.19, which compares several such correlations for a single stoichiometric fuel compiled by Bradley and co-workers [2000]. This figure demonstrates four empirically obtained correlations for laminar burning velocity (a-d) and one numerically derived correlation (e). One of the correlations, (a) by Bradley et al.

[1998] took into account the effect of flame stretch and instability while other studies, such as Metghalchi and Keck [1982] calculated the laminar burning velocity using pressure data on the basis of idealised flame growth (without optical access windows being used), thus neglected or negated real world effects such as flame cellularity, which leads to higher apparent burning velocity and the tendency towards which is aided by elevated pressure. In the currently reported work, the observations of faster burning when stoichiometric are in good agreement with both Gülder and Beeckmann but under lean conditions the correlations of Gülder seem to deviate (Figure 6.20). It is important to note that such faster burning when stoichiometric and lean is in good agreement with other recent studies of ethanol in another optical single cylinder at similar speeds and loads [Cairns et al., 2009 & 2010].

Set out in Figure 6.21 is a comparison of the shape factor for the lean and rich cases respectively. Under lean operation the slower burning iso-octane case was exposed to the turbulent spectrum for a longer period of time, with associated increased bulk flame distortion apparent. Otherwise an increased degree of "saw-toothing" can generally be seen in the lean data, which was also potentially associated with increased distortion in the third dimension influencing the planar two-dimensional analysis of the distortion. Under rich conditions the bulk distortion observed was reduced for both fuels, with closer agreement in the apparent flame speed values at a given flame radius and similar combustion durations. Under rich conditions it might be argued that lack of oxygen availability plays a limiting role and the potential for improved availability of oxygen with the oxygenated fuel was relatively limited under the homogeneous rich conditions studied.

6.2.4 Effects of Carbon Levels in Alcohol (MBT, λ=1)

Shown in Figures 6.22 and 6.23 are the in-cylinder pressure data, load and combustion stability figures comparing the two alcohol fuels. As discussed in Chapter 2, several researchers have studied the use of high carbon alcohols, such as butanol, in place of low carbon alcohols, like ethanol, in an effort to reduce fuel consumption, lower hygroscopy and corrosion and control volatility. Butanol 16 (Bu16) was selected for direct comparison to the lower carbon fuel of E10 already

under investigation in this paper as Bu16's oxygen mass weighting is equivalent to E10. The values for in-cylinder pressure and load are near identical for MBT timing, in agreement with Cairns et al. [2009], while the increased stability level for Bu16 c.f. E10 is supported by Merola et al. [2013]. Set out in Figure 6.24 are the key timings extracted from the computed mass fraction burned data while in Figure 6.25 are the traces of the mean flame radii development for the two fuel types. These serve as further evidence that the two blends are ideal for comparison exhibiting equal combustion durations and near identical flame radii development. Differences in engine emissions were considered to be beyond the current scope of work, with such measurements arguably not reliable when using large glass windows. Nonetheless, in terms of turbulent flame propagation and arising combustion rate it can be concluded that E10 and Bu16 exhibit identical performance under the limited conditions examined.

Figure 6.26 sets out the values for flame speed of the two low-carbon fuels again detailing that they possess similar values for flame speed. In a search by this author very little information has been uncovered regarding the laminar burning velocity of butanol blends under typical engine conditions. Beeckmann, Kruse and Peters [2010] investigated laminar burning velocities of neat butanol, iso-octane and ethanol in a bomb, with a further study of Bu10 and E10 blends (blended with PRF96). In this work, it was found that, at stoichiometric running conditions, butanol possessed a slightly higher laminar burning velocity but that by blending it with 90% PRF96, Bu10 was 5cm/s slower than E10 for the same test conditions. While this would indicate that the two fuels are not identical in burn structure and initial propagation, care should be taken as these results are by no means definitive nor are they indicative of standard engine operating conditions.

6.3 Cyclic Variation Phenomena and its impact on Fuel Types

6.3.1 Saw-toothing Effects

Set out in Figure 6.27 are values of peak in-cylinder pressure for the iso-octane MBT case. The cycles marked in green (namely Cycles 19-25) were selected to highlight sporadic "saw-toothing" that was often observed from cycle to cycle. Observing Figure 6.28 this saw-toothing does not seem to correspond to any notable direct trend in the IMEP produced by the engine. However it can been seen in Figure 6.29 that higher values of PMax for the saw-toothing cycles were directly associated with faster combustion durations. When observing the flame radius development in Figure 6.30, the low PMax cycles correspond to a slower rate of flame development. It is interesting to see an amplification effect apparent, where the oscillation of slow to fast between Cycles 19 and 20 is followed by an even wider band of oscillation between slow and fast in Cycles 21 and 22 (with Cycle 22 experiencing the fastest rate of flame development of all cycles within the sequence albeit not favourable in the individual cycle IMEP). Observing the corresponding shape factor data in Figure 6.31 no clear trend associated with this phenomenon can be extracted (with little fluctuation between cases and therefore arguably too much noise in the data due to third dimensional flame distortion effects).

Set out in Figure 6.32 are values of exhaust-to-inlet pressure ratio for each of the cycles. In this data it would appear that a faster burning cycle is preceded by a cycle of higher pressure ratio. It may be postulated that cycles which burn slower possess a lower peak pressure value but a higher pressure during the expansion stroke. This is apparent in the data in Table 6.5, which shows the in-cylinder pressure 10° before Exhaust Valve Opening (EVO) for each cycle.

Cycle	19	20	21	22
In-Cylinder Pressure (bar) at EVO	3.27	3.17	3.5	3.17

Table 6.5 – In-cylinder pressure 10° CA before EVO.

During the blowdown phase of the exhaust this higher pressure may help to scavenge the cylinder of residuals. Towards the end of the exhaust stroke with a

higher backpressure it is then possible that increased backflow may occur from exhaust to inlet during the valve overlap phase. However, in this engine the overlap was limited to 25° crank angle, centred about TDC and it would seem that any backflow was minimal as indicated by the faster burn. The exception is Cycle 23, which exhibits a slower burn than expected for this trend to hold true. Interestingly the flame image processing from this cycle illustrated the lowest value of shape factor, which is also counterintuitive based upon the prior argument when discussing fuel effects. However it is important to note that these are individual cycles that may not represent mean observations in the engine (with such mean observations used earlier to identify the fuel effects). In this cycle it may be that other differences exist e.g. adverse flame stretch effects were observed out of plane in the third dimension. Alternatively differences in charge homogeneity and/or in-cylinder heat transfer or blow-by may have occurred that cannot be quantified here. For example, a slower burning cycle with higher pressure and temperature during expansion and exhaust may have increased the wall temperatures during those phases, which may have then raised gas temperatures in the next cycle (where a higher temperature would aid the burning velocity).

In order to clarify these observations further, Cycles 19-25 were simulated using Ricardo WAVE with the aim of quantifying the effects of the fluctuating burning durations on the subsequent cycle's mass. The data extracted from WAVE not only focussed on the physical amount of mass in the cylinder during combustion but the flow of mass in and out of the system which would indicate the scavenging efficiency and backflow levels in the system. Set out in Figure 6.33 is the amount of mass in the cylinder at Inlet Valve Closing (IVC) for Cycles 19-22, with corresponding values of PMax and combustion duration also shown again for clarity – while the mass in-cylinder at IVO is tabulated in Table 6.6. Observing the data it would generally appear that the slower burning cycles did indeed incur a slightly lower value of residual mass upon IVO and that the higher pressure during blowdown aided scavenging. In terms of heat transfer effects, the notion that such higher pressures and temperatures resulted in higher wall temperatures and hence gas temperatures on the next cycle could not be extracted readily via WAVE as the

Woschni heat transfer correlation used is based upon the assumption of constant wall temperature from cycle to cycle albeit increasing linearly with piston height.

Cycle	Mass of Residuals at IVO	
	Mass Fraction (%)	Mass (g)
19	99.95	0.0599
20	99.95	0.0629
21	99.95	0.0589
22	99.95	0.0629

Table 6.6 – Mass fraction and mass of residuals in the cylinder at IVO.

Set out in Figures 6.34 and 6.35 are the computed values of total mass in the cylinder around EVO and IVC respectively. When these figures are studied in conjunction with the data in Tables 6.6 and 6.7 the amount of gasses scavenged from the cylinder becomes clear. Between EVO and IVO both Cycle 20 and Cycle 22 expel 81.6% of the burned charge from the chamber while the lower peak pressure, slower cycles (19 and 21) expel 82.6% of the charge. This is in agreement with the notion posited above that the slower cycles possessed a higher blowdown pressure.

Despite Cycle 23 having been a slower cycle, the scavenging was relatively poor and the high residual level causes high mass levels for Cycle 24. This inhibits combustion and the saw-toothing arguably then gives way to more conventional, low variation combustion.

When studying the effect of ethanol fuel on the cyclical variation it is apparent that ethanol is less susceptible to fluctuations than iso-octane is. Set out in Figure 6.36 are the values of peak in-cylinder pressure for the ethanol MBT cycles with the saw-tooth cycles highlighted in green. When compared to Figure 6.27 it can be seen that there are less than half as many “saw-toothing” cycles for ethanol than iso-octane across the 50 images cycles analysed here. When ethanol does exhibit saw-toothing combustion the combustion duration has a direct impact on the PMax value of the subsequent cycle in a similar manner to iso-octane (Figure 6.37). However, there is no correlation between burning duration and the in-cylinder mass of the subsequent cycle. Further analysis shows that the higher mass

in the chamber (Figures 6.38 and 6.39) doesn't influence combustion as greatly as it does for the iso-octane cycles – this may be indicative of the notion that ethanol is more resistant to variation in levels of residuals than baseline fuels like iso-octane and gasoline. The phenomena identified here for both iso-octane and ethanol was noted at a few other sites during the set of recorded data (Figures 6.27 and 6.36). The other saw-toothing events were located (Cycles 3-9 for iso-octane and Cycles 34-38 for ethanol) and while they may not exhibit clean, one-cycle transitions from high to low PMax they were found to be in good agreement with the observations set out above.

Cycle	19	20	21	22
Mass Fraction of Residuals (%)	11.52	10.77	11.64	11.02
Mass of Residuals (g)	0.0395	0.0369	0.0398	0.0378
Mass Fraction of Air (%)	82.85	83.55	82.76	83.31
Mass of Air (g)	0.2842	0.2864	0.2831	0.2854
Mass Fraction of Fuel (%)	5.63	5.68	5.63	5.67
Mass of Fuel (g)	0.0194	0.0195	0.0193	0.0194
Inlet Pressure (bar)	0.6068	0.0678	0.6066	0.6077
In-Cylinder Pressure (bar)	0.7802	0.7567	0.7719	0.7562
Exhaust Pressure (bar)	0.9368	0.934	0.9370	0.9328

Table 6.7 – Mass of inducted charge constituents and pressures of the inlet, exhaust and in-cylinder at IVC.

6.3.2 Creep Effects

In addition to "saw-toothing" cyclic variation events, some data shows a tendency towards a "creep" in PMax, where the values may steadily increase for a few cycles before a decline in PMax in line with the saw-toothing events. An example series is highlighted in red in Figure 6.27, from Cycles 10 to 14. The creep at first appears contradictory to the observations made above but can perhaps be explained in terms of flame distortion effects. From Cycle 10 to 12 PMax steadily increases, despite an apparent increase in combustion duration and a drop in IMEP for Cycle 11, as apparent in Figures 6.40 and 6.41. In this middle cycle increased large scale distortion of the flame is noted, which leads to a slower combustion

event (in agreement with prior noted effects). The early flame propagation at first appears aided by the higher shape factor (Figure 6.42), with faster 0-10% mass fraction burned, earlier 50% MFB timing and higher PMax. However as the flame propagates further across the bore, the later mass burning is prolonged. This may have been associated with axial swirl effects in the 3-valve setup, with the higher velocities leading to detrimental stretch effects later on.

As with the saw-tooth cycles, further computational analysis was completed for Cycles 10-14 using Ricardo WAVE. Observing Figure 6.43, the levels of in-cylinder mass indicate a similar fluctuating pattern to that seen when studying saw-toothing combustion. The difference however is that the slow burning cycles do not create a subsequent fast cycle with low residual mass levels and higher PMax and vice versa. With the “creep” cycles analysed here the slowest cycle was Cycle 11 but this directly precedes the cycle with the highest mass content in the chamber (Figure 6.43). While Cycle 11 has the slowest overall combustion duration this is due entirely to a dramatic slowing of the latter stage of combustion, most likely due to unseen axial swirl effects touched upon above. Hence it may be argued that while breathing influences the residuals which may at least partially control "saw-toothing" type effects, the variation in the in-cylinder flow may override such occurences and dominate. As shown in Figure 6.44 the steadily increasing residual levels at IVO is overriden by the flame distortion. In the case of ethanol less saw-toothing events were observed which may indicate less sensitivity to variation in residuals due to cycle-by-cycle changes in breathing at the low valve overlap conditions studied.

These creeping cycle phenomena were also explored for the entire combustion set to ensure that the findings discussed above were true at all sites that exhibit the creeping PMax values. These were identified as Cycles 26-28 for iso-octane and 10-12 for ethanol. As with the sawtoothing cycles, these too offer good agreement with the observations detailed in the above section.

6.4 Valve Overlap Duration Sweep

As introduced in Chapter 2.4, the use of EGR presents one viable method of reducing pumping, improving fuel economy and reducing emissions in gasoline engines. This can be achieved either with external rerouting of exhaust gases or via phasing of either the intake or exhaust cams (or both) to create an overlap period in which the (largely inert) exhaust gases are encouraged to backflow into the intake manifold, reducing the available volume for fresh charge and enforcing a wider open throttle. It is this method of EGR that will be employed in this study due to the ease with which the system can be implemented into the existing setup with less chance of loss of products such as water due to the natural cooling of the extracted charge. In addition the use of such EGR reduces peak gas temperatures and heat transfer rates and may allow more optimum expansion ratios (e.g. so called over-expansion events achieved via the valve timings).

The remainder of this chapter seeks to investigate how ethanol, iso-octane and E10 perform in this single-cylinder engine with differing durations of valve overlap. For this work the inlet cam timing was maintained at a MOP of 110° aTDC while the exhaust cam MOP was advanced and retarded to provide three overlap durations: 20°, 25° (the baseline) and 30° crank angle. Set out in Figure 6.45 are the valve lift profiles studied. For all fuel and overlap settings, each test site utilised spark timings and fuel durations mapped for MBT and stoichiometry respectively with the spark timings set out in Table 6.8. Considering the iso-octane case as a baseline, it was at first surprising to see the spark timing retard with increased overlap as an increased amount of residual might be expected (albeit only a small increase in overlap has been studied). This has been associated with the retarded exhaust valve opening point and associated influence on the blowdown phase of the exhaust, as described in more detail below.

Overlap Duration (deg CA)	Iso-Octane	Ethanol	E10
20°	30	24.8	26.5
25°	28.5	25.5	29
30°	25.7	24.3	25.5

Table 6.8 – MBT spark timings for each fuel and overlap setting.

Shown in Figure 6.46 are values of the 0-10% MFB for each fuel and overlap setting. Set out in Figure 6.47 are corresponding values of the 10-90% MFB (combustion duration). In general it can be seen that in all cases the combustion becomes quicker with the highest valve overlap setting, with the ethanol exhibiting marginally faster burning as would be expected based upon prior observations. Shown in Figures 6.48 and 6.49 are the corresponding values of IMEP and COV of IMEP. The iso-octane case shows improving combustion stability with the faster burning and increased overlap. However the ethanol fuels both exhibit an initial drop in stability as the overlap is first increased. In part this seems likely to be attributed with the accuracy of the load setting. For the intermediate overlap case (25 degrees) it can be seen that all three fuels were slight low in terms of IMEP. As a result the in-cylinder gas temperatures and pressures will have been marginally lower which may have negatively influenced the combustion speed and stability. However at the higher overlap setting it can be seen improved accuracy in load setting was achieved, where the stability has a lower value than the baseline valve setting cases.

In order to better understand why the EGR levels apparently reduced with increasing valve overlap Ricardo WAVE was once more adopted. The corresponding computed estimates of EGR are illustrated in Table 6.9 below (shown for the iso-octane case). Also shown in the table are the values of in-cylinder pressure 10 degrees before EVO and the EGR level immediately prior to IVO. The differences are small but it can be seen that the residual does indeed decrease with increased overlap.

Overlap Duration (deg CA)	Maximum Cycle Residual Gas Fraction (%)	Residual Gas Fraction at IVO (%)	In-cylinder Pressure at 10° bEVO (bar)
20°	12.9	99.96	3.08
25°	11.25	99.95	3.28
30°	9.92	99.96	2.76

Table 6.9 Levels of residual gas relative to valve overlap duration.

As was observed in the previous section, the blowdown phase seems to dominate the residual levels achieved with such moderate overlap duration. In the case of reduced overlap (with the exhaust event more advanced), the higher pressure at EVO again seems to aid the initial scavenging of the engine. This is so far counter-intuitive with a higher residual setting with lower overlap. However the observation of lower pressure upon EVO leading to reduced residual scavenging during blowdown is in good agreement with prior observations of cyclic variation effects.

Further analysis using WAVE shows the pressure difference across the valves both during the overlap period (Figure 6.50) and from the start of the valve events to the end (Figure 6.51). Marked on the two figures are the individual valve events for each overlap duration setting. The greater level of backflow with the lowest overlap setting caused by the increased pressure difference between the valves during the valve overlap event. As the exhaust valve was retarded in an attempt to increase residual content, the magnitude of the pressure difference from exhaust to inlet was actually reduced, which reduced the residual gas content with the highest valve overlap setting studied. The high pressure difference between the valves can also be seen on the in-cylinder pressure traces (Figure 6.52) as the 'bump' about TDC reduces in size as the overlap increases. It was put forward in Chapter 5.2 during the engine characterisation phase of the project that this was caused by the deactivated exhaust valve. Such effects help to highlight the non-linear variation in EGR that may occur during valve phasing events. In reality it seems likely that if the exhaust valve had been retarded much further than the residual would begin to increase, especially given the sucking action associated with

the dropping piston during high retarded high valve overlap events (Cairns, Blaxill and Irlam, 2006). In the current work the study of increased overlap was somewhat limited by the high potential for valve clash with the side mounted valves. In the future it is strongly recommended that external EGR be adopted to further study high EGR rate effects.

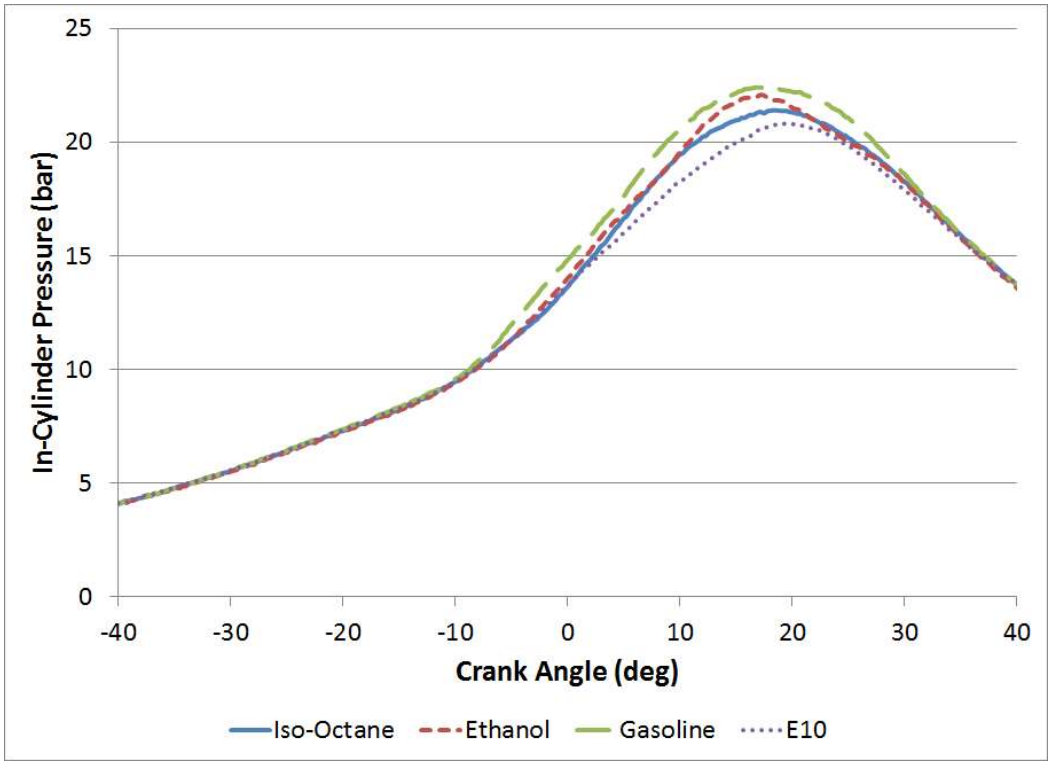

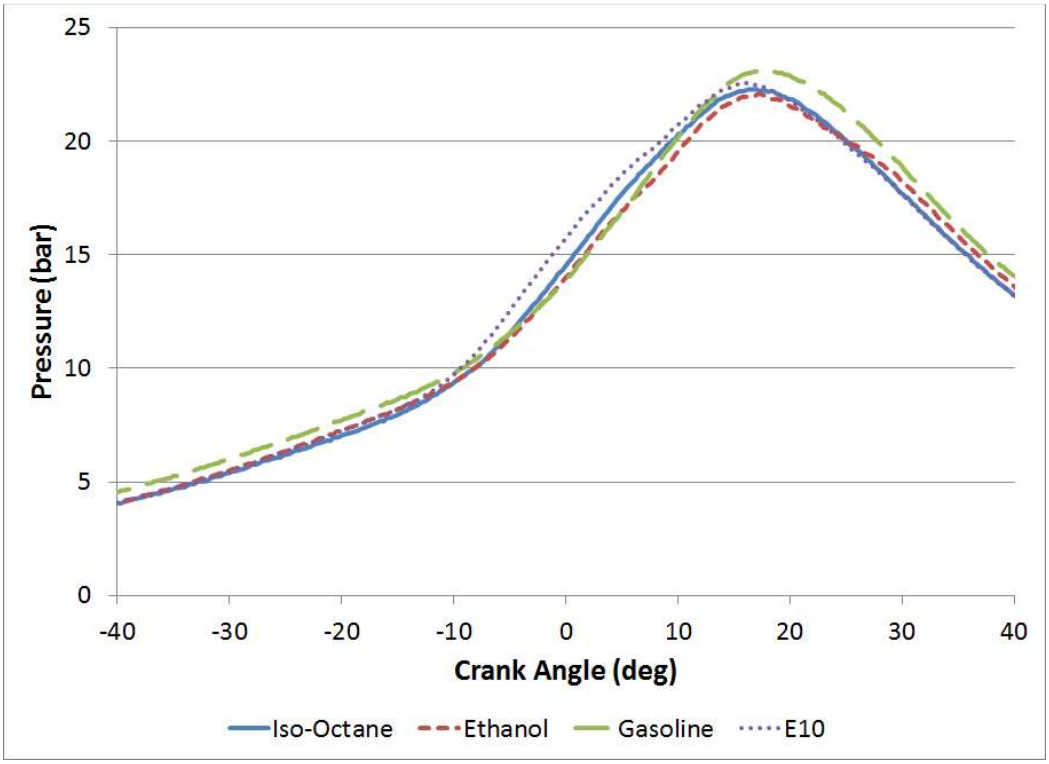

Figure 6.1 – In-Cylinder Pressure Traces for the cycle closest to the optical mean for each fuel series under fixed spark conditions and MBT conditions (top and bottom respectively).

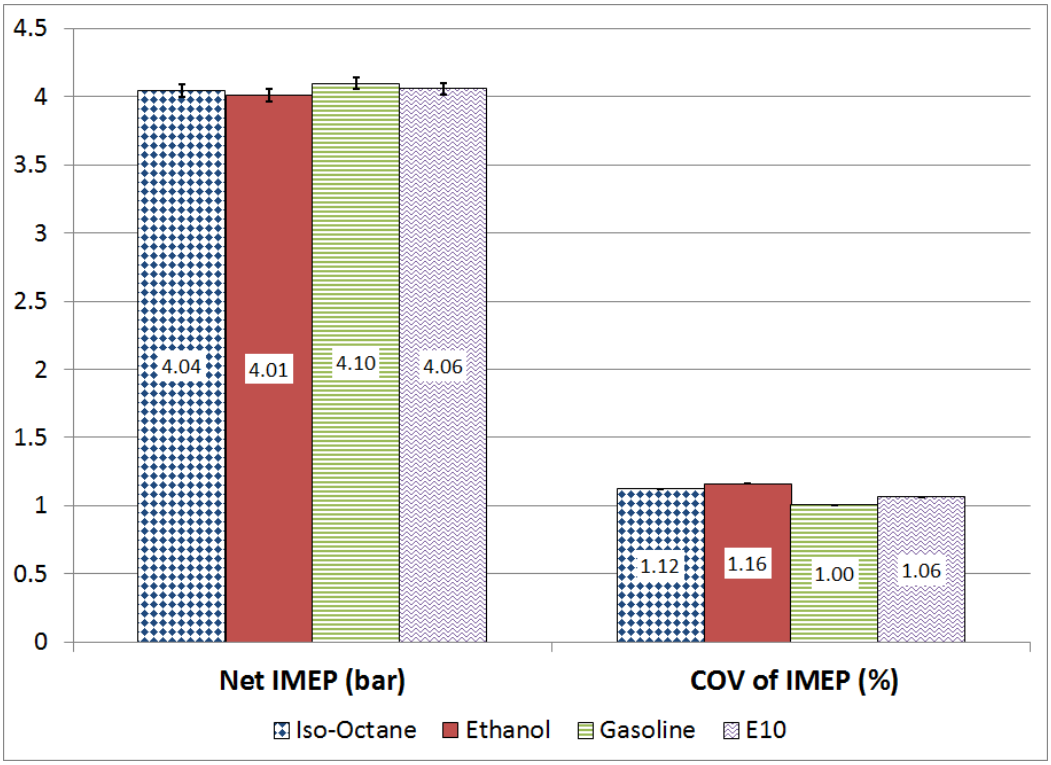

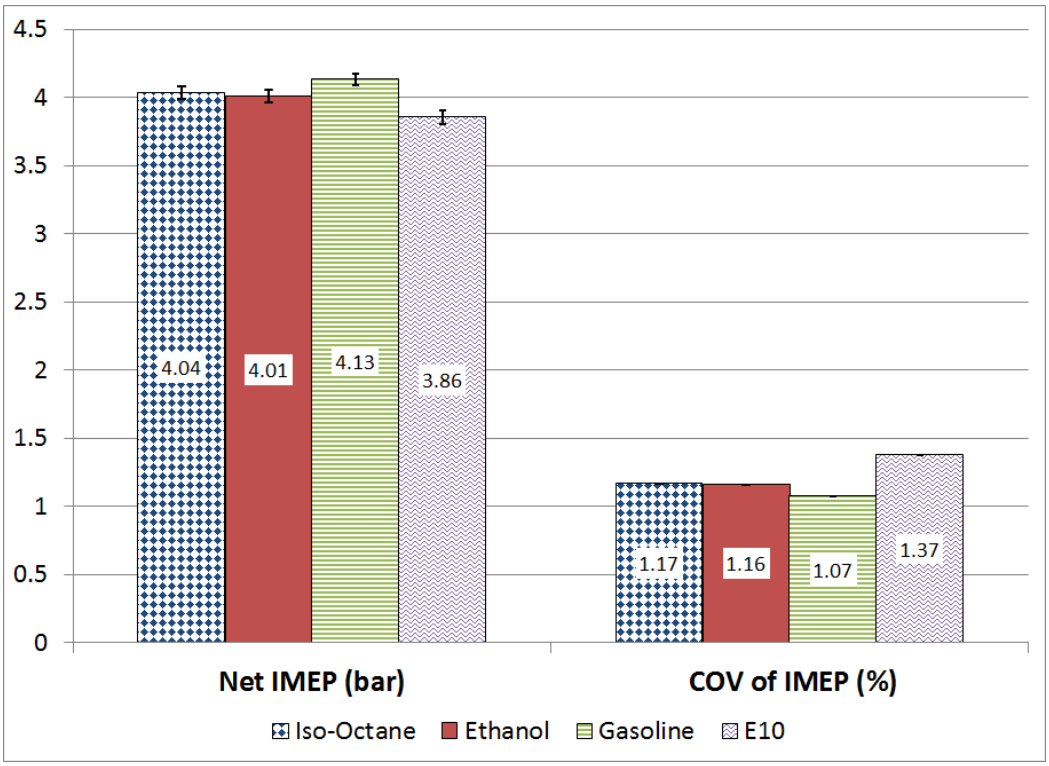

Figure 6.2 – Net IMEP and combustion stability figures for the cycle closest to the optical mean for each fuel series under fixed and MBT spark conditions (top and bottom respectively).

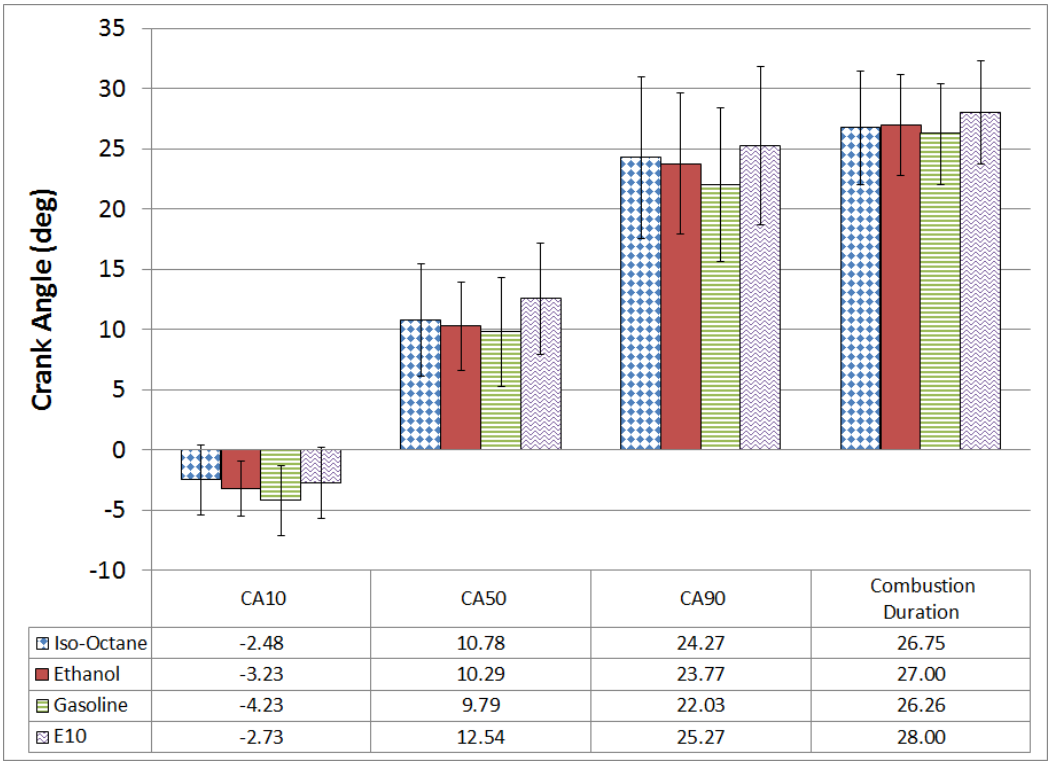

	CA10	CA50	CA90	Combustion Duration
Iso-Octane	-2.48	10.78	24.27	26.75
Ethanol	-3.23	10.29	23.77	27.00
Gasoline	-4.23	9.79	22.03	26.26
E10	-2.73	12.54	25.27	28.00

Figure 6.3 – Key mass fraction burned timings for all fuels under fixed spark conditions.

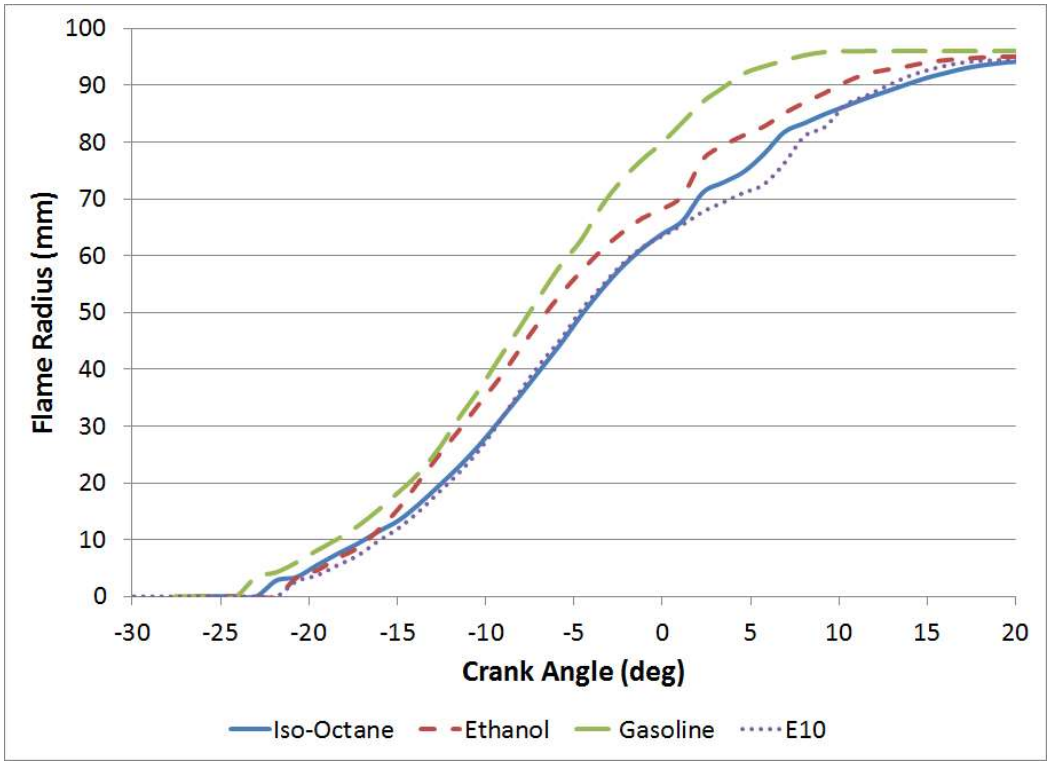

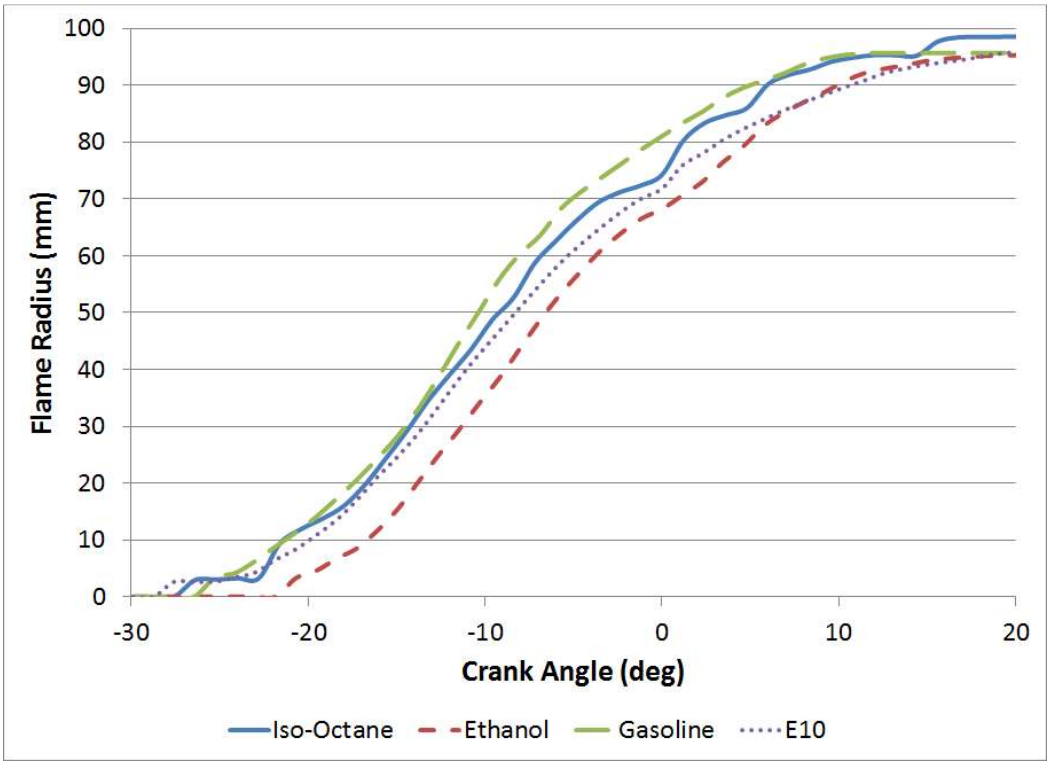

Figure 6.4 – Mean flame radius development for the natural light flame imaged cycles at both fixed and MBT spark conditions (top and bottom respectively).

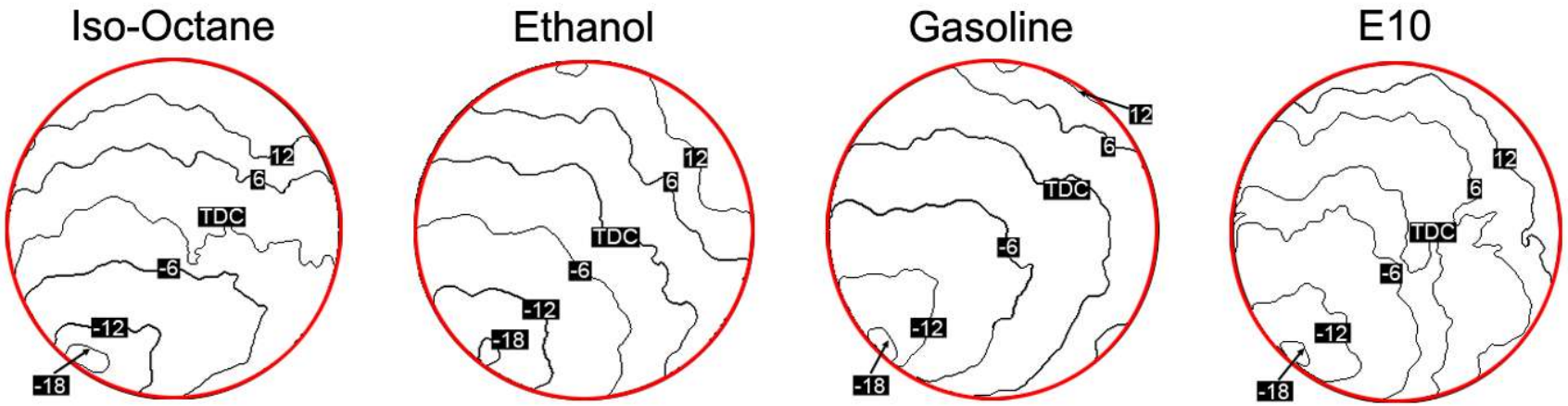

Figure 6.5 – Developing flame contours for each of the mean optical cycles of each fuel run under fixed spark conditions. The first contour shown is at 18°bTDC/0.6ms after ignition; subsequent frames are a further 6°CA/0.6ms.

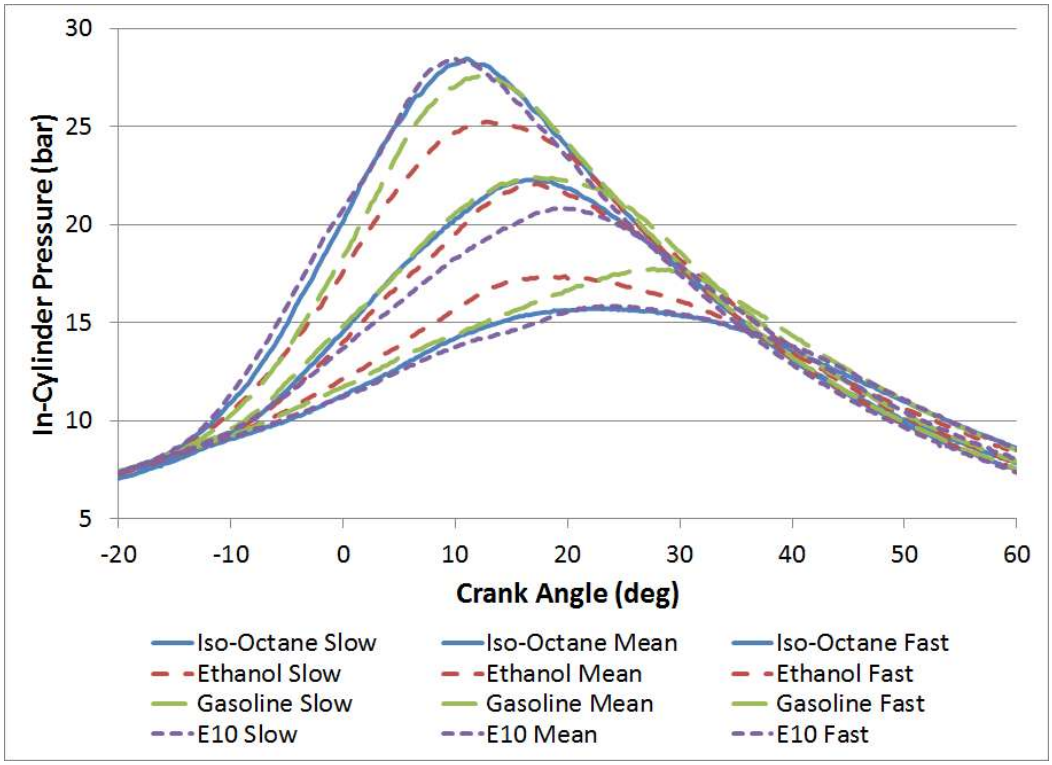

Figure 6.6 – Experimental in-cylinder pressure data for the mean optical cycles and relevant fastest and slowest cycles.

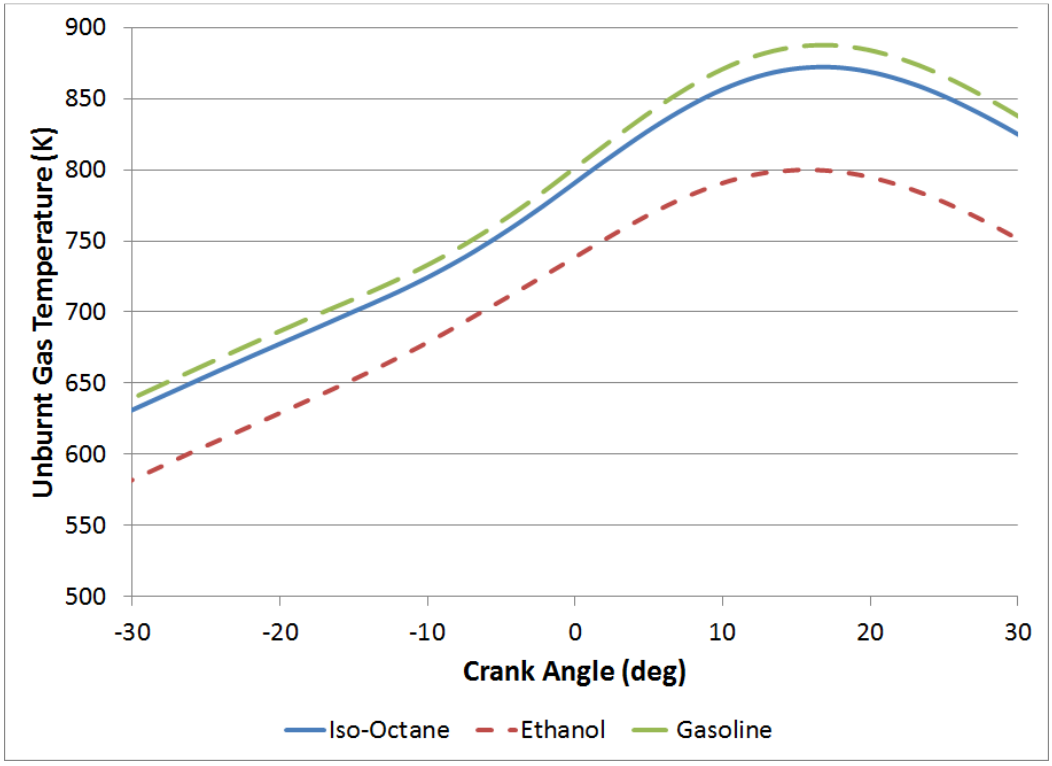

Figure 6.7 – Computed values of unburnt gas temperatures for the three base fuels obtained from the Ricardo WAVE simulation model.

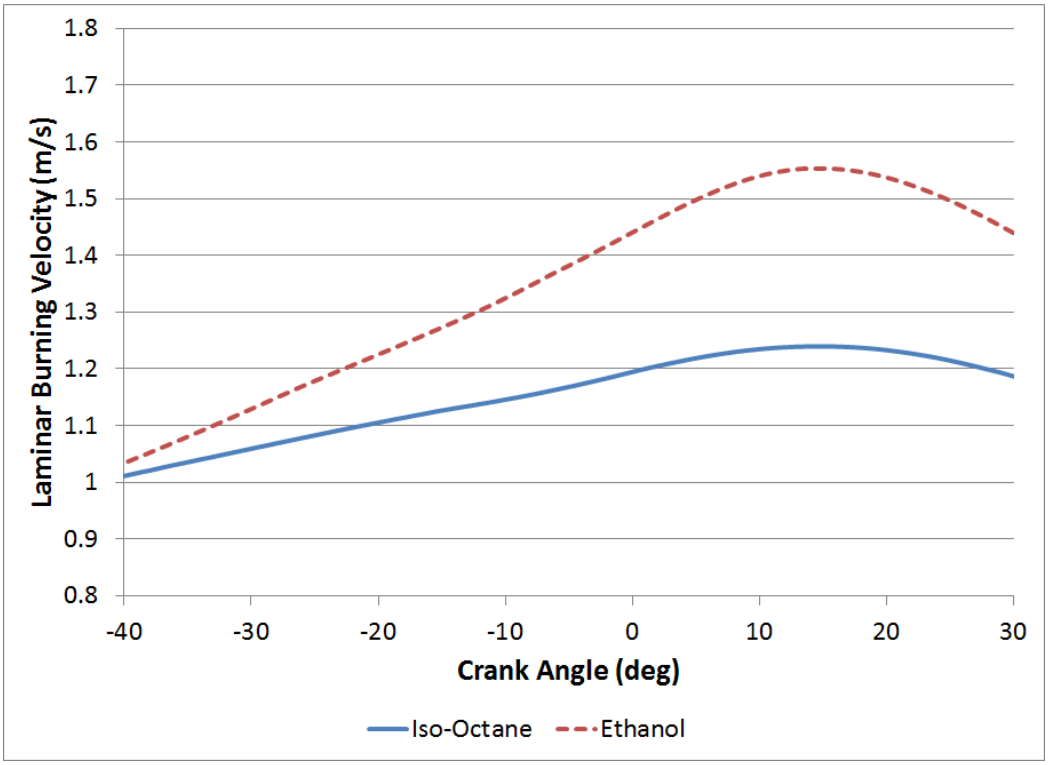

Figure 6.8 – Computed values of laminar burning velocity for the three base fuels obtained from the Ricardo WAVE simulation model.

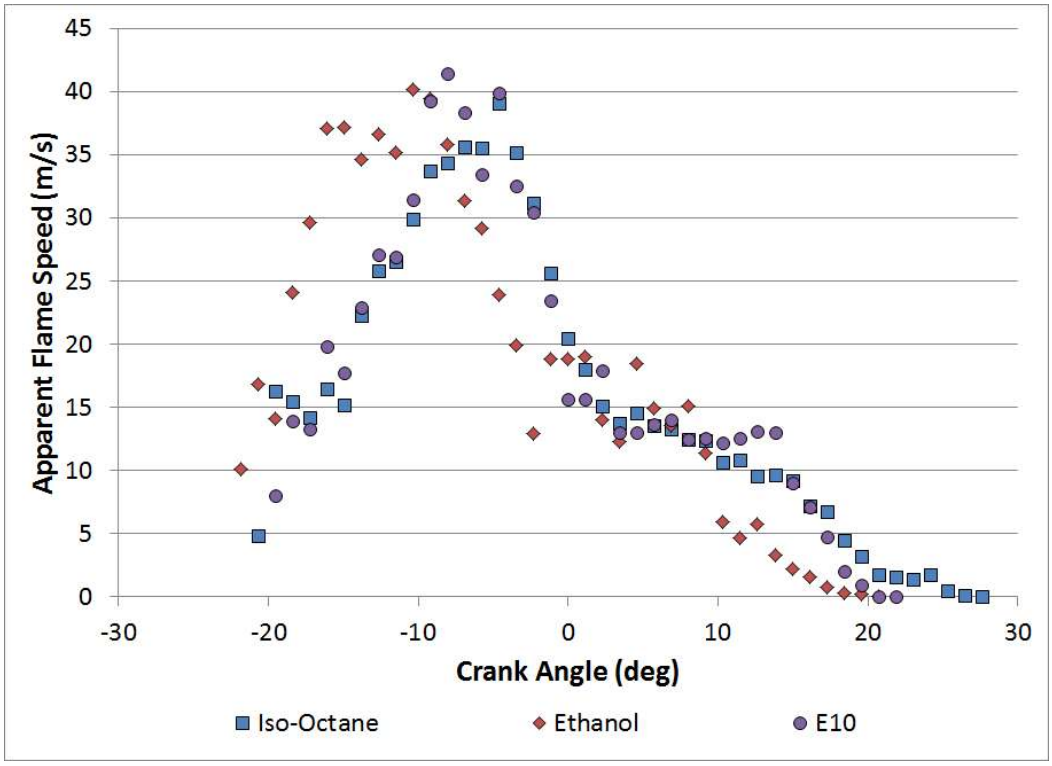

Figure 6.9 – Calculated values of flame speed for the three base fuels taken from the natural light flame imaged cycles at fixed spark conditions.

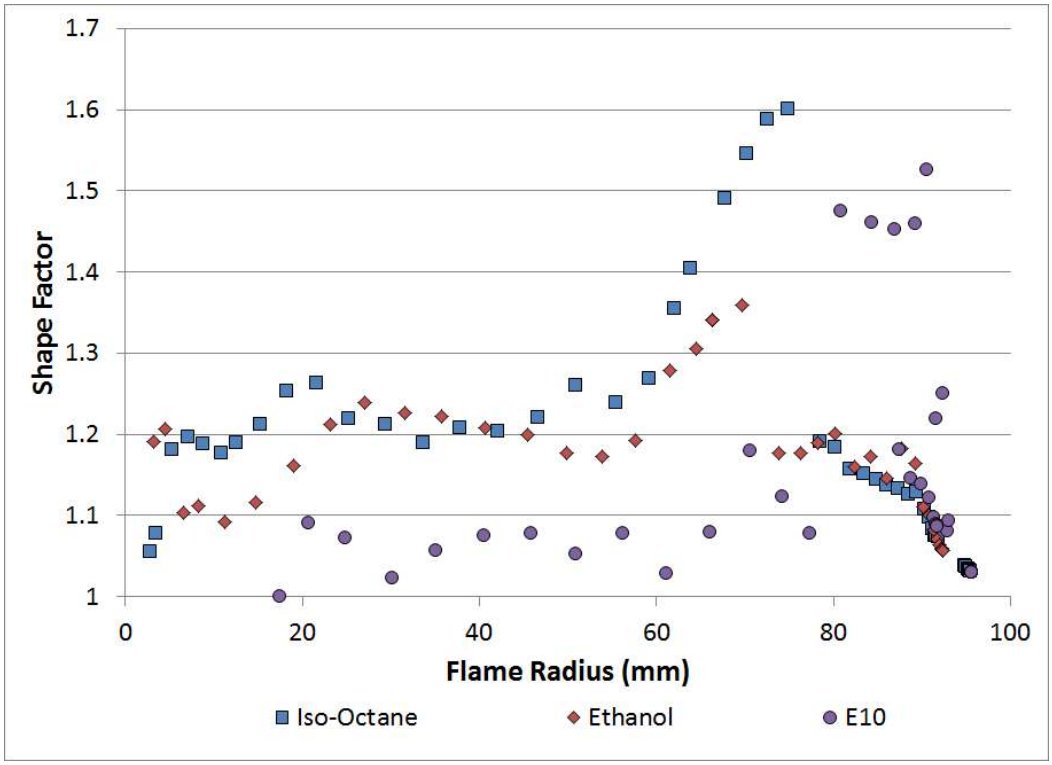

Figure 6.10 – Calculated values of shape factor for the three base fuels against the flame radius taken from the natural light flame imaged cycles at fixed spark conditions.

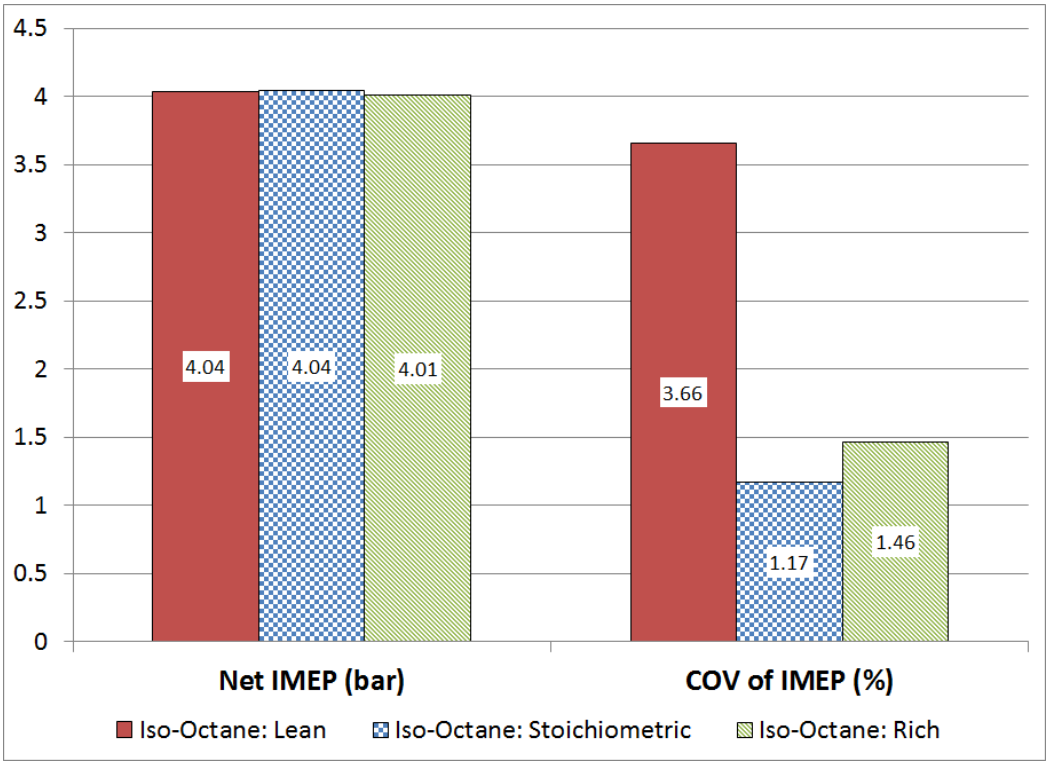

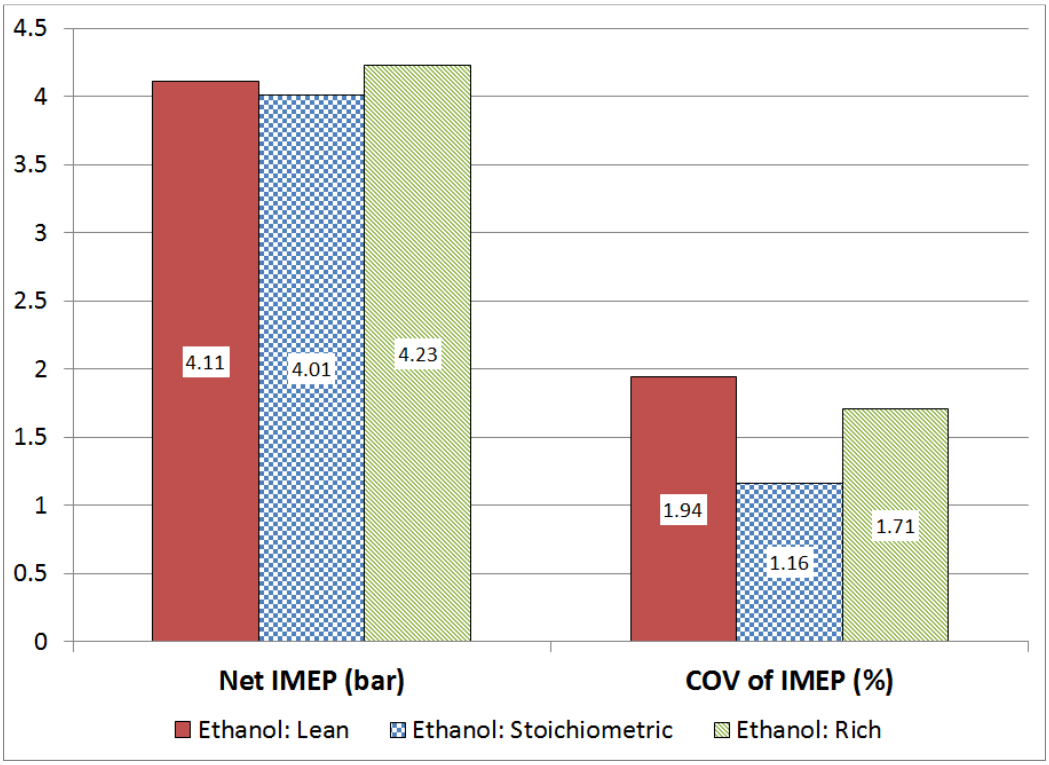

Figure 6.11 - Net IMEP and combustion stability figures of the mean optical cycles and relevant lean and rich cycles for each fuel. From top to bottom: Iso-Octane and Ethanol.

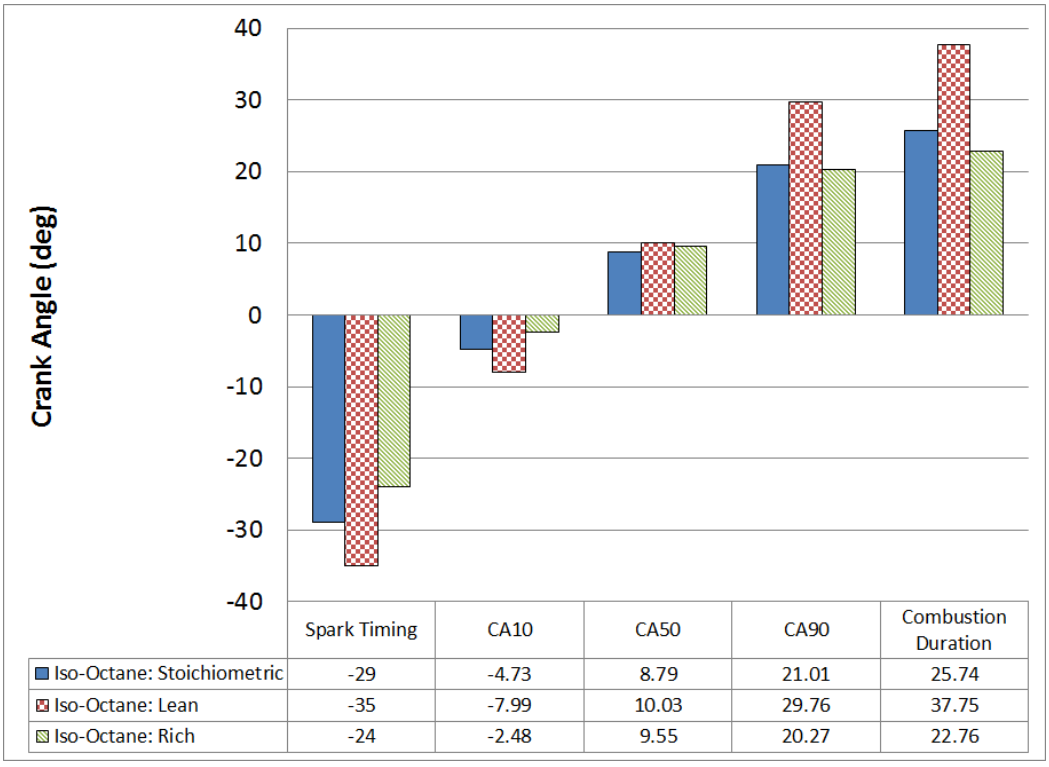

	Spark Timing	CA10	CA50	CA90	Combustion Duration
Iso-Octane: Stoichiometric	-29	-4.73	8.79	21.01	25.74
Iso-Octane: Lean	-35	-7.99	10.03	29.76	37.75
Iso-Octane: Rich	-24	-2.48	9.55	20.27	22.76

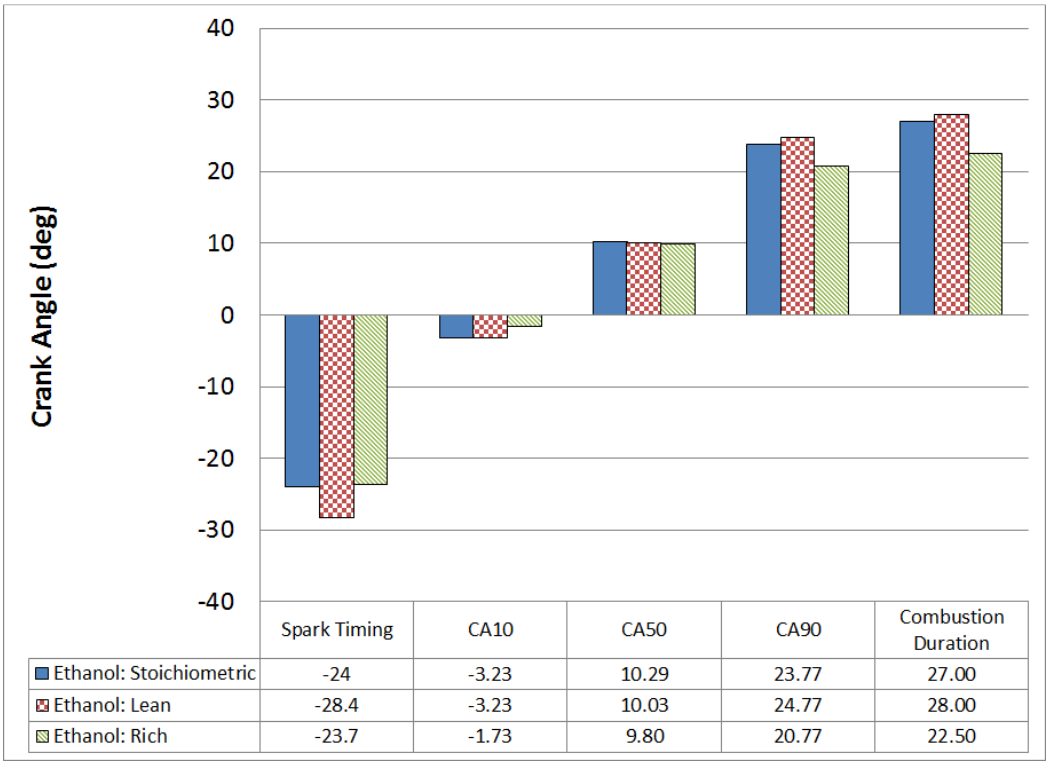

	Spark Timing	CA10	CA50	CA90	Combustion Duration
Ethanol: Stoichiometric	-24	-3.23	10.29	23.77	27.00
Ethanol: Lean	-28.4	-3.23	10.03	24.77	28.00
Ethanol: Rich	-23.7	-1.73	9.80	20.77	22.50

Figure 6.12 - Various mass burned intervals for the mean optical cycles and relevant lean and rich cycles for each fuel. From top to bottom: Iso-Octane and Ethanol.

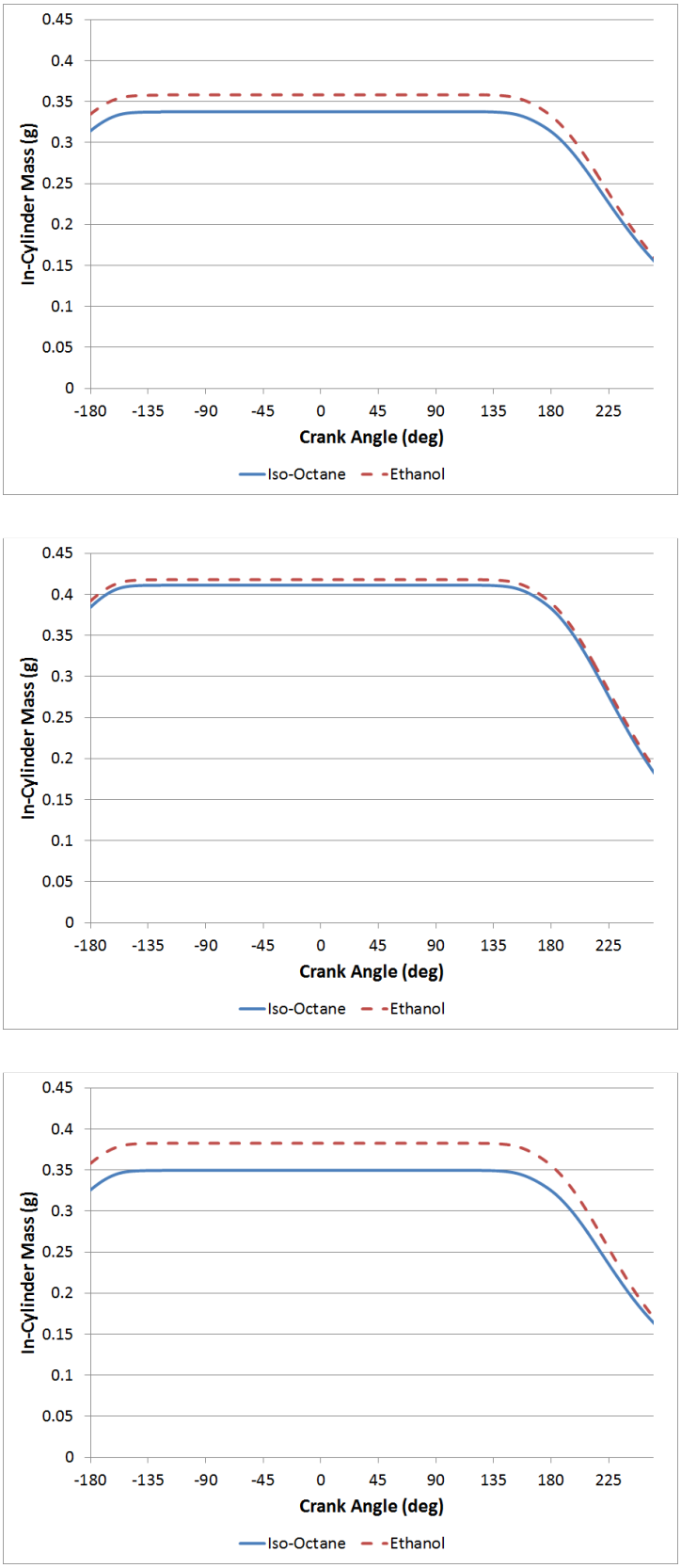

Figure 6.13 – Computed values for in-cylinder mass during combustion obtained from the Ricardo WAVE simulation model for each fuel. From top to bottom: Stoichiometric, Lean & Rich.

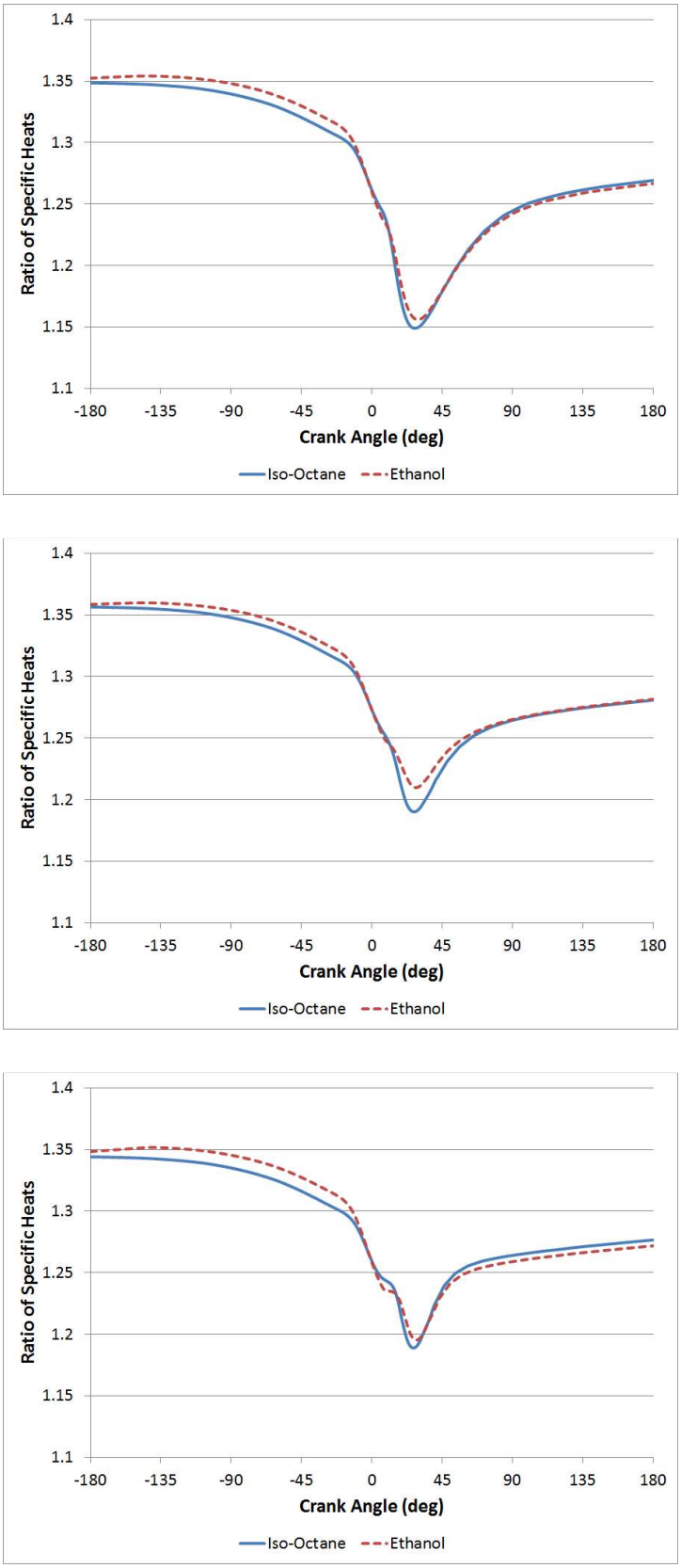

Figure 6.14 – Computed values for the ratio of specific heats during combustion obtained from the Ricardo WAVE simulation model for each fuel. From top to bottom: Stoichiometric, Lean and Rich.

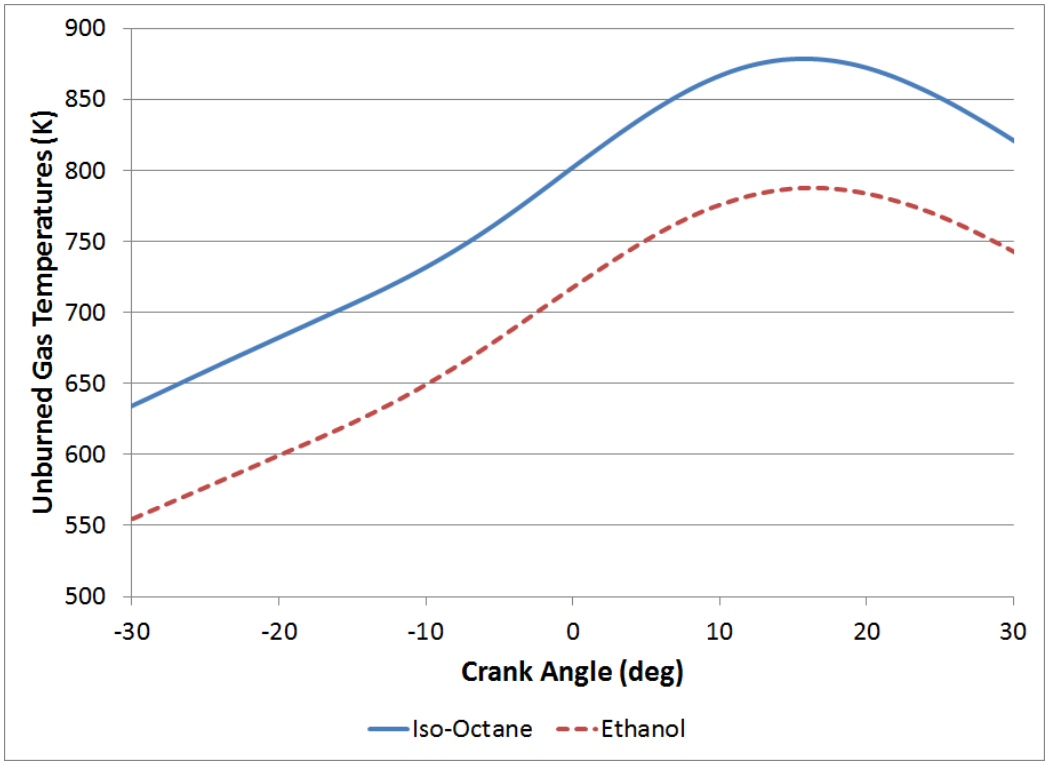

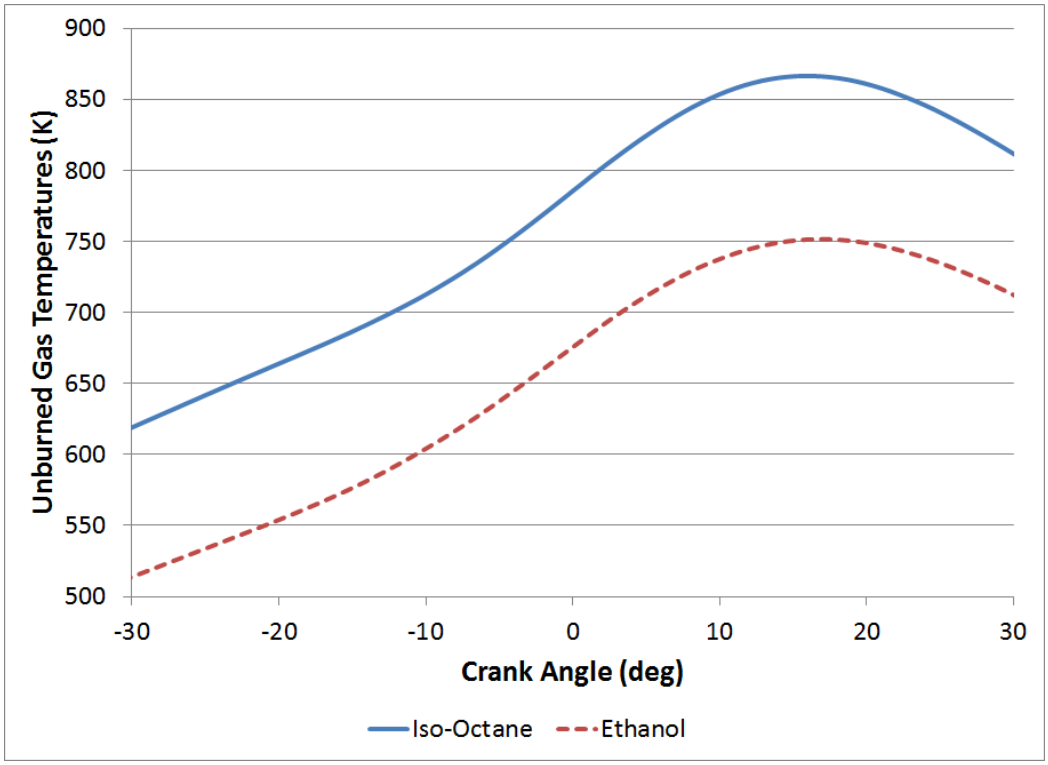

Figure 6.15 - Computed values for unburned gas temperature during combustion obtained from the Ricardo WAVE simulation model for each fuel. From top to bottom: Lean and Rich.

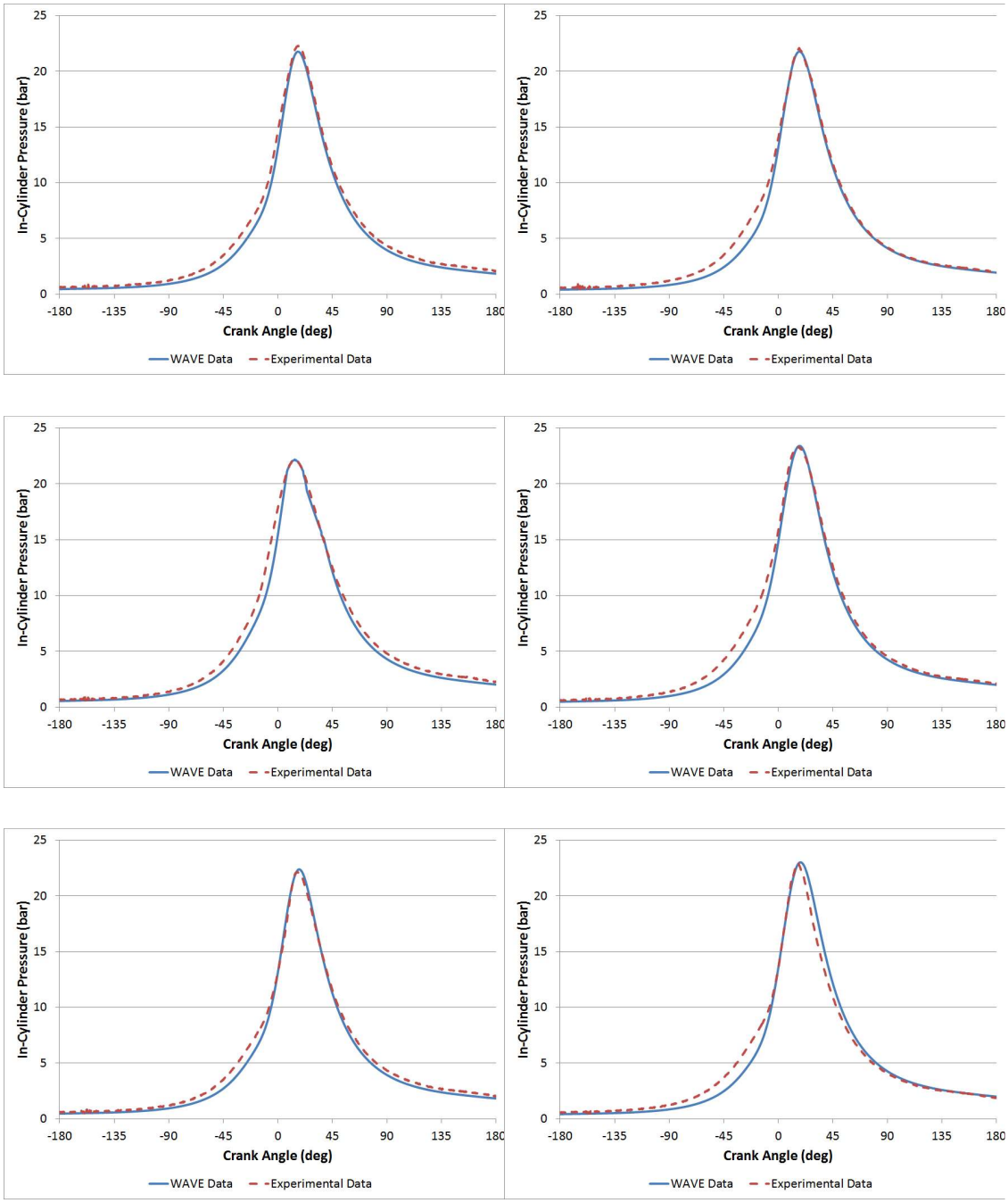

Figure 6.16 – Computed values for in-cylinder pressure obtained from the Ricardo WAVE simulation model compared to experimental data for each fuel. On the left: Iso-Octane and on the right: Ethanol; from top to bottom: Stoichiometric, Lean and Rich.

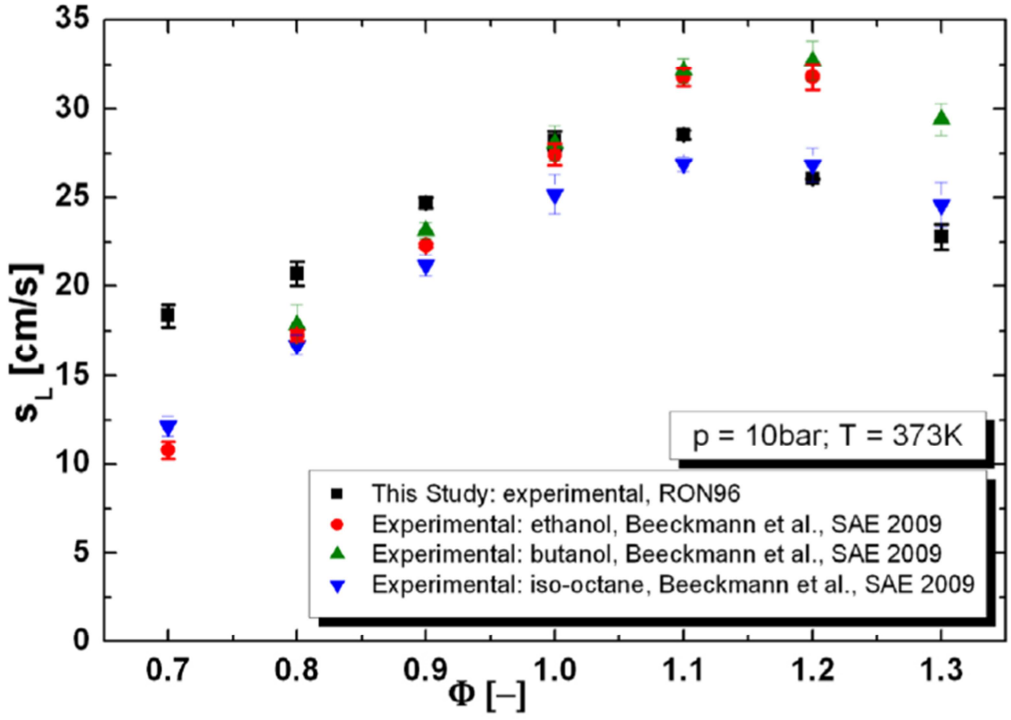

Figure 6.17 – Laminar burning velocity correlations of gasoline/air, ethanol/air, butanol/air and iso-octane/air mixtures [adapted from Beeckmann, Kruse and Peters, 2010].

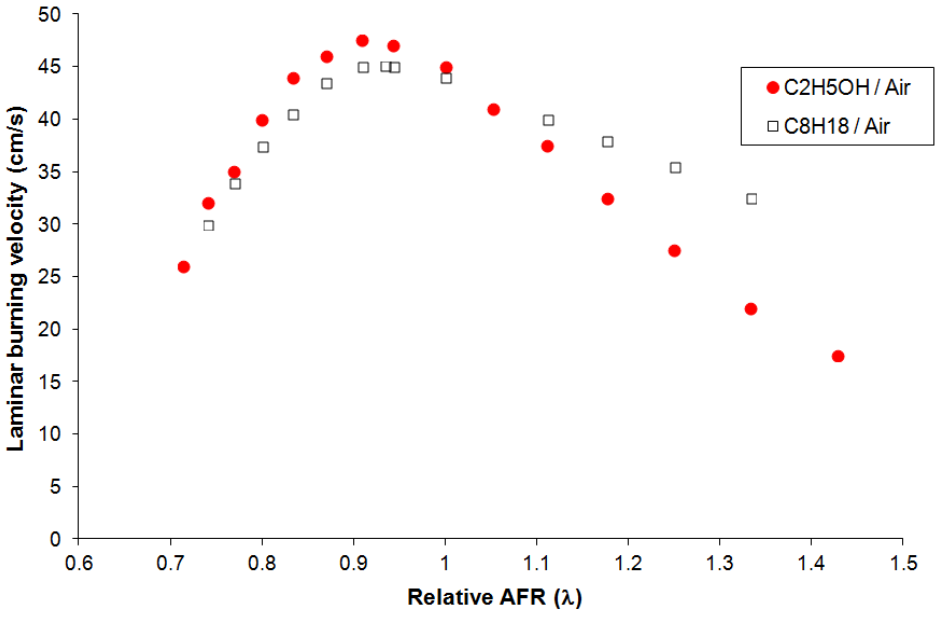

Figure 6.18 – Laminar burning velocity correlations of iso-octane/air and ethanol/air mixtures [adapted from Gülder, 1982].

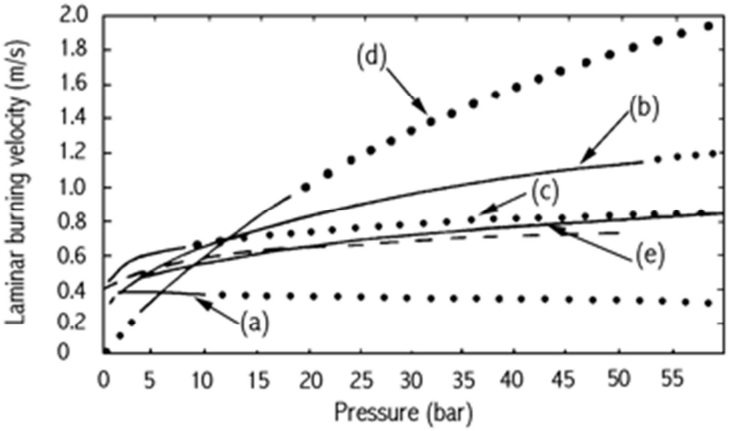

Figure 6.19 – Laminar burning correlations from various authors [Bradley, Lawes and Sheppard, 2000].

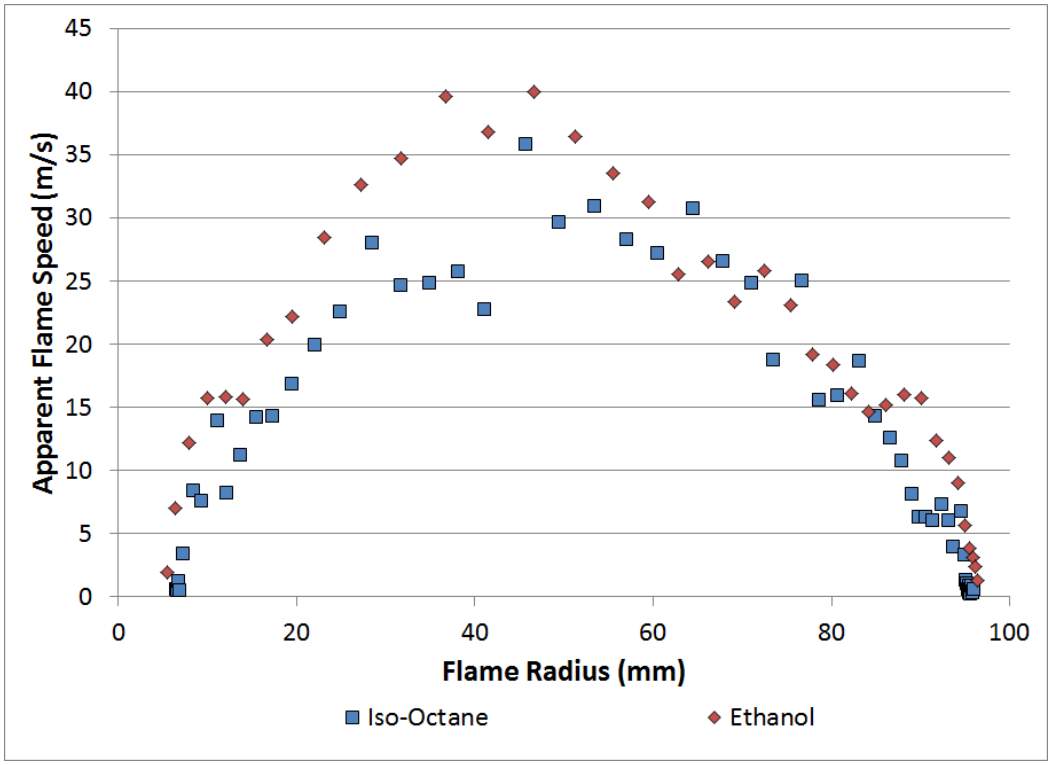

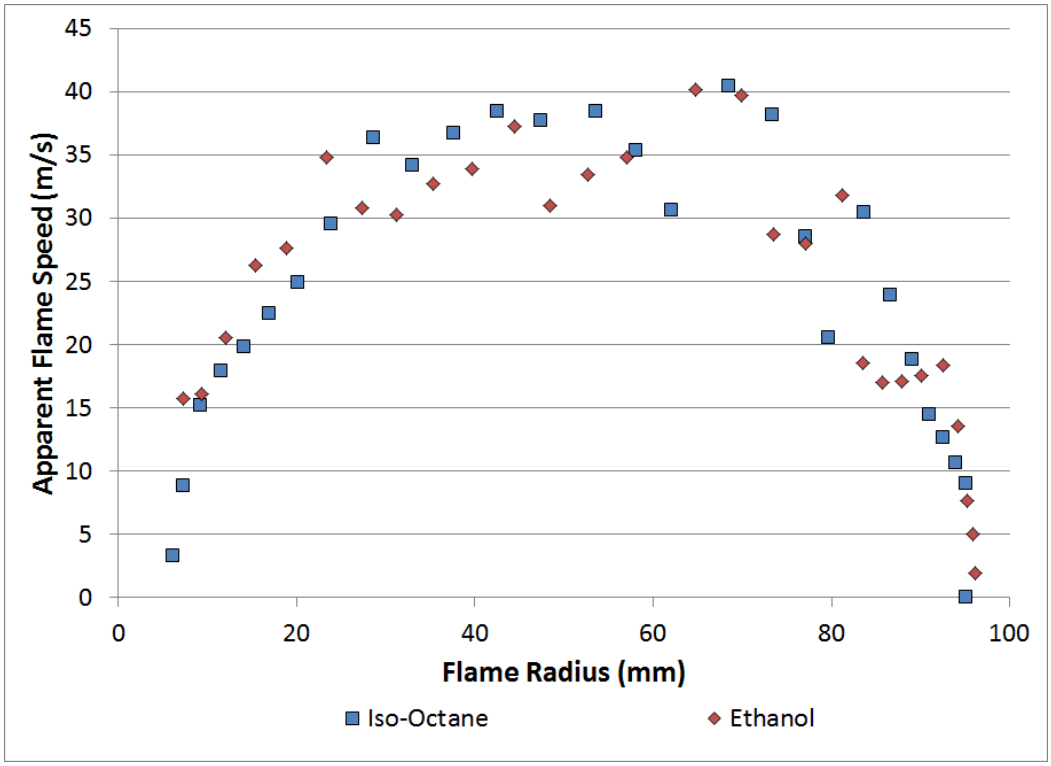

Figure 6.20 – Calculated values of flame speed against flame radius for the two fuel sets taken from the natural light flame imaged cycles for the lean and rich combustion cycles (top and bottom respectively).

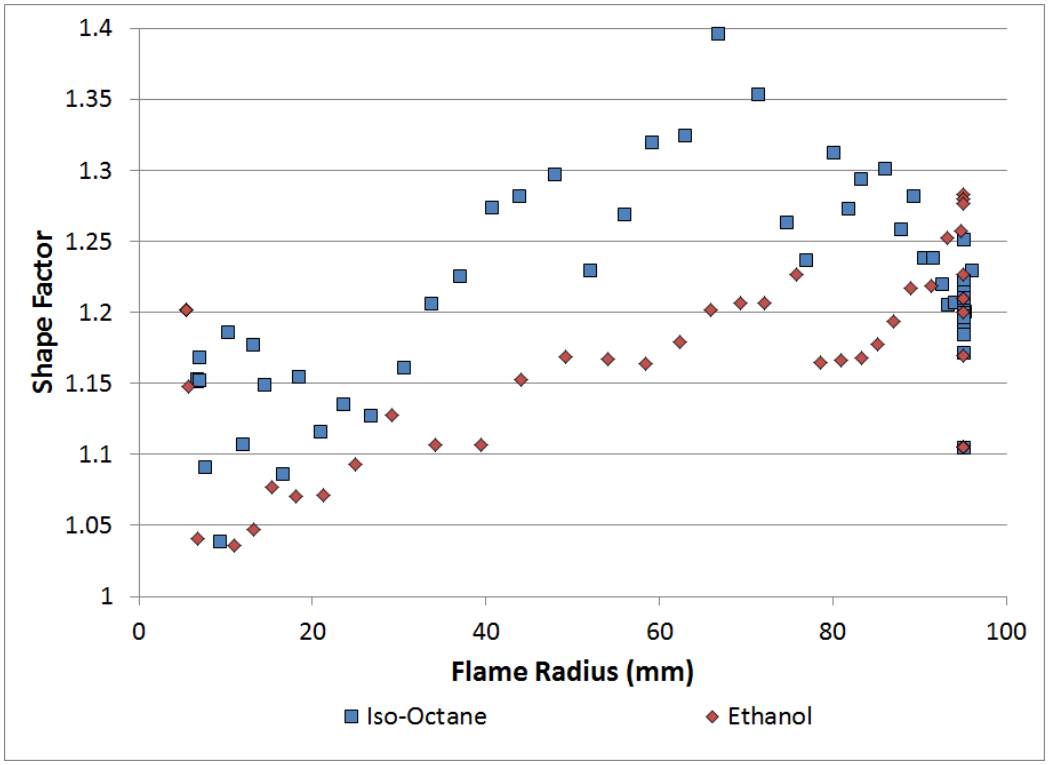

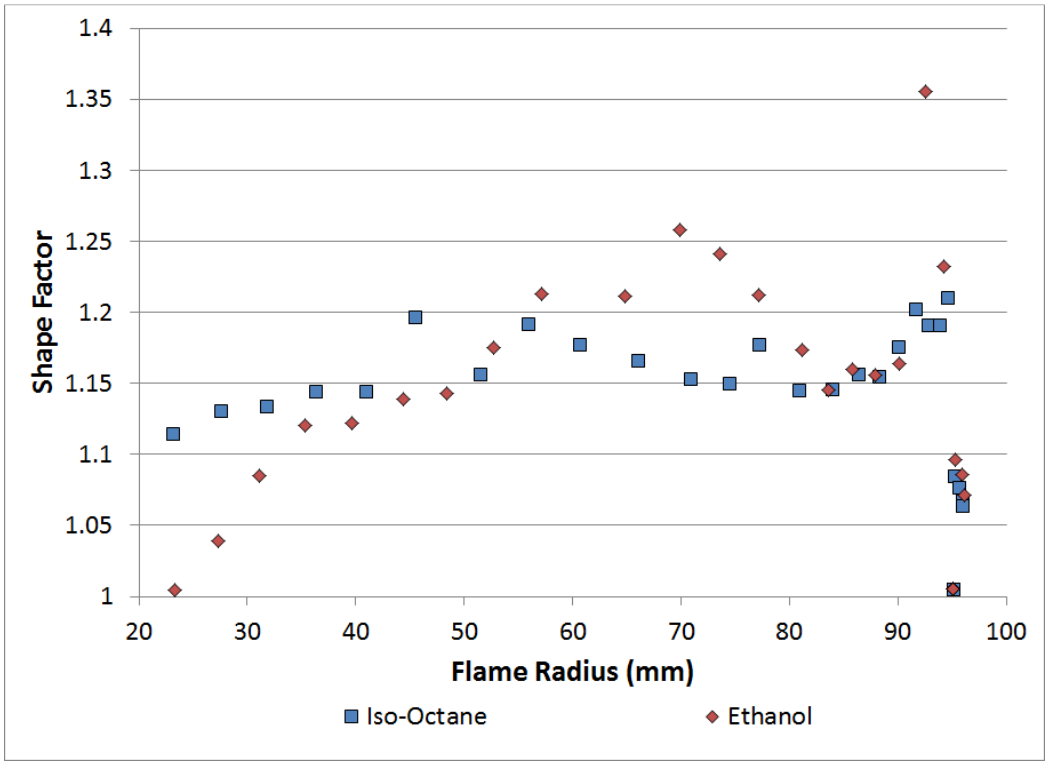

Figure 6.21 – Calculated values of shape factor against flame radius for the two fuel sets taken from the natural light flame imaged cycles for the lean and rich combustion cycles (top and bottom respectively).

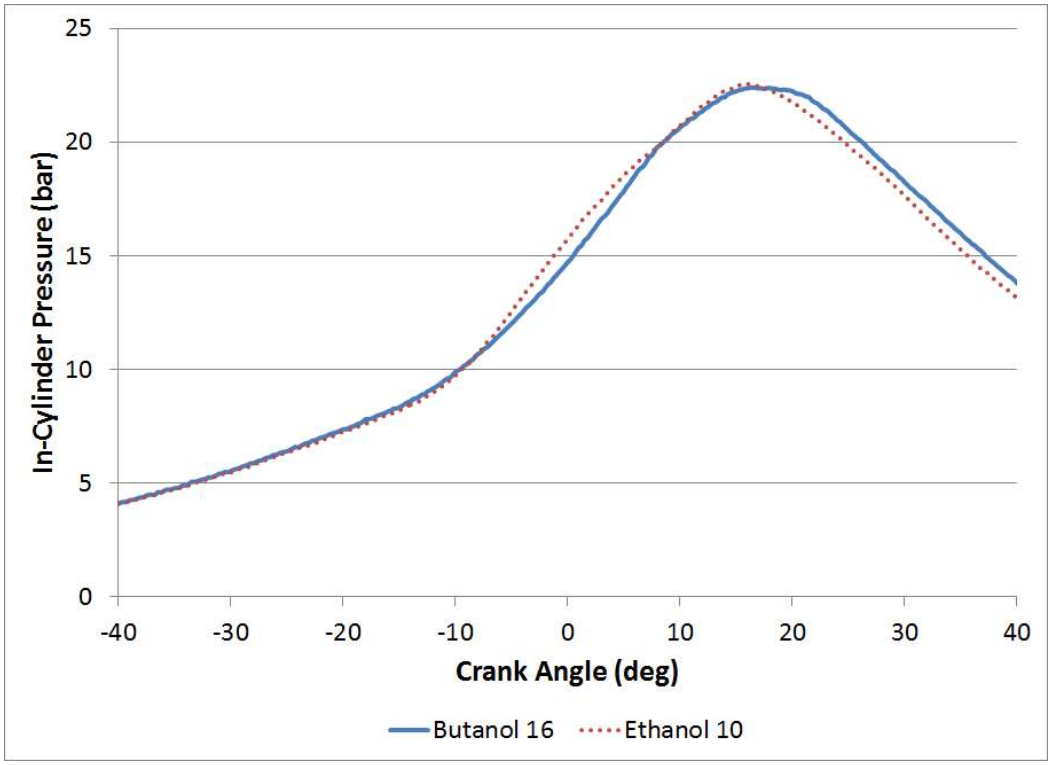

Figure 6.22 – In-cylinder pressure traces for the cycle closest to the mean for the two fuel series under stoichiometric MBT conditions.

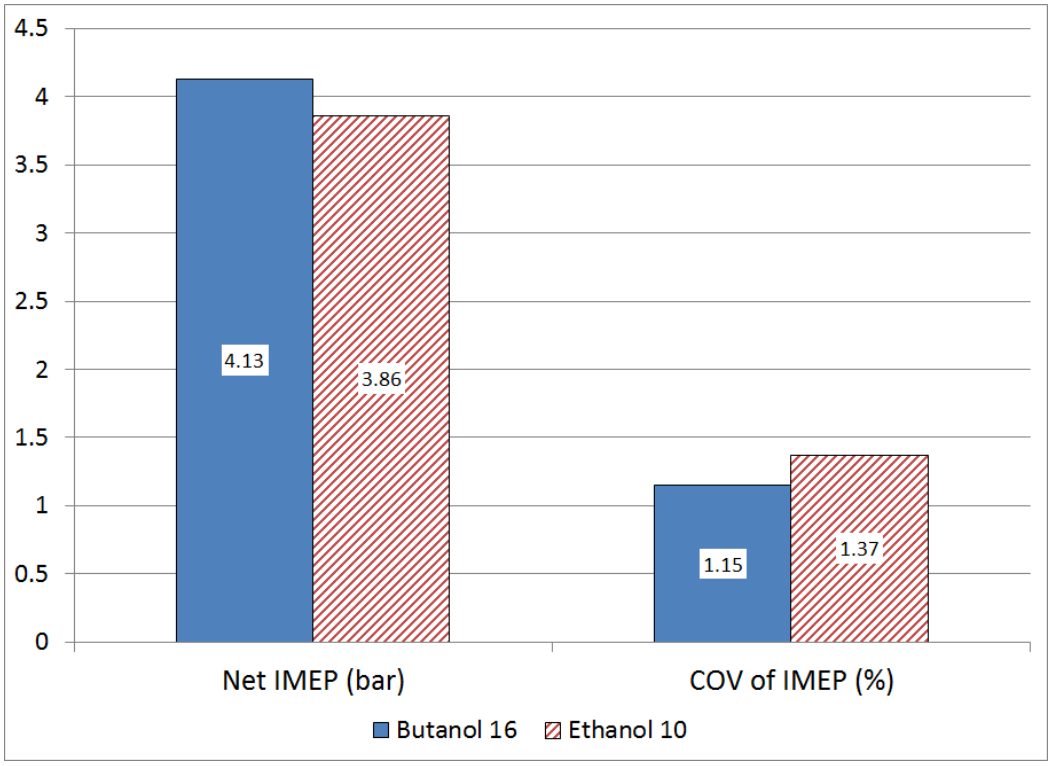

Figure 6.23 – Net IMEP and combustion stability figures for the cycle closest to the mean for the two fuel series under stoichiometric MBT conditions.

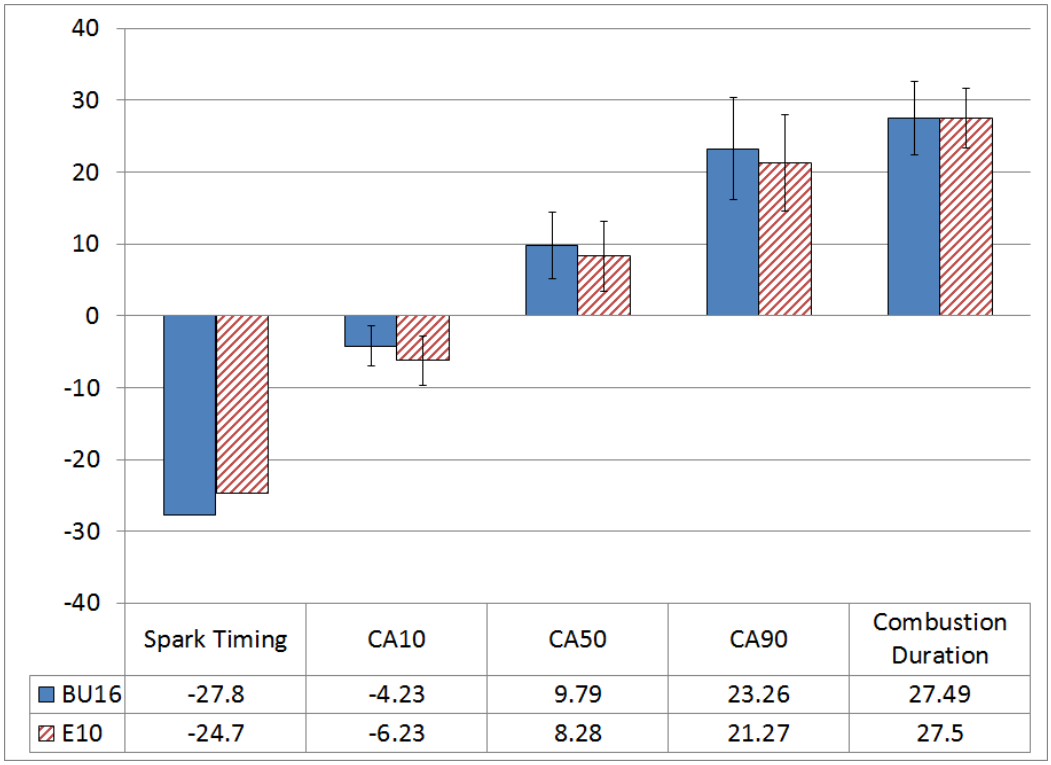

	Spark Timing	CA10	CA50	CA90	Combustion Duration
BU16	-27.8	-4.23	9.79	23.26	27.49
E10	-24.7	-6.23	8.28	21.27	27.5

Figure 6.24 – Key mass fraction burned timings for the cycle closest to the mean for the two fuel series.

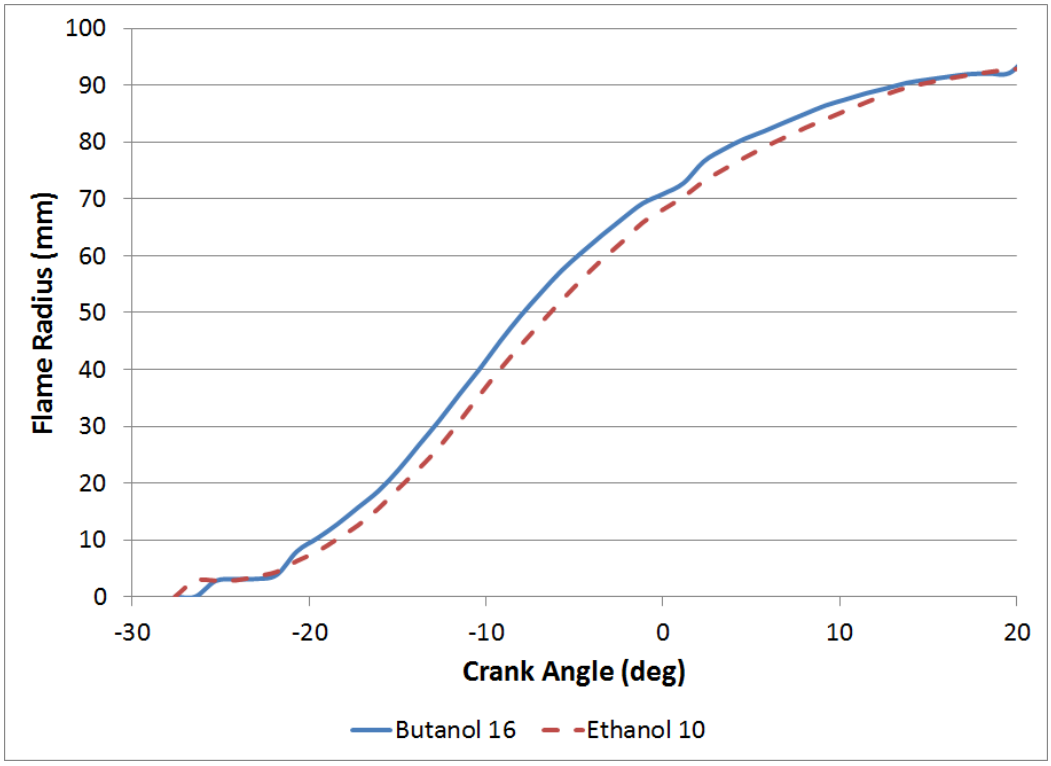

Figure 6.25 - Mean flame radius development for the natural light flame imaged cycles of the two fuel series.

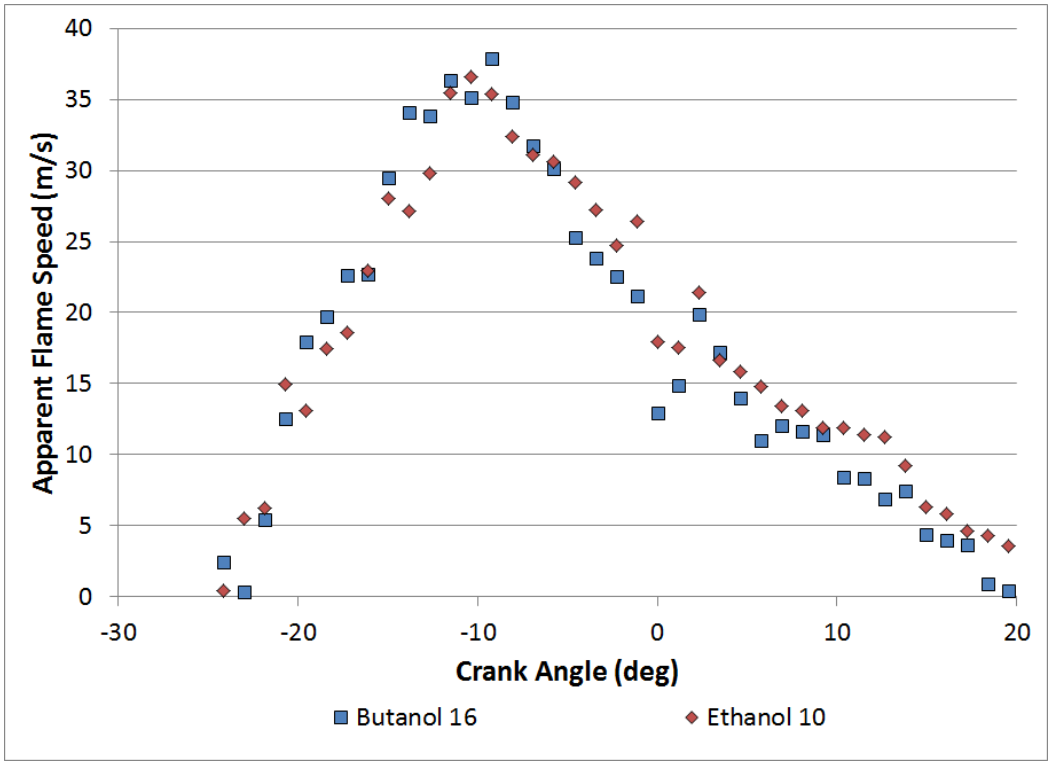

Figure 6.26 – Calculated values of shape factor taken from the natural light flame imaged cycles of the two fuel series.

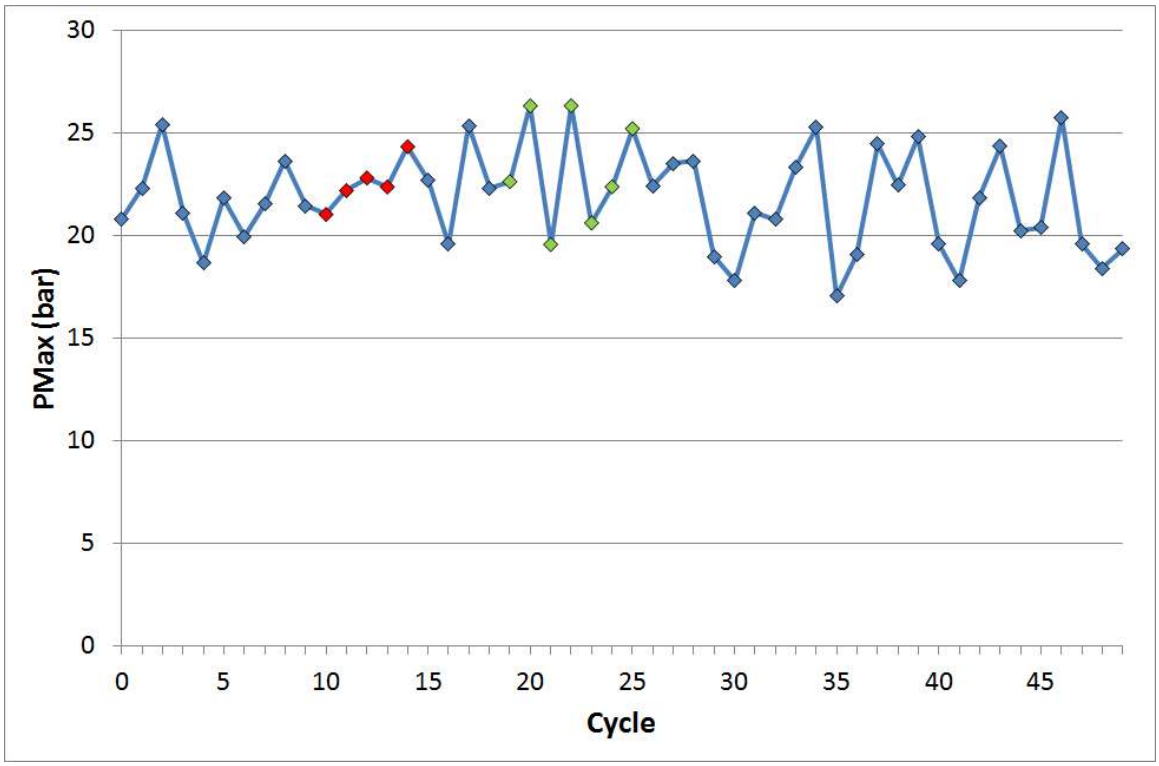

Figure 6.27 – Maximum in-cylinder pressure values relating to each imaged combustion cycle for iso-octane MBT combustion. Creep cases are identified in red, saw-toothing cases in green.

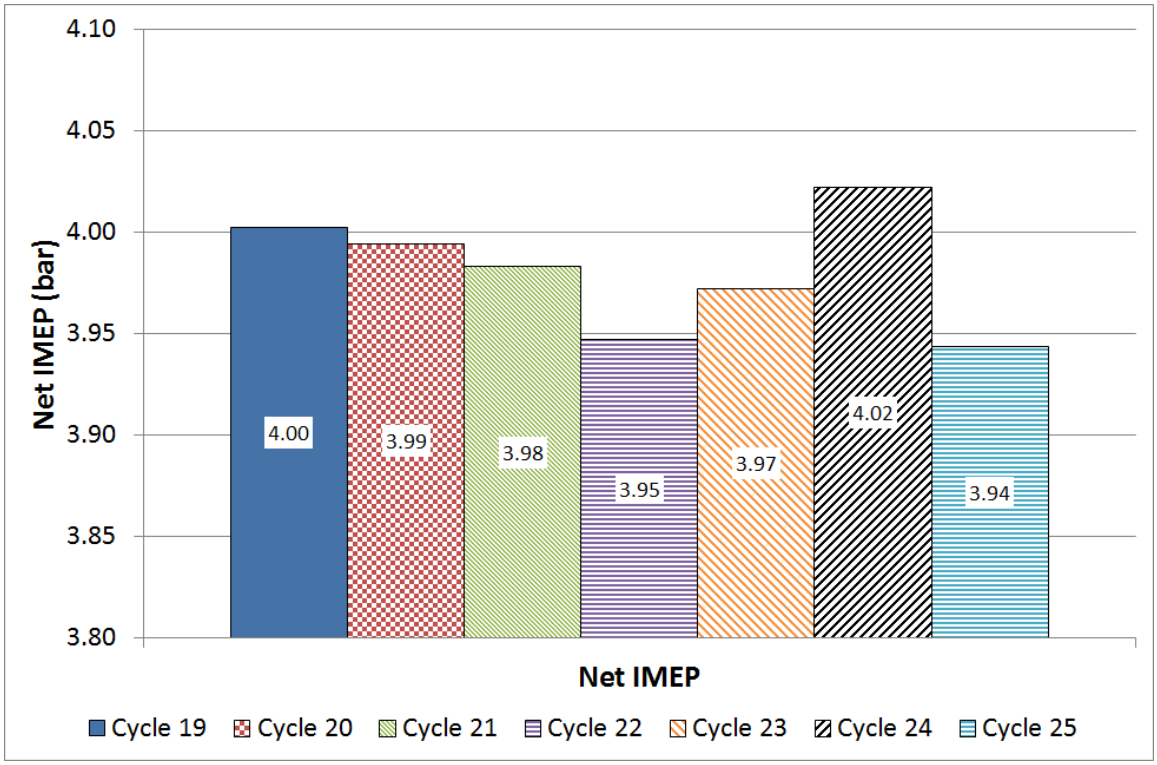

Figure 6.28 – Net IMEP figures for the iso-octane saw-tooth cycles identified in green in Figure 6.27.

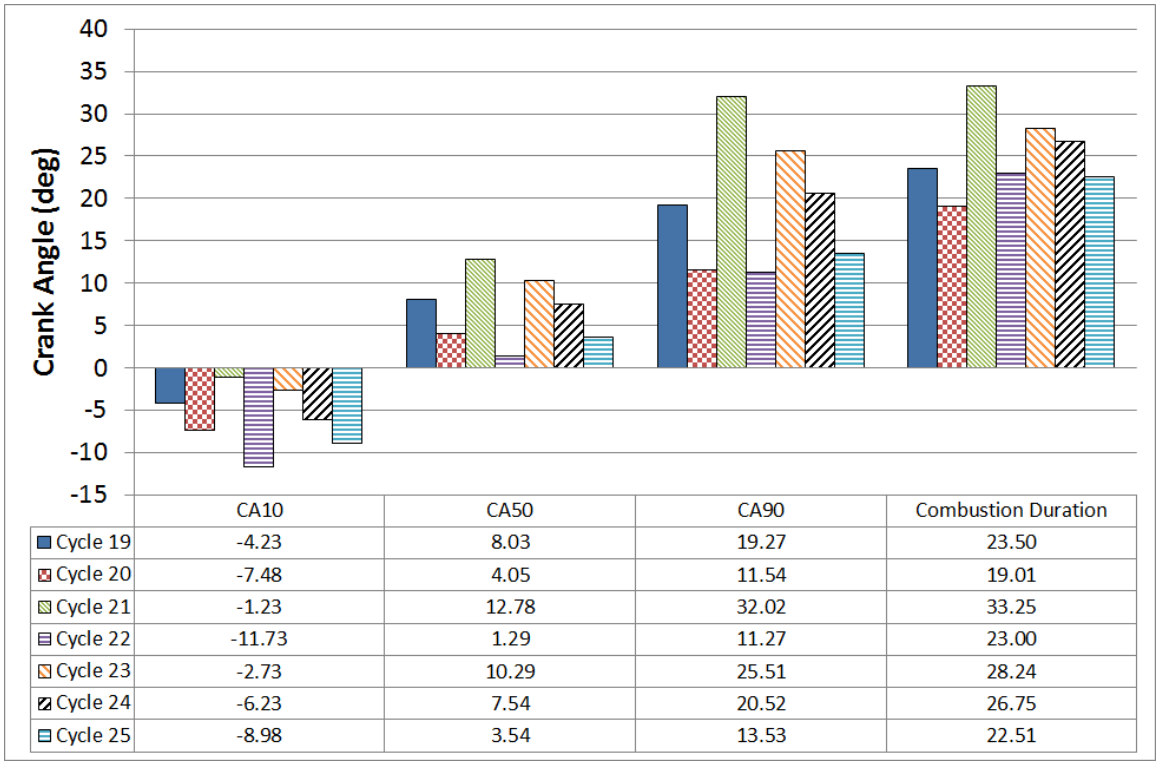

	CA10	CA50	CA90	Combustion Duration
Cycle 19	-4.23	8.03	19.27	23.50
Cycle 20	-7.48	4.05	11.54	19.01
Cycle 21	-1.23	12.78	32.02	33.25
Cycle 22	-11.73	1.29	11.27	23.00
Cycle 23	-2.73	10.29	25.51	28.24
Cycle 24	-6.23	7.54	20.52	26.75
Cycle 25	-8.98	3.54	13.53	22.51

Figure 6.29 – Key mass fraction burned timings for the iso-octane saw-tooth cycles identified in green in Figure 6.27.

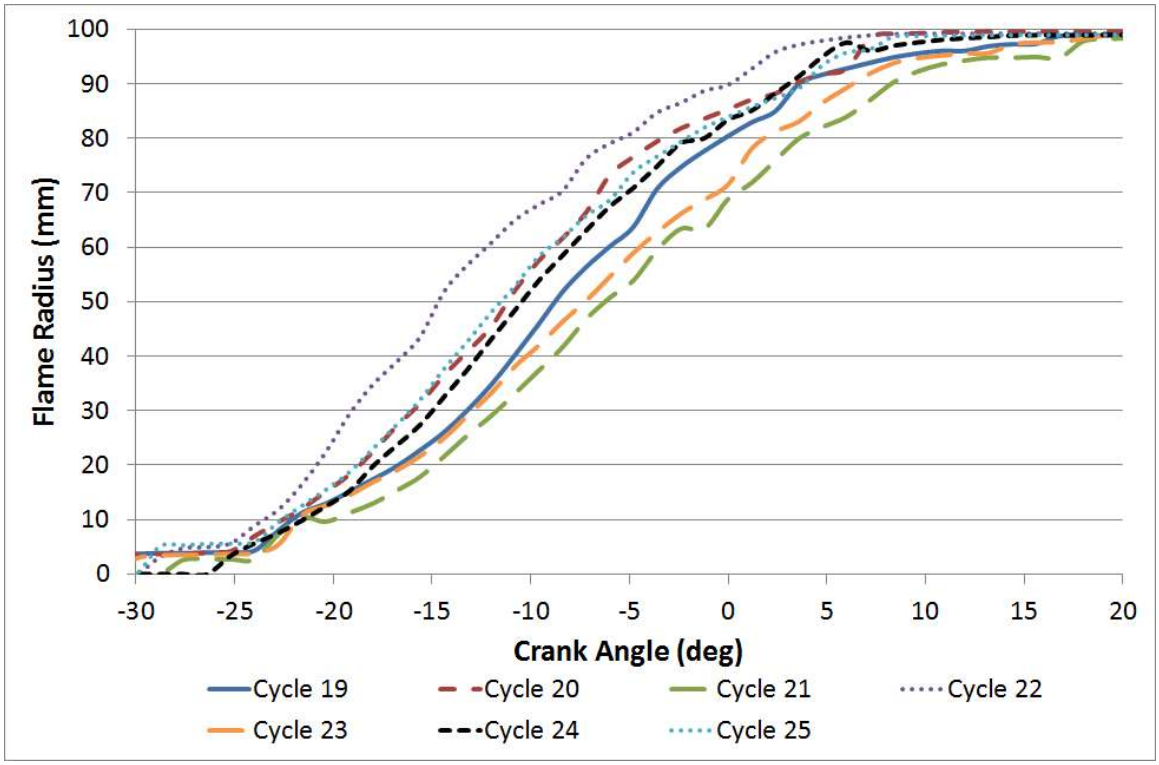

Figure 6.30 – Mean flame radius development for the natural light imaged cycles for the iso-octane saw-tooth cycles identified in green in Figure 6.27.

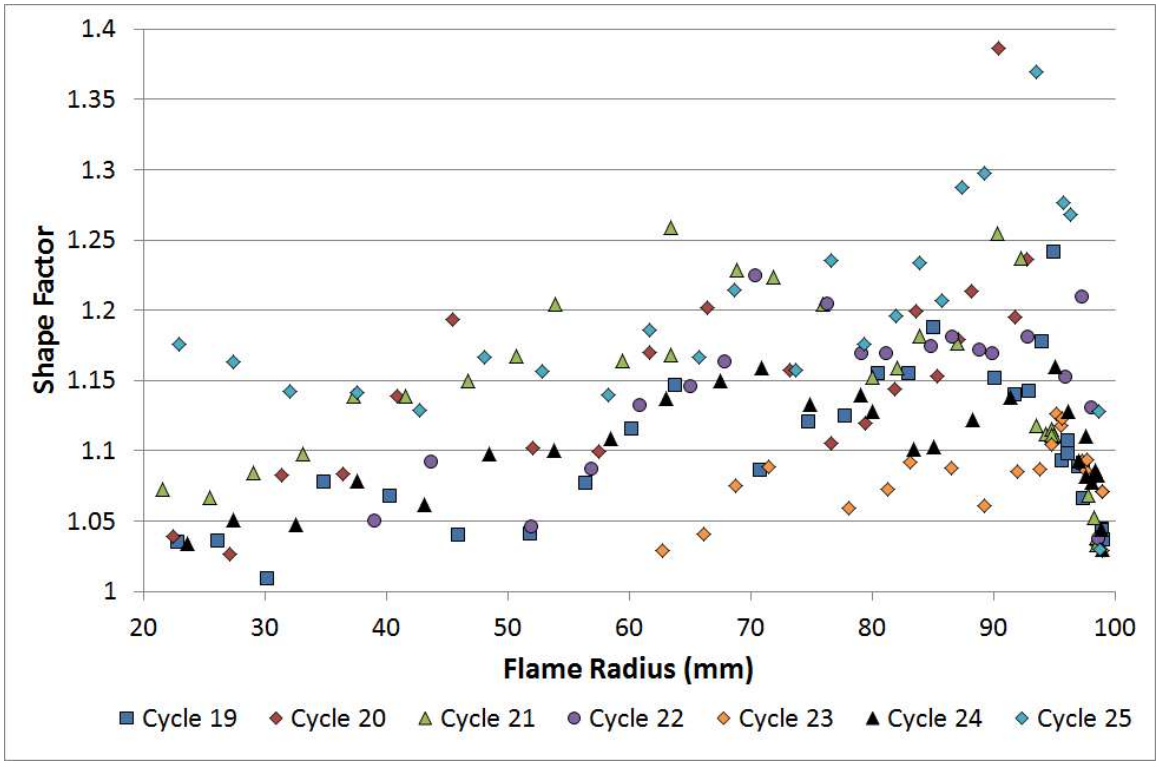

Figure 6.31 – Calculated values for shape factor for the natural light imaged cycles for the iso-octane saw-tooth cycles identified in green in Figure 6.27.

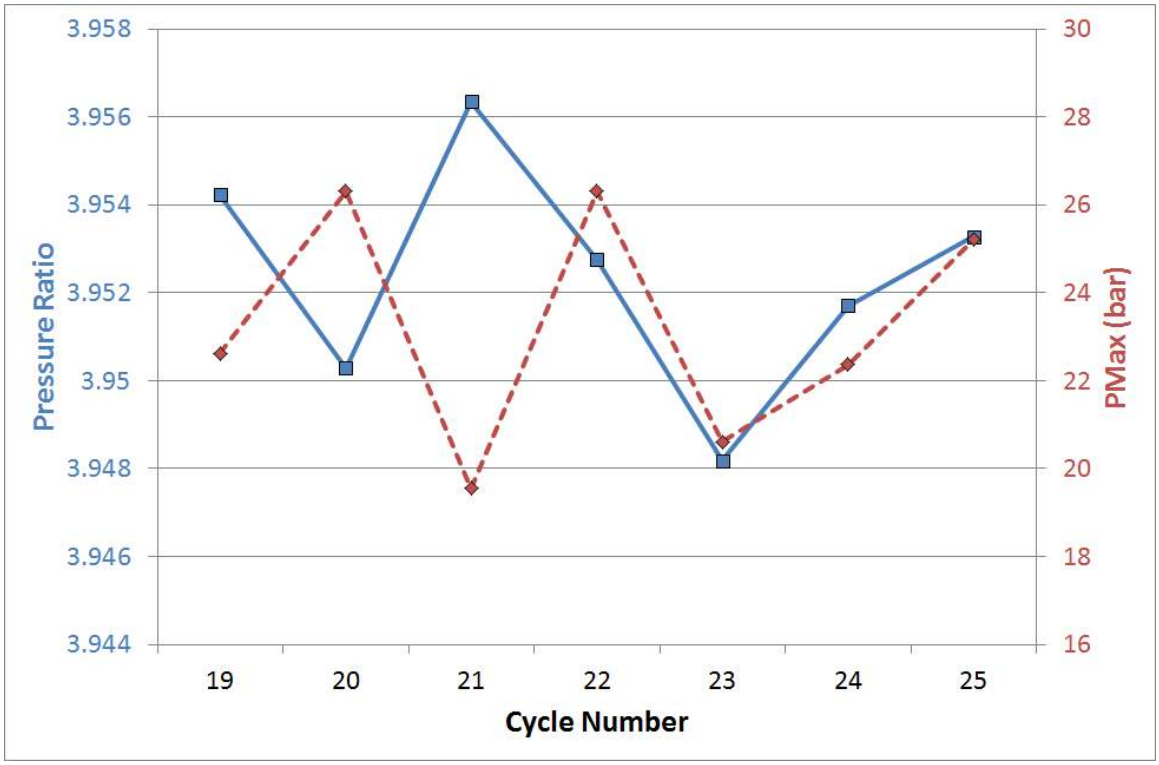

Figure 6.32 – Ratio of exhaust-to-inlet pressures for the iso-octane saw-tooth cycles identified in green in Figure 6.27, set against PMax values for said cycles.

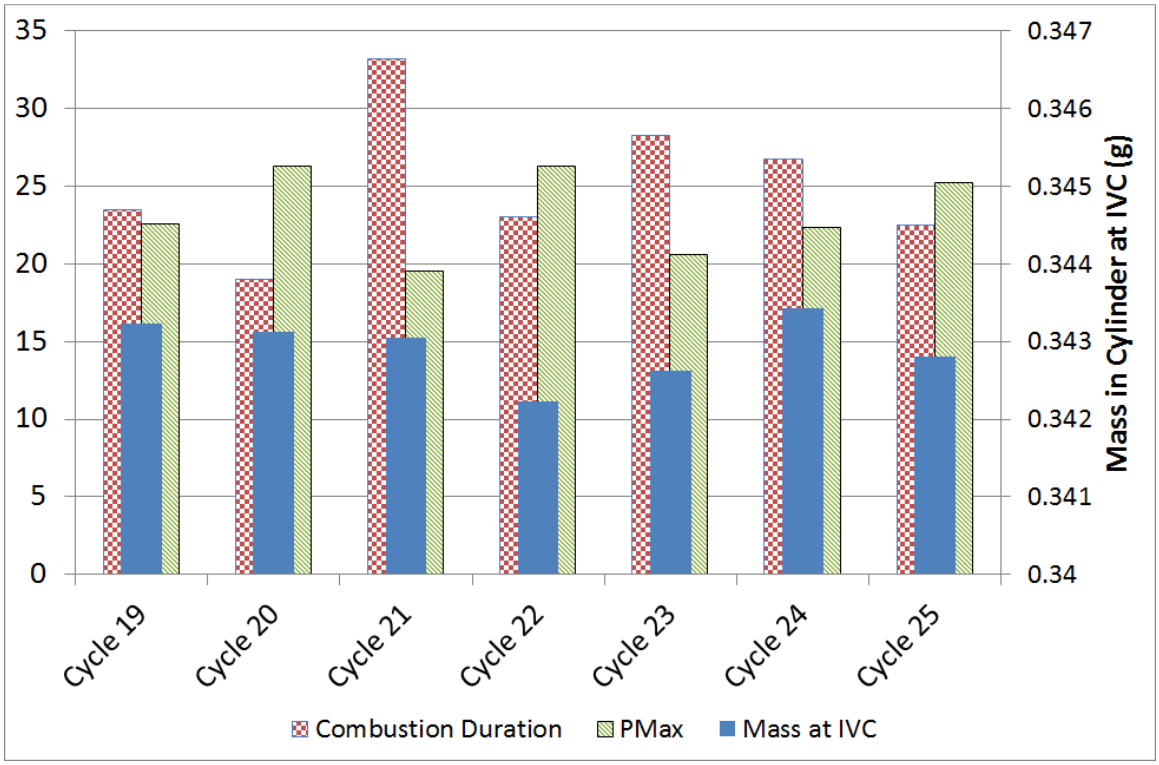

Figure 6.33 – Computed values for in-cylinder mass at IVC for the iso-octane saw-tooth cycles identified in green in Figure 6.27.

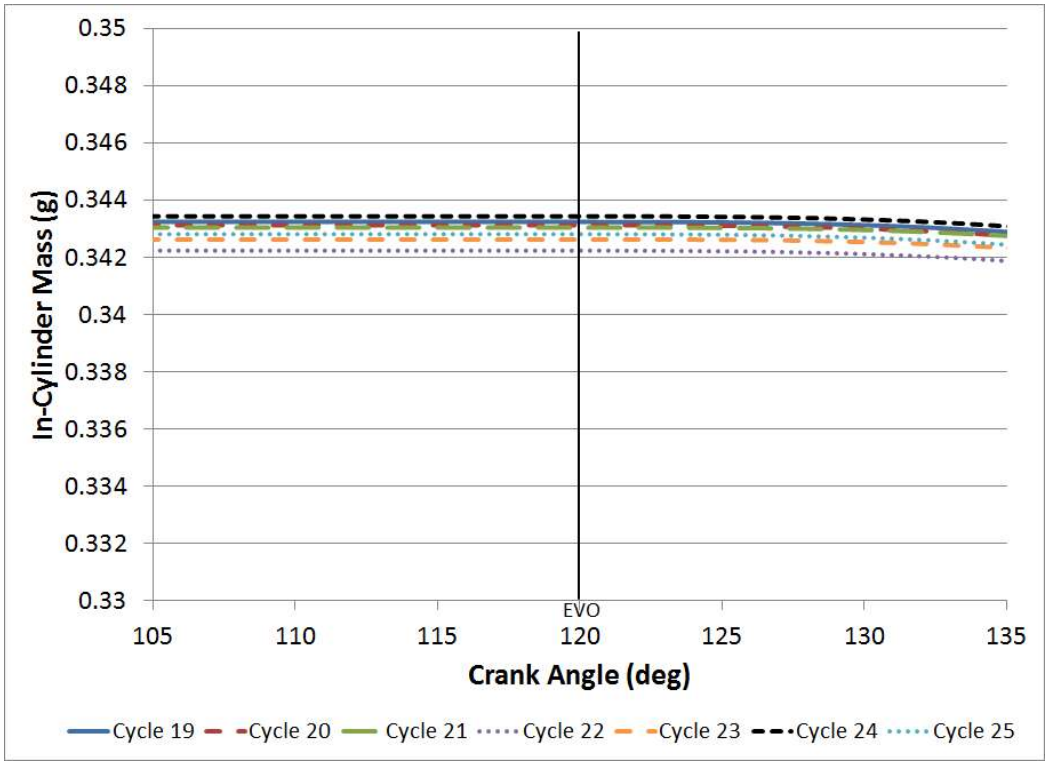

Figure 6.34 – Computed values for in-cylinder mass at EVO for the iso-octane saw-tooth cycles identified in green in Figure 6.27.

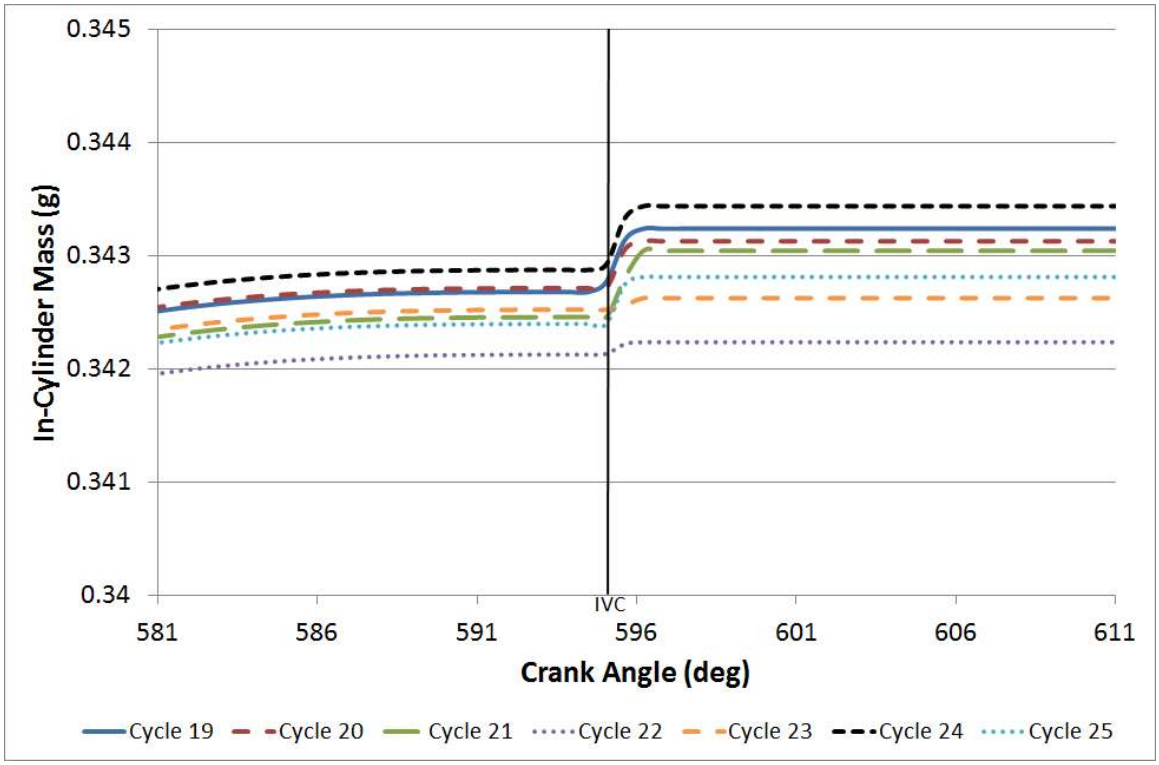

Figure 6.35 – Computed values for in-cylinder mass at IVC for the iso-octane saw-tooth cycles identified in green in Figure 6.27.

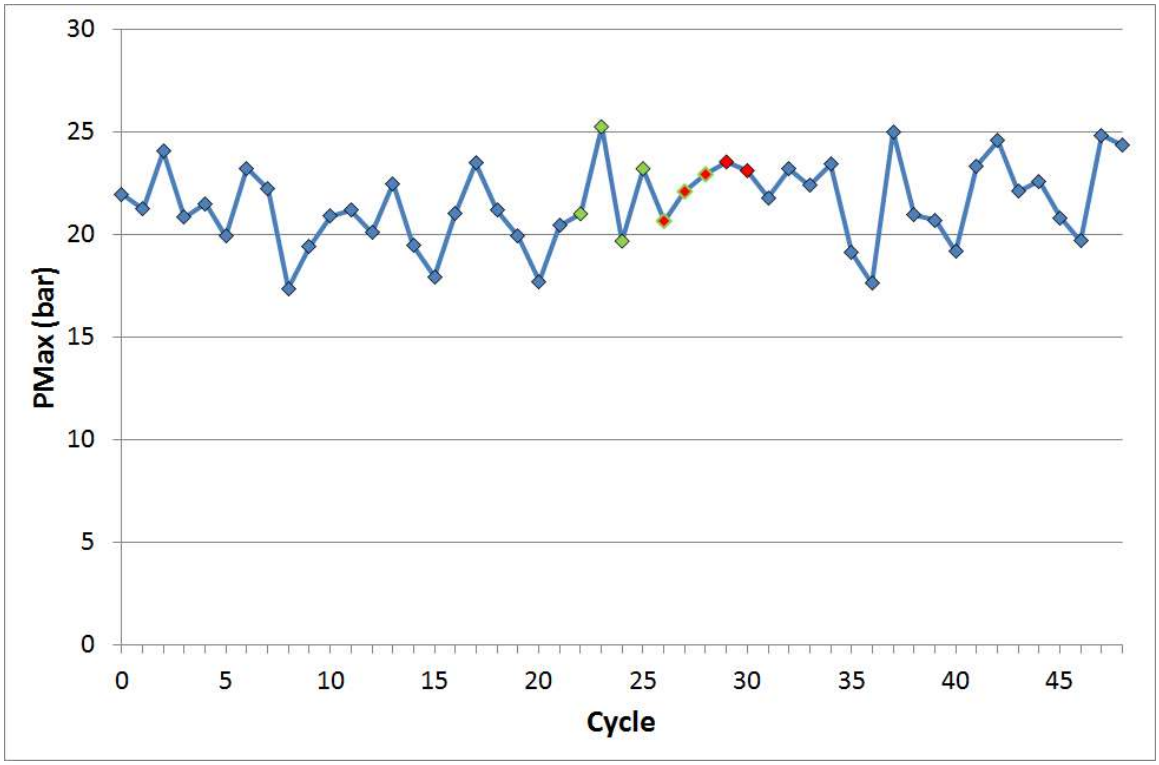

Figure 6.36 – Maximum in-cylinder pressure values relating to each imaged combustion cycle for ethanol MBT combustion. Creep cases are identified in red, saw-toothing cases in green.

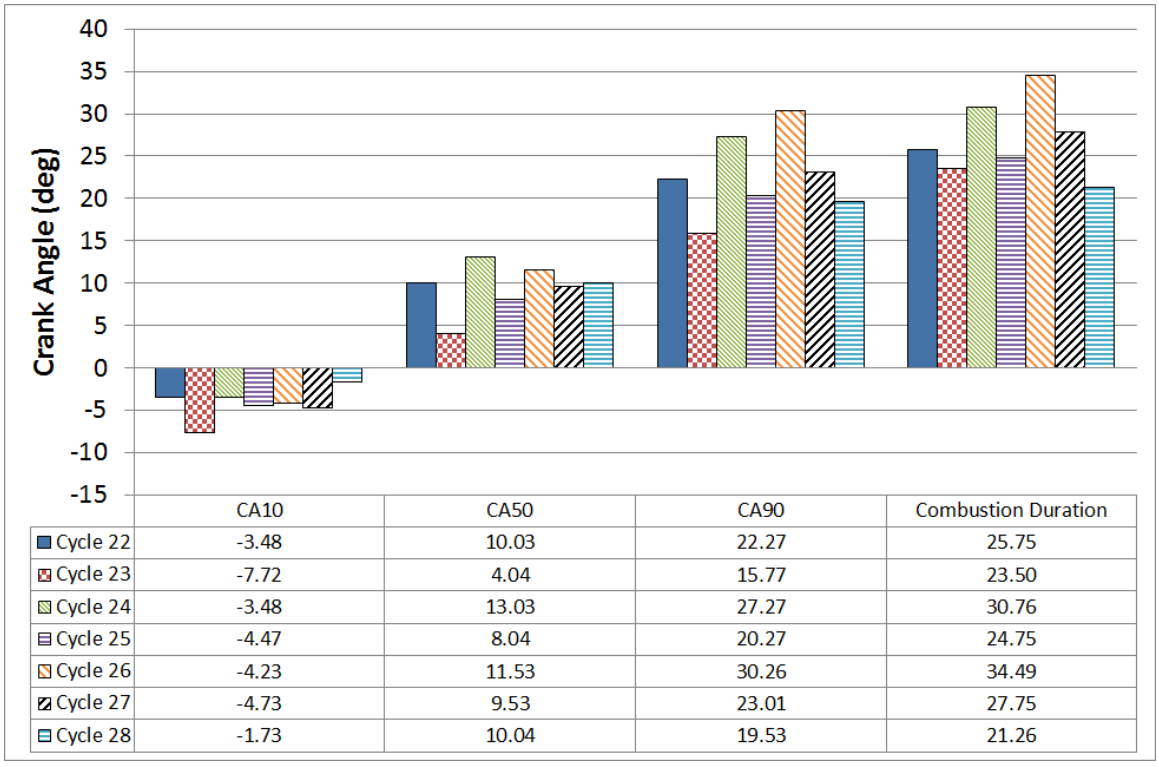

	CA10	CA50	CA90	Combustion Duration
Cycle 22	-3.48	10.03	22.27	25.75
Cycle 23	-7.72	4.04	15.77	23.50
Cycle 24	-3.48	13.03	27.27	30.76
Cycle 25	-4.47	8.04	20.27	24.75
Cycle 26	-4.23	11.53	30.26	34.49
Cycle 27	-4.73	9.53	23.01	27.75
Cycle 28	-1.73	10.04	19.53	21.26

Figure 6.37 – Key mass fraction burned timings for the ethanol saw-tooth cycles identified in green in Figure 6.36.

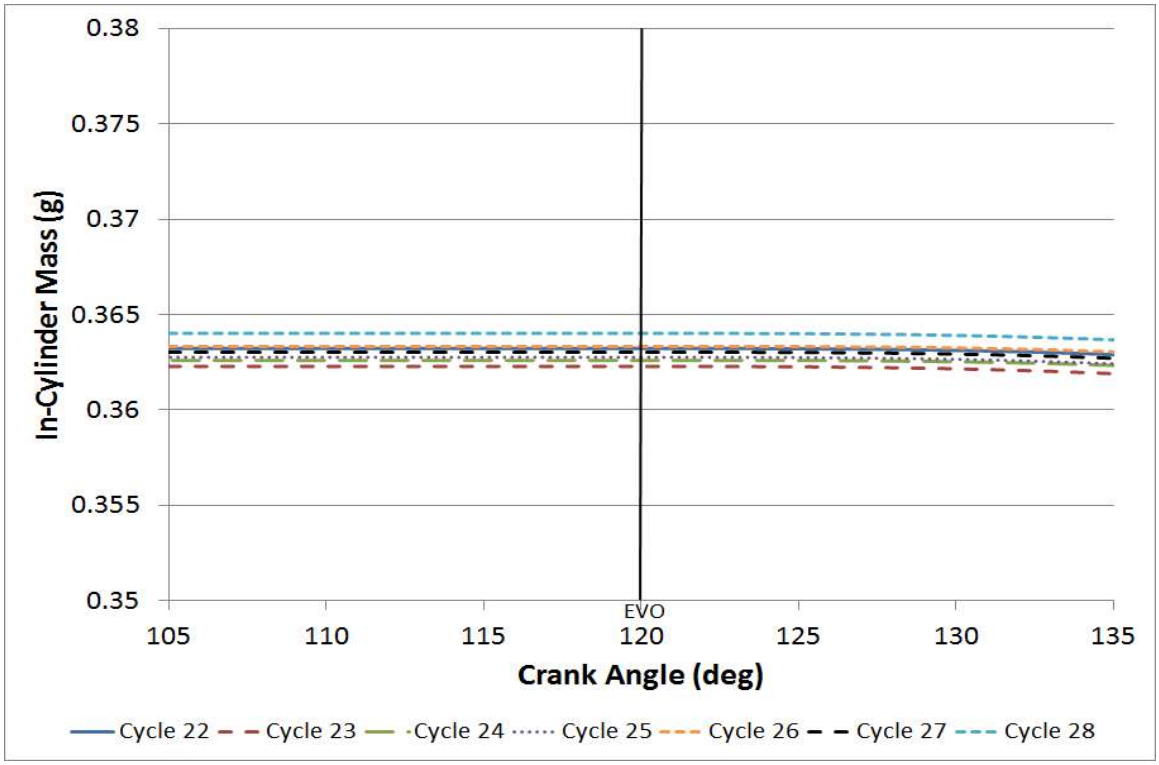

Figure 6.38 – Computed values for in-cylinder mass at EVO for the ethanol saw-tooth cycles identified in green in Figure 6.36.

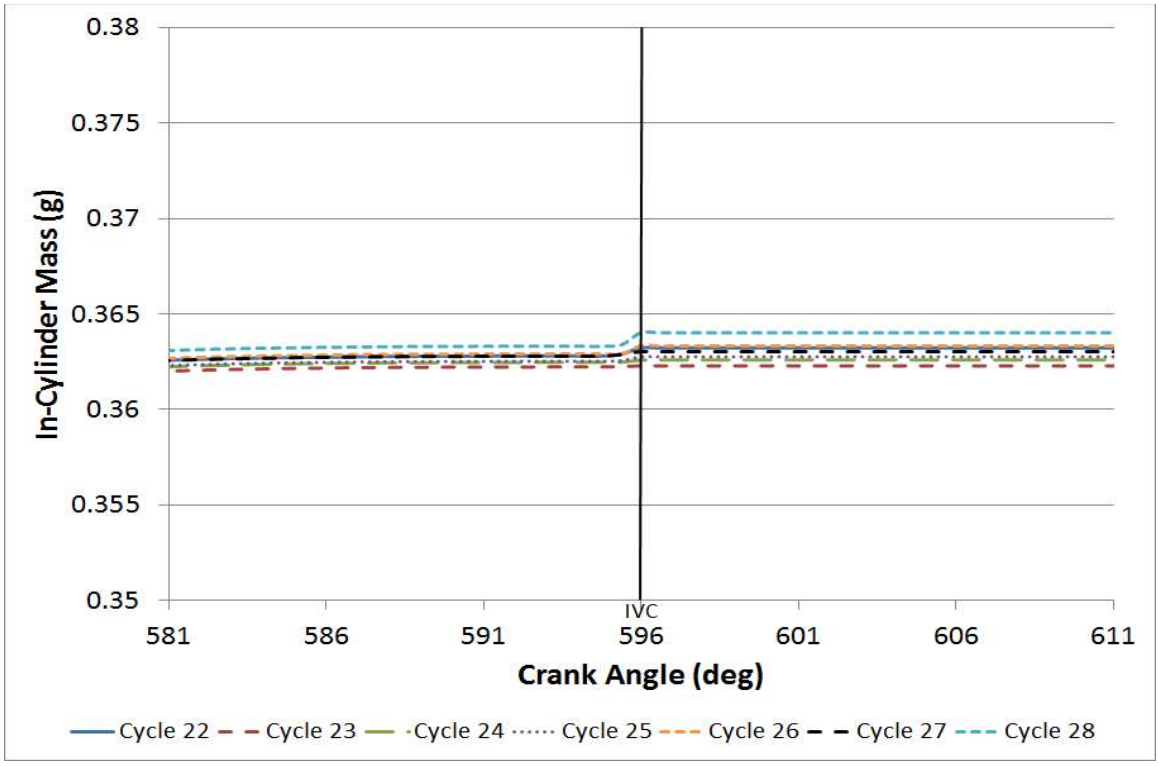

Figure 6.39 – Computed values for in-cylinder mass at IVC for the ethanol saw-tooth cycles identified in green in Figure 6.36.

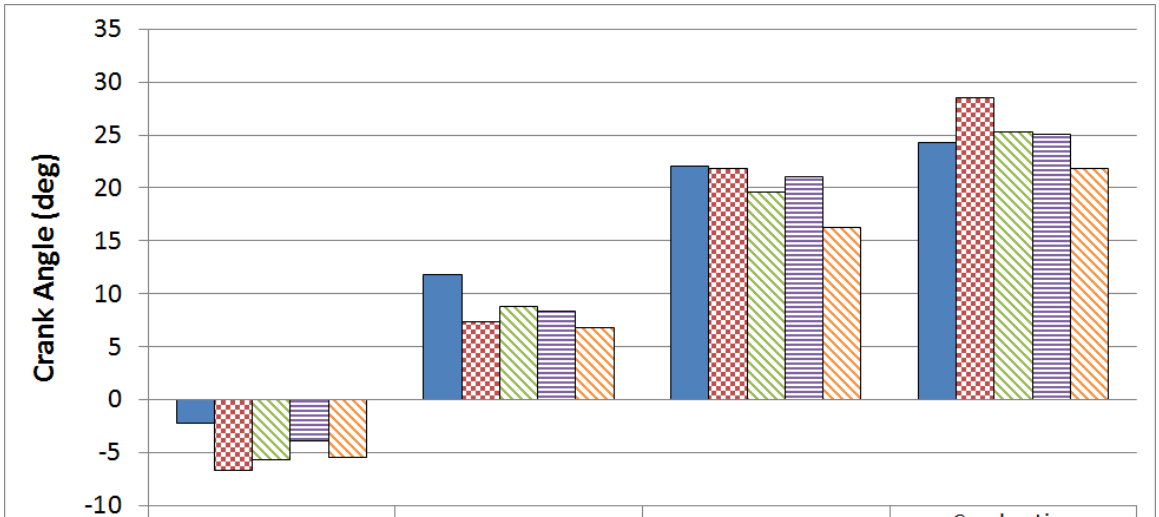

	CA10	CA50	CA90	Combustion Duration
Cycle 10	-2.23	11.79	22.02	24.25
Cycle 11	-6.73	7.28	21.77	28.50
Cycle 12	-5.73	8.79	19.52	25.26
Cycle 13	-3.98	8.29	21.02	25.00
Cycle 14	-5.48	6.80	16.27	21.75

Figure 6.40 – Key mass fraction burned timings for the iso-octane creep cycles identified in red in Figure 6.27.

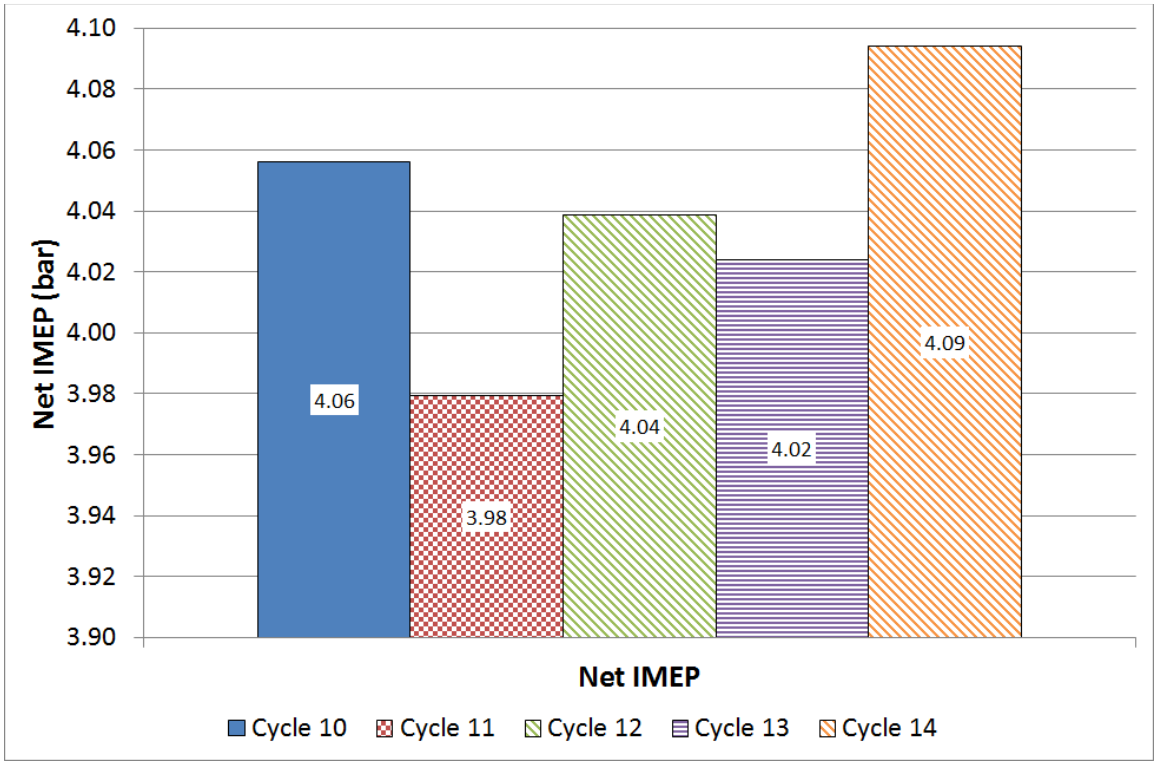

Figure 6.41 – Net IMEP figures for the iso-octane creep cycles identified in red in Figure 6.27.

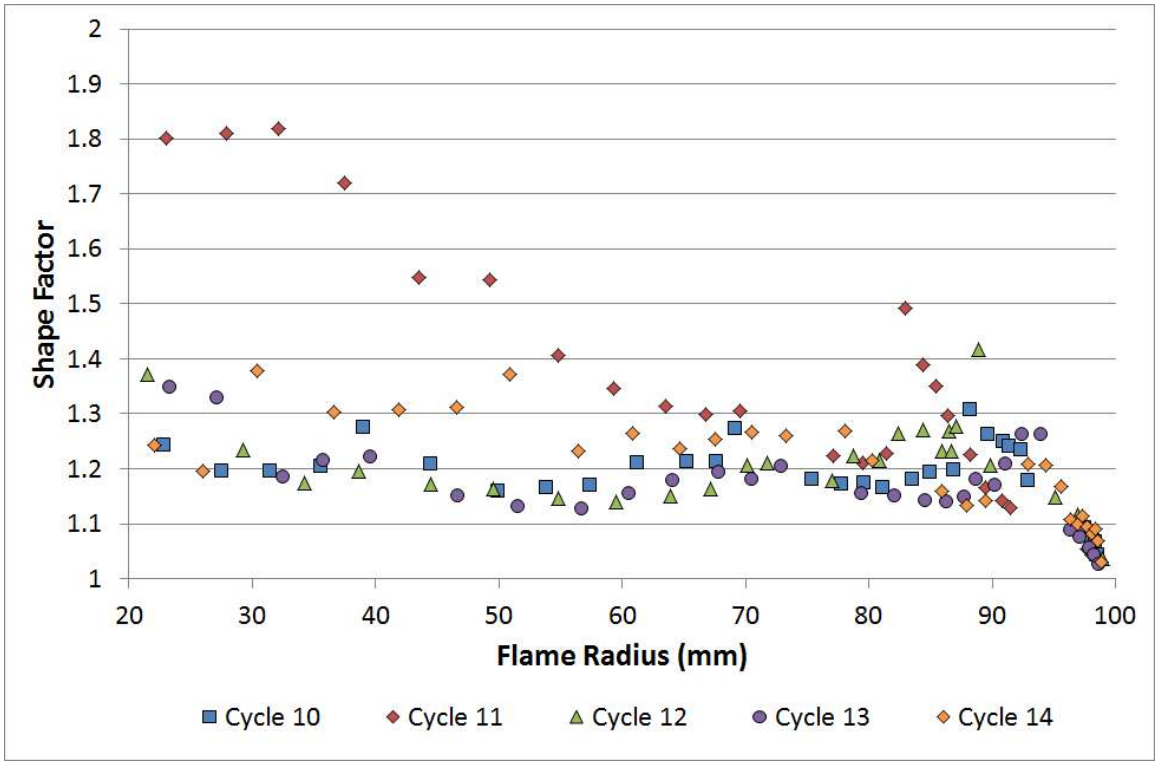

Figure 6.42 – Calculated values for shape factor for the natural light imaged cycles for the iso-octane creep cycles identified in red in Figure 6.29.

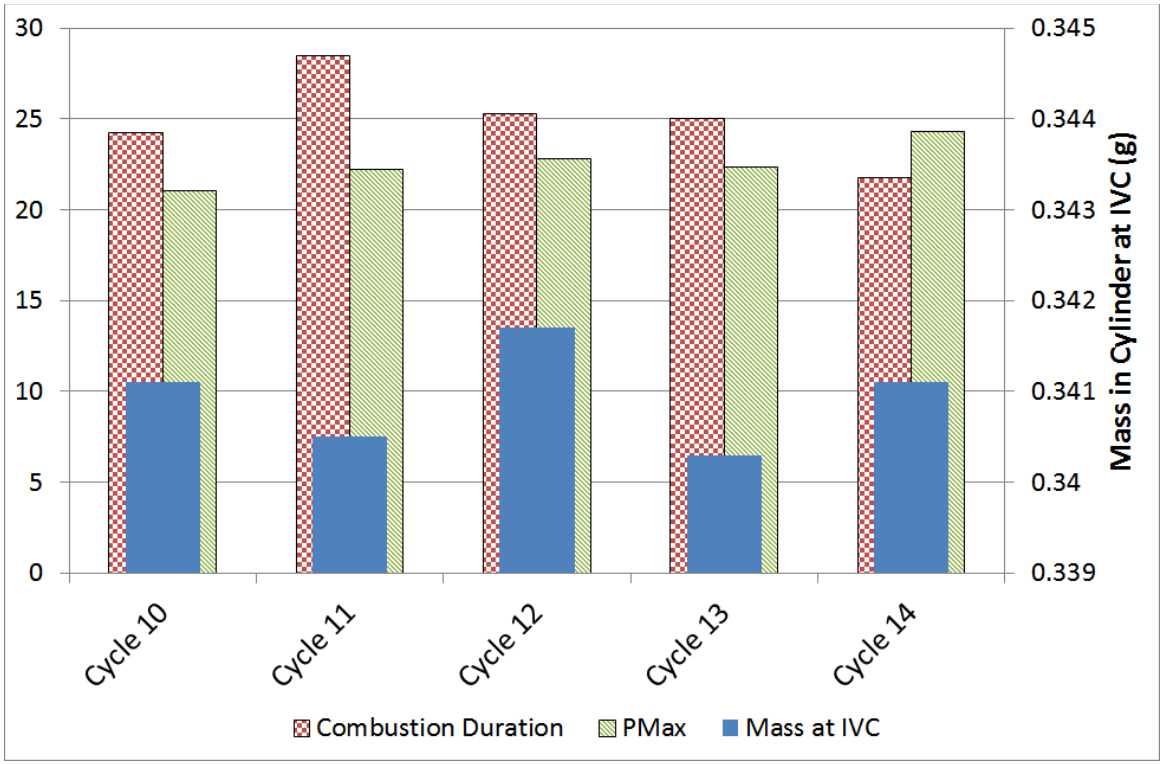

Figure 6.43 – Computed values for in-cylinder mass at IVC for the iso-octane creep cycles identified in red in Figure 6.27.

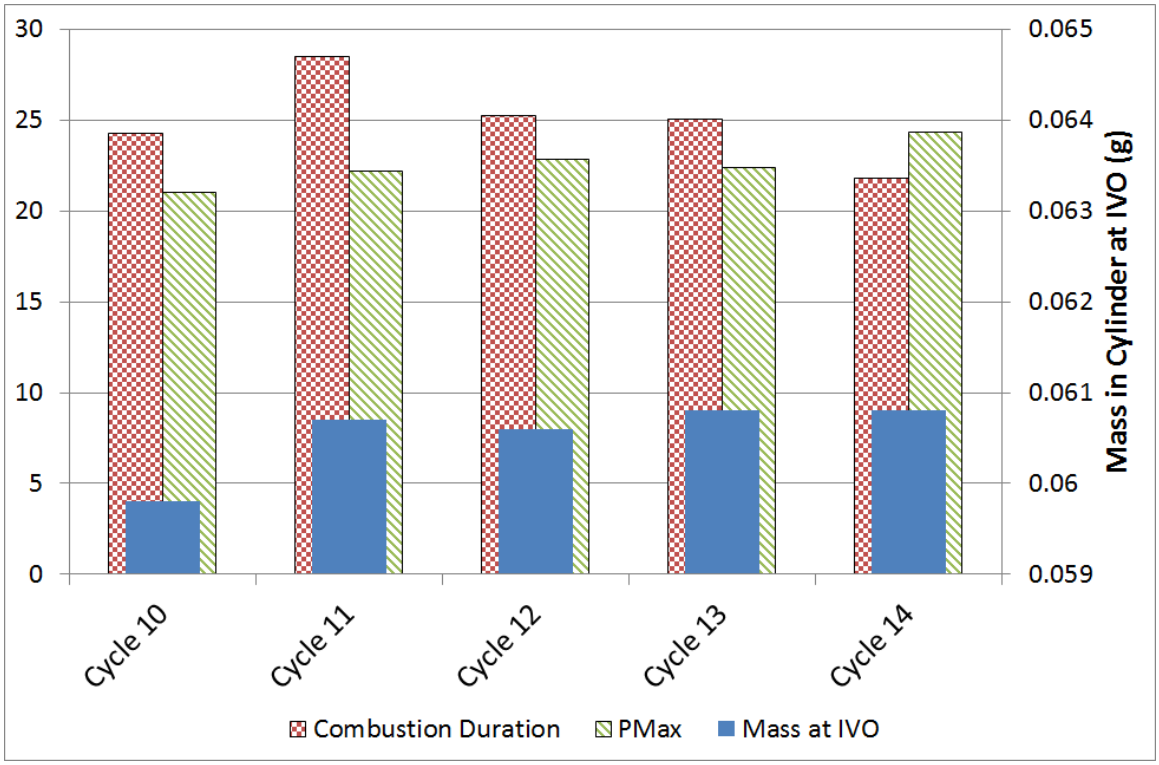

Figure 6.44 – Computed values for in-cylinder mass at IVO for the iso-octane creep cycles identified in red in Figure 6.27

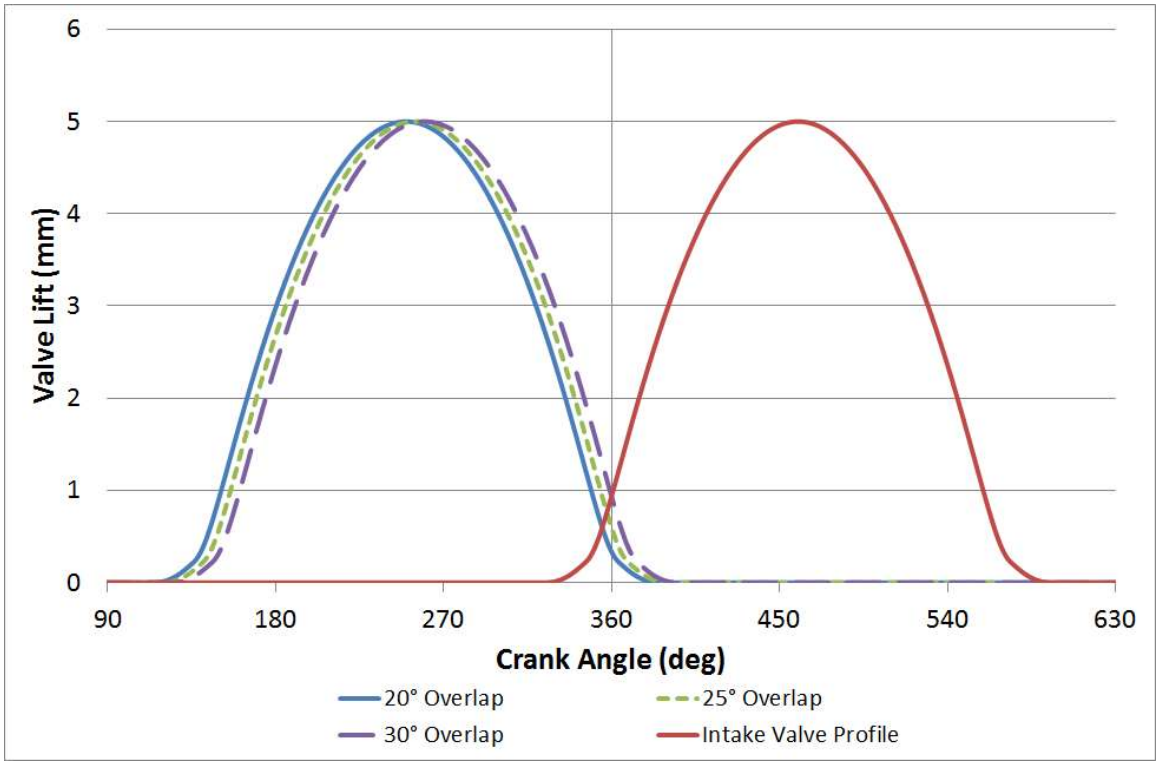

Figure 6.45 – Valve lift profiles of the inlet cam and the exhaust cam positions for the three overlap cases.

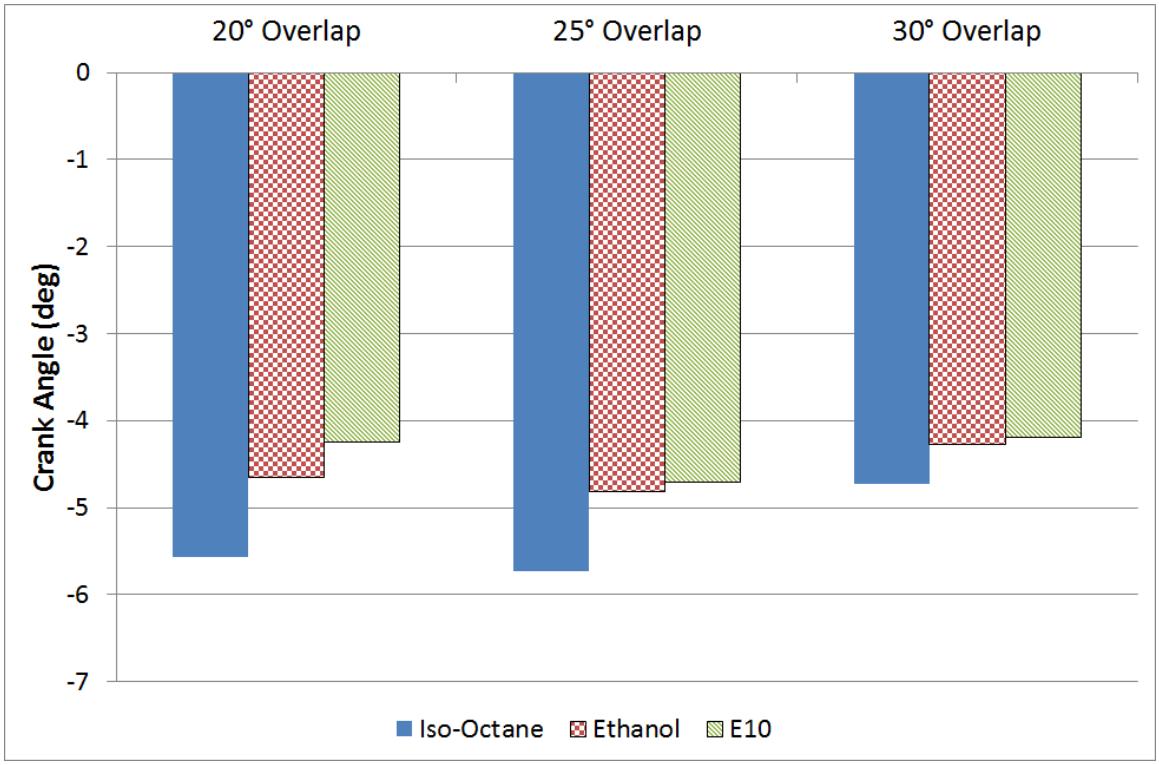

Figure 6.46 – Early combustion duration (0-10% mass fraction burned) for each fuel series for the three overlap cases.

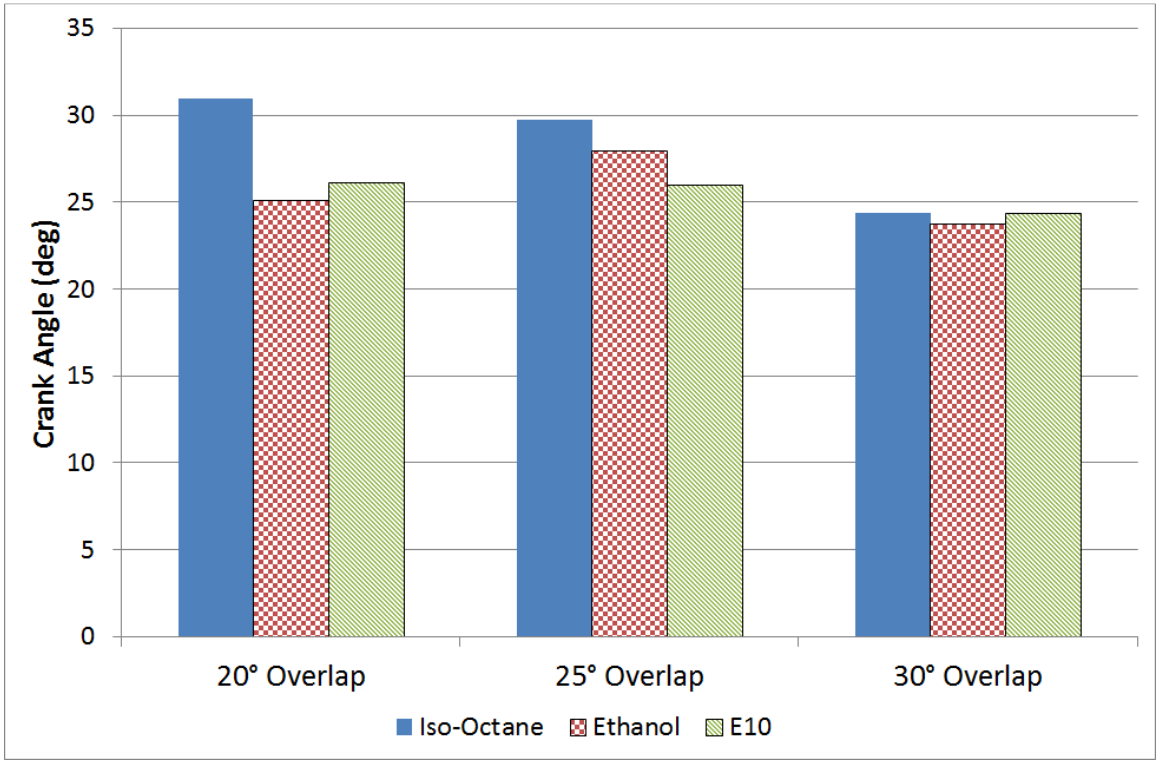

Figure 6.47 – Combustion duration (10-90% mass fraction burned) values for each fuel series running the three overlap cases.

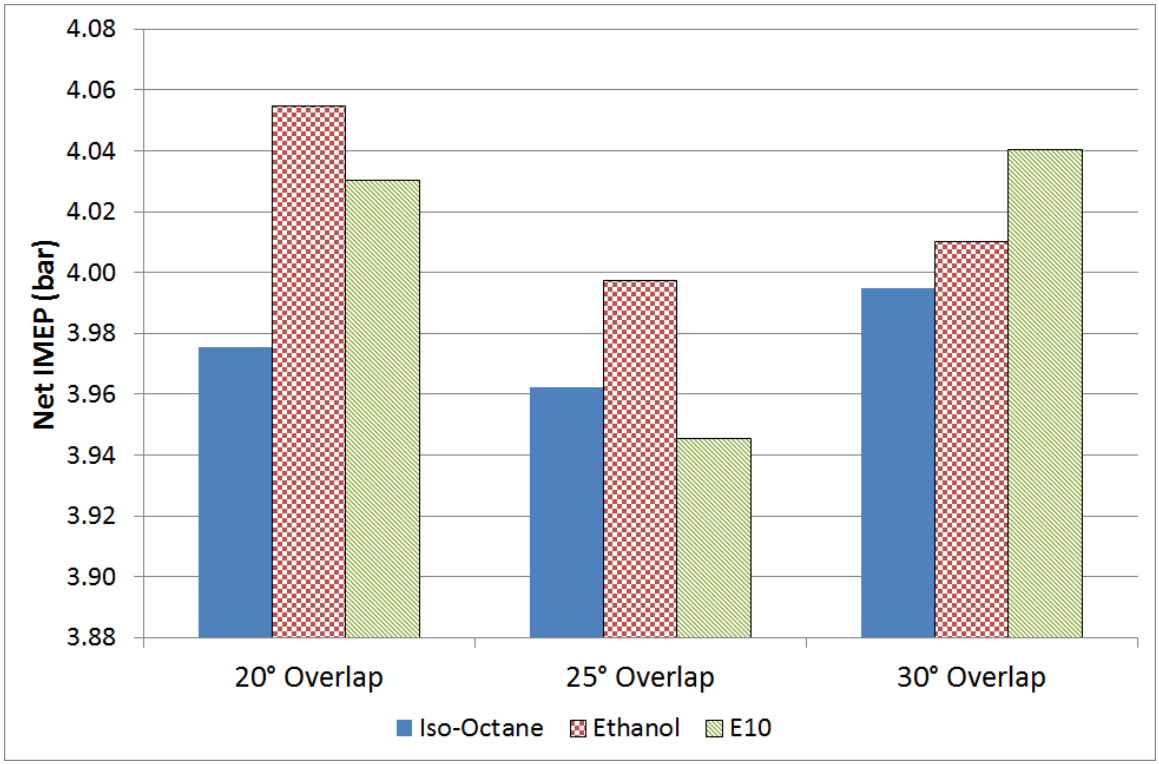

Figure 6.48 – Values for net IMEP for each fuel series running the three overlap cases.

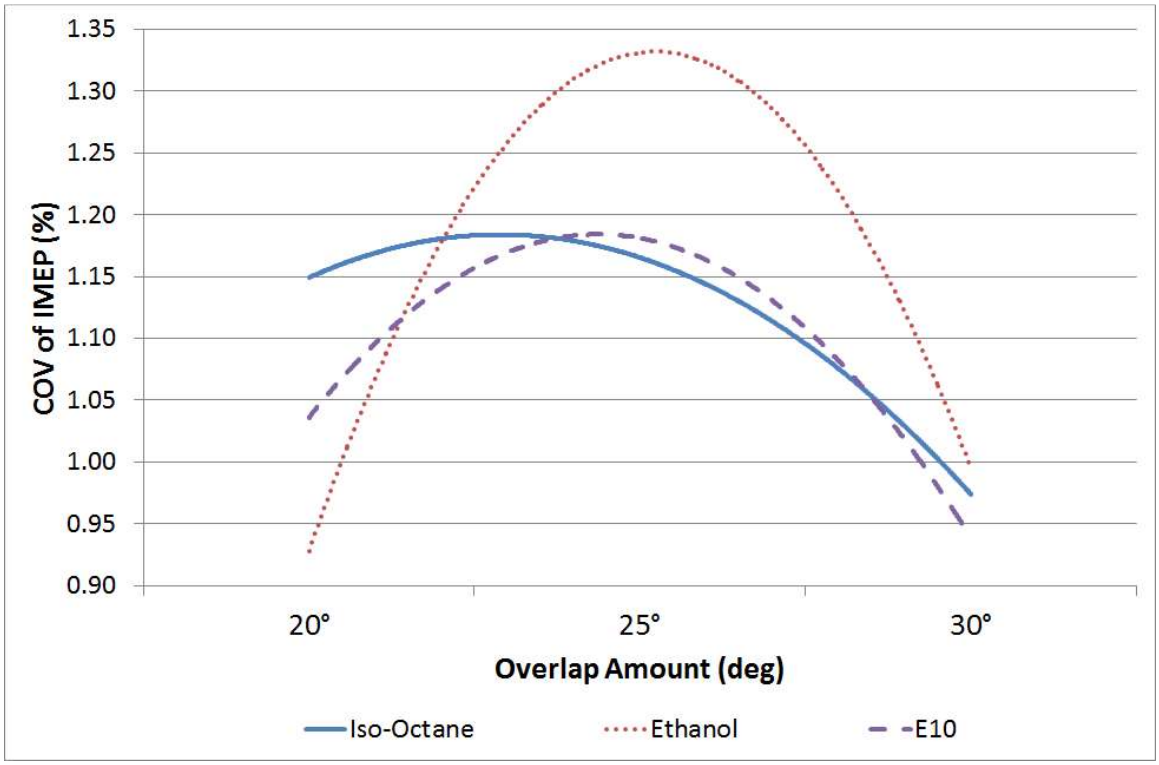

Figure 6.49 – COV of IMEP trendlines for the arithmetic mean for each fuel series for the three valve overlap cases.

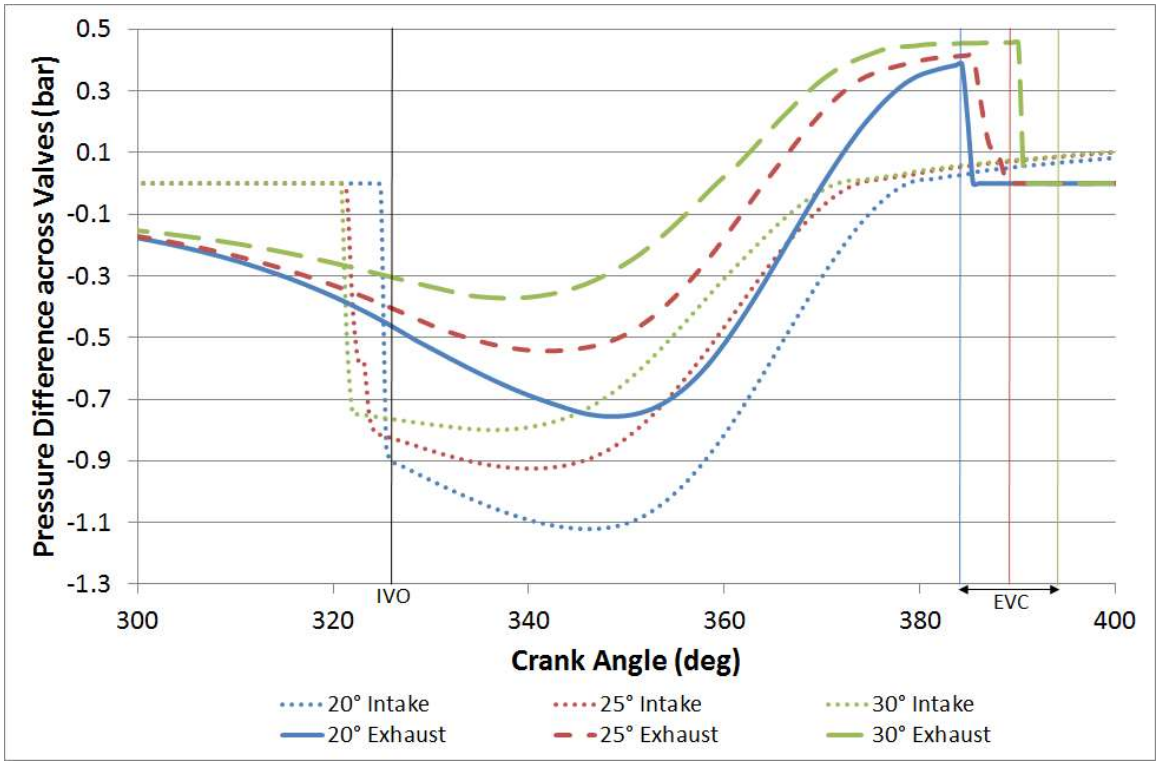

Figure 6.50 – Computed pressure difference between the intake and exhaust valves for the three overlap cases running iso-octane during the overlap period.

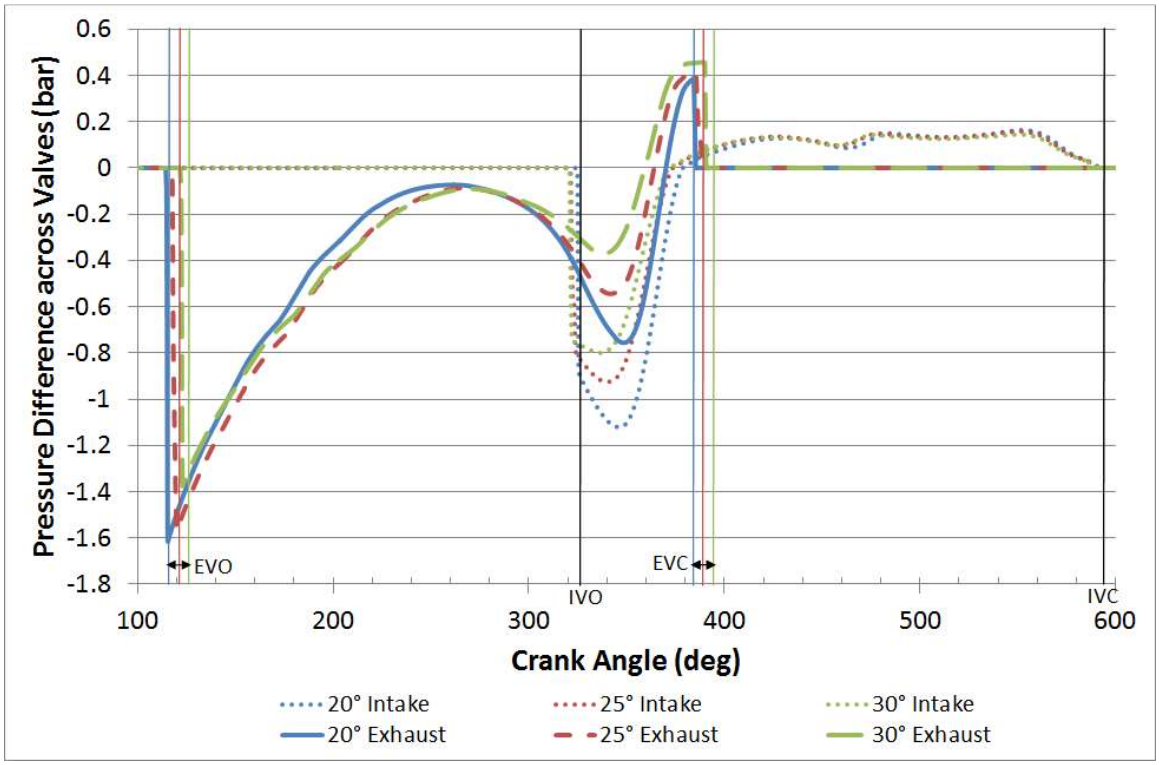

Figure 6.51 – Pressure difference across the values between EVO and IVC for the three overlap cases running iso-octane.

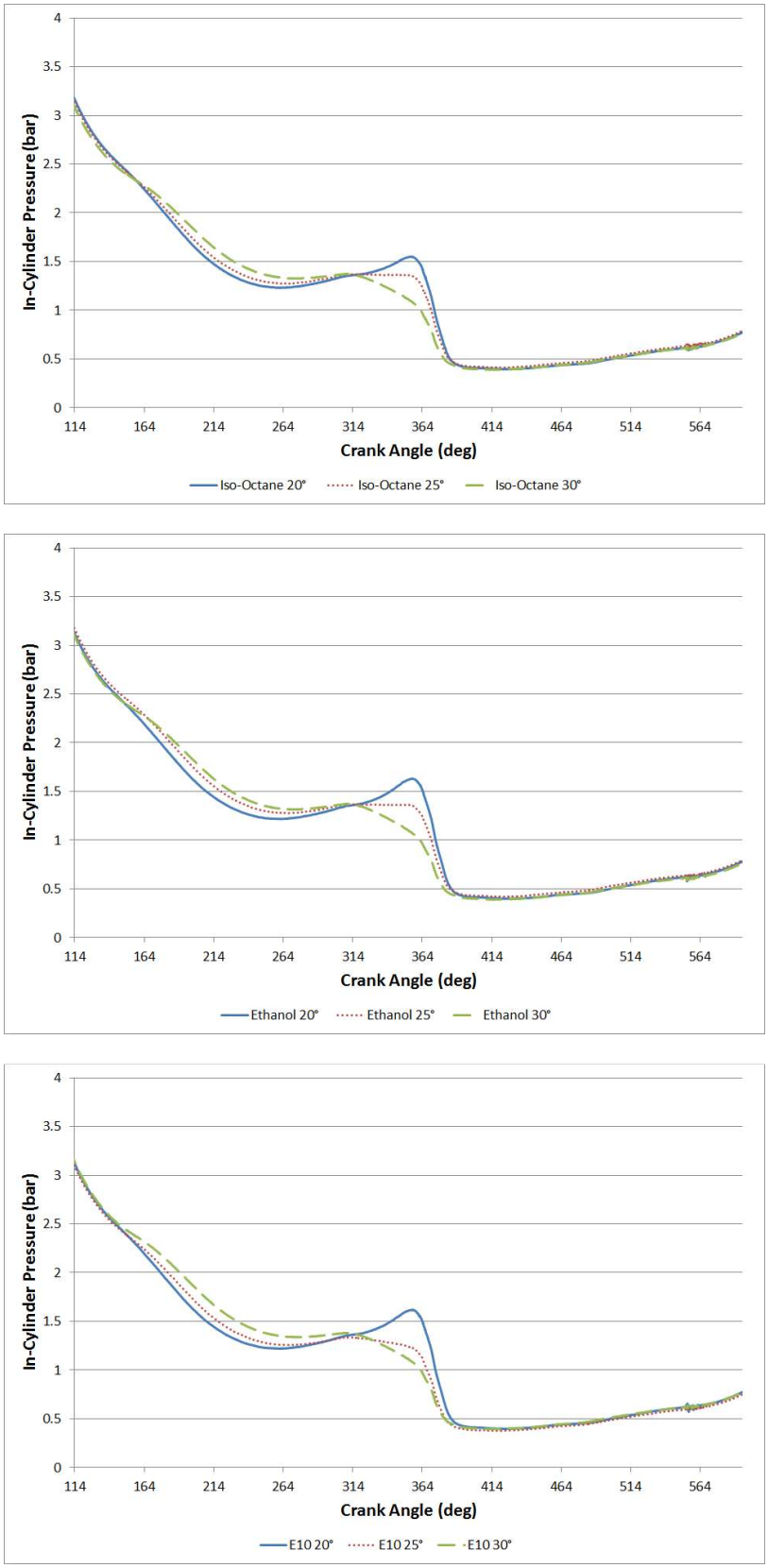

Figure 6.52 – In-Cylinder Pressure for the three fuel sets and overlap cases during the overlap durations.

Chapter 7

Conclusions & Recommendations

7.1 Summary of Findings

The work reported within this thesis was concerned with a series of complementary experimental studies investigating and analysing the impact of alcohol fuel blends on basic indicated combustion parameters in the Brunel University optical research engine. The research involved a number of separate investigations, including:

- Optical and thermodynamic study of the mean cycle effects with differing alcohol fuel blends under varying spark timing conditions
- Direct optical and thermodynamic comparison between cycle-to-cycle variations of ethanol and iso-octane fuels
- A study of mixture strength and its effect on combustion and performance
- A direct thermodynamic comparison between one high carbon content and one low carbon content alcohol fuel
- A study of the impact of varying valve timings and the impact upon breathing in the unique engine

Below is a summary of the main conclusions and analysis drawn from the work. Following at the end of this chapter will be a collection of suggestions for future research.

This first section of work was related to the influence of the fuel type under typical part-load stoichiometric combustion with a desire to gain a greater understanding of the interaction between each baseline fuel, namely iso-octane, ethanol, gasoline and E10, and the turbulence scales in the engine. Under fixed low valve overlap conditions, MBT and fixed spark timings were compared for all

baseline fuels tested. The fixed spark timing was set to equal that of the MBT timing for ethanol. In terms of load fluctuations between the two spark timings the variation was minimal (<5% for the worst performing fuel) and in terms of combustion stability the worst performing fuel was still operating well below the imposed limit of 5% COV of IMEP.

With this performance difference found to be negligible, the remaining experiments in this first section were then ignited at identical spark timing allowing for the key differences between each fuel's combustion to become apparent. For example, when observing the values for combustion duration, it was noted that E10 performed worse than the two constituent fuels included (10% ethanol and 90% iso-octane). This was unexpected given the faster laminar burning velocity reported for the ethanol. One explanation may be the combined fuel performed as an azeotrope, as suggested by Kar, Cheng and Ishii [2009], whereby the newly blended mixture takes on different characteristics not equal to the sum of its parent fuels. It is possible that this blend of E10 inherited a slightly retarded laminar burning velocity more aligned to iso-octane than ethanol. This can be seen when studying the flame radius development of the three fuels.

An important parameter in the assessment of a fuel's stability and comparative pressure development is that of the cyclic variation. When the fastest, slowest and mean cycles for each of the baseline fuels were overlaid the variation of each fuel became apparent. Despite identical mean development, the slower burning fuels (iso-octane and E10) were shown to exhibit the widest ranges of in-cylinder pressure development between the slowest and fastest cycles. The faster burning exhibited by pure ethanol fuel was shown to be the result of marginally higher initial laminar-like burning providing a "head start" to the turbulent flame development process, with the turbulent spectrum thereafter more quickly encroached**.**

During transition toward a fully developed state the flame can only be wrinkled by scales of turbulence smaller than the flame itself; larger scales merely serve to convect and distort the flame rather than directly improving enflamed area. If the

initial flame develops more quickly (primarily due to faster chemistry) it follows that more of the turbulent spectrum will become available more quickly to aid flame wrinkling and improve the rate of unburned mass entrainment into the flame. Such physical effects have been shown to be brought about by the faster initial chemical reaction rates with high ethanol content fuels in SI engines, but become amplified as the turbulent spectrum is faster encroached. While the chemical differences are often cited, such physical interactions have been widely overlooked within recent literature relating to ethanol use in modern SI engines.

Meanwhile the opposite was true of the slower burning fuels, while ethanol was aided by the knock-on effect of a faster laminar burning velocity, fuels with a slower laminar burning velocity may be negatively influenced by the flow. Due to a lower laminar burning velocity, the slower flame kernel may be more heavily distorted by the turbulent spectrum, which may also convect the kernel around the bore. While larger flame area does encourage a greater level of mass entrainment, the benefits are sometimes outweighed by the detrimental effects of flame stretch.

The next section of work was concerned with the impact of altering the mixture strength with varying fuels. Under lean conditions the excess air setting was set to the lean combustion limit of iso-octane while the rich lambda value was set to mirror the offset about the stoichiometric setting. It was found that when the mixture strength was altered this had an impact upon the ratio of specific heat and unburned gas temperature which led to large combined differences in burning velocity and flame speed.

When running a lean mixture the differences between iso-octane and ethanol in terms of in-cylinder mass and the ratio of specific heats (γ) was reduced, leading to ethanol having a lower end gas temperature upon combustion c.f. stoichiometric. Despite this lower gas temperature ethanol still possessed a faster laminar burning rate than iso-octane, though the apparent flame speed is largely similar to iso-octane. When the mixture strength is increased, ethanol's mass and gamma are increased creating slightly higher gas temperatures and a faster laminar burning velocity which leads to a higher apparent flame speed.

It is worth noting that the lean limit of this engine could be influenced by the charge motion which is influenced by the flow characteristics and layout of the intake ports. The current near-horizontal intake port layout of the engine has a direct impact on the flow structure of the inducted charge, potentially creating high tumble and turbulence intensity. In addition, the deactivated exhaust valve creates a restriction in scavenging and, when running the baseline overlap of 25°, ~11% residual gas fraction was predicted. The mean flow and turbulence levels should be experimentally quantified in future work to better understand such events.

The following section of work was concerned with comparing and contrasting two alcohol-isooctane blends with similar oxygen mass. One a high-carbon alcohol fuel source (butanol) and one a low-carbon alcohol fuel source (ethanol). This comparison was made in an effort to understand better the impact of using butanol as an additive in a mainstream fuel source. Some researchers have begun investigating the benefits of this biofuel due to the ability to use more sustainable and cheaper alcohol fuel in a blend, thus saving gasoline and reducing costs.

With regards to the comparison between the two alcohol fuels, in terms of combustion duration, pressure development and flame radius development (and therefore flame speed) the two blends were near identical. The only perceptible difference between them was an improvement in combustion stability and load output from the engine when operating the butanol iso-octane blend. The similarity is to be expected as the fuels were blended to the same oxygen mass (3.35%) but further proves that butanol has the potential, from a thermodynamic point of view, to be used as a gasoline additive.

In addition, this work further serves to highlight the difference between a blended fuel's combustion characteristics and those of its constituent fuels. Several authors have conducted studies into burning velocities for different neat alcohol fuels including Beeckmann, Kruse and Peters [2010]. In the latter paper it was reported that butanol has a faster laminar burning velocity than iso-octane and ethanol. Despite this data being gathered in a bomb, it did set out that blended fuels have vastly different laminar burning velocities when compared to their

constituent fuels and even the authors stated they were unsure of the exact reasons as to why this occurred. In addition, Beeckmann et al. stated that E10 was 5cm/s faster than Bu10. While these two fuels were not equal in oxygen content, this result would imply that the two fuels are not identical in burn structure and propagation during the laminar phase, contrary to the results presented here. This highlights that care should be taken when consulting literature for laminar burning velocities as they are by no means definitive nor are they indicative of standard engine operating conditions. Of the five correlations presented from literature, only one factored in flame stretch and instability effects and none accounted for flame cellularity.

Further investigations were made into the nature of cyclic variation after some variation phenomena were noted within the PMax values of iso-octane. These two phenomena were identified and given terms: “saw-toothing” and “creeping” cycles and what follows are the results of a study into what causes them and how they are self-supporting.

When observing the cyclic variation, periods with cycle-by-cycle alternating values of maximum in-cylinder pressure were observed. In addition sometimes such effects were amplified, where a slow cycle would lead to a fast cycle followed by slower still and faster still until the phenomenon broke down (which was associated with over-riding flow effects in the cases reviewed). During this saw-toothing, each of the cycles with higher peak in-cylinder pressure experienced faster combustion, which thereafter led to a lower blowdown pressure and higher amounts of residual mass (inhibited scavenging). This poorly scavenged cycle led to a lower peak in-cylinder pressure and slower cycle with improved blowdown scavenging, which in turn thereafter led to a fast cycle (or even amplified faster in some cases). Such oscillation was repetitive (albeit not always amplified due to the other sources of cyclic variation occurring in tandem) until such point that "normal" chaotic combustion continued. This phenomenon was concluded to be one of the main drivers of the fluctuations in pressure development and hence engine load. Potentially, therefore, if such events could be managed or controlled in the future

(via fast in-cycle fuelling, ignition and/or breathing control for example) then engine stability could be altered to aid combustion and performance as desired.

Some data exhibited a tendency towards a creep in peak in-cylinder pressure, where the values would steadily increase for a few cycles before a decline in pressure in line with the saw-toothing events but with an apparent reduction in residual content during the slow cycle. While saw-toothing is partially controlled by the residual level in the cylinder, which is dictated by the breathing this phenomenon was contradictory. This contradiction can be associated with bulk flame distortion effects, where increased large scale distortion of the flame sometimes led to an otherwise unexpected overall slower combustion event. Such events may have been associated with persisting bulk air motions with the current engine setup, with the high mean velocities leading to detrimental stretch effects later on.

When both creep and sawtooth events were identified in the PMax trace of the optically captured iso-octane cycles, the ethanol cycles were investigated for similar events. While these two phenomena were again identified in the trace, there were less events and the severity and duration of these events was also reduced c.f. iso-octane. It was concluded that the faster initial chemistry (and aforementioned knock-on effects) also helped to improve resistance to variations in both the flow and residual gas levels (with improved EGR tolerance with ethanol under stoichiometric conditions also widely acknowledged in the literature)

The final investigation of this thesis was concerned with the impact of differing levels of valve overlap on combustion of ethanol, iso-octane and E10. Under the varied valve overlap conditions studied the blowdown phase seemed to dominate the mass of residual gases ultimately trapped. It was at first surprising to see the MBT spark timing retard with increased overlap as an increased amount of residual might be expected (albeit only a small increase in overlap was studied). This has been associated with the retarded exhaust valve opening point and associated influence on the blowdown phase of the exhaust. Such effects help to highlight the

non-linear variation in EGR that may occur during valve phasing events of relatively low valve overlap setting located nearer to TDC.

The results set out in Chapter 6 demonstrate that the combustion duration of ethanol was less affected by small changes in the level of residual gas compared to iso-octane. This is in agreement with much of the literature presented in Chapter 2, with good agreement that ethanol presents good synergy with EGR under typical part-load stoichiometric SI conditions. It should be noted however that the amount of overlap studied here was limited and a wider sweep of valve overlap would be beneficial to give a greater understanding of the different fuels' interaction with residual gases.

7.2 Recommendations for Future Work

The flame imaged data in this study have provided a valuable insight into the interaction between alcohol fuels and the turbulence scales present in a port-fuelled SI engine. To gain a greater understanding of these effects, particle imaging and particle tracking work could be carried out to quantify the turbulence intensity in the engine during stoichiometric combustion. This study would allow for improved predictions of the flow patterns in the chamber, how repeatable they are and how they could be manipulated to possibly promote more ideal combustion events.

The cylinder head could also be altered to accept a wider laser sheet. This would be easiest achieved by inserting a silica disc between the cylinder liner and the head. This may also have to involve some changes to the piston design to avoid optical liner damage. With Mie scatter laser sheet imaging further study could be accurately undertaken into the small scale flame wrinkling and three-dimensional effects that are assumed to occur, in particular during the investigations into the cyclic variation in a suite of combustion data.

The fixed valve overlap sweep experimentation resulted in counter-intuitive results with regards to the residual gas levels in the cylinder between cycles. However this could be largely due to the unique exhaust valve configuration of the engine. A new cylinder head should be obtained with both exhaust valves working

allowing the user to run from very low residual gas fraction to the maximum possible without the throttling effects due to the deactivated valve. Once this has been installed then a wider sweep of valve timings and overlap variations should be executed to gain a better understanding of the role that residual gas levels play in the combustion of alcohol fuels. From the data presented above, ethanol was found to be less sensitive to the increase in residual gas fraction but a further quantification of ethanol's synergy with EGR would be valuable.

With a greater control of the residual gas level in the cylinder then a further study to evaluate the two cyclic variation phenomena seen here could be undertaken. Both are heavily influenced by the levels of residual gas in the cylinder from cycle to cycle therefore to be able to run the engine with near zero levels of residual gas, theory would suggest that the severity of sawtoothing and creep would decline. A sweep of valve overlap durations would allow for a future researcher to identify how the level of latent residual gas in the cylinder impacts on the cycles prior to any breathing effects and scavenging efficiency variations that cause the cycle-to-cycle phenomena.

Several researchers have touted butanol as a good gasoline additive with some suggestion of supplanting ethanol and, purely based on performance terms examined here the two fuels look very similar in terms of flame and pressure development. However, one area not examined here was the impact upon emissions when running the higher carbon fuel. Various papers have implied a higher release of HC emissions [Cairns et al., 2010] (as logic would dictate) but the fuller picture of emissions is less well known. Some authors say that NOx and CO emissions are lower [Stansfield et al., 2012] some say higher [Cairns et al., 2010; Merola, et al. 2013]. In future work, a study into the emissions of running this alcohol blend would be beneficial however care must be taken when obtaining emissions data from an optical engine due to the heat transfer properties of the window. Either a characterisation study should take place to quantify the impact of the glass on emissions when compared to a fully thermodynamic engine, thus allowing for emissions measurement correlation to specific optical cycles or

emissions could be obtained solely from a thermodynamic engine, devoid of glass to present more real-world conditions.

In addition, when discussing the differences between ethanol and iso-octane in this study, the author was able to return to the computed values of laminar burning velocity and the knock-on benefit that a faster laminar burning velocity has on combustion for ethanol. This study should be extended out to include butanol, thus allowing for a greater understanding of the differences between the two types of alcohol fuel. This work would involve the running of neat butanol in the computational model and in the test cell to allow for model validation and imaged data to be extracted for analysis. While presenting two blended fuels for conclusion has presented very closely matched fuels in terms of combustion and output, as stated earlier in this chapter, a blended fuel may not always exhibit combustion parameters equivalent to that of its constituent fuels, thus the butanol and ethanol comparison requires further attention in future work.

Finally it has been demonstrated in this work that the existing laminar and turbulent burning velocity correlations for such new fuels are somewhat sparse and contradictory, at least those within the public domain. It is only with such correlations that fundamental turbulent flame development effects can be fully understood and potentially modelled in the future to reduce engine development costs. A vital recommendation to emerge from this work is for a future user to evaluate the laminar burning velocity of ethanol, iso-octane, gasoline and butanol in a bomb at the reference conditions of 1 bar and 293°K across a sweep of mixture strengths, then to transfer those fuels to an optical SI engine (such as the one employed in this work) and quantify the impact of those empirically-obtained laminar burning velocities on flame structure, propagation and speed at traditional engine speeds and loads with a quantified and constant turbulence intensity.

Chapter 8

References

Abraham, J., Williams, F. A. and Bracco, F. V. (1985), *A Discussion of Turbulent Flame Structure in Premixed Charges*, SAE Technical Paper 850345.

Abdel-Gayed, R.G., Bradley, D. and Lawes, M. (1987), *Turbulent burning velocities: a general correlation in terms of straining rates*, Proc. R. Soc. London A414, pp. 389-413.

Abdi Aghdam, E. (2003), *Improvement and Validation of a Thermodynamic SI Engine Simulation Code*, PhD Thesis, University of Leeds.

Abu-Jrai, A., Tsolakis, A., Theinnoi, K., Cracknell, R., Megaritis, A., Yyszynski, M. L. and Golunski, S.E. (2006), *Effect of Gas-to-Liquid Diesel Fuels on Combustion Characteristics, Engine Emissions, and Exhaust Gas Fuel Reforming - Comparative Study*, Energy Fuels, Vol. 20, Iss. 6, pp. 2377-2384.

Aleiferis, P. G., Malcolm, J. S., Todd, A. R., Cairns, A. and Hoffmann, H. (2008), *An Optical Study of Spray Development and Combustion of Ethanol, Iso-Octane and Gasoline Blends in a DISI Engine*, SAE Technical Paper 2008-01-0073.

Al-Farayedhi, A., Al-Dawood, A. M. and Gandhidasan, P. (2000), *Effects of Blending Crude Ethanol with Unleaded Gasoline on Exhaust Emissions of SI Engine*, SAE Technical Paper 2000-01-2857.

Amann, C. A. (1985), *Cylinder-Pressure Measurement and its use in Engine Research,* SAE Technical Paper 852067.

Arcoumanis, C. (1988), *Internal Combustion Engines*, Academic Press: San Diego, ISBN 978-0-12-059790-1.

Automotive Council UK (2013), *Passenger Car Low Carbon Technology Roadmap*, Accessed online: http://www.automotivecouncil.co.uk/wp-content/uploads/2013/09/Passenger-car.jpg. [Last accessed 10th December 2013].

AVL (2013), *Pressure Sensor for Combustion Analysis: Data Sheet*, Accessed online: https://www.avl.com/c/document_library/get_file?uuid=04bf17cd-447b-44d7-b50f-7b5cd0b7029d&groupId=10138&download. [Last Accessed 1st August 2013].

Bai, S., Li, G., Zhao, H. and William, D. J. T. (2009), *Experiment Study of Stratified Combustion at Different Boost Pressure*, Power and Energy Engineering Conference, DOI – 10.1109/APPEEC.2009.4918350.

Bergström, K. (2007), *ABC- Alcohol Based Combustion Engines Challenges and Opportunities*, 16th Aachener Kolloquium Fahrzeug- und Motorentechnik.

Beeckmann, J., Kruse, S. and Peters, N. (2010), *Effect of Ethanol and n-Butanol on Standard Gasoline Regarding Laminar Burning Velocities*, SAE Technical Paper 2010-01-1452.

Beretta, G. P., Rashidi, M. and Keck, J.C. (1983), *Turbulent Flame Propagation and Combustion in Spark Ignition Engines*, Combustion and Flame, Vol. 52, pp. 217-245.

Bisordi, A., OudeNijeweme, D., Bassett, M., Stansfield, P., Williams, J. and Ali, R. (2012), *Evaluating Synergies between Fuels and Near Term Powertrain Technologies through Vehicle Drive Cycle and Performance Simulation*, SAE Technical Paper 2012-01-0357.

Borghi, R. (1988), *Turbulent Combustion Modelling*, Progress in Energy and Combustion Science, Vol. 14, Iss. 4, pp. 245-292.

Bowditch, F. W. (1960), *Cylinder and Piston Assembly*, US Patent 2,919,688.

Bradley, D., Haq, M. Z., Hicks, R. A., Kitagawa, T., Lawes, M., Sheppard, C. G. W. and Woolley, R. (2003), *Turbulent burning velocity, burned gas distribution and associsated flame surface definition*, Combustion and Flame, Vol. 133, Iss. 4, pp. 415-430.

Bradley, D., Hicks, R. A., Lawes, M., Sheppard, C. G. W. and Wooley, R. (1998), *The measurement of laminar burning velocities and Markstein numbers for iso-octane-air and iso-octane-n-heptane-air mixtures at elevated temperatures and pressures in an explosion bomb*, Combustion and Flame, Vol. 115, pp.126.

Bradley, D., Lawes, M. and Sheppard, C.G.W. (2000), *Combustion and the thermodynamic performance of spark ignition engines*, Proc. Instn. Mech. Engrs. – Part C: Journal of Mechanical Engineering Science, Vol. 214, pp. 257-268.

Bradley, D., Lau, A. K. C. and Lawes, M. (1992), *Flame Stretch Rate as a Determinant of Turbulent Burning Velocity*, Phil. Trans. R. Soc. London A338, pp. 359-387.

Bradley, D. and Lung, F. K-K. (1987), *Spark Ignition and the Early Stages of Turbulent Flame Propagation*, Combustion and Flame, Vol. 69, pp. 71-93.

Brewster, S. (2007), *Initial Development of a Turbo-Charged Direct injection E100 Combustion System*, SAE Technical Paper 2007-01-3625.

Broustail, G., Seers, P., Halter, F., Moréac, G. and Mounaim-Rousselle, C. (2011), *Experimental determination of laminar burning velocity for butanol and ethanol iso-octane blends*, Fuel, Vol. 90, Iss. 1, pp. 1-6.

Browning, L. H. (1991), *Abnormal Combustion in Methanol-Fuelled, Crankcase-Scavenged Two-Stroke Engines – A Theoretical Study*, SAE Technical Paper 911304.

Buran, D. (1998), *Turbulent flame propagation in a methane fuelled spark ignition engine*, PhD Thesis, University of Leeds.

Cairns, A. (2001), *Turbulent Flame Development in a Spark Ignition Engine*, PhD thesis, University of Leeds.

Cairns, A. and Sheppard, C. G. W. (2000), *Cyclically Resolved Simultaneous Flame and Flow Imaging in a SI Engine*, SAE Technical Paper 2000-01-2832.

Cairns, A., Blaxill, H. and Irlam, G. (2006), *Exhaust Gas Recirculation for Improved Part and Full Load Fuel Economy in a Turbocharged Gasoline Engine*, SAE Technical Paper 2006-01-0047.

Cairns, A., Fraser, N. and Blaxill, H. (2008), *Pre Versus Post Compressor Supply of Cooled EGR for Full Load Fuel Economy in Turbocharged Gasoline Engine,* SAE Technical Paper 2008-01-0425.

Cairns, A., Stansfield, P., Fraser, N., Blaxill, H., Gold, M., Rogerson, J. and Goodfellow, C. (2009), *A Study of Gasoline-Alcohol Blended Fuels in an Advanced Turbocharged DISI Engine,* SAE Technical Paper 2009-01-0138.

Cairns, A., Todd, A., Aleiferis, P., Fraser, N. and Malcolm, J. (2010), *A Study of Alcohol Blended Fuels in an Unthrottled Single Cylinder Spark Ignition Engine*, SAE Technical Paper 2010-01-0618.

Cheng, W. (2011), *Bio-fuels and hybrids,* [Presentation given to Brunel CAPF, Tuesday 3rd May 2011].

Chomiak, J. (1972), *Application of Chemiluminescence Measurement to the Study of Turbulent Flame Structure*, Combustion and Flame, Vol. 18, Iss. 3, pp. 429-433.

Coryton Advanced Fuels (2013), *Certificate of Analysis*, Data of Fuel Blend No. CAF-W 13/041.

Council Regulation EC 443/2009 (2009), *Setting emission performance standards for new passenger cars as part of the Community's integrated approach to reduce CO_2 emissions from light-duty vehicles*, OJ L140/1.

Cowart, J. S., Boruta, W. E., Dalton, J. D., Dona, R. F., Rivard II, F. L., Furby, R. S., Piontkowski, J. A., Seiter, R. E. and Takai, R. M. (1995), *Powertrain Development of the 1996 Ford Flexible Fuel Taurus,* SAE Technical Paper 952751.

Cracknell, R., Prakash, A. and Head, R. (2012), *Influence of Laminar Burning Velocities on Performance of Gasoline Engine*, SAE Technical Paper 2012-01-1742.

Cummins Jr., C. L. (1976), *Internal Fire*, Carnot Press/Graphic Arts Centre: Oregon, USA. ISBN 978-0-89-883765-0.

Damköhler, G. (1940), *The effect of Turbulence on Flame Velocity in Gas Mixtures*, Z. Elektrochemie Angewandte Phys. Chem., Vol. 46.

Davis, G. W., Bouboulis, J. and Heil, E. (1999), *The Effect of Multiple Spark Discharge on the Cold-Startability of an E85 Fuelled Vehicle*, SAE Technical Paper 1999-01-0609.

Dec, J. E. and Espey, C. (1998), *Chemiluminescence Imaging of Auto ignition in a DI Diesel Engine*, SAE Technical Paper 982685.

DECC (2011), *The Carbon Plan: Delivering our low carbon future*, London: UK Government.

Dimopoulos, P., Rechsteiner, C., Soltic, P., Laemmle, C. and Boulouchos, K. (2007), *Increase of passenger car engine efficiency with low engine-out emissions using hydrogen-natural gas mixtures: A thermodynamic analysis,* International Journal of Hydrogen Energy, Vol. 32, No. 14, pp. 3073-3083.

Dingle, S. (2014), "The Effects of Future Fuels and Lubricants on Combustion in Future Spark Ignition Engines", PhD thesis, Brunel University London.

Dohmel, K. (2008), *Future Mobility from a Fuels Perspective*, 29 Internationales Wiener Motorensymposium.

EC Comission (2001), *Communication on alternative fuels for road transportation and on a set of measures to promote the use of biofuels*, COM (2001) 547.

Euractiv (2012), *EU agrees 10% 'green fuel' target in renewables deal,* Accessed online: http://www.euractiv.com/transport/eu-agrees-10-green-fuel-target-r-news-220953. [Last accessed 18th June 2012].

Foong, T. M., Morganti, K. J., Brear, M. J., de Silva, G., Yang, Y. and Dryer, F. L. (2013), *The Effect of Charge Cooling on the RON of Ethanol/Gasoline Blends*, SAE Technical Paper 2013-01-0886.

Fujimoto, M. and Tabat, M. (1993), *Effect of Swirl Rate on Mixture Formation in a Spark Ignition Engine Based on Laser 2-D Visualisation Techniques*, SAE Technical Paper 931905.

Gander, W., Golub, G. H. and Strebel, R. (1994), *Fitting of circles and ellipses – least squares solution*, Institut für Wissenschaftliches Rechnen, ETH Zurich, Technical Report 217.

Gatowski, J. A., Heywood, J. B. and Deleplace, C. (1984), *Flame Photographs in a Spark Ignition Engine*, Combustion and Flame, Vol. 56, pp. 71-81.

Galante-Fox, J., Von Bacho, P., Notaro, C. and Zizelman, J. (2007), *E85 Fuel Corrosivity: Effects of Port Fuel Injector Durability Performance*, SAE Technical Paper 2007-01-4072.

GEMS (2011), *1200 Series/1600 Series – OEM Transducers Featuring Exceptional Proof Pressure and Stability Specifications,* Accessed online: http://www.gemssensors.com/~/media/GemsNA/CatalogPages/1200-and-1600-series-cat.ashx. [Last accessed 1st August 2013].

Gillespie, L. (1998), *Imaging and Analysis of Turbulent Flame Development in Spark Ignition Engines*, PhD Thesis, University of Leeds.

Gillespie, L., Lawes, M., Sheppard, C. G. W. and Wooley, R. (2000), *Aspects of Laminar and Turbulent Burning Velocity Relevant to SI Engines*, SAE Technical Paper 2000-01-0192.

Gingrich, J., Alger, T. and Sullivan, B. (2009), *Ethanol Flex-fuel Engine Improvements with Exhaust Gas Recirculation and Hydrogen Enrichment*, SAE Technical Paper 2009-01-0140.

Glyde, H. S. (1930), *Experiments to Determine Velocities of Flame Propagation in a Side Valve Petrol Engine*, Journal of the Institute of Petroleum Technology, Vol. 16, pp. 756-776.

Griffin, W.M., Lave, L.B. and MacLean, H.L. (2001), *Promise and Cost of Cellulosic Ethanol for the US Light-Duty Fleet*, SAE Technical Paper 2001-01-2474.

Gülder, Ö. L., (1982) Burning Velocities of Ethanol-Isooctane Blends, Combustion and Flame, Vol. 56, pp. 261-168.

Gu, X. J., Haq, M. Z., Lawes, M. and Wooley, R. (2000), *Laminar Burning Velocity and Markstein length measurements for methane-air mixtures*, Combustion and Flame, Vol. 121, Iss. 1-2, pp. 41–58.

Hall, M. J. and Bracco, F. V. (1987), *A Study of Velocities and Turbulence Intensities Measured in Firing and Motored Engines*, SAE Technical Paper 870453.

Hanson, R. K., Seitzman, J. M. and Paul, P. H. (1990), *Planer laser-induced fluorescence imaging of combustion gases*, Appl. Phys. B, Vol. 50, Iss. 6, pp. 441-454.

Harper, C. M. (1989), *Turbulence and Combustion Instabilities in Engines,* PhD Thesis, University of Leeds.

Hattrell, T. (2007), *A Computational and Experimental Study of Spark Ignition Engine Combustion*, PhD Thesis, University of Leeds.

Heywood, J. B. (1988), *Internal Combustion Engine Fundamentals*, McGraw-Hill: New York, USA. ISBN 978-0-07-700499-2.

Hicks, R. A., Lawes, M., Sheppard, C. G. W. and Whitaker, B. J. (1994), *Multiple Laser Sheet Imaging Investigation of Turbulent Flame Structure in a Spark Ignition Engine*, SAE Technical Paper 941992.

Hillier, V. A. W. and Coombes, P., (2004), *Hilliers Fundamentals of Motor Vehicle Technology, 5th Edition,* Nelson Thornes Ltd: Cheltenham, UK. ISBN 978-0-7487-8082-2.

Kameoka, A., Nagai, K., Sugiyama, G. and Seko, T. (2005), *Effect of Alcohol Fuels on Fuel-Line Materials of Gasoline Vehicles*, SAE Technical Paper 2005-01-3708.

Kar, K., Last, T. Haywood, R. and Raine, R. (2008), *Measurement of vapour pressures and enthalpies of the vaporisation of gasoline and ethanol blends and their effects on mixture preparation in an SI engine*, SAE Technical Paper 2008-01-0317.

Kar, K., Cheng, W. and Ishii, K. (2009), *Effects of Ethanol Content on Gasohol PFI Engine Wide-Open Throttle Operation*, SAE Technical Paper 2009-01-1907.

Karman, D. (2003), *Ethanol fuelled motor vehicle emissions: A literature review*, Air Health Effects Division, Health Canada.

Keck, J. C. (1982), *Burning velocities of mixtures of air with methanol, isooctane, and indolene at high pressure and temperature*, Combustion and Flame, Vol. 48, pp. 191-210.

Kirkpatrick, A. T. (2006), *Simple Finite Heat Release Model*, Colorado State University, Accessed online: http://www.engr.colostate.edu/~allan/thermo/page6/page6.html [Last accessed 28th May 2013].

König, G. and Sheppard, C. G. W. (1990), *End Gas Auto ignition and Knock in a Spark Ignition Engine*, SAE Technical Paper 902135.

Kramer, U. and Philips, P. (2002), *Phasing Strategy for An Engine With Twin Variable Cam Timing*, SAE Technical Paper 2002-01-1101.

Kremer, F. G. and Fachetti, A. (2000), *Alcohol as Automotive Fuel – Brazilian Experience*, SAE Technical Paper 2000-01-1965.

Kremer, F. G., Jardim, J. L. F. and Maia, D. M. (1996), *Effects of Alcohol Composition on Gasohol Vehicle Emissions*, SAE Technical Paper 962094.

Kulzer, A., Christ, A., Rauscher, M., Sauer, C., Würfel, G. and Blank, T. (2006), *Thermodynamic Analysis and Benchmark of Various Gasoline Combustion Concepts*, SAE Technical Paper 2006-01-0231.

Kurada, S., Rankin, G. W. and Sridhar, K. (1993), *Particle-imaging techniques for quantitative flow visualization: a review*, Optics & Laser Technology, Vol. 25, No. 4, pp. 219-233.

Li, Y., Zhao, H. and Brouzos, M. (2008), *CAI Combustion with Methanol and Ethanol in an Air-Assisted Direct-Injection Engine*, SAE Technical Paper 2008-01-1673.

Li, Y., Zhao, H., Peng, Z. and Ladommatos, N. (2001), *Analysis of Tumble and Swirl Motions in a Four-Valve SI Engine*, SAE Technical Paper 2001-01-3555.

Louis, J.J.J. (2001), *Well-to-Wheel Energy Use and Greenhouse Gas Emissions for Various Vehicle Technologies*, SAE Technical Paper 2001-01-1343.

Lozano, A., Yip, B and Hanson, R. K. (1992), *Acetone: a tracer for concentration measurements in gaseous flows by planar laser-induced fluorescence*, Exp. in Fluids, Vol. 13, Iss. 6, pp. 369-376.

Lyon, D. (1986), *Knock and cyclic dispersion in a spark ignition engine*, Petroleum Based Fuels and Automotive Application, I. Mech. E. Conf. Proc. Paper C307/86, pp. 105-115.

Ma, F., Shen, H., Liu, C., Wu, D, Li, G. and Jiang, D. (1996), *The Importance of Turbulence and Initial Flame Kernel Centre Position on the Cyclic Combustion Variations for Spark-Ignition Engine*, SAE Technical Paper 961969.

Male, T. (1949), *Photographs at 500,000 Frames per Second of Combustion and Detonation*, Proc. 3rd Symposium on Combustion, pp. 721-726.

Malcolm, J.S., Aleiferis, P.G., Todd, A.R., Cairns, A., Hume, A., Blaxill, H., Hoffmann, H. and Rückauf, J. (2007), *A Study of Alcohol Blended Fuels in a New Optical Spark-Ignition Engine*, IMechE Performance, Fuel Economy and Emissions Conference, London.

Maunula, T. and Kinnunen, T. (2009), *Effect of Oxygen Containing Biofuels on the Emissions with Exhaust Gas Catalysts*, SAE Technical Paper 2009-01-2737.

McCarthy, T. (2011), *Ford's Perspective on Future Fuels and Their Engines* [Presentation given to University of Wisconsin Engine Research Centre Symposium, June 8th 2011].

Merola, S. S., Marchitto, L., Tornatore, C., Valentino, G. and Irimescu, A. (2013), *UV-visible Optical Characterization of the Early Combustion Stage in a DISI Engine Fuelled with Butanol-Gasoline Blend*, SAE Technical Paper 2013-01-2638.

Metghalchi, M. and Keck, J. C. (1980), *Laminar burning velocities of Propane- Air Mixtures at High Temperature and Pressure*, Combustion and Flame, Vol. 38, pp. 143-154.

Metghalchi, M. and Keck, J. C. (1982), *Burning velocities of Mixtures of Air with Methanol, Iso-Octane and Indolene at High Temperature and Pressure*, Combustion and Flame, Vol. 48, pp. 191-210.

Moro, D., Minelli, G. and Serra, G. (2001), *Thermodynamic Analysisof Variable Valve Timing Influence on SI Engine Efficiency*, SAE Technical Paper 2001-01-0667.

Moxey, B.G., Cairns, A., Ganippa, L., Zhao, H. and Bassett, M. (2012), *A Study of Combining Gasoline Engine Downsizing and Controlled Auto-Ignition Combustion*, Journal of KONES Powertrain and Transport, Vol. 19, No. 1, pp. 289-300.

Murad, A. E. M. (2006), *Flow and Combustion in disc and pent-roof SI engines*, PhD Thesis, Leeds University.

NACE (2001), *Determining Corrosive Properties of Cargoes in Petroleum Product Pipelines*, NACE TM0172-2001.

Nagayama, I., Araki, Y. and Iioka, Y. (1977), *Effects of Swirl and Squish on SI Engine Combustion and Emissions*, SAE Technical Paper 770217.

Nakajima, S., Saiki, R. and Goryozono, Y. (2007), *Development of an Engine for Flexible Fuel Vehicles (FFV)*, SAE Technical Paper 2007-01-3616.

Nordgren, H., Hildingsson, L., Johansson, B., Dahlén, L. and Konstanzer, D. (2003), *Comparison Between In-Cylinder PIV Measurements, CFD Simulations and Steady-Flow Impulse Torque Swirl Meter Measurements*, SAE Technical Paper 2003-01-3147.

Nori, V. and Seitzman, J. (2008), *Evaluation of chemiluminescence as a combustion diagnostic under varying conditions*, 46th AIAA Aerospace Sciences Meeting and Exhibit, Reno, NV, pp. 7-10.

OECD (2010), *Reducing Transport Greenhouse Gas Emissions: Trends and Data,* International Transport Forum.

ORNL (2011), *Biomass Energy Data Book*, Accessed online: http://cta.ornl.gov/bedb/index.shtml [Last accessed 11th July 2013].

Owen, K. and Coley, T. (1995), *Automotive Fuels Reference Book,* Second Edition, SAE: Warrendale, USA. ISBN 978-1-56-091589-8.

Pearson, R. J., Turner, J. W. G., Eisaman, M. D. and Littau, K. A. (2009), *Extending the Supply of Alcohol Fuels for Energy Security and Carbon Reduction*, SAE Technical Paper 2009-01-2764.

Peng, Z., Zhao, H. and Ladommatos, N. (2003), *Visualisation of the HCCI/CAI combustion process using two-dimensional planar laser-induced fluorescence imaging of formaldehyde,* Proc. Instn. Mech. Engrs. Part D: J. of Automobile Engineering, Vol. 217, Iss. 12, pp. 1125-1134.

Peters, N. (1986), *Laminar Flame Concepts in Turbulent Combustion*, 21st Int. Symp. on Combustion, pp. 1231-1250.

Pickett, L. M., Kook, S. and Williams, T. C. (2009), *Visualization of Diesel Spray Penetration, Cool-Flame, Ignition, High-Temperature Combustion, and Soot Formation Using High-Speed Imaging*, SAE Technical Paper 2009-01-0658.

Pulkrabek, W. W. (2004), *Engineering Fundamentals of the Internal Combustion Engine,* Second Edition, Editorial Prentice Hall: New Jersey, USA. ISBN 978-0-13-191855-9.

Qi, D., Leick, M., Liu, Y and Lee, C.F. (2011), *Effect of EGR and injection timing on combustion and emission characteristics of split injection strategy DI-diesel engine fuelled with biodiesel*, Fuel, Vol. 90, No. 5, pp. 1884-1891.

Rassweiler, G. and Withrow, L. (1938), *Motion Pictures of Engine Flames Correlated with Pressure Cards*, SAE Technical Paper 380139.

Ricardo, H. R. (1968), *The Internal Combustion Engine (Vol. 2)*, Blackie and Sons: London. ISBN 978-0-21-689026-8.

Roberts, C. E. and Stanglmaier, R. H. (1999), *Investigation of Intake Timing Effects ofn the Cold Start Behaviour of a Spark Ignition Engine*, SAE Technical Paper 1999-01-3622.

Royal Society, The (2008), *Sustainable biofuels: prospects and challenges*, London: The Royal Society ISBN 978-0-85-403662-2.

Schäfer, J. and Balko, J. (2007), *High Performance Electric Camshaft Phasing System*, SAE Technical Paper 2007-01-1294.

Schelp, H. (1936), *Alcohol Blends in Gasoline*, SAE Technical Paper no. 360058.

Settles, G. S. (2001), *Schlieren and Shadowgraph Techniques: Visualising Phenomena in Transparent Media*, Berlin: Springer-Verlag. ISBN 978-3-54-066155-9.

Siewart, R. M. and Groff, E. G. (1987), *Unassisted cold starts to -29°C and steady-state tests of a direct-injection stratified-charge (DISC) engine operating neat alcohol,* SAE Technical Paper 872066.

Smith, J. R. (1982), *Turbulent Flame Structure in a Homogeneous-Charge Engine*, SAE Technical Paper 820043.

Srinivasan, C. A. and Saravanan, C. G. (2010), *Emission Reduction on Ethanol-Gasoline Blends using 1, 4 Dioxan*, Proceedings of the World Congress on Engineering 2010 Vol. 2. ISBN 978-988-18210-7-2.

Stansfield, P. A., Bisordi, A., OudeNijeweme, D., Williams, J., Gold, M. and Ali, R. (2012), *The Performance of a Modern Vehicle on a Variety of Alcohol-Gasoline Fuel Blends*, SAE Technical Paper 2012-01-1272.

Stone, R. (1992), *Introduction to Internal Combustion Engines, 2nd Edition,* MacMillan Press, Hampshire, UK. ISBN 978-0-33-355084-7.

Suga, T. and Hamazaki, Y. (1992), *Development of Honda Flexible Fuel Vehicle*, SAE Technical Paper 922276.

Suyabodha, A., Pennycott, A. and Brace, C.J. (2013), *A preliminary approach to simulating cyclic variability in a port-fuel injection spark ignition engine,* Proc. Instn. Mech. Engrs. Part D: J. of Automobile Engineering, Vol. 227, Iss. 5, pp. 665-674.

Tabaczynski, R.J. (1976), *Turbulence and Turbulent Combustion in Spark-Ignition Engines*, Progress in Energy and Combustion in Science, Vol. 2, Iss. 3, pp. 143-165.

Tanaka, T. and Tabata, M. (1994), *Planar Measurements of OH Radicals in an S.I. Engine Based on Laser Induced Fluorescence*, SAE Technical Paper 940477.

Taniguchi, S., Yoshida, K. and Tsukasaki, Y. (2007), *Feasibility Study of Ethanol Applications to a Direct Injection Gasoline Engine*, JSAE 20077079.

Taylor, J., Fraser, N. and Wieske, P. (2010), *Water Cooled Exhaust Manifoldand Full Load EGR Tehcnology Applied to a Downsized Direct Injection Spark Ignition Engine*, SAE Technical Paper 2010-01-0356.

Thorlabs (2012), *Diffuser Transmission vs. Output Angle,* Thorlabs website, Accessed online: http://www.thorlabs.de/newgrouppage9.cfm?objectgroup_id=1132 [Last accessed 15th July 2012].

Tsolakis, A., Megaritis, A., Wyszynski, M. L. and Theinnoi, K. (2007), *Engine performance and emissions of a diesel engine operating on diesel-RME blends with EGR,* Energy Fuels, Vol. 31, Iss. 11, pp. 2072-2080.

Tsolakis, A., Megaritis, A. and Yap, D. (2007), *Application of exhaust gas fuel reforming in diesel and homogeneous charge compression ignition (HCCI) engines fuelled with biofuels*, Energy Fuels, Vol. 33, Iss. 3, pp. 462-470.

Tsukasaki, Y., Yasuda, A., Ito, S. and Nohira, H. (1990), *Study of Mileage-Related Formaldehyde Emission from Methanol Fuelled Vehicle*, SAE Technical Paper 900705.

Tullis, S. and Greeves, G. (1996), *Improving NOx Versus BSFC with EUI 2000 Using EGR and Pilot Injection for Heavy-Duty Diesel Engines*, SAE Technical Paper 960843.

Turner, J. W. G., Pearson, R. J., Bell, A., de Goede, S. and Woolard, C. (2012), *Iso-Stoichiometric Ternary Blends of Gasoline, Ethanol and Methanol: Investigations into Exhaust Emissions, Blend Properties and Octane Numbers*, SAE Technical Paper 2012-01-1586.

Turner, J. W. G., Pearson, R. J., Curtis, R and Holland, B. (2009), *Effects of Cooled EGR Routing on a Second-Generation DISI Turbocharged Engine Employing an Integrated Exhaust Manifold,* SAE Technical Paper 2009-01-1487.

Turner, J. W. G., Pearson, R. J., Holland, B. and Peck, R. (2007), *Alcohol Based Fuels in High Performance Engines*, SAE Technical Paper 2007-01-0056.

Turner, J. W. G., Pearson, R. J., Purvis, R., Dekker, E., Johansson, K. and Bergström, K. (2011), *GEM Ternary Blends: Removing the Biomass Limit by using Iso-Stoichiometric Mixtures of Gasoline, Ethanol and Methanol*, SAE Technical Paper 2011-24-0113.

Turner, J. W. G., Popplewell, A., Patel, R., Johnson, T. R., Darnton, N. J., Richardson, S., Bredda, S. W., Tudor, R. J., Bithell, C. I., Jackson, R., Remmert, S. M., Cracknell. R. F., Fernandes, J. X., Lewis, A. G. J., Akehurst, S., Brace, C. J., Copeland, C., Martinez-Botas, R., Romagnoli, A. and Burluka, A. A. (2014), *Ultra Boost for Efficiency: Extending the Limits of Extreme Engine Downsizing,* SAE Technical Paper 2014-01-1185.

Varde, K. S. and Manoharan, N. K. (2009), *Characterisation of Exhaust Emissions in an SI Engine using E85 and Cooled EGR*, SAE Technical Paper 2009-01-1952.

Wallner, T. and Frazee, R. (2010), *Study of Regulated and Non-Regulated Emissions from Combustion of Gasoline, Alcohol Fuels and their Blends in a DI-SI Engine,* SAE Technical Paper 2010-01-1571.

White, T. L. (1902), *Alcohol as a Fuel for the Automobile Motor*, SAE Technical Paper no. 070002.

Williams, D. J. R. (2002), *The effect of charge stratification on the combustion and emissions of a spark-ignition internal combustion engine*, PhD Thesis, Brunel University London.

Withrow, L. and Boyd, T. A. (1931), *Photographic Flame Studies in the Gasoline Engine*, Industrial and Engineering Chemistry, Vol. 23, No. 5, pp. 539-547.

Withrow, L. and Rassweiler, G. (1936), *Slow motion shows knocking and non-knocking explosions*, SAE Jour 39.2, pp. 297-303.

Woods, J. and Bauen, A. (2003), *Technology Status Review and Carbon Abatement Potential of Renewable Transport Fuels in the UK*, London: Imperial College, URN 03/982.

Woschni, G. (1967), *A Universally Applicable Equation for Instantaneous Heat Transfer Coefficient in the Internal Combustion Engine*, SAE Technical Paper 670931.

Yacoub, Y., Bata, R. and Gautam, M. (1998), *The Performance and Emissions Characteristics of C_1-C_5 Alcohol-Gasoline Blends with Matched Oxygen Content in a Single-Cylinder Spark Ignition Engine*, Proc. Inst. Mech. Engrs., Vol. 212, Part A.

Yang, C. Zhao, H. and Megaritis, T. (2009), *In-Cylinder Studies of CAI Combustion with Negative Valve Overlap and Simultaneous Chemiluminescence Analysis*, SAE Technical Paper 2009-01-1103.

Yeliana, Cooney, C., Worm, J. and Naber, J. D. (2008), *The Calculation of Mass Fraction Burn of Ethanol-Gasoline Blended Fuels Using Single and Two-Zone Models*, SAE Technical Paper 2008-01-0320.

Young, M. B. (1981), *Cyclic Dispersion in the Homogeneous-Charge Spark Ignition Engine – A Literature Survey*, SAE Technical Paper 810020.

Zack, G. W., Rogers, W. E. and Latt, S. A. (1977), *Automatic measurement of sister chromatid exchange frequency*, J. Histochem. Cytochem., Vol. 25, Iss. 7, pp. 741-753.

Zhao, F., Lai, M-C. and Harrington, D.L. (1997), *Automotive spark-ignited direct-injection gasoline engines,* Progress in Energy and Combustion Science, Vol. 25, No. 5, pp. 437-562.

Zhao, H. (2009), *Advanced direct injection combustion engine technologies and development: Gasoline Engines*, Woodhead Publishing Ltd: Cambridge, UK. ISBN 978-1-84569-389-3.

Zhao, H., Hu, J. and Ladommatos, N. (1999), *Spray and Diesel Combustion Studies in a specially designed single cylinder engine*, Journal of KONES, Vol. 6, No. 1-2, pp. 193-203.

Zhao H. and Ladommatos N. (2001), *Engine Combustion Instrumentation and Diagnostics*, SAE: Warrendale, USA. ISBN 978-0-76-800665-0.

Zhao, H., Peng, Z. and Ma, T. (2004), *Investigation of the HCCI/CAI Combustion Process by 2-D PLIF Imaging of Formaldehyde*, SAE Technical Paper 2004-01-1901.